Thermal transport in
van der Waals Solids and Inorganic Clathrates
from first-principles calculations

DANIEL O. LINDROTH

Typeset in X∃LATEX with Times Ten and Akzidenz-Grotesk

Cover: The left jar displays a transition metal dichacogenide, disturbed by vibrations. In front are calculated results for the lattice thermal conductivity in WSe_2 and WS_2. The right jar displays the crystal structure of a type I clathrate. In front are the computed lifetimes for the clathrate $Ba_8Ga_{16}Ge_{30}$.

Thermal transport in
van der Waals Solids and Inorganic Clathrates
from first-principles calculations

DANIEL O. LINDROTH
Department of Physics
Chalmers University of Technology

———

Abstract

Energy management is arguably one of the defining challenges for our modern societies. An ever-increasing demand for energy has to be balanced with the requirement for a sustainable energy economy that minimizes the human impact on the environment. Materials and their ability to transport both electrical and thermal currents play a key role in this area as they are essential components in energy extraction, transport, storage, and consumption technologies. On the macroscopic level, electrical and thermal transport in materials can be described by a set of coupled phenomenological relations that contain material specific transport coefficients. On the microscopic level, these transport coefficients are governed by chemical composition and the specific arrangement of the constituent atoms, the so-called microstructure. Since relatively small differences in this regard can have a dramatic impact on the macroscopic behavior of a material, a detailed understanding of the underlying processes and couplings is essential for materials development and optimization.

In this thesis, the thermal conductivity in two classes of materials of current and future technological importance has been investigated using electronic structure calculations (density functional theory) in combination with methods from statistical physics (Boltzmann transport theory). The first two papers included in this thesis deal with van-der-Waals solids, layered materials that are currently attracting tremendous attention in the scientific community due to their exciting combination of electrical, optical, and thermal properties. In this context, the present thesis provides predictions and a detailed analysis of the lattice thermal conductivity in Mo and W-based transition metal dichalcogenides. Furthermore, a model is developed to explain the extreme structure sensitivity of the conductivity and calculations are presented that elucidate chemical trends and establish bounds.

The third and fourth paper deal with clathrates, inclusion compounds that have been found to exhibit a combination of transport properties that are very well suited for thermoelectric applications. These materials exhibit extremely small thermal conductivities. The present thesis provides an in-depth analysis of the lat-

tice dynamics of these materials, with a special focus on the thermal conductivity and the so-called phonon-glass behavior.

The present thesis provides a stepping stone for future investigations of transport processes in van-der-Waals solids and clathrates, which eventually should lead to the development of devices with higher energy efficiency and better materials for energy extraction technologies.

LIST OF PUBLICATIONS

This thesis consists of an introductory text and the following papers:

I   **Microscopic Origin of Thermal Conductivity Reduction in Disordered van der Waals Solids**
Paul Erhart, Per Hyldgaard and Daniel O. Lindroth
Chemistry of Materials **27**, 5511 (2015)

II   **Thermal expansion and transport in van der Waals solids**
Daniel O. Lindroth and Paul Erhart
Physical Review B **94**, 115205 (2016)

III **Chemical order and transport properties in an inorganic clathrate: Optimal structures by computational design**
Mattias Ångqvist, Daniel O. Lindroth and Paul Erhart
Chemistry of Materials **28**, 6877 (2016)

IV   **Electronic and lattice thermal conductivity in intermetallic clathrates: A first principles perspective**
Daniel O. Lindroth, Erik Fransson, Fredrik Eriksson, Joakim Brorsson, Anders Palmqvist and Paul Erhart
(In preparation)

The author's contributions to the papers:

I   The author carried out first principles calculations of phonon spectra and the lattice thermal conductivity.

II   The author carried out all of the calculations and was the main author of the manuscript.

III The author carried out the Boltzmann transport calculations.

IV   The author carried out the calculations of the lattice contribution to the thermal conductivity and was the main author of the manuscript.

Contents

1

Introduction

1.1 Energy as a resource

It is easy to take energy for granted. At dining tables around the world it is safe to say that the common theme of discussion probably is not the amount of joules needed for enabling the meal at hand. Yet, many joules were spent along the chain from production, to transportation and final preparation.

Energy is such an integral part of our lives that its importance can be hardly overstated, as modern societies are entirely dependent on it. On a personal level for water and food, sanitation, transportation, Internet and communication as well as lighting and heating of our homes. The questions concerning the availability of resources for energy production[1], and their stability over time must be considered among the most important questions for our societies today and in the future.

So, are there any reasons to worry about the available amount of energy in the future? If one compares the total primary energy supply (TPES, An estimate of the available primary energy sources in a region) of the world in 1973 to 2013 the supply has roughly doubled from 6.1 Gtoe (Giga ton of oil equivalent) to 14 Gtoe [2] (Fig. 1.1). At the same time the population has increased from 3.9 to 7.2 billion people, roughly a doubling as well. There is a strong positive correlation between the world population and the global energy consumption. This can be seen when comparing available data for the world population with the global energy consumption in the span from 1980 to 2012 (Fig. 1.2 (a)). Assuming that the world population

---

[1]Energy production and consumption are here used in the more colloquial sense, not in the sense as a violation of the *first law of thermodynamics* which states that energy cannot be created or destroyed, only transformed from one form to another [1].
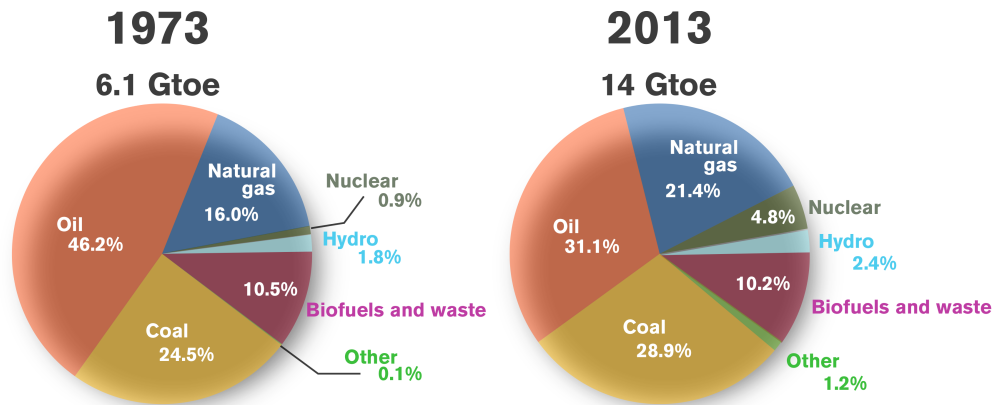
1973

6.1 Gtoe

2013

14 Gtoe

Figure 1.1: Total primary energy supply in the world for different primary energy sources in 1973 and 2013. The data is from the IEA report *Key World Energy Statistics 2015* [2]. The category *Other* includes smaller sources such as geothermal, solar and wind.

is a good estimator for the global energy consumption, up to linear order[2], a linear least squares fit provides a model for estimating the energy consumption based on population size. Using projections of the future world population [4] it is possible to estimate the future energy needs. In a high population scenario the global energy consumption is estimated to steadily increase. Also in a low population scenario the global energy consumption is estimated to increase up until 2050 when it will reach 16 Gtoe after which the demand will start to decline (Fig. 1.2 (b)).

To enable this increase in energy consumption, energy supply must increase as well. In 2013 the global TPES was 81.4 % of the available energy in the form of fossil fuels (coal, oil and natural gas), a small reduction from the 86.2 % in 1973. The oil and gas repositories formed over the last 600 million years [5]. Also coal formed over geological time scales and the fossil fuels are limited resources in that there are finite reserves to extract. Since the reserves are finite the extraction must at some point reach its maximal rate and this sets a physical limit to the possible supply. The point in time where this happens has been coined *the oil peak* [6, 7]. The term *peak* may be used in the context of any type of finite resource and it is reasonable to talk about *peak coal* and *peak gas* besides *peak oil*. Since the contribution of fossil fuel to the TPES is so dominant there is a real concern if the fossil fuels peak without a realistic alternative at hand. According to the estimate

---

[2]There are some deviations from a linear relation connected to economic cycles and stock market crashes. Following the Black Monday stock market crash of October 1987 [3] there is a pause in the growth of global energy consumption during the following years. Similar, in 2009 there is a violation of the linear trend following the stock market crash of 2008.
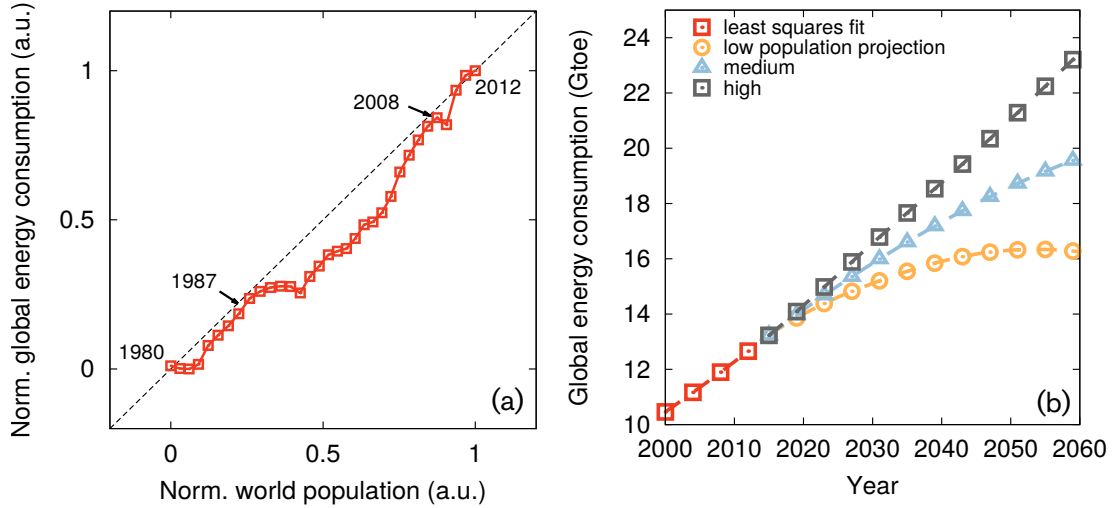
Figure 1.2: (a) Correlation of the world population and yearly total primary energy consumption between the year 1980 and 2011. The data is normalized to the unit interval and received from[4, 10]. (b) Estimations of the future global energy consumption based on three different projections of low, medium and high population growth[4]. The estimates are calculated with a linear model from a least squares fit to the data in the left pane. This gives a connection between yearly energy consumption and the population used in the projections.

the supply necessarily needs to steadily increase. Although debated, claims that the peak of oil is close have been made [8, 9].

There is another concern in the use of fossil fuels as well. The energy source mainly consists of carbon and combustion results in production of carbon dioxide, CO_2, that is deposited into the atmosphere. Carbon dioxide is a so called greenhouse gas in that it is infrared active. The greenhouse gases allow high frequency sunlight to enter the Earth system, heating the ground without any interference. But since the frequencies of the thermal radiation leaving the Earths surface is shifted to the infrared range, some of the radiation will interact with the greenhouse gases and be trapped in the atmosphere. In effect this results in a reduction of the energy flux out of the Earth system resulting in *Global Warming*. The predicted climate change associated with Global Warming is assumed to present a future threat if the emission of CO_2 is not reduced in time to halt the increasing mean temperature of the Earth [11].

The dominating position of fossil fuels in the energy economy makes an exchange of the used resources to alternatives based on the current technologies unrealistic in the near future. And although the power of serendipity can be huge,

3

it is an unreliable force. Either way, better administration of fossil fuels is a reasonable strategy to handle either fossil peaks or overconsumption resulting in global warming. Increasing the efficiency of energy consumption e.g., by recuperation of waste heat can make a substantial contribution to the solution of this problem.

1.2 Energy transport

Most of the energy we utilize originates from the sun, where fusion of hydrogen releases large amounts of energy that reach the Earth in the form of electromagnetic radiation. On Earth the biosphere assimilates the energy mainly through photosynthesis. Historically a lot of this energy has been stored in the form of fossil fuels (oil, coal and natural gas), which formed as the result of geological processes. Besides the sun, we also utilize energy stored in nuclear fuels and to a lesser extent geothermal energy originating from the Earth's core. Solar, nuclear, and geothermal are examples of primary energy sources, that is energy captured directly from the environment. Secondary forms of energy have been derived from a primary source; this includes for example electricity but also fossil as well as synthetic fuels such as gasoline, ethanol and hydrogen [12].

Electricity is often the most useful form of energy in terms of applications. Several processes can be used for transforming different types of energy into electricity, including e.g., electromagnetic induction, the piezoelectric effect, the photoelectric effect, and the thermoelectric effect. Among these, electromagnetic induction dominates as it is the process used in almost all commercial generation of electricity. With respect to this thesis the thermoelectric effect is very interesting because of its importance of low lattice conductivity for the efficiency in thermoelectric materials [13, 14].

1.2.1 Energy transport as a challenge

The energy stored in fossil fuels can not be used directly, it has to be processed and converted to a form suitable for use. This is a general theme[3] for any kind of utilization of an energy source (Fig. 1.3). There are three fundamental sources of energy [12]. Dominating is energy originating from the sun, followed by nuclear energy and lastly geothermal energy originating from inside the Earth. Fossil fuels originated as energy from the sun accumulating in the biomass from where parts eventually ended up in sedimentary rocks that under the right conditions transformed into coal, oil and gas. To access the stored energy the fuel needs to be

---

[3]With some exceptions, heating by direct sunlight is one such exception.

4
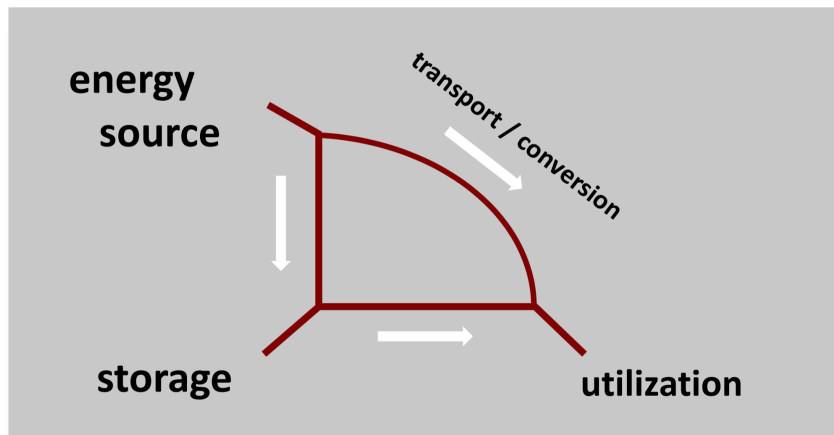
Figure 1.3: After extraction from the energy source it is necessary to store the energy if not directly used. Regardless of the path taken transport processes are present and also one to several types of energy conversion steps.
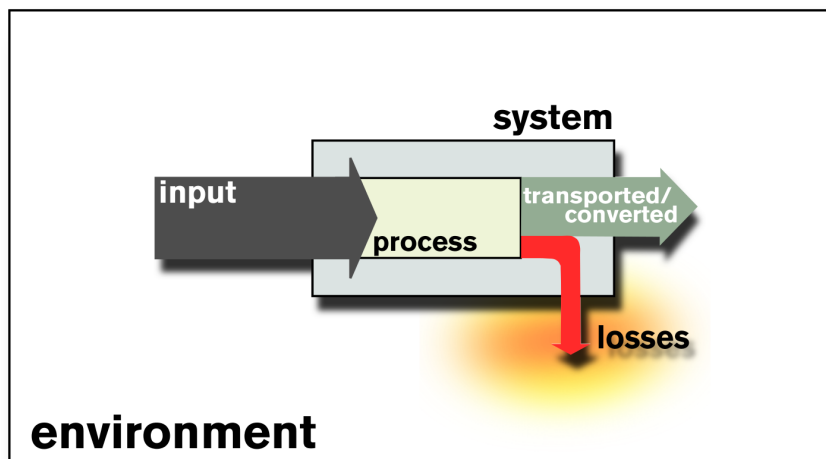
Figure 1.4: Schematics of energy interacting with a system. The energy input is converted and transported through a redirection resulting in useful energy output of transported/converted energy. At the same time, inevitably energy is dissipated to the surrounding environment due to irreversible processes within the system.

5

combusted and further transformed into a useful form e.g., electricity or mechanical work.

In any type of process involving energy transport or conversion there will be energy dissipation to internal degrees of freedom due to irreversibility [15, 16]. This dissipation will eventually transfer into the surrounding environment resulting in energy losses (Fig. 1.4). The result is a degradation of the energy used as input. For thermal processes these losses are substantial. The disadvantage with dissipated energy is its disordered nature with no clear direction. This makes utilization difficult.

1.2.2 Scavenging (waste) heat

Because of the dominating position of thermal processes in the economy, technologies that scavenge dissipated energy and thereby raise the overall energy efficiency are of great interest.

Heat engines convert heat into useful, most commonly mechanical or electrical, energy. A specific type of heat engine is the thermoelectric generator (TEG) [13], which converts heat into electrical current by exploiting the thermoelectric effect. The efficiency is here dependent on several factors, one of which is the thermal conductivity with lower values providing better efficiency. To make TEGs economically feasible the efficiency needs to be high enough, higher than it is today. Because of this an understanding how to engineer the thermal conductivity is important.

At the same time, knowledge about how to lower the conductivity can be used to achieve the opposite, namely increasing the conductivity. This has important implications for heat management in devices. In particular, a high thermal conductivity is important for applications in electronics and opto-electronics to prevent overheating and potential loss of components.

2

Background

2.1 Overview

Thermal transport and conversion can quantitatively be understood from either the macroscopic or the microscopic perspective. Macroscopic theories regarding energy transport are within the field of thermodynamics for systems out of equilibrium. In section 2.2 is non-equilibrium thermodynamics introduced. The notion of entropy in a non-equilibrium setting is discussed, together with its relation to thermodynamic forces and fluxes in the case of thermal and charge imbalance. The corresponding phenomenological laws with the Onsager coefficients are then introduced, together with the relations for the electrical and thermal conductivity, as well as the Seebeck and Peltier coefficients. Because of the close relation to non-equilibrium thermodynamics, and the potential role in heat recuperation, the section ends with an introduction to thermoelectric generation and efficiency, together with the concept of the thermoelectric figure-of-merit.

The following section 2.3, takes a qualitatively look on thermal transport from the kinetic point of view. An estimate for the thermal conductivity is derived by the introduction of a mean free path, mean velocity and specific heat for fluxes of particles in a temperature gradient, while connecting the energy flux with the temperature gradient through Fourier's law.

Section 2.4 introduces quantitative microscopic transport theory through Boltzmann transport theory for both electrons and phonons. The relaxation time approximation is introduced together with a discussion of lifetimes.

Finally, section 2.5 introduces the two classes of material of interest, van der Waals solids and inorganic clathrates.

7

2.2 Non-equilibrium thermodynamics

Tracing all degrees of freedom on the atomic scale is all but tractable since the number of constituents in an analysis of everyday objects typically is of the order 10^{23}. The pragmatic stance is to look for and analyze properties where the degrees of freedom collectively average into macroscopically observable effects, including time- as well as spatial averaging.

In general, classical thermodynamics is the study of the macroscopic properties of systems in *equilibrium*. When in equilibrium, the macroscopic properties are both static and spatially homogeneous, i.e., they do not vary with time and remains constant over the extent of the system. The macroscopic properties are used as state variables, i.e., macroscopic variables that as a set uniquely define the equilibrium state of the system.

One obvious limitation of this description is the lack of time-dependence. In reality, systems can change states from one instant to another. A hot cup of coffee left on the desk is out of equilibrium, it will continuously lose energy through heat until reaching the equilibrium temperature of its surroundings. The end of this process is naturally called the *final state* of the cooling process. Further, assuming spatial homogeneity, one can imagine the beginning of this cooling process as being released from another equilibrium state at a higher temperature, then called the *initial state*. Classical thermodynamics here brackets the cooling process but gives little insight into the actual progression of the cooling. When regarding change within the context of classical thermodynamics, at best, one can view the system as changing from one equilibrium state into another, without departure from the continuum of equilibria. One prerequisite for such evolution is that the transition between states is slow enough, even infinitesimally slow to ensure that the system never leaves equilibrium. Such a process is then called *quasi-static*. At best, this would be an approximation of the real change, and as important, it says nothing about real rates.

A *reversible process* is by definition a quasi-static process, such that both the system and its surroundings go back to the original states if the process is reversed. Such requirements rule out the previous example of cooling. Since cooling is the process of losing energy to the surroundings through heat, the process reversed would be the surroundings losing energy to the coffee through heat. For such reversal, the ambient temperature needs to be higher than the temperature of the coffee, all the way up to the temperature at the initial state. A process that is not reversible is called *irreversible* and includes quasi-static processes that are not reversible, as well as processes that evolve in finite time.

In contrast to the limitations due to lack of dynamics in classical thermodynam-

ics,[1] *non-equilibrium thermodynamics* concerns the study of systems with macroscopic properties subject to time-dependence as well as spatial variations. This time-dependence essentially makes non-equilibrium thermodynamics to be of an irreversible nature, and the general theory is interchangeably referred to as *irreversible thermodynamics*.

In practice, to treat irreversible systems, the most common approach is suitable when processes responsible for internal equilibration occur on time-scales much shorter than the time-scale for macroscopic change in the state variables. It is then possible to evoke the *local-equilibrium hypothesis*. The hypothesis postulates that the total system in question can be artificially divided into subsystems, in such a way that each sub-system is effectively in equilibrium, and can be treated as a macroscopic thermodynamic system. The advantage is that classical thermodynamics is valid within each sub-system and all thermodynamic variables are locally well defined, including entropy and temperature. The hypothesis further assumes that the equilibrium state in a sub-system can change in time due to interactions with neighboring sub-systems and that the state variables can be assumed to be continuously dependent on time and spatial coordinates. In this thesis, the focus will be on systems where the local-equilibrium hypothesis is assumed to be valid.

2.2.1 Entropy and the second law of thermodynamics

In classical thermodynamics, entropy has a central role due to the second law of thermodynamics, which states that the total entropy in a closed system always increases. From a macroscopic perspective when concerned with thermal interactions, the entropy S in thermodynamics is naturally defined as the state function related to the exact differential one obtains after dividing the inexact differential of added heat δQ with the system temperature T, which gives the relation $dS = \delta Q/T$. Hence, entropy depends on the temperature being a well-defined quantity. For a system out of equilibrium, the assumption of a local-equilibrium provides a bridge to definitions of entropy in systems out of equilibrium.

The validity of the local-equilibrium hypothesis implies that the description of local state variables in equilibrium is valid even when the full system is out of equilibrium. The hypothesis enables a definition of entropy for a system out of equilibrium in such a way that the out of equilibrium entropy depends on the same state variables as for the system in equilibrium. The specific entropy, defined as the entropy per unit mass, is then a continuous function in space and time. When the system is described as a fluid of N different components, the specific entropy is a function of the specific energy u, specific volume v, as well as the mass fractions

---

[1]One can argue that thermodynamics, in this regard is an unfortunate name, *thermostatics* would be more proper. However, as for now, the name is cemented into the subject.

c_j of species j

$$s(\boldsymbol{r}, r) = s[u(\boldsymbol{r}, t), v(\boldsymbol{r}, t), c_1(\boldsymbol{r}, t), \dots, c_N(\boldsymbol{r}, t)]. \tag{2.1}$$

In the absence of convective transport, the equivalent differential form is

$$\mathrm{d}s = \left(\frac{\partial s}{\partial u}\right)_{v,c_k} \mathrm{d}u + \left(\frac{\partial s}{\partial v}\right)_{u,c_k} \mathrm{d}v + \sum_{j \neq k}^{N} \left(\frac{\partial s}{\partial c_k}\right)_{u,v,c_j} \mathrm{d}c_k, \tag{2.2}$$

where the expansion coefficients are defined as $1/T$, p/T and μ_k/T respectively. Here, T is the temperature, p the pressure and μ_k the chemical potential for particle species k. With these quantities defined, we have the following equation

$$\mathrm{d}s = \frac{1}{T}\mathrm{d}u + \frac{p}{T}\mathrm{d}v - \sum_{k=1}^{N} \frac{\mu_k}{T}\mathrm{d}c_k. \tag{2.3}$$

When the local equilibrium hypothesis holds, the intensive parameters are effectively in equilibrium on the macroscopic scale. Still, there is a macroscopic evolution dependent on local interactions between subsystems. The time evolution of the specific entropy is directly expressed through the time derivative of Eq. (2.3)

$$\frac{\mathrm{d}s}{\mathrm{d}t} = \frac{1}{T}\frac{\mathrm{d}u}{\mathrm{d}t} + \frac{p}{T}\frac{\mathrm{d}v}{\mathrm{d}t} - \sum_{k=1}^{N} \frac{\mu_k}{T}\frac{\mathrm{d}c_k}{\mathrm{d}t}. \tag{2.4}$$

This equation is central in the theory, since it is used for identification of entropy production. Using conservation laws for the total energy balance, total mass balance, as well as mass fraction balance, Eq. (2.4) is a general statement determining the time evolution of the specific entropy. As discussed in appendix A.2, the equation for local entropy balance is

$$\rho\frac{\mathrm{d}s}{\mathrm{d}t} = -\nabla \cdot \boldsymbol{J}_s + \sigma_s, \tag{2.5}$$

where the entropy flux $\boldsymbol{J}_s$ originates from thermodynamic imbalance to neighboring systems, and the entropy production term is subject to a local constraint $\sigma_s \geq 0$.

2.2.2 Thermodynamic forces and fluxes

When there is a temperature difference in a system, the response is an energy flux with an equilibrating effect on the temperature difference. This equilibration is

associated with heat transport through a heat flux $\boldsymbol{J}_q$. Assuming a linear response, the phenomenological law for heat conduction, Fourier's law, is written as

$$\boldsymbol{J}_q = -\kappa \nabla T, \tag{2.6}$$

where the proportionality tensor κ is known as the thermal conductivity. When entropy is a dependent quantity, the entropic representation is more suitable, in which case Fourier's law is expressed through [2]

$$\boldsymbol{J}_q = \kappa T^2 \nabla \frac{1}{T}. \tag{2.7}$$

The gradient of the inverse of the temperature field acts as the cause, producing the effect of a heat current. It is natural to interpret this cause as a thermodynamic force. When there is no volume change or exchange of matter, Eq. (2.3) reduces to

$$T \frac{\mathrm{d}s}{\mathrm{d}t} = \frac{\mathrm{d}u}{\mathrm{d}t}. \tag{2.8}$$

With the use of the corresponding balance equation for the internal energy

$$\rho \frac{\mathrm{d}u}{\mathrm{d}t} = -\nabla \cdot \boldsymbol{J}_q, \tag{2.9}$$

and Eq. (2.5) for entropy balance, the entropy production associated with heat conduction is

$$\sigma_s^q = \boldsymbol{J}_q \cdot \nabla \frac{1}{T}, \tag{2.10}$$

given that the entropy flow is defined through the heat flow

$$\boldsymbol{J}_s = \frac{\boldsymbol{J}_q}{T}, \tag{2.11}$$

in analogy with classical thermodynamics. The entropy production term is in the form of a flux multiplied by the corresponding thermodynamic force.

If a system is at a constant temperature but has a difference in the electrochemical potential due to an external potential $\varphi = \mu/e$, an electric current flows through the system. According to Ohm's law, the electric current $e\boldsymbol{J}_n$ [3], defined as the particle flux times the elementary charge, is the effect of the external potential acting as a force

$$e\boldsymbol{J}_n = -\sigma \cdot \nabla \varphi, \tag{2.12}$$

---

[2]Using the identity $\frac{\partial}{\partial x} \frac{1}{T} = -T^{-2} \frac{\partial T}{\partial x}$.

[3]The electrical current is here defined so that the direction of positive charge carriers corresponds to a positive current.

where σ is the electrical conductivity tensor. Following a treatment similar to the case of heat flow, with the addition of charge/mass conservation, the entropy flux is

$$J_s = \frac{\varphi}{T} e J_n = \frac{\mu}{T} J_n, \tag{2.13}$$

The entropy production is then

$$\sigma_s = -\frac{1}{T} \nabla \left(\frac{\mu}{e} \right) \cdot \left(-e J_n \right) = \frac{1}{T} \nabla \mu \cdot J_n. \tag{2.14}$$

The entropy production is here associated with potential energy transforming into heat.

If both the temperature and the electrochemical potential varies in the system, the heat flux and the electrical current couples. Assume the system operates under steady state, so that any time dependence vanish. For the coupled system, define a total energy density current J_u, a particle current J_n and an entropy current J_s. Both the total energy current and the particle current is source free, and must therefore be divergence free, i.e., both $\nabla \cdot J_u$ and $\nabla \cdot J_n$ are equal to zero. The entropy on the other hand is not source free, and has source term σ_s, so that $\nabla \cdot J_s = \sigma_s$. From the corresponding balance equations, Eq. (2.3) gives a relation between the fluxes

$$T J_s = J_u - \mu J_n. \tag{2.15}$$

By taking the divergence of this relation, using that the total energy and the particle current is source free, gives the entropy production as

$$\sigma_s = \nabla \cdot J_s = \nabla \frac{1}{T} \cdot J_u - \nabla \frac{\mu}{T} \cdot J_n. \tag{2.16}$$

Define the heat current as $J_q = T J_s$, then Eq. (2.15) gives the heat flux as

$$J_q = J_u - \mu J_n. \tag{2.17}$$

This definition agrees with the intuition of heat as the difference between the total energy and energy related to external energy. The divergence of this expression gives the relation

$$\nabla \cdot J_q = -\nabla \mu \cdot J_n, \tag{2.18}$$

that is, increase in the heat current corresponds to the decrease in the potential energy flux, the potential energy converts into heat. Expressing the entropy production with the use of heat flux gives

$$\sigma_s = \nabla \frac{1}{T} \cdot J_q - \frac{1}{T} \nabla \mu \cdot J_n. \tag{2.19}$$

Using Eq. (2.18) the entropy production can be expressed in a symmetric form

$$\sigma_s = \nabla\frac{1}{T} \cdot \boldsymbol{J}_q + \frac{1}{T}\nabla \cdot \boldsymbol{J}_q, \tag{2.20}$$

showing that the entropy production in part is due to heat transfer caused by a temperature gradient, and part from dispersion of potential energy into heat.

2.2.3 Phenomenological laws and transport coefficients

In general, assuming linear coupling, each flux component can be expanded with phenomenological constants multiplying the corresponding thermodynamic forces causing the fluxes. The phenomenological constants are then to be determined either by experiment or by microscopic theory. The coupling between flux components and the thermodynamics forces F_j are expressed through the relations

$$J_i = \sum_j L_{ij} F_j. \tag{2.21}$$

The phenomenological coefficients L_{ij} are also known as Onsager coefficients or kinetic coefficients. As shown by Onsager, the off-diagonal coefficients fulfill a symmetry condition $L_{ij} = L_{ji}$ when the system is microscopically reversible as a result of the time reversal invariance of physical laws. When the entropy production is stated as the sum of flux and force pairs, using the Onsager coefficients, the entropy production is

$$\sigma_s = \sum_i J_i F_i = \sum_{i,j} F_i L_{ij} F_j \geq 0. \tag{2.22}$$

In the case of coupled heat and electron transfer, the phenomenological equations are

$$-\boldsymbol{J}_n = L_{11}\frac{1}{T}\nabla\mu + L_{12}\nabla\frac{1}{T}, \tag{2.23}$$

$$\boldsymbol{J}_q = L_{21}\frac{1}{T}\nabla\mu + L_{22}\nabla\frac{1}{T}, \tag{2.24}$$

when the fluxes are chosen as the heat flux and the particle flux. [4]

Ohm's law states that the electrical conductivity is the ratio between the electric current and the gradient of the chemical potential at thermal equilibrium. Solving

---

[4]To simplify, it is here assumed that the system is isotropic, so that each type of Onsager coefficient can be represented with a single value instead of a second rank tensor.
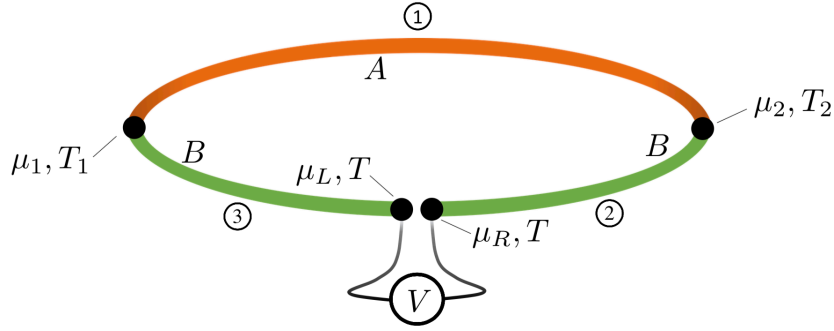
Figure 2.1: Schematic of a thermocouple consisting of joined materials A and B, probed with an ideal voltage meter. The junctions are assumed to be maintained at temperatures T_1 and T_2, resulting in the build-up of an electrochemical potential μ. The voltmeter is assumed to block the charge current, while fully permitting heat to flow so that the temperature is the same on both the immediate left and right side of the voltmeter.

for the ratio $-e\boldsymbol{J}_n/\nabla(\mu/e)$ when $\nabla(1/T) = 0$ in the first phenomenological equation, directly gives the electrical conductivity σ as

$$\sigma = e^2 \frac{L_{11}}{T}. \tag{2.25}$$

The thermal conductivity varies with temperature through an explicit factor of $1/T$. Inverting the expression gives the first Onsager coefficient as

$$L_{11} = \frac{\sigma}{e^2} T, \tag{2.26}$$

expressed through measurable properties.

According to Fourier's law, the thermal conductivity is the heat current per unit thermal gradient when there is no particle current. Assuming $\boldsymbol{J}_n = 0$, solving for the ratio $-\boldsymbol{J}_q/\nabla T$ in the phenomenological equations, while making use of the reciprocity $L_{12} = L_{21}$, gives the thermal conductivity κ expressed in Onsager coefficients and the temperature

$$\kappa = \frac{L_{11}L_{22} - L_{12}^2}{L_{11}T^2}. \tag{2.27}$$

Showing that the thermal conductivity should have a temperature dependence with an explicit factor of $1/T^2$.

The phenomenological equations can also be applied to a thermocouple (Fig. 2.1). A thermocouple consists of two different conductors or semiconductors,

joined at each end. Keeping each junction at different temperatures induces charge carrier diffusion in the system and the build-up of a chemical potential. Assume an idealized voltage meter inserted into one of the legs of the thermocouple. The voltage meter is assumed to block passage of electric current, while freely allowing heat to flow. The electrochemical potential will then be different on each side of the voltage meter, while the temperature will be the same. When there is no current, i.e., $J_n = 0$, the first phenomenological equation gives the relation

$$\nabla \mu = \frac{L_{12}}{L_{11}T} \nabla T. \tag{2.28}$$

This equation can be solved along three different paths, one over the material A, as well as the two separate parts in material B, separated by the volt meter (Marked as 1, 2 and 3 in Fig. 2.1), which gives the system of equations

$$\mu_2 - \mu_1 = \int_{T_1}^{T_2} \frac{L_{12,A}}{T L_{11,A}} \, \mathrm{d}T, \tag{2.29}$$

$$\mu_2 - \mu_L = \int_{T}^{T_2} \frac{L_{12,B}}{T L_{11,B}} \, \mathrm{d}T, \tag{2.30}$$

$$\mu_R - \mu_1 = \int_{T_1}^{T} \frac{L_{12,B}}{T L_{11,B}} \, \mathrm{d}T. \tag{2.31}$$

These equations can be solved for the potential V over the voltage meter by eliminating μ_1 and μ_2

$$V = \frac{\mu_R - \mu_L}{e} = \int_{T_1}^{T_2} \left(\frac{L_{12,A}}{eT L_{11,A}} - \frac{L_{12,B}}{eT L_{11,B}} \right) \mathrm{d}T. \tag{2.32}$$

Defining the absolute Seebeck coefficient for material A as

$$\alpha_A = -\frac{L_{12,A}}{eT L_{11,A}}, \tag{2.33}$$

and define α_B similarly for material B, gives the Seebeck coefficient for the thermocouple as

$$\alpha_{AB} = \alpha_B - \alpha_A. \tag{2.34}$$

The sign in Eq. (2.33) is chosen such that an increase in α_{AB} corresponds to a particle current in the A to B direction at the hotter junction. With the use of Eq. (2.26) the L_{12} coefficient is expressed through physical parameters

$$L_{12} = -\alpha eT L_{11} = -\frac{\alpha \sigma T^2}{e}. \tag{2.35}$$

With expressions for L_{12} and L_{11}, the L_{22} coefficient in Eq. (2.27) can be solved for

$$L_{22} = \alpha^2 \sigma T^3 + \kappa T^2. \tag{2.36}$$

With L_{11}, L_{12} and L_{22} determined, it is now possible to express the entropy flux in terms of measurable quantities

$$\boldsymbol{J}_s = \alpha e \boldsymbol{J}_n + \kappa T \nabla \frac{1}{T}. \tag{2.37}$$

This expression presents a physical interpretation of the Seebeck coefficient, as the amount of entropy transported by each charge carrier in the charge carrier flux. This is an additional contribution to the entropy flux, compared to the decoupled entropy current that is directly associated with the heat current $\boldsymbol{J}_q$.

In the special case of charge carrier flux under isothermal conditions, the heat flux in the phenomenological equation, Eq. (2.24), can be solved in terms of measurable quantities

$$\boldsymbol{J}_q = \alpha T e \boldsymbol{J}_n. \tag{2.38}$$

If this flux is within a thermocouple, over a junction from material A to material B, the difference in heat current over the junction has to be discontinuous by an amount

$$\Delta Q_{AB} = \boldsymbol{J}_{q,B} - \boldsymbol{J}_{q,A} = (\alpha_B - \alpha_A) T e \boldsymbol{J}_n = \alpha_{AB} T e \boldsymbol{J}_n. \tag{2.39}$$

The Peltier coefficient, denoted π_{AB}, is now defined as the amount of heat per unit current that must be supplied, or dissipated, at the junction

$$\pi_{AB} = \frac{\Delta Q_{AB}}{e \boldsymbol{J}_n} = \alpha_{AB} T. \tag{2.40}$$

This shows that the Peltier- and Seebeck coefficients are dependent to each other, related by a factor of T. The two physical effects are not independent. The Seebeck effect corresponds to thermoelectric a transformation of heat flow into an electromotive force. The Peltier effect is the process in reverse, transformation of electric energy into external heat flow.

2.2.4 Thermoelectric generation and thermodynamic efficiency

A heat engine operates under the working principle of transporting thermal energy from a heat source into the engine consisting of some thermodynamic substance

capable of converting part of the transported energy into power output. The working substance then rejects the excess energy to a colder reservoir. This rejection is necessary which can be understood by considering a heat engine working in cycles. Along with the thermal energy transported, there is an influx of entropy to the working substance. If the engine is irreversible, there is also entropy produced in the conversion process. For the thermodynamic system to go back to the original state of the cycle, entropy must leave the system, usually by transport of heat to the heat sink.

The efficiency η of the energy conversion is defined as the ratio between the energy transformed into work and the energy supplied to the heat engine. For an idealized reversible heat engine there is no entropy produced and therefore characterizes the maximal efficiency achievable by a heat engine. The efficiency of a reversible heat engine is called the Carnot efficiency and is only dependent on the temperature of the energy source T_H and the temperature of the reservoir for heat rejection T_C, such that

$$\eta_{Carnot} = 1 - \frac{T_C}{T_H}. \tag{2.41}$$

For real heat engines the production of entropy further reduces the efficiency by some factor. The factor

$$\gamma = \frac{\eta}{\eta_{Carnot}} \tag{2.42}$$

is then a measure of the deviation from an ideal heat engine, and the value of γ is one important factor when choosing an engine for real applications.

The thermoelectric generator constitutes a specific class of heat engines. The basic unit in the generator is two semiconductors, one of n-type and the other of p-type, joined by a conductor at the hotter side to form a thermocouple. At the colder side, external conductors are attached to the thermocouple (Left panel in Fig. 2.2) allowing for charge carrier diffusion, with the effect of increasing electrostatic potential between the attached wires. The n-type semiconductor has a negative Seebeck coefficient resulting in electrons being diffused from the hotter side to the colder side. In the p-type semiconductor the Seebeck coefficient is positive, so that electron holes is the charge carrier diffusing to the colder side. Closing the circuit over an electric load results in an electric current powering the load, as long as there is a thermal difference maintained over the thermocouple.

A large thermopower together with a high capability of charge conduction and ability to maintain a thermal gradient is essential for an efficient thermoelectric generator. High thermopower strengthens the coupling between heat and the charge carrier current, a large electric conductivity reduces energy losses due to Joule heating, and low thermal conductivity ensures that the thermal gradient
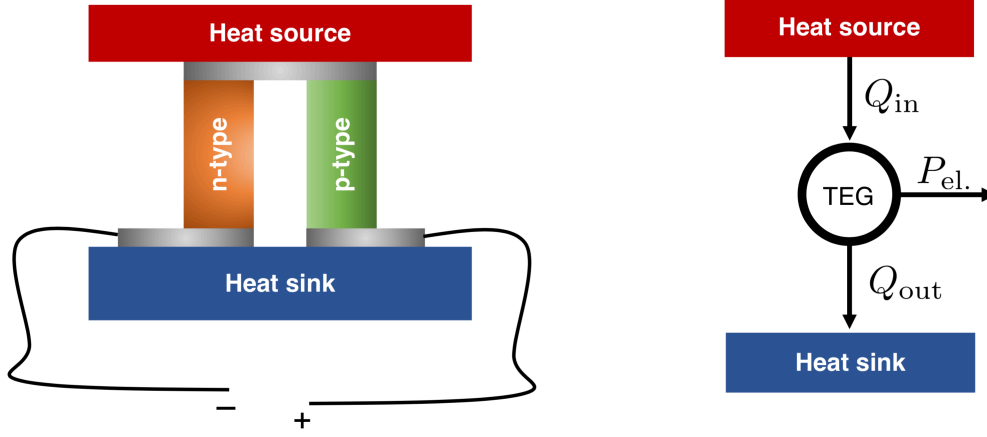
Figure 2.2: The left panel shows the schematics of a basic thermoelectric generator consisting of a thermocouple with legs out of an n-type semiconductor and a p-type semiconductor. The Semiconductors are directly joined by a conductor at the hotter end. At the colder end conducting wires are attached to each leg. The right panel shows the schematics of a thermoelectric generator (TEG) as a heat engine. The generator absorbs heat Q_{in} at the hotter end, converts a portion of Q_{in} to electric power $P_{el.}$, and disposes excessive heat Q_{out} to the heat sink.
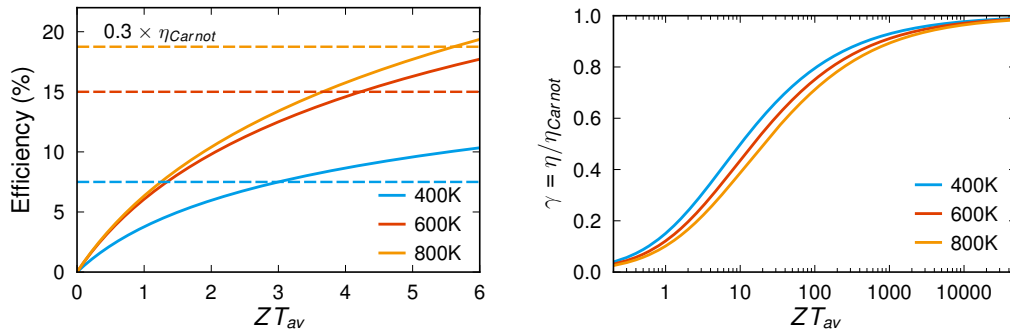
Figure 2.3: The left panel shows the thermodynamic efficiency η (solid lines) for a thermoelectric generator operating at three different temperatures relative a heat sink at 300K. The vertical dashed lines show the efficiency for heat engines operating at 30% of the Carnot efficiency at the same set of working temperatures. The right panel shows the reduced efficiency factor γ for the same temperature differences as in the left panel.

sustains. By formulating a dimensionless parameter, the thermoelectric figure of merit zT, a first measure of a materials suitability for thermoelectric applications is given as

$$zT = \frac{\alpha^2 \sigma}{\kappa} T.$$ (2.43)

To estimate the efficiency of a thermoelectric generator the ratio between the power output $P_{el.}$ and the heat absorbed from the heat source Q_{in} is formed (Fig. 2.2). With the use of the phenomenological expressions for the charge current and the heat current an expression for the reduced efficiency factor γ is derived

$$\gamma = \frac{\sqrt{1 + ZT_{av}} - 1}{\sqrt{1 + ZT_{av}} + T_C/T_H}.$$ (2.44)

Here, T_{av} is the average temperature of the heat source and the cooler reservoir, and ZT a figure of merit suitable when two materials are combined into a thermocouple

$$ZT = \frac{(\alpha_p - \alpha_n)^2 T}{\left(\sqrt{\kappa_n/\sigma_n} + \sqrt{\kappa_p/\sigma_p}\right)^2}.$$ (2.45)

Even though the material parameters in general are temperature dependent, the use of average values should produce values of ZT that are within 10% of the true ZT values [17]. In the theoretical limit of really high ZTs, the factor γ approaches one, and with that the efficiency approaches the Carnot efficiency (Right panel, Fig. 2.3).

When comparing the reduced efficiency for a thermoelectric generator, to the efficiency of other heat engines, it is seen that a thermoelectric generator with a ZT above three starts to become competitive to heat engines operating at 30% of the full Carnot efficiency (Left panel Fig. 2.3). Today, realistic values of ZT values is about one, a factor of three from being competitive with other technologies, efficiency considered. At the same time, others factors than the efficiency can be crucial for how suitable the technology is. Thermoelectric generators have attractive properties in that they are silent, reliable and scalable. These set of properties makes thermoelectric generators ideal for small-scale distributed power generation, for instance in remote locations [13].

2.3 Transport theory

Materials and their ability to transfer charge (electrical currents) and heat (thermal currents) play a key role in energy management as they are essential compo-

nents in energy extraction, transport, storage, and consumption technologies. On a macroscopic level electrical and thermal conduction in a material can be conveniently described using phenomenological theories e.g., in the form of Ohm's law in the case of electrical conduction and Fourier's law in the case of thermal conduction (see below). The corresponding equations contain transport coefficients such as the electrical conductivity, the Seebeck coefficient, or the thermal conductivity. These are tensorial quantities that are material specific and quantify the response to an external force such as an electric field or a thermal gradient[18].

For example, the thermal conductivity can be phenomenologically defined through Fourier's law

$$\boldsymbol{J} = -\kappa \cdot \nabla T, \tag{2.46}$$

where $\boldsymbol{J}$ is the heat current, which quantifies the rate at which thermal energy is transported as the result of a thermal gradient ∇T, and κ denotes the thermal conductivity tensor.

It is illuminating to examine thermal conductivity from a kinetic point of view as a transport problem in a monatomic gas. To this end, let us assume a stationary thermal gradient in the x-direction. When a particle moves from a region at temperature $T + \Delta T$ to a colder region at temperature T where it thermalizes it needs to give up an energy of $C\Delta T$ from the hotter region to equilibrate, where C is the specific heat. The particle will now be in thermal contact with the new region. Assuming that the length scale for thermalization is ℓ (Fig. 2.4), the expression for the temperature difference is

$$\Delta T = \ell \frac{\partial T}{\partial x}. \tag{2.47}$$

The thermal energy is proportional to the temperature $E \sim T$ and the mean velocity squared $E \sim v^2$. Hence, the mean velocity is proportional to the square root of the temperature and the mean velocity at temperature $T + \Delta T$ is

$$v \sim \sqrt{T + \Delta T} = \sqrt{T}\sqrt{1 + \frac{\Delta T}{T}} \approx \sqrt{T}\left(1 + \frac{1}{2}\frac{\Delta T}{T}\right) = \sqrt{T} + \frac{1}{2}\frac{\Delta T}{\sqrt{T}}. \tag{2.48}$$

For relatively small ΔT the mean velocities are therefore the same.

The particle flux per unit area is given by the mean velocity multiplied with the particle density. The energy flux is then the particle flux multiplied by the average energy ε the particles in the stream are transporting. Over a mean free path ℓ there will be a ballistic transport in both directions. The net flux over the middle
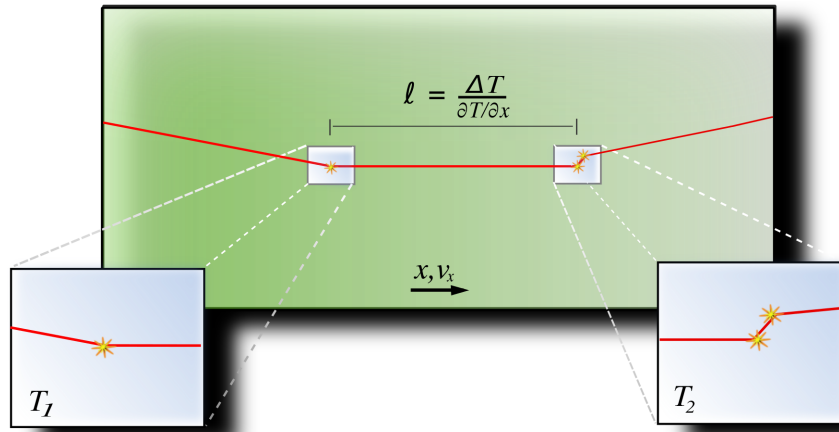
Figure 2.4: The physical picture of the mean free path ℓ in kinetic theory as the length scale between thermalization of a particle propagating in a thermal gradient field.
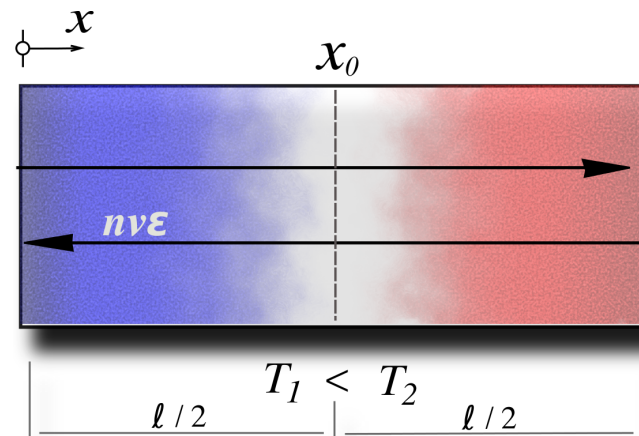

Figure 2.5: The heat flux at x_0 is the net energy flux resulting from ballistic transport over the mean free path ℓ in both directions.

of ℓ (Fig. 2.5) is then

$$
\begin{aligned}
J &= \frac{1}{2}nv\varepsilon\Big|_{x_0-\ell/2} - \frac{1}{2}nv\varepsilon\Big|_{x_0+\ell/2} = \frac{1}{2}v\varepsilon\big(n(x_0 - \ell/2) - n(x_0 + \ell/2)\big) \\
&\approx -\frac{1}{2}v\varepsilon\frac{\mathrm{d}n}{\mathrm{d}x}\ell = -\frac{1}{2}v\ell\frac{\mathrm{d}}{\mathrm{d}T}(\varepsilon n)\frac{\mathrm{d}T}{\mathrm{d}x} = -\frac{1}{2}v\ell c\frac{\mathrm{d}T}{\mathrm{d}x},
\end{aligned}
\tag{2.49}
$$

where c denotes the specific heat per unit volume. An estimate for the thermal conductivity can then be identified from Fourier's law as

$$
\kappa \sim v\ell c. \tag{2.50}
$$

This illustrates that the thermal conductivity ought to depend on the mean velocity with which the energy is transported, the length scale for that transport without inelastic scattering as well as the average energy that a carrier transfers.

In this derivation we implicitly assumed local equilibration such that a thermal gradient can be established. This shows that heat is transported downhill with respect to the thermal gradient in accordance with the second law of thermodynamics as stated by Clausius[1]:

No process is possible whose sole result is the transfer of heat from a colder to a hotter body.

For two regions that are thermally connected there will thus always be heat transfer from the hotter to the colder side, unless there is an additional process reversing the heat current.

Equation Eq. (2.50) was derived for a gas of classical particles but can be used to understand the thermal conductivity in solids as well. The heat carriers in solids are electrons and phonons, and the picture above can be adapted by observing that both of these quasi-particles behave as quantum gases for which the correct statistics have to be used.5

2.4 Boltzmann transport theory

The book keeping associated with tracking the dynamical variables in one mole of substance is an infeasible task. One attempt at a remedy is to severely reduce the system size, impose suitable boundary conditions and see if this reduction still manages to capture the relevant physics. If this does not work or becomes to difficult an alternative strategy is to abandon exact knowledge of the system and instead give a statistical description. For mechanical systems the concept of distribution functions that tracks the number density over phase space is useful.

5For electrons, which are fermions, Fermi-Dirac statistics apply, whereas phonon as bosons obey Bose-Einstein statistics.
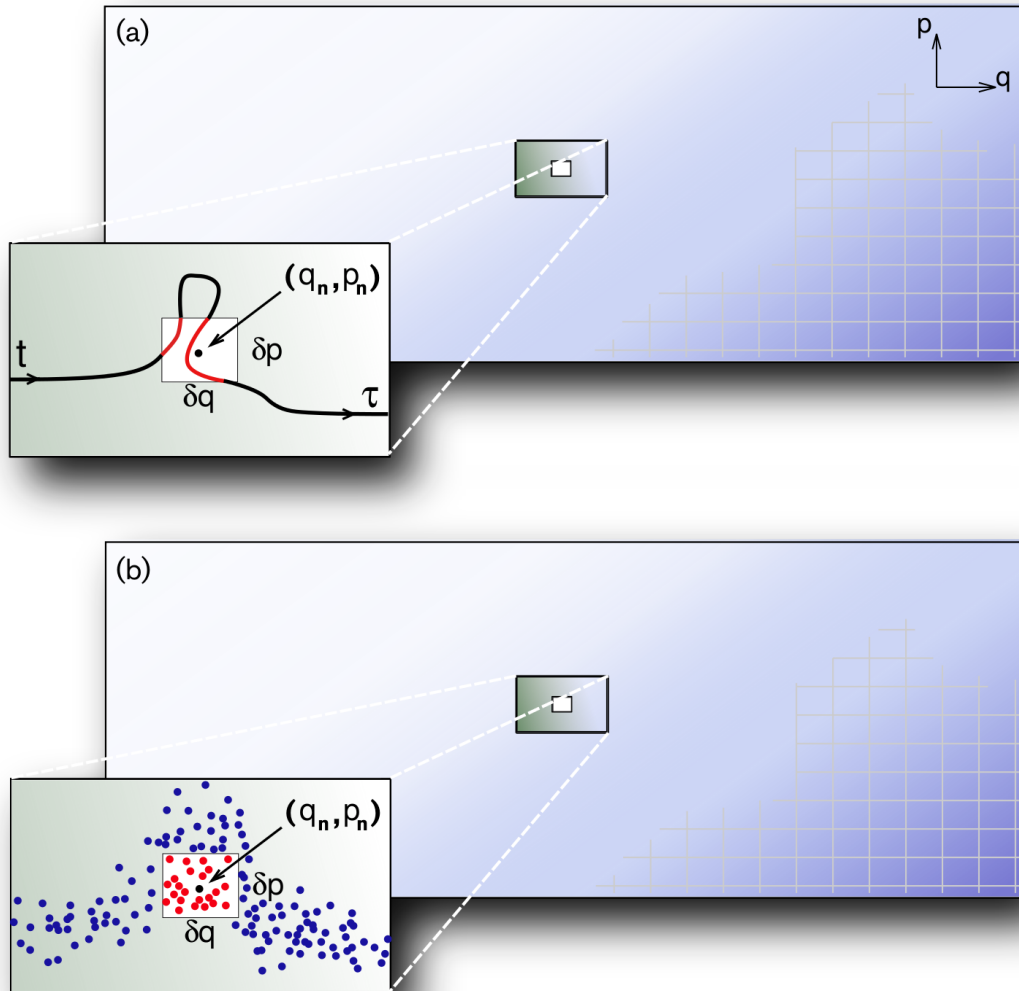
Figure 2.6: Schematic representation of two different views on distribution densities over phase space. (a) Tracking the amount of time a system spends in the neighborhood of a specific phase space point (the red paths) gives a measure for a distribution function. (b) A large enough collection of independent system replicas gives an alternative measure for a distribution function as the ratio between states within a neighborhood to (q, p) and all states.

The phase space for a system of N particles is $6N$ dimensional where $3N$ of the coordinates corresponds to the different particles generalized positions labeled q_α. The remaining $3N$ degrees of freedom correspond to the different canonical momenta labeled p_α. One can introduce Γ as the set $\{q_1, \ldots, q_{3N}, p_1, \ldots, p_{3N}\}$ as a specific point in phase space with corresponding volume element $d\Gamma$. A complete description of the dynamical state of a system constitutes then a point Γ. If the system behaves classically[6] and a governing Hamiltonian is known, in principal the dynamical evolution can be calculated by integrating the canonical equations [19]

$$q_\alpha(t) = \frac{\partial H}{\partial p_\alpha}$$
$$p_\alpha(t) = -\frac{\partial H}{\partial q_\alpha} \tag{2.51}$$

given initial conditions at time t_0. This constitutes $6N$ equations and is an impossible task since N is large, typically at the order of 10^{23} or more for macroscopic systems. In principle though, if the equations were solved the solution would map out a path through the phase space. This can be used to define the notion of a distribution function over the phase space in two different ways.

If a system is observed for a long time τ and the time spent in the neighborhood of a certain point in phase space is denoted as Δt (see Fig. 2.6 (a)), then the limit

$$\rho_N(\Gamma, t) d\Gamma = \lim_{\tau \to \infty} \frac{\Delta t(\Gamma, t)}{\tau} \tag{2.52}$$

defines a N particle probability density $\rho_N(\Gamma)$ corresponding to the uniform probability of finding the system of N particles in a specific state Γ at some time t. Alternatively, one can introduce a large collection constituting independent copies of the system randomly distributed over the phase space. Such a collection is called an ensemble (Fig. 2.6 (b)). One can define the probability density as the ratio between the number of points within the neighborhood of a point Γ and the total number of points.

In Appendix B the *Liouville equation* that governs the evolution of ρ is derived. With the use of the Poisson bracket[7] it is written as

$$\frac{d\rho_N}{dt} = \frac{\partial \rho_N}{\partial t} + \{\rho_N, H\} = 0. \tag{2.54}$$

---

[6]Classical in the sense that the system is well described by Newtonian mechanics.

[7]The Poisson bracket on quantity A is defined as

$$\{A, H\} = \sum_{i=1}^{3N} \left(\frac{\partial A}{\partial q_i} \frac{\partial H}{\partial p_i} - \frac{\partial A}{\partial p_i} \frac{\partial H}{\partial q_i} \right) \tag{2.53}$$

Solving the Liouville equation exactly is an impossible task, but there is some important knowledge gained by its introduction. Due to the conformity to the canonical equations the behavior of the distribution function is that of an incompressible fluid. This has the important implication that a volume element in phase space is invariant in time, a result known as *Liouville's theorem*. The main issue with ρ_N is that it contains to much information. Integrating over all but one of the subspaces, using $d\Gamma_1 = dq_1 dp_1$, produces a new density

$$\rho_1(\boldsymbol{q}, \boldsymbol{p}, t) = V \int \frac{d\Gamma}{d\Gamma_1} \rho_N(\Gamma) \tag{2.55}$$

called the *one particle density* representing a single particle in the averaged environment of all other particles in the system. The volume V of the system is needed so that the probability of finding the particle in a neighborhood of the six dimensional point $(\boldsymbol{q}, \boldsymbol{p})$ is

$$\frac{\rho_1(\boldsymbol{q}, \boldsymbol{p})}{V} d\Gamma_1. \tag{2.56}$$

Integrating Liouville's equation over $d\Gamma/d\Gamma_1$ results in

$$\frac{\partial \rho_1}{\partial t} + \{\rho_1, H\} - \left(\frac{\partial \rho_1}{\partial t}\right)\bigg|_{scattering} = 0, \tag{2.57}$$

where the remaining parts of higher order densities have been collected in the last term, subscripted by scattering since this term contains the interaction between the isolated particle and all other particles. Using the canonical equations this may be reformulated in vector form

$$\frac{\partial \rho_1}{\partial t} = - \underbrace{\boldsymbol{v}}_{=\frac{\partial q}{\partial t}} \cdot \nabla \rho_1 - \underbrace{\boldsymbol{F}_{ext.}}_{=\frac{\partial p}{\partial t}} \cdot \nabla_p \rho_1 + \left(\frac{\partial \rho_1}{\partial t}\right)\bigg|_{scattering}. \tag{2.58}$$

The first term on the right hand side can be identified with a diffusive process and the second one as influenced by external forces so the equation can be written as

$$\frac{\partial \rho}{\partial t} = \left(\frac{\partial \rho}{\partial t}\right)\bigg|_{diffusion} + \left(\frac{\partial \rho}{\partial t}\right)\bigg|_{external\ fields} + \left(\frac{\partial \rho}{\partial t}\right)\bigg|_{scatt.}. \tag{2.59}$$

This is the *Boltzmann equation* in its general form for a classical distribution of distinguishable particles. It states that the change in the one particle distribution is due to a balance between diffusion, external influence from e.g., electromagnetic or gravitational fields and internal scattering. It is an elegant compact description of the complex situation where external fields accelerate the particles feeding
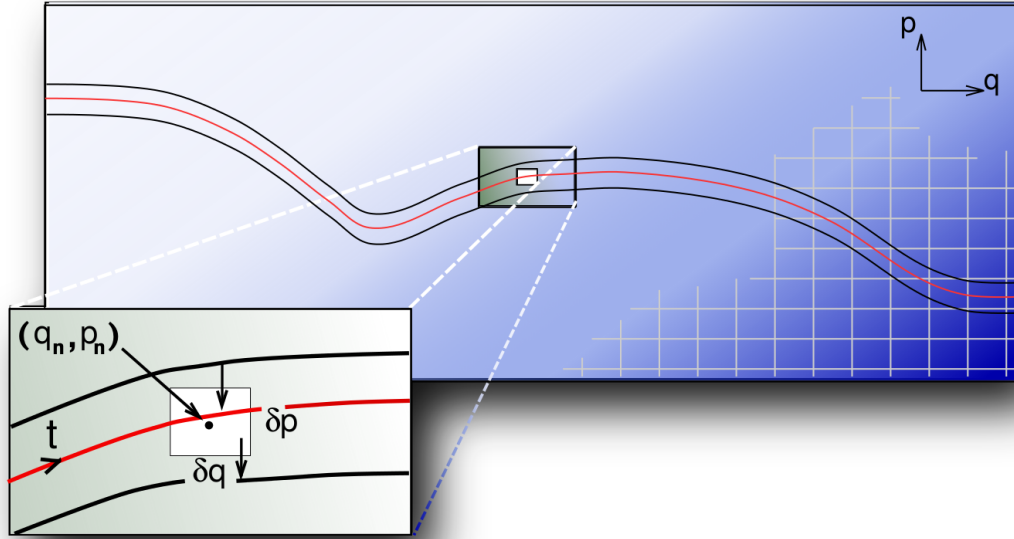
Figure 2.7:   Due to scattering processes different paths in phase space may exchange states. Here it is schematically shown how states of certain momenta are scattered into the neighborhood of the path from the top path while states of certain momenta are scattered out of the neighborhood to the bottom path.

energy into the system shifting the occupation function while scattering events redistribute the energy dissipating it into the structure and relax the perturbed occupation function.

There is an alternative way to derive the Boltzmann equation via Liouville's theorem, that includes some physical intuition. To this end, one starts with neglecting scattering, which is reasonable for a sufficiently diluted system. Then one introduces a distribution $f(\boldsymbol{r}, \boldsymbol{p}, t)$ in the form of an occupation function that counts the number of states at $\boldsymbol{r}$ that have momenta $\boldsymbol{p}$ at time t. Because of Liouville's theorem the number of states in a neighborhood of the point at $(\boldsymbol{r}, \boldsymbol{p})$ at time t must all have been transported from another point in accordance with Newton's equations

$$\mathrm{d}\boldsymbol{r} = \boldsymbol{v}\mathrm{d}t$$
$$\mathrm{d}\boldsymbol{p} = \boldsymbol{F}\mathrm{d}t. \tag{2.60}$$

Within the neighborhood, using a Taylor expansion the following holds true to first order in dt

$$f(\boldsymbol{r}, \boldsymbol{p}, t) = f(\boldsymbol{r} - \boldsymbol{v}dt, \boldsymbol{p} - \boldsymbol{F}dt, t - dt)$$

$$= f(\boldsymbol{r}, \boldsymbol{p}, t) + \frac{\partial f}{\partial r_\alpha}\bigg|_{(\boldsymbol{r}, \boldsymbol{p}, t)} v_\alpha dt + \frac{\partial f}{\partial p_\alpha}\bigg|_{(\boldsymbol{r}, \boldsymbol{p}, t)} F_\alpha dt + \frac{\partial f}{\partial t}\bigg|_{(\boldsymbol{r}, \boldsymbol{p}, t)} dt \qquad (2.61)$$

where the Einstein sum convention applies. Canceling $f(\boldsymbol{r}, \boldsymbol{p}, t)$, identifying the total derivative and writing the equation in vector notation gives

$$\frac{df}{dt} = \frac{\partial f}{\partial t} + \boldsymbol{v} \cdot \nabla f + \boldsymbol{F} \cdot \nabla_p f = 0 \qquad (2.62)$$

which must hold in each point of phase-space. Increasing the concentration the particles start to scatter. This means that particles with a certain momentum may be scattered in to a neighboring point in phase space. Alternatively, particles with a certain momentum can scatter out from a neighborhood (Fig. 2.7). This may be expressed symbolically by introducing a transition probability operator $P_{\boldsymbol{p}' \to \boldsymbol{p}}(\boldsymbol{r}, \boldsymbol{p})$ giving the rate for states into the phase space point $(\boldsymbol{r}, \boldsymbol{p})$. Similarly $P_{\boldsymbol{p} \to \boldsymbol{p}'}$ is the operator that expresses the rate of the states going out from $(\boldsymbol{r}, \boldsymbol{p})$ as a result of scattering. Under normal circumstances it is reasonable to assume the principle of detailed balance, which means that in equilibrium the number of states scattered into a phase space point is balanced by an equal amount of states scattered out of the point. The effect of scattering vanishes and so the scattering term disappears. This suggests that the scattering term should appear as the difference of the two transition rates as

$$S = P_{\boldsymbol{p}' \to \boldsymbol{p}} - P_{\boldsymbol{p} \to \boldsymbol{p}'}. \qquad (2.63)$$

The rate of states transitioning into and out from the phase space point due to scattering must balance the total change of the occupation function. Including this effect of scattering in Eq. (2.64) the Boltzmann equation becomes

$$\frac{df}{dt} = \frac{\partial f}{\partial t} + \boldsymbol{v} \cdot \nabla f + \boldsymbol{F} \cdot \nabla_p f = Sf. \qquad (2.64)$$

2.4.1 The semiclassical assumption

The Boltzmann equation Eq. (2.64) may be rewritten using the quantum mechanical expression for the crystal momentum $\boldsymbol{p} = \hbar \boldsymbol{k}$

$$\frac{df}{dt} = \frac{\partial f}{\partial t} + \boldsymbol{v} \cdot \nabla f + \frac{\boldsymbol{F}}{\hbar} \cdot \nabla_k f = \left(\frac{\partial f}{\partial t}\right)\bigg|_{scattering}. \qquad (2.65)$$

27

The appearance of $\hbar$ indicates that the equation may be applied in a quantum mechanical setting under certain conditions.

The distribution function needs to take into account that particles are indistinguishable. This is accomplished by letting the equilibrium distribution function describe either bosonic or fermionic statistics. In practice this means that the equilibrium distribution is either the Bose-Einstein or the Fermi-Dirac distribution.

In the quantum mechanical description the particles are described by wavefunctions. This has the implication that the velocity appearing in Eq. (2.65) is identified with the group velocity of the waves associated with the states in f. Particle position and momentum then cannot be determined simultaneously with arbitrary precision. Being conjugate operators with a non-vanishing commutator the uncertainty principle limits the precision to

$$\Delta x \Delta p \geq \hbar. \tag{2.66}$$

This is fine as long as Δx can be taken large enough to ensure low uncertainty in p. Since $\hbar$ is of the order 10^{-34} Js a granular view of x may be sufficient and still produce enough precision for the Boltzmann equation. The granularity is sufficient as long as the spatial extent of the wave packet is on a scale less than the mean free path between particle collisions.

According to the *Ehrenfest Theorem* the center of a wavepacket follows the path of a classical particle in a potential [20]. If the wavepacket is sufficiently localized on the scale of the potential the particle may, to a good approximation, be viewed as a classical particle in that potential. This has the implication that the potential must be slowly varying on the length scale of the wave packet. For time varying fields this also sets a temporal constraint so that the frequency associated with the time variation of the field may not become to large.

This is the basis for the semiclassical assumption and restricts the application of the Boltzmann equation to situations, in which quantum interference is not expected.

2.4.2 The relaxation time approximation

The scattering term in Eq. (2.64) is in general a complicated operator. Assuming that there are no external fields and that the system is spatially homogeneous the Boltzmann equation reads

$$\frac{\partial f}{\partial t} = S f. \tag{2.67}$$

If we assume that the system is close to equilibrium the distribution function should be the equilibrium distribution f_0 with an added small perturbation formally writ-

ten as

$$\delta f = f - f_0. \tag{2.68}$$

If the internal scattering is assumed to relax the system, the simplest way to model this is to assume that the rate of change in the distribution function is reduced by the magnitude of the perturbation to the state, over a time scale τ. Equation 2.67 then becomes

$$\frac{\partial f}{\partial t} = \frac{\partial(\delta f)}{\partial t} = -\frac{\delta f}{\tau}. \tag{2.69}$$

with the solution

$$\delta f = \delta f(0)e^{-t/\tau} \tag{2.70}$$

indicating exponential decay of the perturbations over a characteristic time τ. It is natural to call this the relaxation time and the inclusion of the scattering term as in Eq. (2.70) for the *relaxation time approximation* (RTA).

2.4.3 Boltzmann transport for electrons in an electric field

As an example of a solution to the Boltzmann equation within the RTA the case of electrons in a static electric field is presented in this section. The next section considers the Boltzmann equation for phonons in a thermal gradient.

Electrons are fermions and as such obey *Fermi-Dirac* statistics. This is a result of the *Pauli exclusion principle*, which states that two fermions can not simultaneously be in the same quantum state. The occupation in thermal equilibrium at temperature T is then described by the Fermi-Dirac distribution

$$f_0 = \frac{1}{\exp\left(\frac{\varepsilon - \mu}{k_B T}\right) + 1}, \tag{2.71}$$

where ε is the energy of an electron with wave vector $\boldsymbol{k}$ and μ is the chemical potential of the electrons.

If a static electric field $\boldsymbol{E}$ is applied to the material the electrons will experience a Coulomb force accelerating them in the direction opposite to the the electric field. If the fundamental charge is q then the force on the electrons will be $\boldsymbol{F} = -q\boldsymbol{E}$. The electron energy and the chemical potential will then become spatially dependent. Assuming that the RTA holds in the steady state the Boltzmann transport equation is stated as

$$\frac{df}{dt} = \underbrace{\frac{\partial f}{\partial t}}_{=0} + \boldsymbol{v} \cdot \nabla f - \frac{q\boldsymbol{E}}{\hbar} \cdot \nabla_k f = -\frac{\delta f}{\tau}. \tag{2.72}$$

If the perturbations are small compared to f_0 the variation in δf will be negligible compared to variations in f. The gradients of δf may then be dropped and the equation becomes

$$\boldsymbol{v} \cdot \nabla f_0 - \frac{q\boldsymbol{E}}{\hbar} \cdot \nabla_{\boldsymbol{k}} f_0 = -\frac{\delta f}{\tau}. \tag{2.73}$$

The perturbations may then be solved for algebraically as

$$\delta f = -\tau \left(\boldsymbol{v} \cdot \nabla f_0 - \frac{q\boldsymbol{E}}{\hbar} \cdot \nabla_{\boldsymbol{k}} f_0 \right). \tag{2.74}$$

Since the equilibrium distribution is known, this presents a full solution within the RTA up to the free parameters in the form of the relaxation times τ. These parameters must be measured, estimated or calculated from first principles.
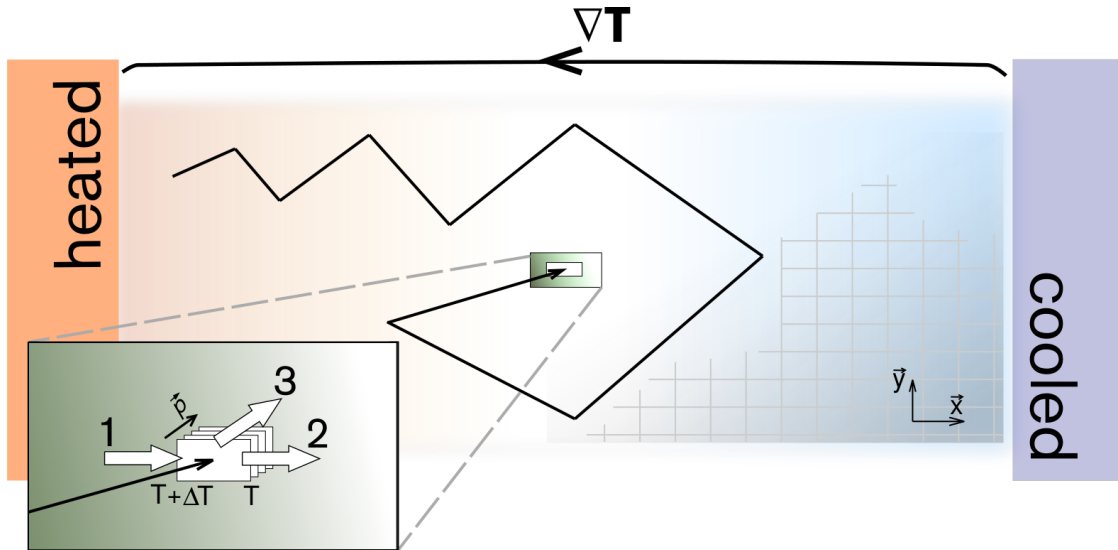

Figure 2.8: A particle experiencing several scattering events here shown in position space.

2.4.4 Boltzmann transport for phonons

In a crystal in thermal equilibrium at temperature T the phonon modes are distributed according to the Bose-Einstein distribution [18]

$$n_{0,\lambda} = \frac{1}{\exp\left(\hbar\omega_\lambda/k_B T\right) - 1}. \tag{2.75}$$

The distribution function counts the number of phonon modes in state λ. Here $\lambda = (q, p)$ is a collective index for a phonon mode with wave-vector q and band index p. The energy carried by a single phonon mode λ is

$$E_\lambda = \frac{\hbar\omega_\lambda}{\exp\left(\hbar\omega_\lambda/k_B T\right) - 1}. \tag{2.76}$$

The specific heat c_λ associated with phonon mode λ is then

$$c_\lambda = \frac{\partial E_\lambda}{\partial T} = k_B \left(\frac{\hbar\omega_\lambda}{k_B T}\right)^2 n_{0,\lambda}(n_{0,\lambda} + 1). \tag{2.77}$$

When there is a thermal gradient present the temperature becomes position dependent. The phonons in question are assumed not to interact with the electromagnetic field and so the force related term drops out. Then in the steady state only the diffusive term from the total derivative survives

$$\frac{dn_\lambda}{dt} = \underbrace{\frac{\partial n_\lambda}{\partial t}}_{= 0} + v_\lambda \cdot \nabla n_\lambda + \underbrace{F\frac{\partial n_\lambda}{\partial p}}_{= 0} = \left(v_\lambda \cdot \nabla T(r)\right)\frac{\partial n_{0,\lambda}}{\partial T}. \tag{2.78}$$

where in the second step the diffusive term has been linearized. Introducing the scattering operator S acting on the distribution the linearized phonon Boltzmann equation in its *canonical form* reads

$$-\left(v_\lambda \cdot \nabla T(r)\right)\frac{\partial n_{0,\lambda}}{\partial T} + S n_\lambda = 0 \tag{2.79}$$

emphasizing the balance between diffusion and scattering in a specific mode. So there is thus a balance between a diffusive process and scattering. Introducing the RTA the scattering term is

$$S n_\lambda = -\frac{n_\lambda - n_{0,\lambda}}{\tau_\lambda} = -\frac{\delta n_\lambda}{\tau_\lambda}. \tag{2.80}$$

and solving for the perturbation gives the solution

$$\delta n_\lambda = -\tau_\lambda \left(v_\lambda \cdot \nabla T(r)\right)\frac{\partial n_{0,\lambda}}{\partial T} = -\tau_\lambda \left(v_\lambda \cdot \nabla T(r)\right)\frac{\hbar\omega_\lambda}{k_B T^2} n_{0,\lambda}(n_{0,\lambda} + 1). \tag{2.81}$$

for a specific phonon mode λ.

2.4.5 Lattice thermal conductivity within the RTA

The microscopic thermal energy current $\boldsymbol{J}_Q$ resulting from phonon transport is the sum of the occupation weighted energy flux of individual phonon modes. The heat flux in the Cartesian direction α is

$$J_{Q,\alpha} = \frac{1}{V} \sum_\lambda \hbar \omega_\lambda n_\lambda \boldsymbol{v}_{\lambda,\alpha} = \frac{1}{V} \sum_\lambda \hbar \omega_\lambda \delta n_\lambda \boldsymbol{v}_{\lambda,\alpha}. \tag{2.82}$$

Here V is the volume of the system under consideration, ω_λ is the frequency, n_λ is the occupation and $\boldsymbol{v}_\lambda = \nabla_q \omega_\lambda$ the group velocity. In the second step the distribution has been replaced with the perturbation. This is because of time reversal symmetry. In equilibrium there will be no energy current since each phonon mode will have an associated mode with an equally energetic phonon in the opposite direction. The terms in Eq. (2.82) cancels in pairs.

Inserting the solution (2.81) in Eq. (2.82) gives an expression for the heat current

$$J_{Q,\alpha} = -\frac{1}{V} \sum_\lambda \tau_\lambda \left(v_{\lambda,\beta} \partial_\beta T \right) \underbrace{k_B \left(\frac{\hbar \omega_\lambda}{k_B T} \right)^2 n_{0,\lambda} (n_{0,\lambda} + 1)}_{= \, c_\lambda}$$

$$= -\left(\underbrace{\frac{1}{V} \sum_\lambda \tau_\lambda v_{\lambda,\alpha} v_{\lambda,\beta} c_\lambda)}_{= \, \kappa_{\alpha,\beta}(T)} \right) \partial_\beta T$$

$$= -\kappa_{\alpha,\beta}(T) \partial_\beta T \tag{2.83}$$

where repeated Cartesian index β is implicitly summed. The introduced quantity $\kappa_{\alpha,\beta}$ can be identified through Fourier's law

$$\boldsymbol{J}_Q = -\kappa \cdot \nabla T \tag{2.84}$$

as the thermal conductivity tensor. The expression for the lattice thermal conductivty has one flaw. It contains free parameters in the τ_λ.

2.4.6 Determination of lifetimes

2.4.6.1 The perturbed lattice Hamiltonian

If a unit cell has the position vector $\boldsymbol{l}$ and an atom in that cell has the relative position $\boldsymbol{b}$ the position of the atom may be denoted $\boldsymbol{r}(\boldsymbol{lb})$, where $\boldsymbol{l}$ and $\boldsymbol{b}$ label the atom, and a displacement of this atom will then be

$$\boldsymbol{u}(\boldsymbol{lb}) = \boldsymbol{r}(\boldsymbol{lb}) - \boldsymbol{l} - \boldsymbol{b}. \tag{2.85}$$

For small displacements in a classical crystal the change in the potential energy can be expressed as a Taylor series in the displacements. Formally this is expressed as

$$U = U_0 + \sum_{lb} \left.\frac{\partial U}{\partial u^\alpha(lb)}\right|_0 u_\alpha(lb)$$
$$+ \frac{1}{2} \sum_{lb} \sum_{l'b'} \left.\frac{\partial^2 U}{\partial u^\alpha(lb)\partial u^\beta(l'b')}\right|_0 u_\alpha(lb)u_\beta(l'b')$$
$$+ \frac{1}{6} \sum_{lb} \sum_{l'b'} \sum_{l''b''} \left.\frac{\partial^3 U}{\partial u^\alpha(lb)\partial u^\beta(l'b')\partial u^\gamma(l''b'')}\right|_0 u_\alpha(lb)u_\beta(l'b')u_\gamma(l''b'') + \dots .$$

(2.86)

The repeated Greek indices, representing Cartesian directions, are implicitly summed over in pairs. The derivatives are taken at the equilibrium positions, hence the first order term vanishes by definition and the constant term is an arbitrary shift of the energy scale and is here chosen as the reference. Since force is the spatial derivative of the potential the first type of derivative can be rewritten as

$$\Phi_{\alpha\beta}(lb, l'b') = \left.\frac{\partial^2 U}{\partial u^\alpha(lb)\partial u^\beta(l'b')}\right|_0 = -\left.\frac{\partial F_\beta(l'b')}{\partial u^\alpha(lb)}\right|_0$$

(2.87)

with the physical interpretation as the change in the force on the atom at $l'b'$ as a response when atom lb is displaced. Similarly for the third order term

$$\Phi_{\alpha\beta\gamma}(lb, l'b', l''b'') = \left.\frac{\partial^3 U}{\partial u^\alpha(lb)\partial u^\beta(l'b')\partial u^\gamma(l''b'')}\right|_0 = -\left.\frac{\partial^2 F_\gamma(l'b')}{\partial u^\alpha(lb)\partial u^\beta(l'b')}\right|_0$$

(2.88)

relating the displacements of atoms to the force on atom $l''b''$ when displacing atoms lb and $l'b'$. These sets of constants are called the second and third order interatomic force constants (IFC). Up to third order the potential is expressed as

$$U = \frac{1}{2} \sum_{lb} \Phi_{\alpha\beta} u_\alpha(lb)u_\beta(l'b') + \frac{1}{6} \sum_{lb} \sum_{l'b'} \Phi_{\alpha\beta\gamma} u_\alpha(lb)u_\beta(l'b')u_\gamma(l''b'').$$

(2.89)

Through quantization by introduction of creation and annihilation operators $a_{q,s}$ and $a^\dagger_{-q,s}$ the displacements may be promoted to operators expressed through the Fourier expansion

$$u_\alpha(lb) = \frac{1}{\sqrt{N}} \sum_{lb} \epsilon_{s,\alpha}(q)e^{-iq\cdot r(lb)} \sqrt{\frac{\hbar}{2m_b\omega_s(q)}} \left(\hat{a}_{q,s} + \hat{a}^\dagger_{-qs} \right),$$

(2.90)

where $\epsilon_{s,\alpha}(\boldsymbol{q})$ is the polarization of the mode and m_b the mass of the atom at position $\boldsymbol{b}$. Using this expansion the first sum in Eq. (2.89) together with the kinetic energy can be shown to give a Hamiltonian

$$H_0 = \sum_{q,s} \hbar\omega_s(\boldsymbol{q}) \left(\frac{1}{2} + \hat{a}^\dagger_{q,s}\hat{a}_{-q,s}\right) \tag{2.91}$$

that is the same as the sum of Hamiltonians for quantum harmonic oscillators. This Hamiltonian acts as an unperturbed state constituting a set of harmonic oscillators and the second series acts as a perturbation on that set. The Hamiltonian extended to the third order in the displacements may be written as

$$H^{(3)} = H_0 + H' \tag{2.92}$$

where

$$H' = \frac{1}{6} \sum_{lb} \sum_{l'b'} \sum_{l''b''} \Phi_{\alpha\beta\gamma} u_\alpha(l\boldsymbol{b}) u_\beta(l'\boldsymbol{b}') u_\gamma(l''\boldsymbol{b}''). \tag{2.93}$$

2.4.6.2 The physical picture

To understand the physical meaning of the perturbed Hamiltonian notice that there are three displacements containing the sum of a creation and an annihilation operator in the third order term in Eq. (2.89). Introducing a phonon field represented by a state-vector with the occupation of individual phonon modes

$$\phi = |n_{q_1,s_1}, n_{q_2,s_2}, \ldots\rangle, \tag{2.94}$$

where the excitations are harmonic oscillators. The creation and annihilation operators then work such that the annihilation operator lowers the phonon occupation $n_{q,s}$ by one phonon

$$\hat{a}_{q,s}|\ldots, n_{q,s}, \ldots\rangle \propto |\ldots, n_{q,s} - 1, \ldots\rangle, \tag{2.95}$$

and the creation operator raises the occupation by one phonon

$$\hat{a}^\dagger_{-q,s}|\ldots, n_{q,s}, \ldots\rangle \propto |\ldots, n_{q,s} + 1, \ldots\rangle. \tag{2.96}$$

Expanding the factors containing sums of creation and annihilation operators gives the following factors

$$\left(\hat{a}_{q,s} + \hat{a}^\dagger_{-q,s}\right)\left(\hat{a}_{q',s'} + \hat{a}^\dagger_{-q',s'}\right)\left(\hat{a}_{q'',s''} + \hat{a}^\dagger_{-q'',s''}\right) =$$

$$\hat{a}_{q,s}\hat{a}_{q',s'}\hat{a}_{q'',s''} + \hat{a}_{q,s}\hat{a}_{q',s'}\hat{a}^\dagger_{q'',s''} + \hat{a}_{q,s}\hat{a}^\dagger_{q',s'}\hat{a}_{q'',s''} + \hat{a}_{q,s}\hat{a}^\dagger_{q',s'}\hat{a}^\dagger_{q'',s''}$$

$$+ \hat{a}^\dagger_{q,s}\hat{a}_{q',s'}\hat{a}_{q'',s''} + \hat{a}^\dagger_{q,s}\hat{a}^\dagger_{q',s'}\hat{a}_{q'',s''} + \hat{a}^\dagger_{q,s}\hat{a}_{q',s'}\hat{a}^\dagger_{q'',s''} + \hat{a}^\dagger_{q,s}\hat{a}^\dagger_{q',s'}\hat{a}^\dagger_{q'',s''}. \tag{2.97}$$

Figure 2.9: Schematic representation of class 1 and class 2 events. Class 1 events corresponds to the collision of two phonons with angular frequency ω and ω' annihilating into a phonon of angular frequency ω''. Class 2 events corresponds to the disintegration of a phonon mode of angular frequency ω annihilating into two phonons with angular frequency ω' and ω''.

Four different kinds of processes can be identified. One with three created phonons, one with three annihilated phonons, two created phonons annihilated into one phonon, and finally one created phonon annihilating into two phonons. The situation with only created or annihilated phonons are prohibited due to energy conservation and do not represent physical processes. Situations in which two phonons collide are called class 1 events and situations in which one phonon disintegrates into two new phonons are called class 2 events (Fig. 2.9). Energy conservation also applies to class 1 and 2 events. This can be expressed through factors of Dirac delta functions expressing energy conservation, $\delta(\omega + \omega' - \omega'')$ for class 1 events and $\delta(\omega - \omega' - \omega'')$ for class 2 events.

Besides energy conservation it is also necessary for the processes to respect the conservation of crystal momentum. A crystal in rest does not have any external momentum but the internal degrees of freedom are associated with a related quantity referred to as crystal momentum. But there is one difference, the crystal momentum must only be conserved up to a reciprocal lattice vector. This can be written as

$$q + q' = q'' + G, \tag{2.98}$$

for class 1 events and

$$q + G = q' + q''$$ (2.99)

for class 2 events.

2.4.6.3 Lifetimes from first principles

It can be shown [21] that there is a relation between the imaginary part of the self energy Γ and the lifetimes through

$$\tau_\lambda = \frac{1}{2\Gamma_\lambda(\omega_\lambda)}$$ (2.100)

where Γ is

$$\Gamma_\lambda(\omega) = \frac{18\pi}{\hbar^2} \sum_{\lambda'\lambda''} |\Phi_{-\lambda\lambda'\lambda''}|^2 \Big\{ (n_{\lambda'} + n_{\lambda''} + 1)\,\delta(\omega - \omega_{\lambda'} - \omega_{\lambda''})$$
$$+ (n_{\lambda'} - n_{\lambda''})\big(\delta(\omega + \omega_{\lambda'} - \omega_{\lambda''}) - \delta(\omega - \omega_{\lambda'} + \omega_{\lambda''})\big) \Big\}.$$ (2.101)

The constants $\Phi_{-\lambda\lambda'\lambda''}$ are the Fourier transforms of the third order IFCs after a transformation to normal modes. This expression can be obtained with a version of Fermi's golden rule. The golden rule states that the rate from an in-state $|\phi_{in}\rangle$ to an out-state $|\phi_{out}\rangle$ due to a perturbation H' is obtained by evaluating

$$P_{in\to out} = \frac{2\pi}{\hbar} |\langle \phi_{out} | H' | \phi_{in} \rangle|^2 \delta(E_{out} - E_{in}).$$ (2.102)

The delta function assures that the energy is conserved in the process. Besides that, the Fourier transform of the IFCs contains a factor that is non-zero only in the case that the crystal momenta is conserved up to a reciprocal vector.

The problem then comes down to calculating the third order IFCs. In this thesis a direct approach has been taken. The constants can be directly calculated by using finite differences on force data obtained from an electron structure calculation (see Sect. 3.2). All the IFCs can be obtained by calculating the forces in structures obtained by displacing one atom for the second order IFCs, and two atoms for the third order IFCs [22, 23]. For efficiency the symmetry of the system should be used to single out an irreducible set of displacements needed for a complete description of the forces in the material.

2.5 Materials

2.5.1 van der Waals solids

The class of materials known as van der Waals solids consists of three-dimensional (3D) structures composed of monolayers of two-dimensional (2D) sheets, where the monolayers are bound together by interlayer van der Waals forces (Fig. 2.10). The sheets, in themselves, constitute a class called 2D materials, also known as single-layer materials. Here, 2D materials consist of a distinct monolayer, with a thickness corresponding to the atomic scale, and with an intralayer bonding of covalent, ionic, or possibly mixed covalent/ionic type.

Monolayers can be isolated from their 3D counterpart, by the use of a top-down approach where the weaker van der Waals bonds are broken without disrupting the in-plane integrity. The separation can, for instance, be done through micromechanical exfoliation using a scotch-tape technique, or exfoliation using liquid intercalation techniques. Alternatively, the monolayers can be synthesized in a bottom-up approach, using, for instance chemical vapor deposition (CVD) techniques [24]. The bottom-up approach allows for manufacturing of novel monolayers with a nonexistent 3D counterpart, for instance, silicene and germanene, the hexagonal monolayer allotropes of silicon and germanium.

With the improvement of manufacturing techniques for monolayers, either top-down or bottom-up, the family of isolated 2D materials has grown considerably in the last decade [25, 26, 24]. After the reported isolation of monolayers of graphite in 2004 [27], since then known as graphene, many other 2D materials have been isolated. Early, well-studied examples consist of hexagonal boron nitride (h-BN) and molybdenum disulfide (MoS_2) from the group of transition metal dichalcogenides (TMDs), a group associated with many different 2D materials. Today, there is a plethora of 2D materials besides the ones introduced. Examples include phosphorene, the monolayer of black phosphorous [28], and to phosphorene the isoelectronic group-IV monochalcogenides such as tin- and germanium selenides and sulfides (SnSe, SnS, GeSe, and GeS). Other interesting examples of monochalcogenides are the gallium and indium monochalcogenides. Worth mentioning, there are also groups of oxides with layered structures that are relevant for the research fields interested in 2D materials.

The electronic character of different 2D materials ranges from metals and semimetals, through semiconductors to dielectric insulators. The forerunners extensively examined within the 2D family, graphene, h-BN, and MoS_2 are individual examples of a 2D semimetal, insulator and semiconductor [29]. Besides graphene, the related silicene and germanene also form hexagonal semimetallic monolayers. The semimetallic character in these materials is related to a linear crossing in the bandstructure, at the Fermi-level, forming the so-called Dirac cones centered
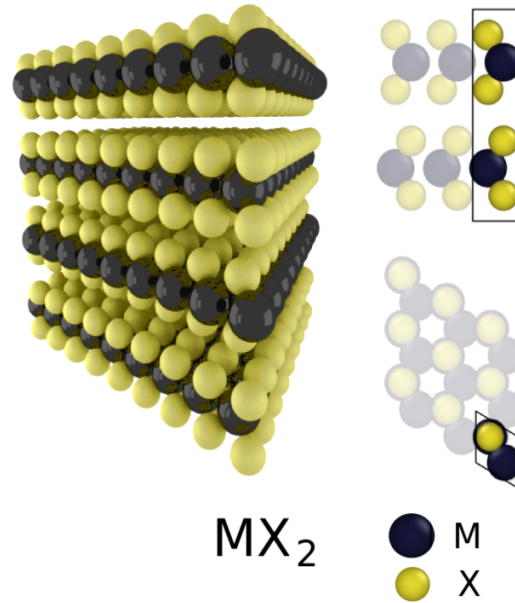
Figure 2.10: The crystal structure of the molybdenum and tungsten based transition metal dichalcogenides. The transition metal corresponds to M and the chalcogenide to X.

around the K and K' points. In the context of 2D materials, h-BN was originally used in its 3D form as an isolating substrate for graphene. Today, single layer h-BN is interesting for electronic applications or as a building block in heterostructures [30, 31, 32]. Among the TMDs, MoS$_2$ has a dominating position in research, in part because of the availability of molybdenite crystals used for exfoliation of mono- and few-layer MoS$_2$. The closely related semiconducting molybdenum and tungsten based dichalcogenides WS$_2$, MoSe$_2$ and WSe$_2$ have not been as extensively investigated although they have similar properties as MoS$_2$.

The properties of a 2D material can differ significantly from its corresponding 3D structure. The exotic band structure of graphene is one illuminating example. In the 3D allotrope graphite, the Dirac cones are not present. The significance of the linear dispersion in the band structure, is the implication of massless electron behavior and a constant universal electron velocity within the cones, in analogy with the universal speed limit associated with massless particles in special relativity [33]. Another illuminating example is the change of electronic properties in MoS$_2$ and WS$_2$ when comparing the electronic properties of the 3D bulk and corresponding 2D monolayers. The 3D bulk has an indirect bandgap of 1.2 eV and 1.3 eV respectively. In the corresponding monolayers, the band structure transforms in that the band gap increases and the bandstructure shifts into a direct band-

gap with values of 1.9 eV respectively 2.1 eV [34]. The nature of the bandgap is very fundamental in applications related to optoelectronic devices. When the bandgap is direct, the semiconductor can easily interact with photons of energies greater than the bandgap through emission and absorption processes. If the bandgap is indirect, an additional phonon has to be involved for the purpose of momentum conservation, rendering much less efficiency in the interaction with the photon field.

The emergence of new types of 2D materials paves the way for novel forms of van der Waals solids, known as van der Waals heterostructures [29]. In a van der Waals heterostructure, different types of monolayers are combined in a regular pattern, with the potential for dramatic changes in the material properties. The family of 2D materials, in themselves, cover a wide range of interesting properties. The concept of heterostructures introduces the promise of more control over these properties [35, 29, 25]. When stacked, the interaction between layers might induce changes in the charge distribution, as well as structural changes, in neighboring monolayers, which opens the possibility for managing these properties. Although the exciting prospect of heterostructures, there are still many obstacles to overcome in that the assembly techniques currently available are limited [25].

One group of van der Waals solids of interest, not only as primitive systems but also in the context of heterostructures, are the molybdenum and tungsten based TMDs. These TMDs has the general stoichiometry MX_2 where (M=Mo, W; X=S, Se, Te). The equilibrium structures are layered with hexagonal symmetry and an ABAB stacking of the planes (Fig. 2.10). The symmetry belongs to the space group $P6_3/mmc$ (International Tables of Crystallography No. 194), except for WTe_2 that has an orthorhombic symmetry in the space group $Pmn2_1$ (ITC No. 31).

Besides the interest in using molybdenum and tungsten based TMDs for electronic [36, 34] as well as optoelectronic applications [34, 37, 38], there is also potential for the use of these TMDs in spintronics [39]. Further, it has also been reported a significant increase in the thermoelectric figure of merit in MoS_2, based on first-principles calculations [40]. Although MoS_2, and related TMDs, have high Seebeck coefficients, the electrical conductivities are low [41, 42]. Yet, improvements might be made to the electron mobility through changes in the band structure by inducing stress in the systems[36]. In these applications is thermal transport important. Either for thermal management in electronic applications [43], or improvement of the thermoelectric efficiency. Thermal management is important for functionality, reliability and stability in electronic devices. And the thermoelectric efficiency can be improved by reduction of the thermal conductivity. It is therefore important to develop a detailed understanding of the thermal conductivity in TMDs.

As a result of the difference in the stronger intralayer bonding compared to out-of-plane van der Waals interaction, the thermal conductivity in the TMDs is highly

anisotropic. The out-of-plane thermal conductivity $\kappa_\perp$ is of the order of 1 W/mK at room temperature [44, 45, 46]. Interestingly, Chiritescu *et al.* reported a $\kappa_\perp$ of 0.05 W/mK in disordered thin films of WSe_2 [44], a reduction by a factor of 30 compared to single crystals. This value is remarkably low, even lower than the theoretical limit [47], and was attributed to randomization of the stacking order. In Paper I is the origin of this reduction investigated in more detail.

In general, the experimental values reported for the thermal conductivity in TMDs shows a considerable spread. In the case of the most investigated TMD, MoS_2, varies the reported value for the in-plane lattice thermal conductivity considerably, from 20 W/mK [48] to 100 W/mK [49]. The reason for this spread is probably related to the difficulties associated with experimental measurements in these type of structures, as well as sample size effects and sensitivity to defects. The different lattice thermal conductivities reported from calculations also show a significant variation. Most calculations are done with monolayers, possibly because the more common exchange-correlation functionals used in density functional theory have difficulties capturing the van der Waals interaction between the layers properly. Paper II investigates the thermal transport in bulk TMDs using Boltzmann transport theory. First-principles calculations with a van der Waals density functional is here used to accurately capture the interlayer interaction.

2.5.2 Inorganic clathrates

Clathrates, in general, are chemical substances with a well-defined lattice structure of an inclusion type [50, 51]. The structure constitutes a caged framework, also commonly referred to as the host structure, with the ability to trap atomic or molecular species, called the guest species. The name clathrate originates from the Latin word *clatratus* with the meaning "protected by a crossbar." One specific class of interest are the inorganic clathrates, e.g., $Ba_8Ga_{16}Ge_{30}$ and $Sr_8Ba_{16}Sn_{30}$, in that they have very favorable properties for thermoelectric performance. They have an intrinsic combination of low thermal conductivities, high Seebeck coefficients, and good dopability [52, 53]. $Ba_8Ga_{16}Ge_{30}$ is a well-studied clathrate and representative for other similar compounds. It has been well investigated both experimentally [54, 55, 56, 57, 58, 59], and theoretically [60, 61, 55, 62, 63], and is the clathrate investigated in Papers III and IV of this thesis.

The inorganic clathrates, also known as intermetallic clathrates, or Zintl clathrates [53], can in general be ordered into six different structure types, built from four different kinds of polyhedra. The most common type of inorganic clathrate, known as the type I clathrate (Fig. 2.11), is built from two of these polyhedra types, namely six larger tetrakaidekahedra, and two smaller pentagonal dodecahedra. The larger tetrakaidekahedra are joined by their hexagonal faces, forming
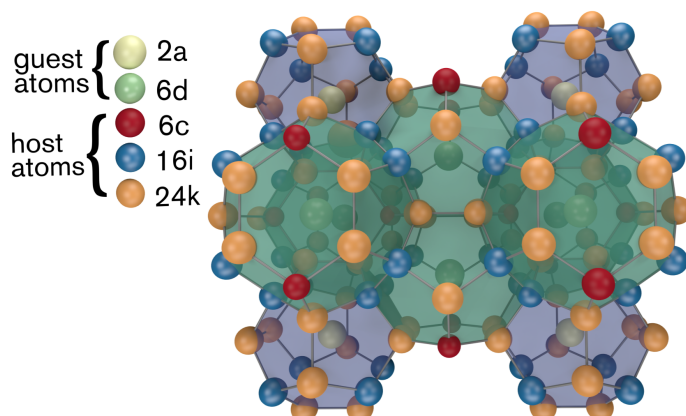
Figure 2.11: Crystal structure of type I clathrates. The guest species (Ba) occupies Wyckoff sites of type $2a$ and $6d$, while the host species (Ga, Ge) occupy Wyckoff sites of type $6c$, $16i$, and $24k$.
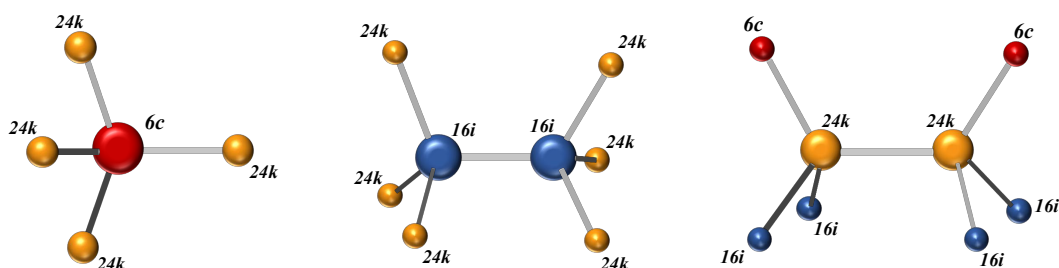
Figure 2.12: The relations between neighboring Wyckoff sites in the host structure of a type I clathrate. As seen from Wyckoff position $6c$ (left panel), position $16i$ (middle panel), and position $24k$ (right panel).

tubes stacked in the three orthogonal directions. The smaller dodecahedra are then fitted into the framework. Each polyhedron now contains a void in which a guest species can be trapped. The ideal type I clathrate structure belongs to space group $P m \bar{3} n$ (international tables of crystallography number 223). The center of the cages in the structure offers eight sites for the guest species, in Wyckoff notation called sites $2a$ in the smaller cages, and sites $6d$ in the larger type of cage. The host system forms a framework of 46 tetrahedrally bonded atom positions, divided over three separate types of crystallographic sites, with Wyckoff symbols $6c$, $16i$ and $24k$, respectively.

A common ternary composition of semiconducting type I clathrates is $A_8 B_{16} C_{30}$,

where A is an alkali earth metal or possibly a divalent rare earth metal, B an element from group 13, and C a group 14 element. The composition can be understood with the Zintl concept, i.e., the host structure is fully charge balanced. Assuming that the guest species donates two valence electrons to the host structure, the composition formula can be balanced for charge neutrality in the host, resulting in a composition ratio 16:30 for the host species [64]. It is common for real materials to deviate from this ratio. If there is a shift so that the amount of B increases, while the amount of C decreases, there is an excess of holes in the structure and the system becomes intrinsically p-doped. If the balance is shifted in the opposite direction, with an excess amount of C, there is an excess of electrons and the system becomes intrinsically n-doped.

The distribution of the elements in the host structure is not random but shows chemical ordering. If the positioning in the cage structure is fully randomized, one is expected to find species B occupying a specific site at approximately 35%, based on the 16:30 ratio. Experimental measurements of the site occupancy factors (SOFs) show that this is not the case [64]. For example, in $Ba_8Ga_{16}Ge_{30}$, the SOF for Ba at the 6c site varies between 60 to 75% in different samples. The SOF for the 16i site is shifted down to about 16-17%, while the 24k site SOF is between 30 and 40%. The reason for this deviation is the unfavorable energy cost for bonds between trivalent elements in the structure, this was established through calculations done by Blake *et al.* [61], and has been more recently investigated using alloy cluster expansions [65]. The unwillingness of sharing bonds with another trivalent element leads to a set of rules for the maximal SOFs for trivalent elements. As an example, the 6c site only connects to 24k sites (Fig. 2.12, left panel), and can in principle allow SOFs up to 100% for a trivalent element [64]. Both the 16i and 24k sites, on the other hand, share a bond with another similar site (Fig. 2.12, middle panel, and right panel), and should both be limited to SOFs of a maximum of 50%. The sum of the SOFs for site 16i and 24k should be less than 50% since the 16i site sees three 24k sites, and each 24k site sees two 16i site (Fig. 2.12, middle panel, and right panel). Then, according to this rule, it is not possible to randomly distribute trivalent elements on the 6i and 24k site.

The lattice thermal conductivities in type I inorganic clathrates are intrinsically very low, about 1 W/mK at room temperature. The low thermal conductivity can be attributed to the complexity of the primitive cell, and the presence of "rattling" guest species in the cages. An investigation of the phonon dispersion in, e.g., $Ba_8Ga_{16}Ge_{30}$ (Fig. 2.13, left panel) shows branches of a localized character, already at lower energies. Starting at approximately 2-3 meV there are numerous localized branches up to about 12 meV. Investigating the partial density of states reveals that it is the Ba guests associated with the 6d Wyckoff site that dominantly contributes to the localized branches at lower energies (Fig. 2.13, right panel). At somewhat higher energies, from 6-7 meV to 12 meV, the localized branches are
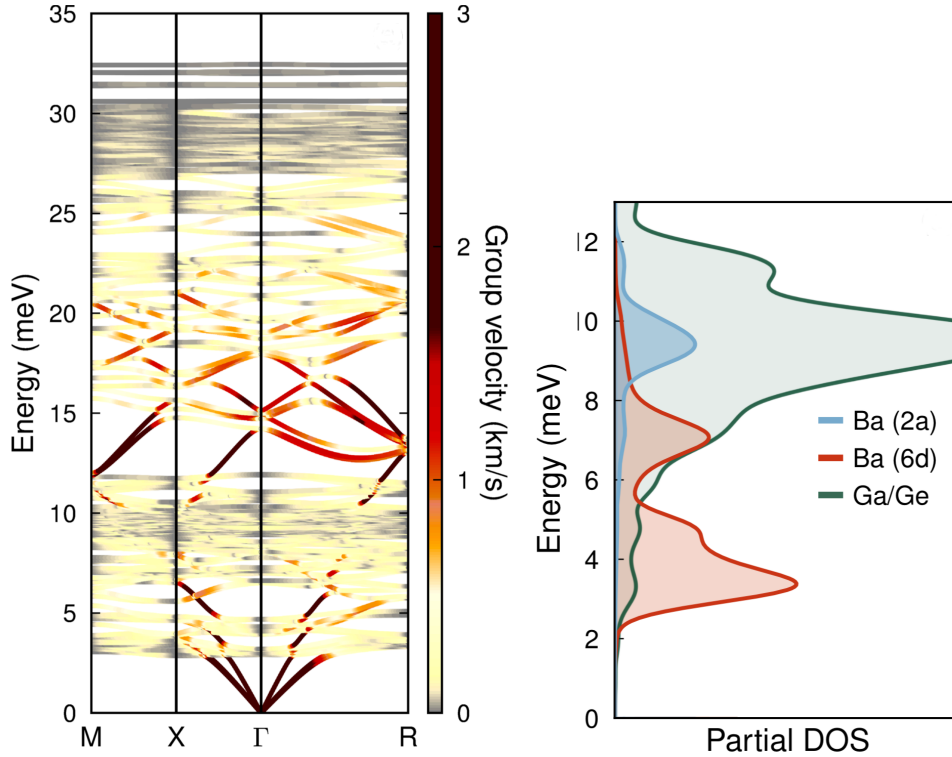
Figure 2.13: The left panel shows the phonon dispersion in $Ba_8Ga_{16}Ge_{30}$, color coded by the group velocity. The right panel shows the partial density of states in $Ba_8Ga_{16}Ge_{30}$, for Ba in the small cages at Wyckoff position $2a$ (blue line), Ba in the larger cage at Wykoff position $6d$ (red line), and the combined Ga/Ge cage (green line).

dominated by contributions from the Ga/Ge host structure.

In general, the trend for the lattice thermal conductivity κ_L in systems of increasing complexity is a reduction in κ_L [66]. A simple system, with a single atom in the primitive cell, can only have acoustic phonon modes. Each addition of an atom to the primitive cell introduces three new optical phonon modes. With increasing complexity, the additional number of optical phonon modes have a significant suppressing effect on the heat carrying acoustic modes, reducing κ_L. In the limit of an amorphous system, the acoustic contribution approaches zero, and the lattice mediated heat transfer is predominantly attributed to diffusion between atomic oscillators. The heat transport is then said to be glass-like.

With the inclusion of guest species, the heat capacity will increase, and κ_L might potentially become higher. On the other hand, if the guest atoms have highly anharmonic potentials, the increase in Umklapp scattering may instead introduce a decrease in κ_L. Further, if the guest species is under-constrained and weakly
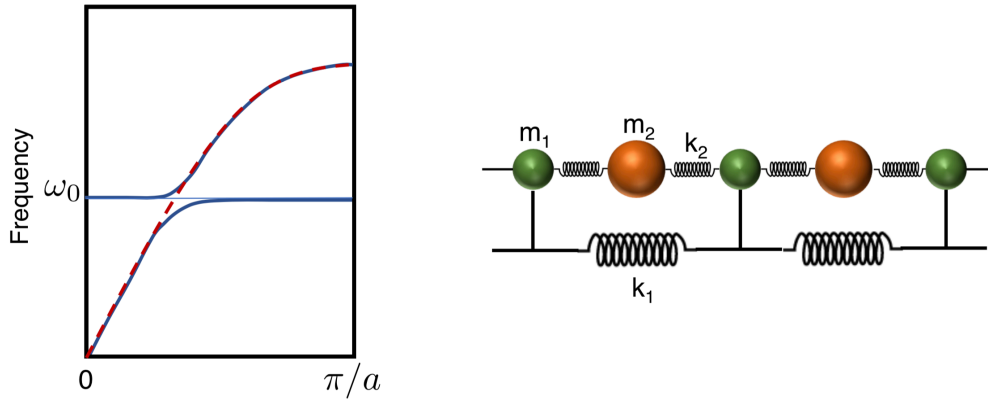
Figure 2.14: The left panel shows a schematic of an avoided band crossing at a resonance frequency ω_0, associated with the one-dimensional mass-spring system, shown in the right panel. The red dashed line correspond to the undisturbed acoustic mode in the absence of rattlers.

bound, the phenomena called rattling may occur. The effect of rattlers was at first thought to affect the phonon relaxation times through resonant scattering, resulting in a reduced κ_L [67]. An alternative mechanism is related to the group velocities. This mechanism can be understood by investigating a one-dimensional model (Fig. 2.14, right panel), analogous to the host/guest system of clathrates [68]. Assuming an alternating chain of masses m_1 coupled to masses m_2, with a coupling k_2. At the same time is the masses m_1 coupled to each other with a coupling k_1. A local resonance can occur when $k_2 \ll k_1$, with the possibility of the optical branch getting shifted to lower frequencies, resulting in an avoided band crossing, where the acoustic branch gets deflected (Fig. 2.14, left panel). The group velocity is then diminished at the resonance frequency resulting in a reduction of κ_L. The existence of rattler modes in clathrates has been theoretically predicted [63], showing good agreement with inelastic neutron scattering experiments. Rattling modes and avoided band crossings in clathrates have also been experimentally observed by Christensen *et al.* using triple axis spectroscopy on single crystal $Ba_8Ga_{16}Ge_{30}$ [68].

The overall effect on the lattice thermal conductivity, as the result of both complexity, and the presence of rattlers, has been theoretically investigated in the case of germanium-based type I clathrates by Dong *et al.* [69], using molecular dynamics with the Green-Kubo method. For pristine germanium in the diamond structure, they computed a lattice thermal conductivity of 114 W/mK at room temperature (the experimental value is 62 W/mK according to Ref. [70]). They further computed an estimate for the lattice thermal conductivity in an empty germanium cage Ge_{46}, resulting in a value of 12.2 W/mK, suggesting that the increased complexity in the caged structure gives an order of magnitude reduction for the conductivity.

Finally they introduced the effect of rattlers through the inclusion of Sr guests in the Ge_{46} framework, calculating a lattice thermal conductivity of 1.64 W/mK (the experimental value of $Sr_8Ga_{16}Ge_{30}$ is 0.89 W/mK [71]). Suggesting yet another order of magnitude reduction in the lattice thermal conductivity with the addition of rattlers. Compared to the thermal conductivity of 0.5 W/mK in amorphous Ge [47], this shows that the combined effect gives a structure with a thermal conductivity comparable to the thermal conductivity in glasses.

Because of the very low thermal conductivity and good performance as thermoelectric materials inorganic clathrates are thought of as a realization of the phonon glass-electron crystal concept [13], i.e., a system with the combination of low thermal conductivity and good electronic properties. The thermal conductivity in glasses typically has a T^2 dependence at really low temperatures [67]. In the following temperature range, the thermal conductivity levels out and plateaus. In the continuing range up to room temperature, the thermal conductivity slowly increases. In contrast, in materials with crystal-like thermal conductivity, the conductivity instead increases to a peak at lower temperatures, eventually followed by a $1/T$ decrease at higher temperatures. Both the crystal-like peak and the glass-like plateau have been reported for the lattice thermal conductivity in different inorganic clathrates [64].

3

Methods

3.1 Molecular dynamics simulations

The Boltzmann equation has some problems handling effects that deviate from bulk homogeneous effects, for instance interfaces. One alternative approach that can handle these difficulties is molecular dynamics (MD) [72].

MD is in general an entirely classical method where, assuming the atomic force fields are known, integration of Newtons equation for a collection of interacting atoms is performed. One illuminating example of the MD method is the use of Verlet integration [73] to Newtons equations. Given interatomic forces F acting on an atom, Newton's equation of motion for that atom are

$$F = ma, \tag{3.1}$$

where m is the mass of the atom and a its acceleration. To integrate Eq. (3.1) one approach is to Taylor expand the position r around some time t giving

$$r(t + \Delta t) = r(t) + v(t)\Delta t + \frac{1}{2}a(t)\Delta t^2 + \frac{1}{6}j(t)\Delta t^3 + \mathcal{O}(\Delta t^4),$$

$$r(t - \Delta t) = r(t) - v(t)\Delta t + \frac{1}{2}a(t)\Delta t^2 - \frac{1}{6}j(t)\Delta t^3 + \mathcal{O}(\Delta t^4), \tag{3.2}$$

where j is the jerk. Addition gives the Verlet integration as

$$r(t + \Delta t) = 2r(t) - r(t - \Delta t) + a(t)\Delta t^2 + \mathcal{O}(\Delta t^4). \tag{3.3}$$

This integration scheme is accurate to fourth order in time, velocity independent and only requires knowledge of the positions in the current as well as the last time

step. Starting from two initial steps it is then possible to evolve the system in accordance with Newton's laws of motion.

Two limitations of MD can be mentioned. First, MD is a completely classical method and as such the average energy per phonon mode is $k_B T$ and can differ quite a bit from the true energy [74] see Eq. (2.76). Secondly, the number of atoms that need to be included can be quite high. To capture the behavior of a phonon the simulation domain should be at least twice as large as the respective phonon mean free path. Since the mean free path can be on the order of tens to hundreds of nanometers the number of atoms in the simulation may become intractable [74].

For MD simulations aiming at calculating the thermal conductivity there are two main approaches, the Green-Kubo method and the "direct method" [75] in the form of non-equilibrium molecular dynamics (NEMD).

The Green-Kubo method is an equilibrium approach where the equilibrium fluctuations are used to determine the lattice thermal conductivity through the Green-Kubo relations [76, 77, 78]. The Green-Kubo method exhibits slower convergence than than NEMD and thus requires more time steps [79]. It has also been demonstrated that there generally is an inconsistency between the results of the two methods in the case of conductance at the interface between two crystals [80].

The direct method, NEMD is much more straight forward. Typically, a simulation domain is set up with one hot region and cold region some distance apart. The outer regions are then connected through a periodic boundary. By fixing the temperature in the hot region a temperature gradient can be established between the hot and the cold region by the use of an appropriate thermostat or swapping method. When a steady state has established and if the simulation has been properly done, the thermal conductivity can be determined with the use of Fourier's law.

3.2   Atomic forces from first principles

The IFCs introduced in Sect. 2.4.6 are calculated from knowledge of the forces between interacting atoms. In the present thesis, these forces were computed using quantum mechanical calculations.

The wave function of a quantum mechanical system $|\Psi\rangle$ is governed by the *Schrödinger equation* [81, 82]

$$i\hbar \frac{\partial |\Psi(t)\rangle}{\partial t} = H |\Psi(t)\rangle, \tag{3.4}$$

where the Hamiltonian H describes both internal and external interactions. The eigenspace of H is given as the solution to the eigenvalue problem

$$H |\psi\rangle = E |\psi\rangle. \tag{3.5}$$

48

The eigenvalues E are by *definition* the possible energies in a quantum mechanical system and thus solving Eq. (3.5) has merits of its own. The vectors $|\psi\rangle$ form a suitable basis for expanding the system $|\Psi\rangle$ and are the building blocks if one wants to construct a solution to Eq. (3.4).

In general, solving the Schrödinger equation directly is an impossible task, just as solving the Liouville equation, Eq. (2.54). The reason being that the quantum mechanical state is multidimensional in nature. This is a result [83] of the indistinguishable nature of quantum particles and the probabilistic interpretation of quantum states in accordance with the Born rule [84].

In matter the Hamiltonian can generally be written [85]

$$H = -\frac{\hbar}{2m_e}\sum_i \nabla_i^2 - \frac{\hbar}{2M_I}\sum_I \nabla_I^2$$
$$+ \frac{1}{2}\frac{1}{4\pi\epsilon_0}\sum_{i\neq j}\frac{e^2}{|\mathbf{r}_i - \mathbf{r}_j|} - \frac{1}{4\pi\epsilon_0}\sum_{i,I}\frac{Z_I e^2}{|\mathbf{r}_i - \mathbf{R}_I|} - \frac{1}{4\pi\epsilon_0}\sum_{I,J}\frac{Z_I Z_J e^2}{|\mathbf{R}_I - \mathbf{R}_J|}, \quad (3.6)$$

where M_I and Z_I are the mass and charge of a nuclei, m_e the mass of an electron, e the fundamental charge and ϵ_0 the permittivity of free space. The position vectors $\mathbf{r}_i$ and $\mathbf{R}_I$ are with respect to an electron respectively a nuclei. The first two sums are operators for the kinetic energy of the electrons and the nuclei. The third sum comprises operators for the Coulomb interaction between electrons. The fourth sum contains interactions between electrons and the nuclei and the fifth, interactions between the nuclei.

The motion of the electrons and the nuclei are usually on such different timescale that the electronic part of the wave function can be separated from the part concerning the nuclei. Then the nuclei can be seen as frozen from the point of the electrons. This allows for a treatment where the electrons are viewed separately from the nuclei as an external potential, here noted V_{ext}. The Hamiltonian can now be written as[1]

$$h = -\frac{1}{2}\sum_i \nabla_i^2 + \frac{1}{2}\sum_{i\neq j}\frac{1}{|\mathbf{r}_i - \mathbf{r}_j|} + V_{ext}. \quad (3.7)$$

When the Schrödinger equation is solved for this system the force on the nuclei can be calculated with the Hellmann-Feynman force theorem [86]. With a solution for the ground-state energy E the theorem states that the force on ion I is given by

$$\mathbf{F}_I = -\frac{\partial E}{\partial \mathbf{R}_I}. \quad (3.8)$$

---

[1]From here on Hartree units will be used. Then action is then measured in units of the reduced Planck constant, charge in units of the fundamental charge and mass in units of electron masses. Finally the vacuum permittivity is set to $1/4\pi$.

Still there is a problem. The Hamiltonian in h generates a problem with many degrees of freedom albeit the great simplification from the Born-Oppenheimer approximation. Also because of the term describing electron interaction the wave function is not separable into one-electron wave functions. There is thus still a need for further simplifications of the electronic structure problem defined by h.

3.3 Density functional theory

Density functional theory (DFT) nowadays refers to a collection of first-principals techniques using the electron density as a fundamental variable. The electron density in a system of electrons is defined as the number density of electrons in a specific state [87]. Suppressing spin the electron density is derived from the many-body electron wave function $|\Psi\rangle$ as

$$\rho(\boldsymbol{r}_1) = N \int d\boldsymbol{r}_2 \dots \boldsymbol{r}_N \left|\Psi\right|^2. \tag{3.9}$$

If possible, the electron density is a much leaner object to work with, compared to the multidimensional wave function.

Fortunately, Hohenberg and Kohn showed in 1964 [88] that the electron density can be considered as a fundamental property of the ground state in that the ground state wave function can be expressed as a functional of the electron density $\rho_0(\boldsymbol{r})$. Hence the ground state energy may be expressed as

$$E_0 = \langle \Psi[\rho_0(\boldsymbol{r})] | h | \Psi[\rho_0(\boldsymbol{r})] \rangle. \tag{3.10}$$

They also showed that there exist a general functional $F[\rho]$ expressing the energy contribution from the kinetic energy as well as the interaction among the electrons. Together with a part giving the interaction energy from electronic interaction with the external potential V_{ext}, the energy can be expressed as

$$E[\rho(\boldsymbol{r})] = F[\rho(\boldsymbol{r})] + \int d\boldsymbol{r} \, \rho(\boldsymbol{r})V_{ext}(\boldsymbol{r}). \tag{3.11}$$

This energy is minimized by the ground state density. Unfortunately the functional is not known in general. The theorem shows its existence but gives no prescription on how to find F. Since the functional contains many-body effects that are not known it is not possible to use this formulation, that is F directly [89].

3.3.1 The Kohn-Sham ansatz

In 1965 Kohn and Sham [90] proposed an ansatz where the system of interacting electrons is recast into a system of non-interacting electrons, a much simpler problem than the original many-body problem. The main assumption is that if one can

formulate an auxiliary problem, with the same ground state solution as in the full many-body problem, then a solution to the auxiliary system also solves the original problem. In the Kohn-Sham ansatz the functional $F[\rho(\boldsymbol{r})]$ in Eq. (3.11) is separated as

$$F[\rho(\boldsymbol{r})] = T_s[\rho(\boldsymbol{r})] + E_H[\rho(\boldsymbol{r})] + E_{xc}[\rho(\boldsymbol{r})]. \tag{3.12}$$

Here $T_s[\rho(\boldsymbol{r})]$ is the kinetic energy for non-interacting electrons and $E_H[\rho(\boldsymbol{r})]$ is the Hartee energy expressed as

$$E_H[\rho(\boldsymbol{r})] = \frac{1}{2} \int d\boldsymbol{r} d\boldsymbol{r}' \, \frac{\rho(\boldsymbol{r})\rho(\boldsymbol{r}')}{|\boldsymbol{r}-\boldsymbol{r}'|}. \tag{3.13}$$

Both of these terms are known. The unknown part $E_{xc}[\rho(\boldsymbol{r})]$ collects the more complicated many-body effects that are usually referred to as exchange and correlation.

In practice an effective potential is formulated as

$$V_{eff} = V_{ext} + V_H + V_{xc} \tag{3.14}$$

where V_H is the Hartree potential

$$V_H(\boldsymbol{r}) = \int d\boldsymbol{r}' \, \frac{\rho(\boldsymbol{r}')}{|\boldsymbol{r}-\boldsymbol{r}'|} \tag{3.15}$$

while the potential for exchange-correlation V_{xc} is the functional derivative of the exchange-correlation energy

$$V_{xc} = \frac{\delta E_{xc}[\rho(\boldsymbol{r})]}{\delta\rho(\boldsymbol{r})}. \tag{3.16}$$

The independence of the electrons allows for separation into single electron equations

$$\left(-\frac{1}{2}\nabla^2 + V_{eff}(\boldsymbol{r})\right)\psi_i(\boldsymbol{r}) = \varepsilon_i\psi_i(\boldsymbol{r}). \tag{3.17}$$

The Kohn-Sham orbitals $\psi_i(\boldsymbol{r})$ are under the constraint that

$$\rho(\boldsymbol{r}) = \sum_i f_i|\psi_i|^2, \tag{3.18}$$

where f_i is an occupation factor for electron state ψ_i. The formulation is exact although the functional for the exchange-correlation energy, $E_{xc}[\rho(\boldsymbol{r})]$ is unknown. Besides that there has been a great reduction in complexity from a quantum many-body problem into separate problems for independent electrons.

3.3.2   Exchange-correlation functionals

The unknown exchange-correlation functionals are in general complicated and approximations are necessary. The approximation presented in the original Kohn and Sham paper [90] assumes that the electron density in a local region is the same as the density in a uniform electron gas of density $\rho(\boldsymbol{r})$. The exchange-correlation energy is then given by

$$E_{xc}^{LDA}[\rho(\boldsymbol{r})] = \int d\boldsymbol{r} \; \rho(\boldsymbol{r})\varepsilon_{xc}^{LDA}[\rho(\boldsymbol{r})] \qquad (3.19)$$

where the exchange-correlation energy for the uniform gas has a known solution [85]. The approximation is relatively simple considering the full problem, but has nonetheless proven itself in many applications over the years.

The LDA assumes a slowly varying electron density, so a natural step is to include effects of local variations in the exchange-correlation functional. This approach is the semi-local *generalized gradient approximation* (GGA). Here the exchange-correlation energy is assumed to be dependent on the electron density as well as the gradient of the density

$$E_{xc}^{GGA}[\rho(\boldsymbol{r}] = \int d\boldsymbol{r} \; \rho(\boldsymbol{r})\varepsilon_{xc}^{GGA}[\rho(\boldsymbol{r}), \nabla\rho(\boldsymbol{r})]. \qquad (3.20)$$

There are many versions of GGAs. Most notable is the PBE functional [91], which has been successfully used in many applications.

3.3.3   van der Waals density functionals

The van der Waals force is the result of non-local correlation between electrons. Because of the non-local nature of the van der Waals force, it is not expected that a local or semi-local approximation will give a correct exchange-correlation energy.

In Papers I and II, first-principles calculations were conducted on van der Waals solids [35]. To describe van der Waals solids properly within DFT it is important to use a proper a van der Waals density functional (vdW-DF) that captures the sparse nature [92] of the materials. In 2003 a vdW-DF addressing layered structures [93] was presented, followed one year later by a vdW-DF for general structures [94].

In the vdW-DF method the correlation energy assumes a non-local form, which is expressed as a double integral over the spatial degrees of freedom [95]

$$E_c^{\mathrm{nl}}[\rho] = \frac{1}{2} \int \int \rho(\boldsymbol{r})\phi(\boldsymbol{r}, \boldsymbol{r}')\rho(\boldsymbol{r}')d^3\boldsymbol{r}d^3\boldsymbol{r}', \qquad (3.21)$$

where the kernel $\phi(\boldsymbol{r}, \boldsymbol{r}')$ represents the non-local coupling of the electron densities at $\boldsymbol{r}$ and $\boldsymbol{r}'$. The correlation energy is usually complemented by a semi-local

exchange functional,

$$E_{xc}^{vdW-DF}[\rho(\boldsymbol{r})] = E_x^{sl}[\rho(\boldsymbol{r})] + E_c^{nl}[\rho(\boldsymbol{r})], \tag{3.22}$$

which historically was adapted from other semi-local exchange-correlation functionals. In 2014 a consistent exchange (CX) part was developed leading to the so-called vdW-DF-CX functional [96], which was used in Papers I and II of the present thesis.

3.3.4 Fourier expansion and pseudopotentials

In a solid, periodic boundary conditions are suitable for calculating bulk properties where surface effects are negligible. This is reasonable if the considered system is large compared to the boundaries. Effectively, by introducing periodic boundaries the computational system becomes infinite. In the case of a wave function, due to the theorem by Bloch [97] it is possible to expand the wave function in a plane wave basis set that is complete as long as the wave vectors in the first Brillouin zone are included. This is done by Fourier expansion over the reciprocal lattice vectors $\boldsymbol{G}$ through the series

$$\psi_{n,k}(\boldsymbol{r}) = \sum_{\boldsymbol{G}} c_{n,k+G} \exp\left[i(\boldsymbol{k}+\boldsymbol{G})\cdot\boldsymbol{r}\right]. \tag{3.23}$$

This sum is infinite and for practical purposes the series must be truncated by a cutoff. The Fourier coefficients $c_{n,k+G}$ decrease for increasing $\left|\boldsymbol{k}+\boldsymbol{G}\right|$ [89]. So introduction of an energy cutoff E_{cut} allows for expansion including only the reciprocal vectors that fulfill the condition

$$\frac{\hbar^2}{2m}\left|\boldsymbol{k}+\boldsymbol{G}\right|^2 < E_{cut}. \tag{3.24}$$

With an increasing number of nodes, a wave function picks up an oscillating behavior near the nuclei [98]. Oscillations are more complicated to handle computationally and cause slow convergence[2]. Since core electrons are not strongly involved in interaction with valence electrons, for the sake of chemical bonding, it is not necessary to have a detailed description of the wave functions close to the nuclei. To overcome this issue one frequently employs so-called pseudopotentials, which replace the full Coulomb potential corresponding to the ionic core with a smoother potential that incorporates the core electrons and has the same scattering properties as the original potential [85]. Common schemes include norm-conserving and ultra-soft pseudopotentials [99]. In the present work the project augmented wave (PAW) [100] method was employed, which represents a bridge between pseudopotential and all-electron type calculations.

---

[2]More coefficients are necessary in the Fourier expansion

Summary of the papers

4.1 Paper I: Ultra-low thermal conductivity in WSe$_2$

Tungsten diselenide (WSe$_2$) is a van der Waals (vdW) solid that consists of two-dimensional sheets with strong intralayer bonding and interplanar vdW coupling. Van der Waals solids have a highly anisotropic thermal conductivity with an out-of-plane conductivity $\kappa_\perp$ for bulk material of 1.5 W/mK at room temperature [44]. It was experimentally demonstrated that $\kappa_\perp$ in turbostratically deposited WSe$_2$ films can be reduced down to 0.05 W/mK. This is a factor of 30 lower than in bulk crystals and thus considerably below the conservative estimate of the minimum thermal conductivity thought achievable.

In this paper a microscopic model was developed to explain this observation of an ultra-low thermal conductivity in disordered thin films of WSe$_2$. This was accomplished within the framework of Boltzmann transport theory and the relaxation time approximation (Sect. 2.4.5) based on second order force constants calculated within density functional theory. To accurately capture nonlocal correlation effects a non-empirical consistent exchange vdW density functional (vdW-DF-cx) was used [96].

First the sensitivity of the lattice thermal conductivity to different planar defects was established. Stacking disorder and strain cause phonon localization and softening of the acoustic modes, which can account for a reduction of $\kappa_\perp$ by a factor of 2 to 4 (green dashed line in Fig. 4.1). In addition the layer disorder introduces a structural limit on the phonon mean free path, which can be reduced to the separation between individual layers. Assuming that this limitation can be modeled by a diffuse boundary scattering model reduces the conductivity as well (green band
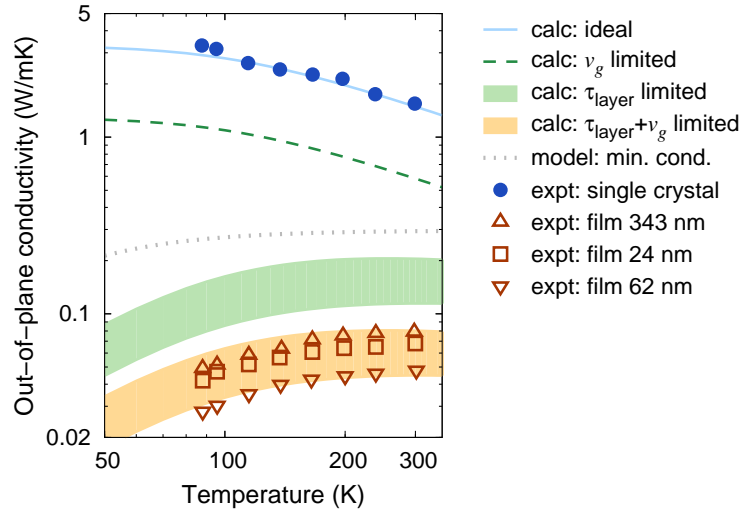
55

Figure 4.1: The experimentally measured reduced lattice thermal conductivity in disordered thin WSe_2 films corresponds to the red triangles and squares (Cahill et. al. [44]). The measured values in a single bulk crystal corresponds to the blue dots. Reduction of group velocities lowers the lattice thermal conductivity to the green dashed line. Lifetime reductions due to strong boundary scattering associated with disorder reduces the conductivity to the green band. Adding the effect of both group velocity reduction as well as lowered lifetime as a result of increased scattering reduces the predicted lattice thermal conductivity to the yellow band.

in Fig. 4.1). If the effect of group velocity and lifetime reduction are combined one obtains a lattice thermal conductivity that is comparable to the measured data (yellow band in Fig. 4.1).

The results show that a reduction of $\kappa_{\perp}$ by 40–60% can be achieved merely by variations in the layer stacking, which is associated with only a small energy cost. This can be important for e.g., thermoelectric applications where a low thermal conductivity in conjunction with a high electrical conductivity is necessary to achieve a high thermodynamic efficiency. Since electrons typically have larger mean free paths than phonons, they are less likely to be affected by changes in the stacking order, thus creating the possibility to decouple electrical and thermal transport properties. While the model was developed for WSe_2 it is likely to be also applicable to similar vdW solids.
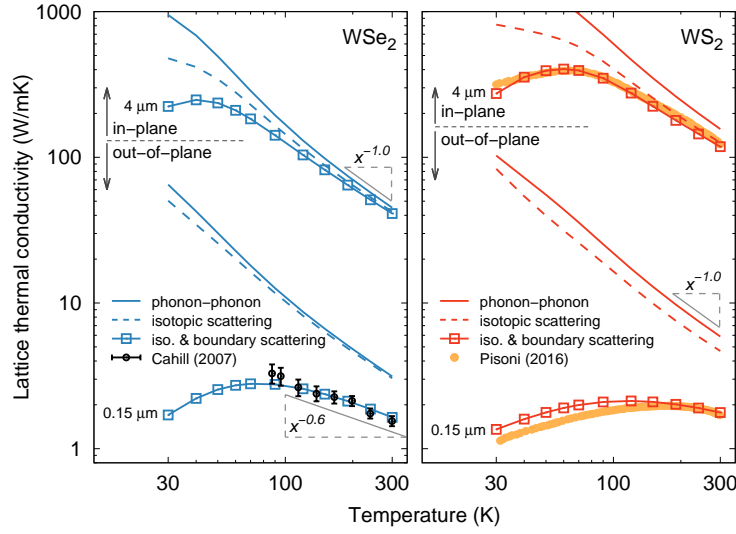
Figure 4.2: Calculated lattice thermal conductivity of WSe$_2$ and WS$_2$ in comparison with experiment. Solid and dashed lines and lines with squares shoe the calculated thermal conductivity obtained when including boundary scattering, isotopic scattering and boundary scattering. The structural length scale is set to 4 μm for the in-plane and 0.15 μm for the out-of-plane conductivity. Experimental data for WS$_2$ and WSe$_2$ were taken from Pisoni (2016) [45] and Chiritescu (2007) [44], respectively.

4.2 Paper II: Thermal conductivity in van der Waals solids

Novel synthesis techniques [29, 101] provide the opportunity to create highly engineered van der Waals (vdW) solids, which emerge as promising candidates for a manifold of applications including electronic components [36], optoelectronic [34, 37, 38], thermoelectrics [40], and spintronics [39]. Since thermal transport plays a key role in many of these situations, it is important to develop a detailed understanding of the thermal conductivity κ in vdW solids.

Unfortunately, values for the thermal conductivities reported in the literature exhibit a wide spread and can differ by more than one order of magnitude. This can be partly attributed to the challenges associated with experimental measurements of the thermal conductivity in nanostructures with pronounced anisotropy, see e.g., [49]. Possibly even more crucial is the sensitivity of the results to defects and sample size effects, as the growth of large high-quality TMD single crystals is very time consuming [49].

Given this motivation the present paper investigates the finite temperature prop-

erties as well as the lattice thermal conductivity κ in Mo and W-based transition metal dichalcogenides (TMDs) employing a combination of density functional and Boltzmann transport theory. Once again the calculations were carried out using the vdW-DF-CX functional, which is shown to yield excellent agreement with experimental lattice constants at room temperature with an average relative error below 0.2%.

With regard to the thermal conductivity it is demonstrated that care must be taken with regard to some computational parameters, in particular the displacement amplitude used for evaluating finite differences. A careful analysis shows that larger values than commonly used for e.g., materials such as silicon, are required in order to balance numerical accuracy with the smallness of vdW forces.

The calculated in-plane conductivities at room temperature are in good agreement with experimental data for high-purity material, when only phonon-phonon and isotopic scattering are included (Fig. 4.2). Explaining the experimental data over the entire temperature, however, requires inclusion of a temperature independent scattering mechanism that limits the phonon mean free path (MFP). The latter effect is even more pronounced in the case of the out-of-plane conductivity (Fig. 4.2).

The sensitivity of the thermal conductivity to structural inhomogeneities can be rationalized in terms of the long MFPs of the modes that contribute the most strongly to κ. The MFP of these modes (including phonon-phonon and isotopic scattering) is at least 1 μm, which is comparable to silicon but much larger than e.g., PbTe. This behavior is promising for thermoelectric applications, where lowering the lattice part of the thermal conductivity is a widely employed approach for increasing the thermodynamic efficiency. On the other hand, it can pose problems for electronic and optoelectronic applications, which require a large κ for rapid heat dissipation.

Overall the present study provides a comprehensive set of lattice thermal conductivities for bulk TMDs that establishes bounds set by phonon-phonon scattering and intrinsic length scales. It thereby forms the basis for future studies on these systems, which could focus e.g., on genuine vdW solids comprising different layers.

4.3 Paper III: Chemical order and transport properties in an inorganic clathrate: Optimal structures by computational design

Clathrates are chemical substances with a defined lattice structure that can trap atomic or molecular species [50, 51]. Inorganic clathrates such as $Ba_8Ga_{16}Ge_{30}$ or $Sr_8Ga_{16}Sn_{30}$ exhibit a combination of electrical and thermal transport properties
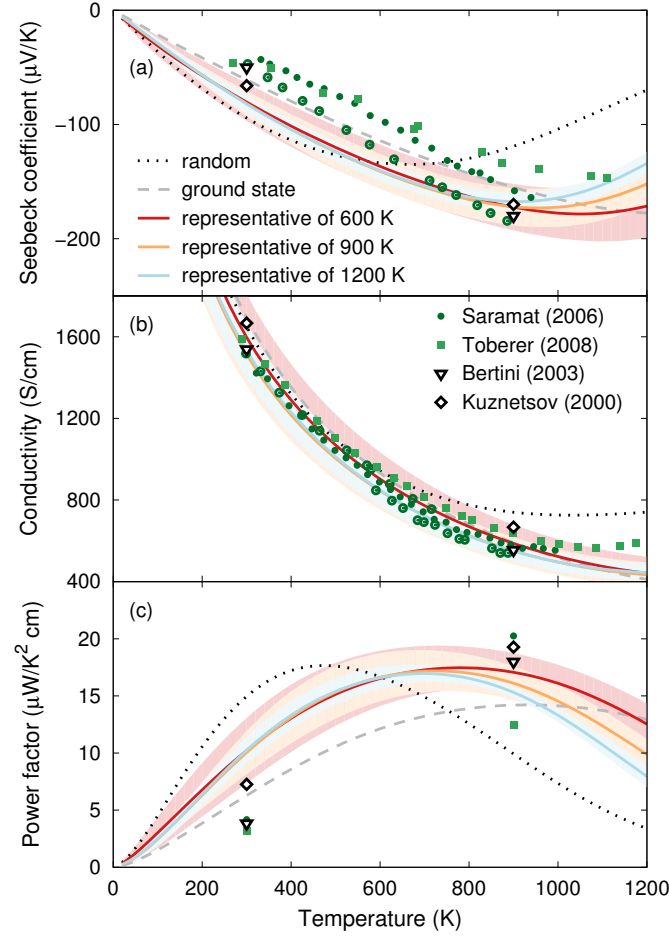
Figure 4.3: Electrical transport properties of n-type $Ba_8Ga_{16}Ge_{30}$ at a carrier density of 3×10^{20} cm^{-3}. (a) Seebeck coefficient, (b) electrical conductivity, and (c) power factor as a function of temperature from calculations in comparison with experimental data.

that are very favorable for thermoelectric applications [52, 53]. Here, the earth alkaline atoms act as guest species that occupy the cages provided by the host structure, where the host structure most commonly is composed of elements from groups 13 and 14. Clathrates, as well as some other thermoelectric materials, are multicomponent systems exhibiting chemical ordering, with the potential to affect transport properties.

This paper focuses on the electrical properties of $Ba_8Ga_{16}Ge_{30}$ due to the chemical order, investigated with the use of alloy cluster expansions. The cluster expansions were trained by density functional theory calculations, in which the chemical order in the form of the site occupancy factors was determined as a function of

temperature. A ground-state structure was determined with the use of a simulated annealing procedure. The ground-state was shown not to have any first neighbor Ga–Ga bonds.

The electrical conductivity σ and Seebeck coefficient S could then be computed under n-type conditions for the ground-state structure, as well as for representative configurations for the chemical order at different temperatures (Fig. 4.3). These computations were conducted using a combination of density functional theory and Boltzmann transport theory, showing good agreement with experimental data for both the electrical conductivity and the power factor $S^2\sigma$. The power factor was shown to peak roughly at 800-900 K consistent with previous experiments.

Finally, by combining density functional theory, Boltzmann transport theory, and Monte Carlo simulations with cluster expansions, a maximization of the power factor could be achieved by searching for optimized configurations. It was found that minimizing the Ga SOFs at the $6c$ Wyckoff site gives a calculated power factor up to $27\,\mu\text{W/K}^2\text{cm}$. The optimized power factors corresponds to an increase of approximately 60% compared to the power factor of non-optimized configurations.

4.4 Paper IV: Electronic and lattice thermal conductivity in intermetallic clathrates: A first principles perspective

Inorganic clathrates are among the most efficient thermoelectric materials [67, 102] with reported figure-of-merit (zT) exceeding values of one [56, 58]. They generally exhibit very low thermal conductivities, comparable to the conductivities of glasses. Hence, inorganic clathrates are though of as realizations of the "phonon glass-electron crystal" concept [13]. The low thermal conductivity originates partly from the heavier caged guest species, which undergo "rattling" motion at low frequencies, due to weak binding. In this paper both the electronic and the lattice thermal conductivity in the representative inorganic clathrate $\text{Ba}_8\text{Ga}_{16}\text{Ge}_{30}$ were investigated in detail. The ground-state configuration, as well as some other representative configurations obtained in Paper III, were used for this purpose.

The lattice thermal conductivity in $\text{Ba}_8\text{Ga}_{16}\text{Ge}_{30}$ is challenging to compute, in part due to the sensitivity to the vibrational spectra of the guest rattlers. The phonon dispersion was calculated from the second order interatomic force constants (IFCs) obtained with density functional theory. The IFCs were then used to examine the thermal expansion within the quasi-harmonic approximation. Because of the impact of the structure on the rattler-modes, the choice of exchange-correlation functional was first scrutinized. The non-empirical consistent-exchange van der Waals functional (vdW-DF-cx) [96] was found to be well suited, compared
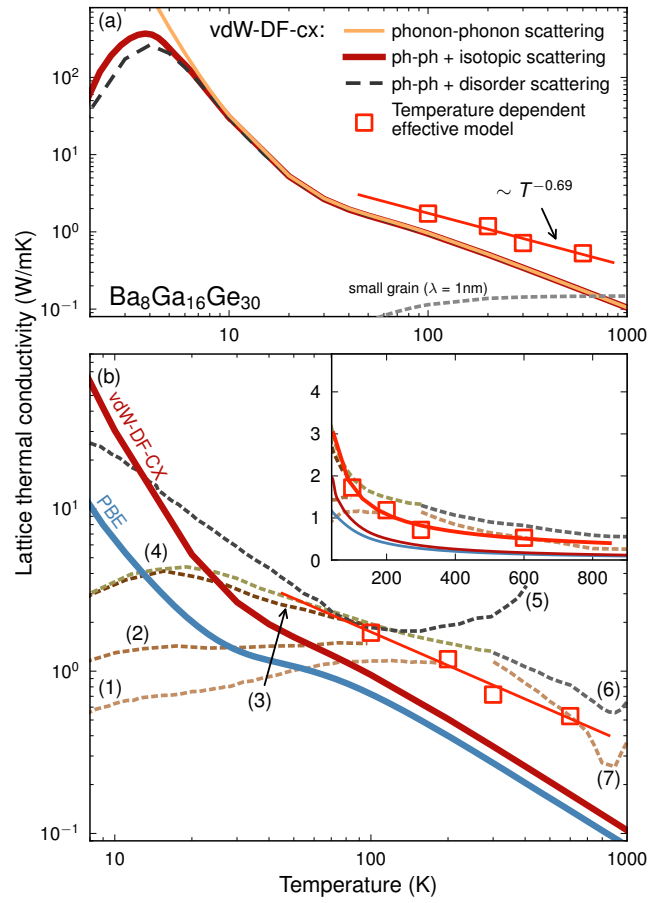
Figure 4.4: Lattice thermal conductivity κ_l of $Ba_8Ga_{16}Ge_{30}$ as a function of temperature. (a) Comparison of κ_l due to different included scattering channels, calculated using IFCs achieved with the vdW-DF-cx functional, as well as a comparison to the computations using temperature dependent effective IFCs. (b) Comparison between computations, using IFCs from the vdW-DF-cx functional (red solid line), the PBE functional (solid blue line), temperature dependent effective models (squares) and experimental data sets (dashed lines marked by numbers). The inset shows the same data on a linear scale. Different experimental data sets are marked (1)-(7).

to the PBE functional, since it predicted a finite temperature lattice constant closer to the experimental data and produced a better vibrational spectrum when compared to the data in Ref. [68].

To address the lattice thermal conductivity the third order IFCs were computed. The static (0 K) IFCs produced lattice thermal conductivities that were systemat-
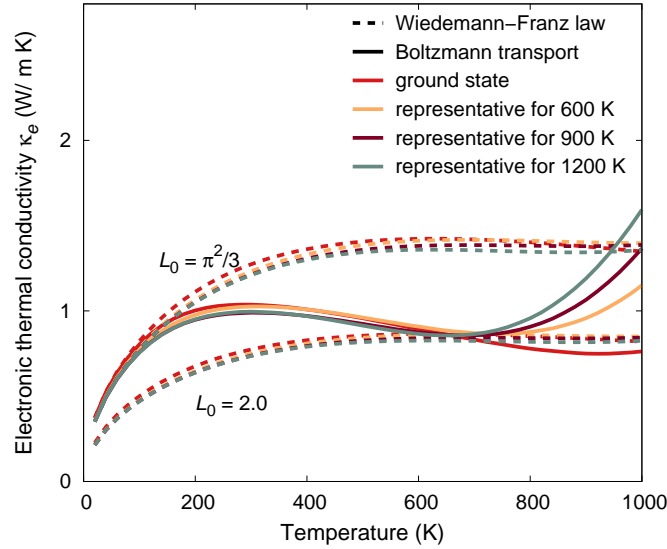
Figure 4.5: Electronic contribution κ_e to the thermal conductivity calculated for the ground state structure as well as for structures extracted from Monte Carlo simulations representative of the chemical order at different temperatures. Data obtained using the Wiedemann-Franz law $\kappa_e = L\sigma T$ are shown by dashed lines, whereas the thermal conductivity obtained within the framework of Boltzmann transport theory is shown by solid lines.

ically underestimating the reported experimental conductivities (Fig. 4.4). Using effective temperature dependent IFCs, obtained with first-principles molecular dynamics simulations, the prediction improved both in magnitude and slope. The success of the effective IFCs indicates that phonon-phonon coupling is important for an accurate representation of the low-frequency region related to the rattler-modes. In agreement with previous work the low-lying guest modes were associated with an avoided band crossing in the phonon dispersion [63, 68]. The underestimation of the rattler modes was linked with the onset of the avoided band crossing at a lower q vector. In addition to the previous studies, which focused on the low energy region, modes at higher energies were identified to contribute to the lattice thermal conductivity significantly.

The electronic contribution to the thermal conductivity was investigated using Boltzmann transport theory, by applying it to the ground-state and some higher temperature configurations. According to Wiedemann-Franz law couples the electronic part of the thermal conductivity κ_e to the electrical conductivity σ through the relation

$$\kappa_e = L\sigma T, \tag{4.1}$$

where $L = L_0(k_B^2/e^2)$ is the Lorenz number. The Wiedemann-Franz law is used to separate the electronic thermal conductivity and the lattice thermal conductivity from the measured total thermal conductivity. The value of L_0 typical ranges from 2 (for semiconductors) to 3.3 (for a degenerate electron gas). The computed κ_e lies between conductivities predicted by Wiedemann-Franz law using these L_0 values (Fig. 4.5). It was seen that lower temperatures are more consistent with the larger Lorenz-factor, and conductivities at higher temperatures are more consistent with the Lorenz-factor typical for a semiconductor. This variation indicates that special care should be taken when applying the Wiedemann-Franz law for interpreting measured thermal conductivities of clathrate systems, especially since the electronic thermal conductivity is of the same order as the lattice thermal conductivity.

5

Outlook

In the present thesis, two different types of materials were investigated with regard to their ability to transport heat. Papers I and II addressed layered materials with very anisotropic properties. Because of the weak interlayer binding, they are prone to form planar defects, which as shown in this thesis can have dramatic effects on their ability to conduct heat. At the same time, the 2D character of the individual sheets enables the fabrication of heterostructures composed of layers of different 2D materials including but not limited to the transition metal dichalcogenides (TMDs) investigated in the present thesis. Thus while in the present thesis the focus has been on homogeneous materials, in the future this research ought to be extended to heterostructures composed of different TMDs and not necessarily limited to Mo and W-based compounds. It was discussed in Paper II how differences in mass and structure affect the phonon dispersion, which in turn determines to a large extent the lattice thermal conductivity. By combining different layers, it becomes possible to engineer these features and to manipulate both out-of-plane and in-plane transport in a very controlled fashion.

The approach taken in Paper III is here potentially very powerful, i.e., by combining transport calculations with effective models (such as the cluster expansions in Paper III) and sampling techniques (e.g., Monte Carlo simulations or genetic algorithms) one can computationally design structures with specified transport properties. This "inverse design" approach was adopted in Paper III to optimize electrical transport properties in clathrates but is in principle equally applicable to thermal transport. Conversely, it would be interesting to explore electrical transport in van der Waals solids and specifically to explore strategies for controlling electron-phonon coupling and decoupling electronic and thermal transport.

Besides planar defects are different point defects in the TMDs interesting to investigate. As a result of the manufacturing process for single or few-layers TMDs,

65

in conjunction with low defect formation energies for point defects, can considerable defect concentrations be expected, and with that the possibility for substantial effects on the thermal conductivity [103]. For this investigation is a first-principles Greens-function approach [104] suitable for quantifying the effect of scattering due to point defects.

The use of effective interatomic force constants in Paper IV was crucial for a functional description of the rattler-modes and with that the correct prediction of the lattice thermal conductivity. This approach could be interesting to apply for other systems, e.g., filled skutterudites, that also show signs of strongly damped quasi-particles when described with static interatomic force constants [105]. A more rigorous approach is also desirable. The effective model takes the phonon-phonon coupling with the vibrational spectra into account. Applying self-consistent phonon theory, for renormalization of the spectra, would be an interesting step.

The insight and results gained in this thesis are not only important for our understanding of van der Waals solids and thermoelectric materials but for thermal transport in general. In the future, the goal will be to implement the concepts developed here in experimental settings and to push the limits of materials and transport. In this fashion this thesis will ultimately contribute to the vast and important field of energy management.

Balance equations in thermodynamics

The fundamental questions within theories dealing with transport, are how much of a quantity is within a specific region of space, and in which way is this amount changing over time? In general there are only three different kinds of mechanisms that can change the amount of quantity within the region. The quantity can be transported over the boundary to the surroundings, or the quantity can be either produced or annihilated within the boundary. The mathematical relations describing theses processes are called *balance equations*.

Under the assumption that the continuum hypothesis is valid, an extensive quantity E can be associated with a material point, such that

$$\lim_{\Delta M \to 0} \frac{\Delta E}{\Delta V} = \rho e, \tag{A.1}$$

where M is the mass occupying the volume V, ρ is the mass density and e the specific value of E. Given a description of the specific distribution of a quantity, the total quantity within a region Ω is then given by summing up all contributions

$$E_\Omega = \int_\Omega \rho e \, \mathrm{d}V, \tag{A.2}$$

where $\mathrm{d}V$ is the volume element to Ω. With the use of the Reynolds transport theorem [106], the rate of change of E_Ω is expressed as

$$\frac{\mathrm{d}E_\Omega}{\mathrm{d}t} = \frac{\mathrm{d}}{\mathrm{d}t} \int_\Omega \rho e \, \mathrm{d}V = \int_\Omega \rho \frac{\partial e}{\partial t} \, \mathrm{d}V, \tag{A.3}$$

where the partial derivative is in the local sense. In principle, as stated in the introduction to this section, the only possibility to change the ammount of the quantity within Ω is to either have the quantity leave or enter the boundary $\partial\Omega$, or that the quantity is produced or annihilated within Ω. The flow of the quantity e is readily described as a flux $\boldsymbol{J}_e$. Each component of the flux, by definition, is the amount of E flowing through a unit area perpendicular to the corresponding unit vector, in unit time. Defining $\boldsymbol{n}$ as the outbound normal to $\partial\Omega$, the total flow F entering Ω through the boundary in unit time is then

$$F = -\int_{\partial\Omega} \boldsymbol{J}_e \cdot \boldsymbol{n}\,\mathrm{d}S = -\int_{\Omega} \nabla \cdot \boldsymbol{J}_e\,\mathrm{d}V. \tag{A.4}$$

Here, $\mathrm{d}S$ is the surface element to $\partial\Omega$ and the divergence theorem is used to transform the expression into a volume integral. The rate of production is expressed by a function σ_e, that describes the local production when positive, and local annihilation when negative. The total production P in unit time within Ω, due to σ_e is then

$$P = \int_{\Omega} \sigma_e\,\mathrm{d}V. \tag{A.5}$$

By invoking the principle of balance, the rate of change within Ω is the sum of transport over the boundary and internal production

$$\frac{\mathrm{d}E_\Omega}{\mathrm{d}t} = F + P, \tag{A.6}$$

or in integral form expressed as

$$\int_{\Omega} \rho\frac{\partial e}{\partial t}\,\mathrm{d}V = -\int_{\Omega} \nabla \cdot \boldsymbol{J}_e\,\mathrm{d}V + \int_{\Omega} \sigma_e\,\mathrm{d}V. \tag{A.7}$$

The integrals are over the same volume, and since the volume element is arbitrary the integrand must vanish identically. The general balance law, written in local form, is then

$$\rho\frac{\partial e}{\partial t} = -\nabla \cdot \boldsymbol{J}_e + \sigma_e. \tag{A.8}$$

In the special case where the quantity is only exchanged through fluxes, i.e., when there is no production term, the quantity is said to be conserved and the balance equation may be expressed as

$$\rho\frac{\partial e}{\partial t} + \nabla \cdot \boldsymbol{J}_e = 0, \tag{A.9}$$

which takes on the simple form of a *conserved continuity equation*.

A.1 Balance equations for the internal energy

From the broader perspective, *the first law of thermodynamics* implicitly invokes a balance law, simply stating that the *total energy* is conserved. For practical purposes, some context is needed. Within the context of continuum mechanics, the law states that the material derivative of the total energy of a body equals the total power input from both work W and heat Q

$$\frac{\mathrm{d}K}{\mathrm{d}t} + \frac{\mathrm{d}U}{\mathrm{d}t} = W + Q. \tag{A.10}$$

Where K is the macroscopic kinetic energy and U the internal energy. The input from work associates with two types of processes affecting the macroscopic state of the system, either acceleration and deformation of the bulk due to coupling to external fields or deformation and acceleration of the boundaries due to external traction. Heat can be either in the form of a heat flux $\boldsymbol{J}_q$ over the system boundary, or from internal generation σ_q. Internal generation can originate, e.g., from radioactive decay, or in the case of fluids from frictional losses due to viscous interaction with the surroundings as well as turbulent internal dissipation, or in the case of an electric current transmitted through the system from irreversible energy transfer due to Joule heating.

Following a standard treatment, such as the one in Reddy [107], the first law, Eq. (A.10), gives the local form of energy balance for the internal energy density u, expressed as

$$\rho\frac{\mathrm{d}u}{\mathrm{d}t} = -\nabla \cdot \boldsymbol{J}_q + \sigma : S + \sigma_q. \tag{A.11}$$

Here $\sigma : S$ is the double scalar product[1] between the internal stress tensor and the symmetric part of the strain rate tensor. The term has the interpretation of a source due to internal work.

In the case of a transmitted electric current, the electrons is accelerated in a collective manner due to a difference in the electric potential, introducing a drift velocity to the electron population. At the same time the electrons scatter, which introduces a random component in the velocity distribution. The result is an increase in the part of the entropy pertaining to the electrons, introducing a dissipation of the kinetic energy carried in the field direction.

$$\rho\frac{\mathrm{d}u}{\mathrm{d}t} = -\nabla \cdot \boldsymbol{J}_q + \sigma : S + \boldsymbol{E} \cdot \boldsymbol{i}. \tag{A.12}$$

---

[1]The double scalar product is here defined as the double sum $A : B = \sum ij\, A_{ij} B_{ji}$.

A.2 Balance equations for entropy

In classical thermodynamics, the entropy S_0 is only defined for systems in equilibrium. In non-equilibrium thermodynamics, due to the local-equilibrium hypothesis the entropy concept can be extended to systems out of equilibrium, resulting in an extensive quantity S that must obey a transport law of its own.

Since entropy is an extensive quantity, it is reasonable to separate changes in a systems entropy into an entropy flow $\boldsymbol{J}_s$, and an entropy production σ_s. As stated with *the second law of thermodynamics*, entropy is a *non-conserved quantity* that can not be annihilated. Hence the production term must be either zero or greater than zero

$$\sigma_s \geq 0. \tag{A.13}$$

This is a stronger statement than the one given in classical thermodynamics, where the increase of entropy is assumed to be increasing globally.

The balance equation for the change of a systems entropy is now expressed as

$$\frac{\mathrm{d}S}{\mathrm{d}t} = \frac{\mathrm{d}_e S}{\mathrm{d}t} + \frac{\mathrm{d}_i S}{\mathrm{d}t}. \tag{A.14}$$

Here the total entropy is given by integrating the specific entropy s

$$S = \int_\Omega \rho s \, \mathrm{d}V. \tag{A.15}$$

The exchange of entropy with the surroundings is expressed through the entropy flux

$$\frac{\mathrm{d}_e S}{\mathrm{d}t} \int_{\partial\Omega} \boldsymbol{J}_s \, \mathrm{d}S, \tag{A.16}$$

and the internal production is

$$\frac{\mathrm{d}_i S}{\mathrm{d}t} \int_\Omega \sigma_s \, \mathrm{d}V. \tag{A.17}$$

By invoking the divergence and the Reynold's transport theorems the equation for local entropy balance is

$$\rho \frac{\mathrm{d}s}{\mathrm{d}t} = -\nabla \cdot \boldsymbol{J}_s + \sigma_s. \tag{A.18}$$

Liouville's theorem

The following short section gives a derivation of *Liouville's theorem*. This theorem is of importances in the theoretical framework of a statistical treatment of transport phenomena [108] and the foundation on which the *Boltzmann equation* is formally derived.

Start by introducing a compact notation for the $6N$ generalized coordinates and momenta in phase space as $q = q_1, \ldots, q_{3N}$ and $p = p_1, \ldots, p_{3N}$. Let the corresponding volume element be $dqdp = dq_1 \cdots dq_{3N} dp_1 \cdots dp_{3N}$. Let $\rho(q, p, t)$ be the number density of states in phases space so that

$$\rho(q, p, t)\, dqdp \tag{B.1}$$

corresponds to the number of states in the volume element at time t. Let V be a constant volume in phase space and S the surface that enclose V. The rate of change in the number of states in V is then

$$\frac{\partial}{\partial t} \int_V \rho\, dqdp. \tag{B.2}$$

As long as no states are produced or destroyed within V the rate at wich the number of states changes must equal the net transport of states over S

$$\frac{\partial}{\partial t} \int_V \rho\, dqdp = -\int_S \rho\, \boldsymbol{v} \cdot \boldsymbol{n}\, dS. \tag{B.3}$$

Here $\boldsymbol{v}$ is the velocity field [1] across the surface and $\boldsymbol{n}$ the outbound normal. Using

---

[1]A velocity field in the generalized sense that

$$\boldsymbol{v} = \left(\frac{\partial q_1}{\partial t}, \ldots, \frac{\partial q_{3N}}{\partial t}, \frac{\partial q_1}{\partial t}, \ldots, \frac{\partial p_{3N}}{\partial t} \right).$$

the divergence theorem the surface integral can be changed into a volume integral over the divergence of $\rho\boldsymbol{v}$. Since the control volume is not changing the time derivative can be taken inside the volume integral over ρ and a re-arrangement gives

$$\int_V \left(\frac{\partial \rho}{\partial t} + \nabla \cdot (\rho \boldsymbol{v}) \right) dV = 0. \tag{B.4}$$

The volume is arbitrarily chosen so the integrand must vanish identically. Hence

$$\frac{\partial \rho}{\partial t} + \nabla \cdot (\rho \boldsymbol{v}) = 0. \tag{B.5}$$

Applying the product rule on the terms in the expanded divergence in the continuity equation equals

$$\frac{\partial \rho}{\partial t} + \sum_{i=1}^{3N} \left(\frac{\partial \rho}{\partial q_i} \frac{\partial q_i}{\partial t} + \frac{\partial \rho}{\partial p_i} \frac{\partial p_i}{\partial t} \right) + \rho \sum_{i}^{3N} \left(\frac{\partial^2 q_i}{\partial q_i \partial t} + \frac{\partial^2 p_i}{\partial p_i \partial t} \right) = 0. \tag{B.6}$$

For each pair of conjugate variables the canonical equations read [109]

$$
\begin{aligned}
\frac{\partial q_i}{\partial t} &= \frac{\partial H}{\partial p_i} \\
\frac{\partial p_i}{\partial t} &= -\frac{\partial H}{\partial q_i},
\end{aligned}
\tag{B.7}
$$

where $H(q, p)$ is the Hamiltonian, and so each term in the last sum in Eq. (B.6) is identically zero since partial derivatives commute. Due to the chain rule combined with the Poisson bracket [2] the remaining part of the continuity equation can now be written as the total derivative

$$
\begin{aligned}
\frac{d\rho}{dt} &= \frac{\partial \rho}{\partial t} + \sum_{i=1}^{3N} \left(\frac{\partial \rho}{\partial q_i} \frac{\partial q_i}{\partial t} + \frac{\partial \rho}{\partial p_i} \frac{\partial p_i}{\partial t} \right) \\
&= \frac{\partial \rho}{\partial t} + \sum_{i=1}^{3N} \left(\frac{\partial \rho}{\partial q_i} \frac{\partial H}{\partial p_i} - \frac{\partial \rho}{\partial p_i} \frac{\partial H}{\partial q_i} \right) \\
&= \frac{\partial \rho}{\partial t} + \{ \rho, H \} = 0.
\end{aligned}
\tag{B.8}
$$

---

[2]The Poisson bracket for a quantity A related to a dynamical system governed by the Hamiltonian H is defined as

$$\{A, H\} = \sum_{i=1}^{3N} \left(\frac{\partial A}{\partial q_i} \frac{\partial H}{\partial p_i} - \frac{\partial A}{\partial p_i} \frac{\partial H}{\partial q_i} \right).$$

This resembles the result for an incompressibel fluid and one can think of the number densities of states in phase space as constituting an incompressible fluid. In the fixed frame of reference it is then shown that the total derivative of the number density function is zero. In the opposite frame, the co-moving frame that follows the fluid motion the number density doesn't change with time. This has the implication that a volume element in phase-space is invariant over time. This is the result known as *Liouville's theorem* and equation Eq. (B.8) is called *Liouville's equation*.

Acknowledgments

Bibliography

[1]   M. Kardar, *Statistical Physics of Particles*, 1 edition ed. (Cambridge University Press, Cambridge : New York, 2007).

[2]   International Energy Agency, *Key World Energy Statistics 2015*, `http://www.iea.org`, 2015, accessed: 2016-05-14.

[3]   R. Bookstaber, *A Demon of Our Own Design: Markets, Hedge Funds, and the Perils of Financial Innovation* (Wiley, Hoboken, N. J., 2008).

[4]   United Nations - Department of Economic and Social Affairs, `http://esa.un.org/unpd/wpp/Download/Standard/Population/`, data accessed: 2016-05-14.

[5]   H. D. Klemme and G. F. Ulmishek, *Effective Petroleum Source Rocks of the World: Stratigraphic Distribution and Controlling Depositional Factors (1)*, AAPG Bulletin **75**, 1809 (1991).

[6]   G. Bowden, *The Social Construction of Validity in Estimates of US Crude Oil Reserves*, Social Studies of Science **15**, 207 (1985).

[7]   K. Aleklett, M. Lardelli, and O. Qvennerstedt, *Peeking at peak oil* (Springer, New York ; London, 2012).

[8]   K. Aleklett, M. Höök, K. Jakobsson, M. Lardelli, S. Snowden, and B. Söderbergh, *The Peak of the Oil Age – Analyzing the world oil production Reference Scenario in World Energy Outlook 2008*, Energy Policy **38**, 1398 (2008).

[9]   I. Chapman, *The end of Peak Oil? Why this topic is still relevant despite recent denials*, Energy Policy **64**, 93 (2014).

[10]   U. S. Energy Information Agency, *International Energy Statistics - Total Primary Energy Production*, `http://www.eia.gov/cfapps/ipdbproject/IEDIndex3.cfm`, data accessed: 2016-05-14.

Bibliography

[11]   Intergovernmental Panel on Climate Change, *Climate Change 2013 - The Physical Science Basis: Working Group I Contribution to the Fifth Assessment Report of the Intergovernmental Panel on Climate Change*, 1 edition ed. (Cambridge University Press, New York, 2014).

[12]   Y. Demirel, *Energy: production, conversion, storage, conservation, and coupling*, *Green energy and technology* (Springer, London ; New York, 2012).

[13]   *CRC Handbook of Thermoelectrics*, 1 edition ed., edited by D. M. Rowe (CRC Press, Boca Raton, FL, 1995).

[14]   D. M. Rowe, *Thermoelectrics handbook: macro to nano-structured materials* (CRC Press, Boca Raton, FL, 2005).

[15]   H. B. Callen, *Thermodynamics and an introduction to thermostatistics* (Wiley, New York, 1985).

[16]   S. R. D. Groot and P. Mazur, *Non-Equilibrium Thermodynamics*, dover ed edition ed. (Dover Publications, New York, 2011).

[17]   *Thermoelectrics Handbook: Macro to Nano*, edited by D. Rowe (CRC Press, Boca Raton, 2005).

[18]   J. M. Ziman, *Electrons and phonons* (Clarendon Press, Oxford, 1960).

[19]   H. Goldstein, *Classical Mechanics*, 2nd edition ed. (Addison-Wesley, Reading, Mass, 1980).

[20]   J. J. Sakurai and S. F. Tuan, *Modern quantum mechanics*, rev. ed ed. (Addison-Wesley, Reading, Mass, 1994).

[21]   G. P. Srivastava, *The physics of phonons* (Hilger, Bristol, 1990).

[22]   W. Li, J. Carrete, N. A. Katcho, and N. Mingo, *ShengBTE: A solver of the Boltzmann transport equation for phonons*, Comp. Phys. Comm. **185**, 1747 (2014).

[23]   A. Togo, L. Chaput, and I. Tanaka, *Distributions of phonon lifetimes in Brillouin zones*, Phys. Rev. B **91**, 094306 (2015).

[24]   A. Gupta, T. Sakthivel, and S. Seal, *Recent development in 2D materials beyond graphene*, Progress in Materials Science **73**, 44 (2015).

[25]   K. S. Novoselov, A. Mishchenko, A. Carvalho, and A. H. Castro Neto, *2D materials and van der Waals heterostructures.*, Science (New York, N.Y.) **353**, aac9439 (2016).

[26] R. Mas-Ballesté, C. Gómez-Navarro, J. Gómez-Herrero, and F. Zamora, *2D materials: to graphene and beyond*, Nanoscale **3**, 20 (2011).

[27] K. S. Novoselov, A. K. Geim, S. V. Morozov, D. Jiang, Y. Zhang, S. V. Dubonos, I. V. Grigorieva, and A. A. Firsov, *Electric Field Effect in Atomically Thin Carbon Films*, Science **306**, 666 (2004).

[28] H. Liu, A. T. Neal, Z. Zhu, Z. Luo, X. Xu, D. Tománek, and P. D. Ye, *Phosphorene: An Unexplored 2D Semiconductor with a High Hole Mobility*, ACS Nano **8**, 4033 (2014).

[29] A. K. Geim and I. V. Grigorieva, *Van der Waals heterostructures*, Nature **499**, 419 (2013).

[30] K. Watanabe, T. Taniguchi, and H. Kanda, *Direct-bandgap properties and evidence for ultraviolet lasing of hexagonal boron nitride single crystal*, Nature Materials **3**, 404 (2004).

[31] P. J. Zomer, S. P. Dash, N. Tombros, and B. J. Van Wees, *A transfer technique for high mobility graphene devices on commercially available hexagonal boron nitride*, Applied Physics Letters **99**, 2009 (2011).

[32] C. R. Dean, A. F. Young, I. Meric, C. Lee, L. Wang, S. Sorgenfrei, K. Watanabe, T. Taniguchi, P. Kim, K. L. Shepard, and J. Hone, *Boron nitride substrates for high-quality graphene electronics*, Nature Nanotechnology **5**, 722 (2010).

[33] W. Rindler, *Introduction to special relativity* (Clarendon Press, Oxford, 1991).

[34] Q. H. Wang, K. Kalantar-Zadeh, A. Kis, J. N. Coleman, and M. S. Strano, *Electronics and optoelectronics of two-dimensional transition metal dichalcogenides*, Nature Nanotech. **7**, 699 (2012).

[35] G. Gao, W. Gao, E. Cannuccia, J. Taha-Tijerina, L. Balicas, A. Mathkar, T. N. Narayanan, Z. Liu, B. K. Gupta, J. Peng, Y. Yin, A. Rubio, and P. M. Ajayan, *Artificially Stacked Atomic Layers: Toward New van der Waals Solids*, Nano Lett. **12**, 3518 (2012).

[36] B. Radisavljevic, A. Radenovic, J. Brivio, V. Giacometti, and A. Kis, *Single-layer MoS$_2$ transistors*, Nature Nanotech. **6**, 147 (2011).

[37] X. Hong, J. Kim, S.-F. Shi, Y. Zhang, C. Jin, Y. Sun, S. Tongay, J. Wu, Y. Zhang, and F. Wang, *Ultrafast charge transfer in atomically thin MoS$_2$/WS$_2$ heterostructures*, Nature Nanotech. **9**, 682 (2014).

[38] M. Massicotte, P. Schmidt, F. Vialla, K. G. Schädler, A. Reserbat-Plantey, K. Watanabe, T. Taniguchi, K. J. Tielrooij, and F. H. L. Koppens, *Picosecond photoresponse in van der Waals heterostructures*, Nature Nanotech. **11**, 42 (2016).

[39] W. Han, *Perspectives for spintronics in 2D materials*, APL Materials **4**, 032401 (2016).

[40] H. Guo, T. Yang, P. Tao, Y. Wang, and Z. Zhang, *High pressure effect on structure, electronic structure, and thermoelectric properties of MoS_2*, J. Appl. Phys. **113**, 013709 (2013).

[41] S. Thakurta and A. Dutta, *Electrical conductivity, thermoelectric power and hall effect in p-type molybdenite (MoS2) crystal*, Journal of Physics and Chemistry of Solids **44**, 407 (1983).

[42] J.-Y. Kim, S.-M. Choi, W.-S. Seo, and W.-S. Cho, *Thermal and Electronic Properties of Exfoliated Metal Chalcogenides*, Bulletin of the Korean Chemical Society **31**, 3225 (2010).

[43] A. L. Moore and L. Shi, *Emerging challenges and materials for thermal management of electronics*, Materials Today **17**, 163 (2014).

[44] C. Chiritescu, D. G. Cahill, N. Nguyen, D. Johnson, A. Bodapati, P. Keblinski, and P. Zschack, *Ultralow Thermal Conductivity in Disordered, Layered WSe_2 Crystals*, Science **315**, 351 (2007).

[45] A. Pisoni, J. Jacimovic, R. Gaál, B. Náfrádi, H. Berger, Z. Revay, and L. Forró, *Anisotropic transport properties of tungsten disulfide*, Scripta Materialia **114**, 48 (2016).

[46] P. Jiang, X. Qian, X. Gu, and R. Yang, *Probing Anisotropic Thermal Conductivity of Transition Metal Dichalcogenides MX2 (M = Mo, W and X = S, Se) using Time-Domain Thermoreflectance*, Advanced Materials **29**, 1 (2017).

[47] D. G. Cahill, S. K. Watson, and R. O. Pohl, *Lower limit to the thermal conductivity of disordered crystals*, Physical Review B **46**, 6131 (1992).

[48] A. Pisoni, J. Jacimovic, O. S. Barišic A. Walter, B. Náfrádi, P. Bugnon, A. Magrez, H. Berger, Z. Revay, and L. Forró, *The Role of Transport Agents in MoS_2 Single Crystals*, J. Phys. Chem. C **119**, 3918 (2015).

[49] J. Liu, G.-M. Choi, and D. G. Cahill, *Measurement of the anisotropic thermal conductivity of molybdenum disulfide by the time-resolved magneto-optic Kerr effect*, J. Appl. Phys. **116**, 233107 (2014).

[50] A. D. McNaught and A. Wilkinson, *IUPAC. Compendium of Chemical Terminology*, 2nd ed. (Blackwell Scientific Publications, Oxford, 1997), XML on-line corrected version: http://goldbook.iupac.org (2006-) created by M. Nic, J. Jirat, B. Kosata; updates compiled by A. Jenkins.

[51] G. P. Moss, P. A. S. Smith, and D. Tavernier, *Glossary of class names of organic compounds and reactivity intermediates based on structure (IUPAC Recommendations 1995)*, Pure and Applied Chemistry **67**, 1307 (2009).

[52] P. Rogl, *Thermoelectrics Handbook* (CRC Press, Boca Raton, 2005), Chap. 32, pp. 1–24.

[53] A. V. Shevelkov and K. Kovnir, in *Zintl Phases*, No. 139 in *Structure and Bonding*, edited by T. F. Fässler (Springer, Berlin, Heidelberg, 2011), pp. 97–142.

[54] B. C. Sales, B. C. Chakoumakos, R. Jin, J. R. Thompson, and D. Mandrus, *Structural, magnetic, thermal, and transport properties of $X_8Ga_{16}Ge_{30}$ (X=Eu, Sr, Ba) single crystals*, Phys. Rev. B **63**, 245113 (2001).

[55] J. D. Bryan, N. P. Blake, H. Metiu, G. D. Stucky, B. B. Iversen, R. D. Poulsen, and A. Bentien, *Nonstoichiometry and chemical purity effects in thermoelectric $Ba_8Ga_{16}Ge_{30}$ clathrate*, Journal of Applied Physics **92**, 7281 (2002).

[56] A. Saramat, G. Svensson, A. E. C. Palmqvist, C. Stiewe, E. Mueller, D. Platzek, S. G. K. Williams, D. M. Rowe, J. D. Bryan, and G. D. Stucky, *Large thermoelectric figure of merit at high temperature in Czochralski-grown clathrate $Ba_8Ga_{16}Ge_{30}$*, J. Appl. Phys. **99**, 023708 (2006).

[57] M. Christensen, N. Lock, J. Overgaard, and B. B. Iversen, *Crystal Structures of Thermoelectric n- and p-type $Ba_8Ga_{16}Ge_{30}$ Studied by Single Crystal, Multitemperature, Neutron Diffraction, Conventional X-ray Diffraction and Resonant Synchrotron X-ray Diffraction*, J. Am. Chem. Soc. **128**, 15657 (2006).

[58] E. S. Toberer, M. Christensen, B. B. Iversen, and G. J. Snyder, *High temperature thermoelectric efficiency in $Ba_8Ga_{16}Ge_{30}$*, Phys. Rev. B **77**, 075203 (2008).

[59] D. Cederkrantz, A. Saramat, G. J. Snyder, and A. E. C. Palmqvist, *Thermal stability and thermoelectric properties of p-type $Ba_8Ga_{16}Ge_{30}$ clathrates*, J. Appl. Phys. **106**, 074509 (2009).

[60] N. P. Blake, S. Latturner, J. D. Bryan, G. D. Stucky, and H. Metiu, *Band structures and thermoelectric properties of the clathrates $Ba_8Ga_{16}Ge_{30}$,*

$Sr_8Ga_{16}Ge_{30}$, $Ba_8Ga_{16}Si_{30}$, and $Ba_8In_{16}Sn_{30}$, J. Chem. Phys. **115**, 8060 (2001).

[61] N. P. Blake, D. Bryan, S. Latturner, L. Mollnitz, G. D. Stucky, and H. Metiu, *Structure and stability of the clathrates $Ba_8Ga_{16}Ge_{30}$, $Sr_8Ga_{16}Ge_{30}$, $Ba_8Ga_{16}Si_{30}$, and $Ba_8In_{16}Sn_{30}$*, J. Chem. Phys. **114**, 10063 (2001).

[62] G. K. H. Madsen, K. Schwarz, P. Blaha, and D. J. Singh, *Electronic structure and transport in type-I and type-VIII clathrates containing strontium, barium, and europium*, Phys. Rev. B **68**, 125212 (2003).

[63] G. K. H. Madsen and G. Santi, *Anharmonic lattice dynamics in type-I clathrates from first-principles calculations*, Phys. Rev. B **72**, 220301 (2005).

[64] M. Christensen, S. Johnsen, and B. B. Iversen, *Thermoelectric clathrates of type I*, Dalton Trans. **39**, 978 (2010).

[65] M. Ångqvist and P. Erhart, *Understanding Chemical Ordering in Intermetallic Clathrates from Atomic Scale Simulations*, Chemistry of Materials **29**, 7554 (2017).

[66] E. S. Toberer, A. Zevalkink, and G. J. Snyder, *Phonon engineering through crystal chemistry*, Journal of Materials Chemistry **21**, 15843 (2011).

[67] J. L. Cohn, G. S. Nolas, V. Fessatidis, T. H. Metcalf, and G. A. Slack, *Glasslike Heat Conduction in High-Mobility Crystalline Semiconductors*, Phys. Rev. Lett. **82**, 779 (1999).

[68] M. Christensen, A. B. Abrahamsen, N. B. Christensen, F. Juranyi, N. H. Andersen, K. Lefmann, J. Andreasson, C. R. H. Bahl, and B. B. Iversen, *Avoided crossing of rattler modes in thermoelectric materials*, Nature Mater. **7**, 811 (2008).

[69] J. Dong, O. F. Sankey, and C. W. Myles, *Theoretical Study of the Lattice Thermal Conductivity in Ge Framework Semiconductors*, Phys. Rev. Lett. **86**, 2361 (2001).

[70] M. Asen-Palmer, K. Bartkowski, E. Gmelin, M. Cardona, A. Zhernov, A. Inyushkin, A. Taldenkov, and V. Ozhogin, *Thermal conductivity of germanium crystals with different isotopic compositions*, Physical Review B - Condensed Matter and Materials Physics **56**, 9431 (1997).

[71] G. S. Nolas, J. L. Cohn, G. A. Slack, and S. B. Schujman, *Semiconducting Ge clathrates: Promising candidates for thermoelectric applications*, Applied Physics Letters **73**, 178 (1998).

[72] D. Frenkel and B. Smit, *Understanding Molecular Simulation* (Academic Press, London, 2001).

[73] L. Verlet, *Computer "Experiments" on Classical Fluids. I. Thermodynamical Properties of Lennard-Jones Molecules*, Physical Review **159**, 98 (1967).

[74] D. G. Cahill, P. V. Braun, G. Chen, D. R. Clarke, S. Fan, K. E. Goodson, P. Keblinski, W. P. King, G. D. Mahan, A. Majumdar, H. J. Maris, S. R. Phillpot, E. Pop, and L. Shi, *Nanoscale thermal transport. II. 2003–2012*, Applied Physics Reviews **1**, 011305 (2014).

[75] D. G. Cahill, W. K. Ford, K. E. Goodson, G. D. Mahan, A. Majumdar, H. J. Maris, R. Merlin, and S. R. Phillpot, *Nanoscale thermal transport*, jap **93**, 793 (2003).

[76] M. S. Green, *Markoff Random Processes and the Statistical Mechanics of Time-Dependent Phenomena. II. Irreversible Processes in Fluids*, The Journal of Chemical Physics **22**, 398 (1954).

[77] R. Kubo, M. Yokota, and S. Nakajima, *Statistical-Mechanical Theory of Irreversible Processes. II. Response to Thermal Disturbance*, Journal of the Physical Society of Japan **12**, 1203 (1957).

[78] M. Toda, R. Kubo, and N. Hashitsume, *Statistical physics. 2, Nonequilibrium statistical mechanics*, No. 31 in *Springer series in solid-state sciences*, 2. ed ed. (Springer, Berlin ; New York, 1991).

[79] P. K. Schelling, S. R. Phillpot, and P. Keblinski, *Comparison of atomic-level simulation methods for computing thermal conductivity*, Physical Review B **65**, 144306 (2002).

[80] S. Merabia and K. Termentzidis, *Thermal conductance at the interface between crystals using equilibrium and nonequilibrium molecular dynamics*, Phys. Rev. B **86**, 094303 (2012).

[81] E. Schrödinger, *An Undulatory Theory of the Mechanics of Atoms and Molecules*, Physical Review **28**, 1049 (1926).

[82] R. Shankar, *Principles of quantum mechanics*, 2. ed ed. (Plenum, New York, 1994).

[83] H. Kroemer, *Quantum Mechanics For Engineering: Materials Science and Applied Physics* (Pearson, Englewood Cliffs, N.J, 1994).

[84] M. Born, *Quantenmechanik der Stoßvorgänge*, Zeitschrift für Physik **38**, 803 (1926).

[85] R. M. Martin, *Electronic Structure* (Cambridge University Press, Cambridge, 2004).

[86] R. P. Feynman, *Forces in Molecules*, Physical Review **56**, 340 (1939).

[87] R. G. Parr and W. Yang, *Density-Functional Theory of Atoms and Molecules* (Oxford University Press, New York, 1989).

[88] P. Hohenberg and W. Kohn, *Inhomogeneous Electron Gas*, Phys. Rev. **136**, B864 (1964).

[89] P. J. Kohanoff, *Electronic Structure Calculations for Solids and Molecules: Theory and Computational Methods*, 1 edition ed. (Cambridge University Press, Cambridge, UK ; New York, 2006).

[90] W. Kohn and L. J. Sham, *Self-Consistent Equations Including Exchange and Correlation Effects*, Phys. Rev. **140**, A1133 (1965).

[91] J. P. Perdew, K. Burke, and M. Ernzerhof, *Generalized Gradient Approximation Made Simple*, Phys. Rev. Lett. **77**, 3865 (1996), erratum, *ibid.* **78**, 1396(E) (1997).

[92] D. C. Langreth, B. I. Lundqvist, S. D. Chakarova-Käck, V. R. Cooper, M. Dion, P. Hyldgaard, A. Kelkkanen, J. Kleis, L. Kong, S. Li, P. G. Moses, E. Murray, A. Puzder, H. Rydberg, E. Schröder, and T. Thonhauser, *A density functional for sparse matter*, J. Phys. Condens. Matter **21**, 084203 (2009).

[93] H. Rydberg, M. Dion, N. Jacobson, E. Schröder, P. Hyldgaard, S. I. Simak, D. C. Langreth, and B. I. Lundqvist, *Van der Waals Density Functional for Layered Structures*, Phys. Rev. Lett. **91**, 126402 (2003).

[94] M. Dion, H. Rydberg, E. Schröder, D. C. Langreth, and B. I. Lundqvist, *Van der Waals Density Functional for General Geometries*, Phys. Rev. Lett. **92**, 246401 (2004).

[95] K. Berland, C. Arter, V. R. Cooper, K. Lee, B. I. Lundqvist, E. Schröder, T. Thonhauser, and P. Hyldgaard, *van der Waals density functionals built upon the electron-gas tradition: Facing the challenge of competing interactions*, J. Chem. Phys. **140**, 18A539 (2014).

[96] K. Berland and P. Hyldgaard, *Exchange functional that tests the robustness of the plasmon description of the van der Waals density functional*, Phys. Rev. B **89**, 035412 (2014).

[97] F. Bloch, *Über die Quantenmechanik der Elektronen in Kristallgittern*, Zeitschrift für Physik **52**, 555 (1929).

[98] B. H. Bransden and C. J. Joachain, *Physics of atoms and molecules*, 2. ed ed. (Prentice Hall, Upper Saddle River, N.J, 2003).

[99] D. Vanderbilt, *Soft self-consistent pseudopotentials in a generalized eigenvalue formalism*, Phys. Rev. B **41**, 7892 (1990).

[100] P. E. Blöchl, *Projector augmented-wave method*, Phys. Rev. B **50**, 17953 (1994).

[101] Y. Gong, J. Lin, X. Wang, G. Shi, S. Lei, Z. Lin, X. Zou, G. Ye, R. Vajtai, B. I. Yakobson, H. Terrones, M. Terrones, B. K. Tay, J. Lou, S. T. Pantelides, Z. Liu, W. Zhou, and P. M. Ajayan, *Vertical and in-plane heterostructures from WS_2/MoS_2 monolayers*, Nature Mater. **13**, 1135 (2014).

[102] B. B. Iversen, A. E. Palmqvist, D. E. Cox, G. S. Nolas, G. D. Stucky, N. P. Blake, and H. Metiu, *Why are Clathrates Good Candidates for Thermoelectric Materials?*, J. Solid State Chem. **149**, 455 (2000).

[103] A. Katre, J. Carrete, B. Dongre, G. K. Madsen, and N. Mingo, *Exceptionally Strong Phonon Scattering by B Substitution in Cubic SiC*, Physical Review Letters **119**, 1 (2017).

[104] T. Wang, J. Carrete, A. Van Roekeghem, N. Mingo, and G. K. Madsen, *Ab initio phonon scattering by dislocations*, Physical Review B **95**, 1 (2017).

[105] W. Li and N. Mingo, *Thermal conductivity of fully filled skutterudites: Role of the filler*, Physical Review B - Condensed Matter and Materials Physics **89**, 1 (2014).

[106] F. Irgens, *Continuum mechanics* (Springer Science & Business Media, Berlin Heidelberg, 2008).

[107] J. N. Reddy, *An introduction to continuum mechanics*, 2. ed. ed. (Cambridge University Press, New York, 2013).

[108] L. E. Reichl, *A Modern Course in Statistical Physics*, 2 edition ed. (Wiley-VCH, New York, 1998).

[109] R. K. Pathria, *Statistical Mechanics*, 2nd ed. (Butterworth-Heinemann, Oxford, 1996).

Paper I

Microscopic Origin of Thermal Conductivity Reduction in Disordered van der Waals Solids
Paul Erhart, Per Hyldgaard and Daniel O. Lindroth

Microscopic Origin of Thermal Conductivity Reduction in Disordered van der Waals Solids

Paul Erhart,*,[†] Per Hyldgaard,[‡] and Daniel O. Lindroth[†]

[†]Chalmers University of Technology, Department of Applied Physics, SE-412 96 Gothenburg, Sweden
[‡]Chalmers University of Technology, Department of Microtechnology and Nanoscience, SE-412 96 Gothenburg, Sweden

ABSTRACT: Films of layered substances like WSe_2 can exhibit a reduction in the out-of-plane thermal conductivity of more than 1 order of magnitude compared to that of the bulk, effectively beating the glass limit (*Science* **2007**, *315*, 351). Here, we investigate the microscopic contributions that govern this behavior within the framework of Boltzmann transport theory informed by first-principles calculations. To quantitatively reproduce both the magnitude and the temperature dependence of the experimental data, one must account for both phonon confinement effects (softening and localization) and interlayer scattering. Both stacking order and layer spacing are shown to have a pronounced effect on the thermal conductivity that could be exploited to tune the balance between electrical and thermal conductivity.
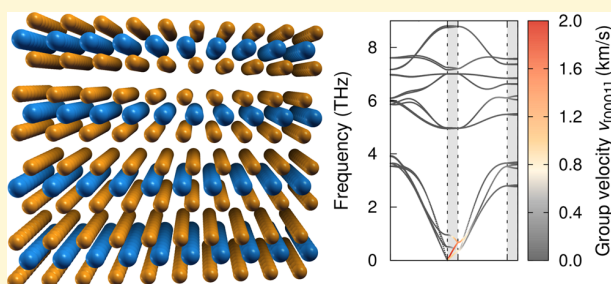
1. INTRODUCTION

The ability to manipulate the thermal conductivity is crucial in various contexts, including refrigeration, heat insulation, thermoelectric energy recovery, and rapid heat dissipation. Nanostructuring is a very powerful tool for tuning thermal conductivity, in particular for ultralow thermal conductors[1−4] and thermoelectrics.[5−7]

Here we focus on one of these systems, namely tungsten diselenide (WSe_2). It is a prototypical layered compound and a bulk crystalline example for a class of materials for which the phrase van der Waals (vdW) solid has been coined.[8] These materials are comprised of two-dimensional sheets with strong mixed covalent−ionic bonding character, which are coupled to each other by comparably weak vdW interactions[9,10] and can be engineered to form multilayers as well as heterostructures.[11−13]

As a result of the significant difference between intra- and intersheet bonding characteristics, vdW materials exhibit strong anisotropy in many properties, including thermal conductivity. The out-of-plane conductivity $\kappa_\perp$ of, e.g., WSe_2 is already low for perfectly crystalline material at a level of 1.5 W/mK at room temperature.[1] Chiritescu et al. demonstrated that in films deposited at room temperature $\kappa_\perp$ can be further reduced by a factor of up to 30 compared to that of single-crystalline material, yielding values considerably below the theoretical limit.[1,14,15] This dramatic reduction was attributed to the localization of lattice vibrations due to a randomization of the stacking order of WSe_2 sheets. In the work presented here, we explore this finding within the framework of Boltzmann transport theory and first-principles calculations with the objective of discriminating the essential microscopic factors and quantifying their respective contribution. Eventually, the goal is to identify pathways for generalizing the approach to other materials.

The paper is organized as follows. The next section describes our methodological approach and summarizes computational details. In section 3, the effect of structure on the out-of-plane thermal conductivity is investigated, specifically considering stacking sequence and homogeneous out-of-plane expansion. The changes in the phonon band structure that underlie the structural sensitivity of the conductivity are analyzed in section 4. On the basis of the data presented in section 3, a model is formulated in section 5 that captures the experimentally observed increase in average and variance of the interlayer spacing as well as interlayer scattering. The final model is found to match the experimental data both in magnitude and in temperature dependence and provides the basis for a discussion of the importance of different microscopic mechanisms and their implications in section 6.

2. METHODOLOGY

2.1. Calculation of Thermal Conductivity. We seek to resolve the microscopic factors that give rise to the drastic reduction in the out-of-plane thermal conductivity $\kappa_\perp$ observed experimentally. As WSe_2 has a rather larger band gap and the temperature range of interest is small, electronic contributions are negligible, so we focus our attention entirely on the phononic (lattice) contribution. To obtain the latter, we analyze $\kappa_\perp$ within the framework of semiclassical Boltzmann transport theory, which in the relaxation time approximation (RTA) yields the following expression for the thermal conductivity tensor[16]

$$\kappa_{\alpha\beta} = \frac{1}{\Omega N_q} \sum_{i\mathbf{q}} v_{\alpha,i}(\mathbf{q}) v_{\beta,i}(\mathbf{q}) \tau_i(\mathbf{q}, T) c_i(\mathbf{q}, T)$$

(1)

where Ω is the unit cell volume, N_q is the number of $\mathbf{q}$ points in the summation, and $v_{\alpha,i}(\mathbf{q}) = \partial \omega_i / \partial q_\alpha$ is the group velocity of mode i along Cartesian direction α at point $\mathbf{q}$ of the Brillouin zone with ω_i being the mode frequency. Both phonon frequencies and group velocities can be derived from the second-order force constant matrix.[17] The mode specific heat capacity $c_i(\mathbf{q}, T)$ is given by

$$c_i(\mathbf{q}, T) = k_B \frac{x^2 \exp x}{(1 - \exp x)^2} \text{ with } x = \frac{\hbar \omega_i(\mathbf{q})}{k_B T}$$

(2)

The lifetime $\tau_i(\mathbf{q},T)$ is limited by a number of scattering processes, including phonon−phonon, isotope mass variation, and disorder. According to the simplest approximation, known as Matthiessen's rule, their respective contributions are inversely additive, i.e., $\tau_{tot}^{-1} = \sum_k \tau_k^{-1}$.

Calculation of phonon−phonon scattering rates requires knowledge of not only the second-order but also the third-order force constants.[18,19] This contribution has been previously addressed using first-principles calculations for (ideal) bulk WSe$_2$.[20] The phonon−phonon scattering channel dominates only for relatively large single-crystalline samples with a comparably low defect density. It is therefore of minor importance in this work, which is concerned with the effect of structural defects and disorder on thermal conductivity. For the sake of simplicity, we therefore assume a mode and $\mathbf{q}$-independent phonon−phonon scattering limited lifetime, which follows a simple temperature dependence ($\tau_{ph-ph} = \alpha T^{-b}$), motivated by analytic theory.[21] Specifically, we choose $b = 0.8$ and $\alpha = 27$ ps K^b, which reproduces the experimentally measured out-of-plane conductivity (see section 3 and Figure 1).[22]

In sections 3 and 4, we will focus on structural effects on group velocities and frequencies. We will return to the discussion of scattering channels, specifically in connection with structural defects, in section 5.
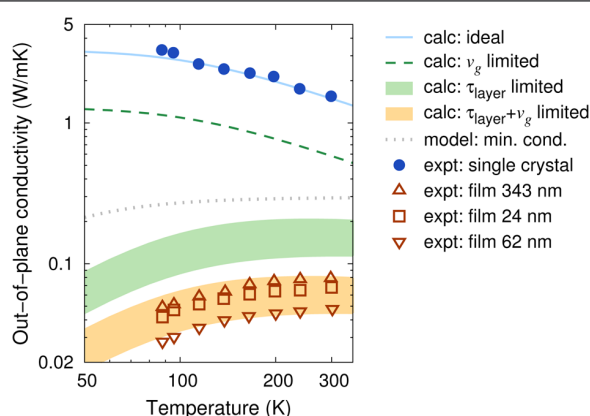

Figure 1. Out-of-plane lattice thermal conductivity $\kappa_\perp$ for various samples of WSe$_2$ from experiment (ref 1) and calculation. Blue circles and lines show the temperature dependence of $\kappa_\perp$ for ideal bulk material from experiment and calculation, respectively. Taking into account the effect of out-of-plane expansion and stacking disorder on the group velocities yields the $\kappa_\perp$ data shown by the dashed green curve (v_g limited). If only the effect of interlayer scattering on the lifetime is included, one obtains the green data range (τ_{layer} limited), where the upper and lower limits correspond to $d = c = 13$ Å and $d = c/2 = 6.5$ Å, respectively. To reach the experimental range of $\kappa_\perp$ obtained for disordered thin films (empty red symbols), one must account for both group velocity reduction and interlayer scattering (yellow range, $\tau_{layer} + v_g$ limited). The minimal thermal conductivity that is predicted by the model introduced in ref 14 is shown by the dotted gray line.

2.2. Computational Details. Phonon dispersion relations were analyzed using the PHONOPY package[23] based on force constants obtained from density functional theory (DFT) calculations. The latter were conducted using the projector augmented wave method[24] as implemented in the Vienna ab initio simulation package (VASP).[25] We employed a plane wave energy cutoff of 290 eV and sampled the Brillouin zone using Γ-centered $12 \times 12 \times 3$ k-point grids with respect to the primitive cell. The bulk of the force constant calculations were conducted using supercells comprising $2 \times 2 \times 2$ primitive unit cells. Convergence tests with systems composed of up to $6 \times 6 \times 3$ unit cells showed no significant changes in phonon dispersion.

To assess the sensitivity of our results to the treatment of exchange correlation effects, we used both the local density approximation (LDA) and the van der Waals density functional (vdW-DF) method that captures nonlocal correlations.[9,26−28] Our nonempirical vdW-DF studies are based on the new consistent exchange version (vdW-DF-cx)[29] as implemented in VASP.[30,31]

As shown in Table 1, both LDA and vdW-DF-cx yield good agreement with experimental data for bulk WSe$_2$ with respect to

Table 1. Properties of Tungsten Diselenide from Experiment (refs 32, 37, and 38) and Calculation[a]

method	T	a	c	z_{Se}	c_{33}	c_{44}
LDA	0	3.249	12.819	0.620	52.5	21.2
	300	3.250	12.832	0.620		
vdW-DF-cx	0	3.280	13.014	0.620	57.3	21.1
	300	3.282	13.061	0.621		
experiment	300	3.282	12.96	0.6211	52.1	18.6

^{a}The 0 K data do not include zero-point vibrations. The in-plane and out-of-plane lattice constants a and c, respectively, are given in angstroms. z_{Se} denotes the internal coordinate associated with Se. The elastic constants c_{33} and c_{44} are given in gigapascals, and the temperature T is given in kelvin.

crystallographic parameters and elastic constants. Here, finite temperature effects were taken into account on the level of the quasi-harmonic approximation. Note that the good agreement obtained with the LDA functional for bulk WSe$_2$ is fortuitous[9] as it is the result of error cancellation.[34] This problem becomes apparent under uniaxial expansion perpendicular to the layers as the LDA is incapable of reproducing the correct asymptotic behavior and thus cannot be expected to properly describe the response of the materials under these conditions. Unless noted otherwise, below we report results obtained using the vdW-DF-cx functional.

3. OUT-OF-PLANE CONDUCTIVITY AND STRUCTURE

3.1. Defect-Free Material. Figure 1 shows the calculated out-of-plane conductivity as a function of temperature for different conditions in comparison with experiment. It represents the key results of this work, and in the following sections, we will successively discuss the different data.

The perfectly crystalline (ideal) system represents the starting point for the study of structural effects. As indicated above, in this study we do not explicitly compute phonon−phonon scattering rates. Instead, we use a simple lifetime model ($\tau_{ph-ph} = \alpha T^{-b}$) that is adjusted to reproduce the experimental single-crystal data. The more important parameter is the prefactor α, while the b parameter has only a minor effect; values approximately in the range of 0.8−1.0 yield almost identical results.

3.2. Stacking Disorder. To determine the impact of stacking disorder and layer separation on the out-of-plane conductivity $\kappa_\perp$, a number of different stacking faults were considered, which are illustrated in Figure 2a. They were obtained by altering the number and specific sequence of WSe$_2$
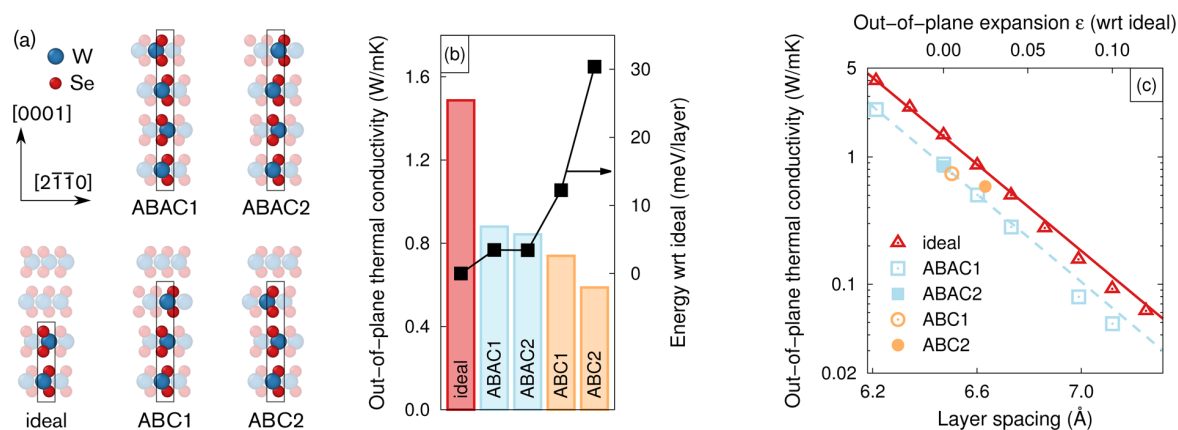
Figure 2. (a) Overview of the different types of stacking disorder considered in this study. The black boxes represent the respective unit cells. Out-of-plane thermal conductivity at 300 K (b) for the stacking disorder models shown in panels a and c as a function of layer spacing. The black solid curve in panel b shows the energy of the respective stacking sequence relative to the ideal structure. The atomic simulation environment[35] was used for structure creation and manipulation and OVITO was used for structural analysis and visualization.[36]

layers. In the equilibrium structure, the W atoms occupy Wyckoff sites $2c$ and thus form a hexagonal closed packed[37] lattice with successive layers along [0001] labeled A and B, respectively. The Se atoms occupy Wyckoff sites $4f$ and form a sublattice, which follows the same stacking sequence as the W sublattice except that each layer comprises two Se atoms that have the same in-plane coordinate but are split along [0001]. In stacking sequence ABAC1, the W atoms follow an ABAC sequence while the Se atoms remain in ABAB sequence. Conversely, in stacking sequence ABAC2, the Se atoms follow an ABAC pattern whereas the W atoms maintain the ABAB order. The ABC1 stacking fault configuration comprises Se and W atoms in ABC and ABB sequences, respectively, while in the ABC2 configuration, the Se and W patterns are swapped. Each configuration was fully relaxed prior to the computation of the lattice thermal conductivity. For ABAC-type stacking, the calculations yield a very small energy increase relative to the ground state of only 3 meV/layer; slightly larger values of 12 and 30 meV/layer are obtained for ABC1 and ABC2 stacking sequences, respectively.

Figure 2b shows the out-of-plane thermal conductivity that we have thus obtained for different stacking sequences. This reveals a reduction in $\kappa_\perp$ by 30−50%, which is still much less than the factor of 30 observed experimentally.[1] The effect of simple disorder in the stacking disorder is of similar magnitude for all configurations and thus does not exhibit a strong dependence on the number of affected layers. This is expected because the interaction between neighboring layers is already weak; therefore, long-range coupling should be even weaker. While our exploration of possible forms of stacking disorder is (computationally) limited, it therefore appears unlikely that a reduction by >1 order of magnitude can be solely attributed to stacking disorder.

3.3. Interlayer Separation. To proceed with our analysis, it is relevant to revisit the information that is available from experiments concerning the structure and chemistry of turbostratically deposited thin films with ultralow thermal conductivity. The layer spacing obtained from X-ray diffraction is on average approximately 1.9−2.6% larger than the value for bulk WSe$_2$ (compare Table 1 and refs 1 and 2). Cross-sectional transmission electron micrographs[38] furthermore suggest a rather pronounced variation in layer separation.

As the first step in the analysis of these effects, Figure 2c shows the variation of the out-of-plane conductivity $\kappa_\perp$ with layer separation, which reveals an exponential dependence with a reduction by a factor of 10 at 8% expansion. In these calculations, the in-plane lattice constant was kept fixed at its zero-stress equilibrium value. The figure also contains equivalent data obtained for the ABAC1 stacking fault model as well as data for the other stacking sequences corresponding to their respective equilibrium layer spacing. Ideal stacking and ABAC1 stacking exhibit a very similar dependence on layer spacing, suggesting that the stacking disorder and out-of-plane lattice expansion are not strongly coupled and can be considered additively. Furthermore, it is apparent that the variation among the nonideal stacking sequences can at least partially be rationalized in terms of variations in the layer spacing that result from full ionic relaxation.

4. ANALYSIS OF PHONON DISPERSION RELATIONS

From our results, it is apparent that even a moderate interlayer expansion produces a reduction in the thermal conductivity considerably larger than that with stacking disorder alone. As will be elaborated below, the exponential dependence of $\kappa_\perp$ on the layer spacing implies that one does not require a strong increase in the average layer spacing to achieve a dramatic reduction in $\kappa_\perp$ but merely local variations in layer spacings. We will return to this aspect in section 5. First, we will address the microscopic mechanisms behind the reduction of $\kappa_\perp$ and compare the calculated vibrational properties with experiment, where possible.

4.1. Accordion Effect. To resolve the microscopic origin of the variation of $\kappa_\perp$ with layer separation, we analyzed the relative contributions of different phonon modes and **q** vectors to the summation in eq 1. Figure 3a shows the phonon dispersion for the fully relaxed structure. As we assume the relaxation time to be mode- and **q**-independent, there are two terms that determine the contribution of any given mode to thermal conductivity. The heat capacity $c_i(T,\mathbf{q})$ depends only on the frequency. As shown in Figure 3b, near room temperature this contribution is already close to saturation, i.e., one k_B per mode, for all available frequencies.

The most important term is therefore the group velocity $v_{\alpha,i}(\mathbf{q})$ along [0001], which is indicated by the color scale in
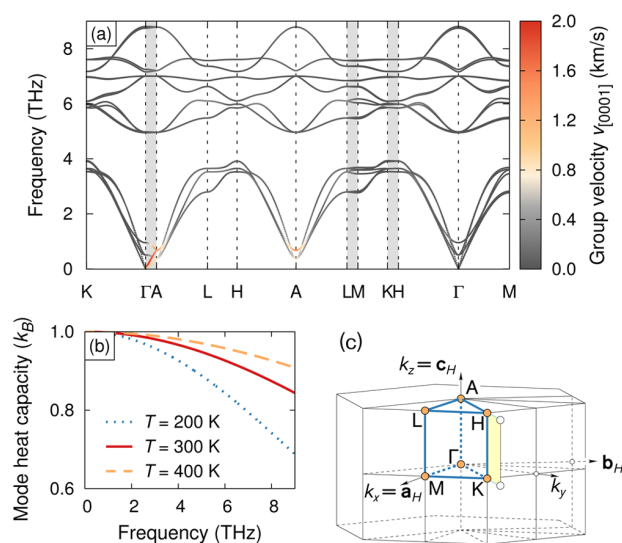
Figure 3. (a) Phonon dispersion relation for the fully relaxed equilibrium structure. The color scale indicates the group velocity along the z-direction for the respective mode. (b) Frequency dependence of the mode specific heat capacity. (c) Brillouin zone for space group $P6_3/mmc$ (International Tables of Crystallography No. 194, D_{6h}^4, ref 39).

Figure 3a. It is obvious that only modes with **q** vector components along [0001] have non-zero $v_{\alpha,j}(\mathbf{q})$ values. The color coding in Figure 3a suggests that the dominant contributions to $\kappa_\perp$ stem from modes in the immediate vicinity of the $\Gamma-A$ direction. A close-up of this branch is shown in Figure 4a at the equilibrium layer spacing as well as for out-of-plane expansions of 4% (Figure 4b) and 8% (Figure 4c).

From Figure 4a, it is apparent that the main contribution to $\kappa_\perp$ at the equilibrium layer separation stems from the longitudinal acoustic (LA) branch and, to a lesser extent, the lowest longitudinal optical (LO) mode. The atomic displacement patterns associated with these modes are shown in Figure 4d. With increasing layer separation, the LA branch softens while the LO branch localizes, leading to a considerable decrease in group velocity. This is further illustrated in Figure 4e, which shows the variation of the lowest-energy zone center and boundary modes with layer spacing. The A_2 breathing mode is a measure of the softness of the LA branch, whereas

the difference between the B_{2g}^2 and A_2 breathing modes is associated with the localization of the lowest LO mode.

The stability limit of the material with respect to an expansion of the layer spacing is determined by the breathing modes, as they are the first modes to become unstable at ~11% expansion according to vdW-DF-cx (7% from LDA) (see Figure 4e). This demonstrates that the material can tolerate a rather substantial level of expansion.

4.2. Comparison with Experiment. The E_{2g}^2 shear mode is Raman active, and its frequency has been experimentally measured as 0.72 THz (24 cm^{-1}).[33] We obtain values of 0.82 THz (27 cm^{-1}) and 0.75 THz (25 cm^{-1}) from vdW-DF-cx and LDA calculations, respectively, where the latter value agrees with previous calculations.[33,40] Our calculations also agree well with experimental data for higher-frequency Raman modes[41] as shown in Table 2.

Table 2. Raman Frequencies (cm^{-1}) of Bulk WSe$_2$ from Experiment and Calculation

	A_{1g}	E_{2g}^1	E_{1g}	E_{2g}^2
experiment (ref 33)				24
experiment (ref 41)	253	250	178	25
LDA	255	249	177	25
vdW-DF-cx	250	243	173	27

The longitudinal sound velocity along [0001] is determined by the group velocity in the long-wave limit, which gives approximately $c_{l,[0001]} = 2.0$ km/s at the equilibrium layer spacing. This value is related to the elastic constant c_{33} via $c_{l,[0001]} = \sqrt{c_{33}/\rho}$, where ρ is the mass density. The softening of the LA branch should therefore also be evident in the c_{33} elastic constant. In fact, while an experimental c_{33} value of 52 GPa has been obtained for bulk WSe$_2$,[33] a value of only 25 GPa was reported for WSe$_2$ with ultralow thermal conductivity.[142] The observed (average) softening of the materials is thus approximately consistent with our calculations, which predict a reduction by one-half for an expansion of approximately 3−4% for both vdW-DF-cx and LDA.

5. MICROSCOPIC MODEL FOR $\kappa_\perp$ REDUCTION

5.1. Variations in Layer Spacing. We are now in the position to provide a microscopic rationalization of the ultralow
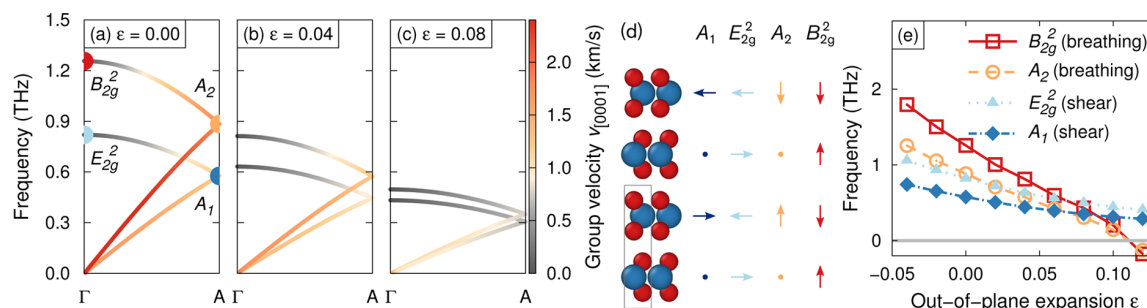
Figure 4. (a−c) Phonon dispersion along $\Gamma-A$ for three different values of the out-of-plane expansion ε. The color scale indicates the group velocity along the z-direction. The colored circles in panel a indicate the zone center and boundary modes, whose atomic displacement patterns (representing phonon polarization vectors) are shown in panel d. These modes correspond to rigid shifts of layers with respect to each other as illustrated by the arrows. Panel e shows the dependence of the frequency of these modes on the out-of-plane expansion. The stability limit of the material with respect to out-of-plane expansion is determined by the breathing modes, whose frequencies become imaginary at approximately 11% when using vdW-DF-cx (7% for LDA).

thermal conductivity in WSe$_2$ films on the basis of our data. Recall that structural investigations of these films indicate that lower thermal conductivity is correlated with a decreasing coherence between crystallites in the films, a greater degree of misorientation,[2,38] an increase in the average layer spacing of 1.9–2.6%, and a rather substantial variation in layer spacing along the out-of-plane direction.[43]

We first formulate a simple model to describe the average out-of-plane thermal conductivity $\kappa_\perp$ that results from a distribution in layer spacings. To approximate the experimental structure, let us consider a stack of layers as schematically depicted in Figure 5a with a distribution of layer spacings $l_1 =$

Figure 5. (a) One-dimensional model for a stack of WSe$_2$ layers with a distribution of layer spacings. The horizontal dashed lines indicate th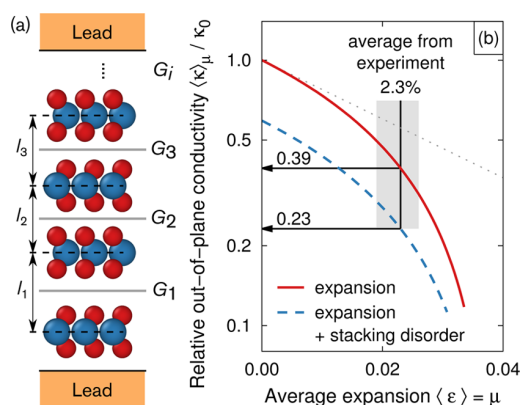e "interfaces" between adjacent layers. (b) Effective out-of-plane conductivity across a stack with an exponential distribution of layer spacings as a function of the average out-of-plane expansion $\langle \varepsilon \rangle = \mu$. For reference, the exponential dependence of $\kappa_\perp$ obtained upon a homogeneous out-of-plane expansion (see Figure 2c) is represented by the dotted gray line. The gray bar represents the range of experimentally observed average expansions (1.9–2.6%).

$l_0(1 + \varepsilon_i)$, where ε_i is the out-of-plane expansion relative to the ideal single crystal layer spacing l_0. The local thermal conductivity $\kappa(\varepsilon_i)$ reflects the expansion, and $G_i = \kappa(\varepsilon_i)[l_0(1 + \varepsilon_i)]^{-1}$ characterizes the thermal conductance across the "interface" between the ith pair of layers.[44] In perfect single-crystalline WSe$_2$, the conductivity and intersheet conductance are $\kappa_0 = \kappa(0)$ and $G(0) = \kappa_0/l_0$, respectively.

As there is very limited information about the distribution of intersheet spacings except for the average expansion[1] $\langle \varepsilon \rangle$, we simply assume an exponential distribution[45] $f(\varepsilon > 0) = \mu^{-1} \exp(-\varepsilon/\mu)$, where the mean of the distribution, μ, represents the average out-of-plane expansion $\langle \varepsilon \rangle = \mu$. Figure 2c indicates an approximately exponential dependence of the out-of-plane conductivity on ε for the case of homogeneous expansion. We therefore set $\kappa(\varepsilon)/\kappa_0 = \exp(-a\varepsilon)$, where an a of 25.5 gives a reasonable fit to our first-principles data.

For a stack of N sheets, the total thermal impedance is $G_N^{-1} = \sum_i G_i^{-1}$, where $Nl_0(1 + \mu)G_N$ must approach the average effective thermal conductivity $\langle \kappa \rangle_\mu$ in the large N limit. Replacing the N-stack thermal impedance by the distribution average[46]

$$\langle G^{-1} \rangle = \int d\varepsilon \, G^{-1}(\varepsilon) f(\varepsilon) / \int d\varepsilon f(\varepsilon) \qquad (3)$$

we obtain $\langle \kappa \rangle / \kappa_0 = [\langle G^{-1} \rangle G(0)]^{-1}(1 + \mu)$. Discarding the last small factor $(1 + \mu)$ but keeping the expansion effects in the

ensemble averaging then yields the relative out-of-plane thermal conductivity as a function of average expansion

$$\frac{\langle \kappa \rangle_\mu}{\kappa_0} = \frac{1 - a\mu}{1 + \mu/(1 - a\mu)} \qquad (4)$$

which is shown in Figure 5b.

For an average out-of-plane expansion of 2.3%, representing the experimentally observed range of 1.9–2.6%, which was discussed above, the model predicts a reduction in $\kappa_\perp$ by approximately 60% compared to the ideal structure. Stacking disorder causes a further reduction as indicated by the dashed blue curve in Figure 5b. It is because of the variation of layer spacings that the reduction predicted by the model is noticeably stronger than for the case of a pure homogeneous expansion, which is shown for comparison by the dotted gray line (also compare Figure 2c).

5.2. Lifetime Limitation by Interface Scattering. Until now, the discussion has focused on structural effects on group velocities and frequencies. According to the analysis in the previous section, an increase in the average layer spacing along with local variations can explain a reduction in $\kappa_\perp$ of ~60% (also see Figure 1), with stacking fault disorder having a slightly smaller effect. The temperature dependence of the "v_g limited" out-of-plane conductivity is indicated by the dashed green curve in Figure 1. The thus obtained reduction is still noticeably greater than both the minimal conductivity model[14] and the values obtained for disordered WSe$_2$ films. This suggests that yet another mechanism is at work.

In fact, the perturbation of the periodicity perpendicular to the layers due to stacking faults and variations in layer spacing should not only affect the group velocities v_g but also limit the mean free path of phonon modes with out-of-plane components. This is equivalent to the effect of boundary scattering[17,47,48] and can be formally expressed in the form of another lifetime[49]

$$\tau_{\text{layer}} = \frac{d}{v_{g,\perp}} \frac{1 + p}{1 - p} \qquad (5)$$

where $v_{g,\perp}$ is the projection of the group velocity on the out-of-plane direction, d represents the upper limit on the phonon mean free path,[50] and p is a specularity parameter, which ranges from 0 for a completely rough edge to 1 for a perfectly smooth edge. In the case of a sample with perturbed periodicity and associated disorder, d should be comparable to the layer spacing, i.e., approximately between 6.5 and 13 Å. In fact, combining phonon–phonon scattering ($\tau_{\text{ph–ph}}$) and layer scattering (τ_{layer} with $p = 0$) with the group velocity limited thermal conductivity yields excellent agreement with the experimental data as shown by the yellow shaded region in Figure 1 ($\tau_{\text{layer}} + v_g$ limited), where the lower (upper) limit corresponds to $d = 6.5$ Å (13 Å). Note that this calculation not only reproduces the experimental range for $\kappa_\perp$ at room temperature but, as a result of the temperature independence of τ_{layer}, also captures the experimental temperature dependence of $\kappa_\perp$, which is primarily derived from the heat capacity (see Figure 4b).

It is important to point out that layer scattering alone cannot account for the experimental observations as demonstrated by the green shaded region (τ_{layer} limited). The latter can actually be considered the "glass limit" for the bulk material, in which the phonon mean free path is bound by the interatomic distance along the out-of-plane direction.

6. DISCUSSION

The results and analysis presented in the previous sections allow us to provide a comprehensive description of the experimentally observed reduction of $\kappa_\perp$. The experimental characterization of WSe_2 films with ultralow thermal conductivity has revealed a pronounced degree of stacking disorder as well as an increase in not only the average layer spacing but also its variance. On a microscopic level, the lattice thermal conductivity is determined by the group velocities v_g and lifetimes τ of the phonons in the material (see eq 1). A reduction in $\kappa_\perp$ can thus result from mode localization and softening (reducing v_g) as well as scattering (limiting τ).

The effects of stacking disorder and layer expansion on v_g were separately quantified in section 3. Stacking disorder causes a reduction in $\kappa_\perp$ due to localization and softening by 40−60%. While the homogeneous expansion of the out-of-plane separation gives rise to an exponential decrease in $\kappa_\perp$, it is not a realistic model for the structure of the material. The experimentally observed variation in layer spacing was therefore described in section 5 using a simple analytic model for the distribution of layer spacings. Overall, the analysis suggests that pure phonon localization and softening ("phonon confinement"[51,52]) can give rise to a reduction in $\kappa_\perp$ of a factor of 2−4 (see Figure 1).

The disorder in the WSe_2 films furthermore imposes a limit on the phonon mean free path in the out-of-plane direction, corresponding to an interface scattering limit on lifetime τ. The minimum layer spacing in the out-of-plane direction (i.e., half the out-of-plane lattice constant, $d \approx c/2$, in eq 5) in combination with a completely rough interface/boundary ($p = 0$) provides a lower bound for this scattering channel and effectively corresponds to the "glass limit".

To describe both the magnitude and the temperature dependence of the experimental $\kappa_\perp$, one must account for both the depression of group velocities and lifetimes assuming an effective interface spacing of only one to two lattice spacings (6.5−13.0 Å). Models that rely on phonon softening and localization only are thus insufficient to describe the reduction of $\kappa_\perp$ in its entirety.[53]

The final value for $\kappa_\perp$ is naturally dependent on τ_{layer} as well as the effective reduction of $\kappa_\perp$, as indicated by the $\kappa_\perp$ range shown in Figure 1. This merely reflects the fact that $\kappa_\perp$ is sensitive to small structural variations among different samples as is evident from the experimental data.

It is interesting to note that the calculations presented in section 3 demonstrate that a very significant reduction of 40−60% is possible by simply manipulating the stacking sequence. This effect can in principle be accomplished without introducing significant layer scattering (which is primarily the result of layer disorder). Given the small energy cost of ABAC-type stacking sequences and the recent advances in controlled deposition of vdW materials, this possibility might be in fact realizable. Such an approach would be very interesting with respect to, e.g., thermoelectric properties, for which one seeks to combine a relatively high electrical conductivity with minimal lattice thermal conductivities.[5] Electronic carriers typically have mean free paths longer than those of phonons and therefore should be less sensitive to stacking order. Nanostructuring is of course well-established in thermoelectric materials, primarily in the form of dopant, precipitate, and grain boundary engineering (see, e.g., ref 7). Anisotropic structures offer additional and complementary possibilities as recently demonstrated for tilted multilayer structures.[54]

An even more significant reduction in $\kappa_\perp$ can be achieved by controlling the layer spacing. The latter could in principle be affected by strain, intercalation, or more generally defect engineering. Further studies are in order to obtain a achieve an understanding of these mechanisms.

7. CONCLUSIONS

In summary, in this paper, we have shown that the experimentally observed dramatic reduction of the out-of-plane thermal conductivity in disordered WSe_2 films can be quantitatively explained by a combination of Boltzmann transport theory and first-principles calculations. To explain the experimental result, one must account for the effect of disorder on both group velocities (phonon softening and localization) and lifetimes (scattering channels), as these mechanisms are individually insufficient to explain the experimental result. The results obtained here are of general relevance with respect to layered materials as the mechanisms described here are a result of variations in structure rather than chemistry. Finally, we note that controlling stacking disorder and layer spacing without scattering can be a powerful tool for manipulating phonon transport in a manner at least partly independent of charge carrier transport. The latter ability is of interest in the context of, e.g., thermoelectric materials and heat management.

■ AUTHOR INFORMATION

Corresponding Author
*E-mail: erhart@chalmers.se.
Notes
The authors declare no competing financial interest.

■ ACKNOWLEDGMENTS

■ REFERENCES

(1) Chiritescu, C.; Cahill, D. G.; Nguyen, N.; Johnson, D.; Bodapati, A.; Keblinski, P.; Zschack, P. Ultralow Thermal Conductivity in Disordered, Layered WSe_2 Crystals. *Science* **2007**, *315*, 351−353.

(2) Nguyen, N. T.; Berseth, P. A.; Lin, Q.; Chiritescu, C.; Cahill, D. G.; Mavrokefalos, A.; Shi, L.; Zschack, P.; Anderson, M. D.; Anderson, I. M.; Johnson, D. C. Synthesis and Properties of Turbostratically Disordered, Ultrathin WSe_2 Films. *Chem. Mater.* **2010**, *22*, 2750−2756.

(3) Losego, M. D.; Grady, M. E.; Sottos, N. R.; Cahill, D. G.; Braun, P. V. Effects of chemical bonding on heat transport across interfaces. *Nat. Mater.* **2012**, *11*, 502−506.

(4) Ong, W.-L.; Rupich, S. M.; Talapin, D. V.; McGaughey, A. J. H.; Malen, J. A. Surface chemistry mediates thermal transport in three-dimensional nanocrystal arrays. *Nat. Mater.* **2013**, *12*, 410−415.

(5) Snyder, G. J.; Toberer, E. S. Complex thermoelectric materials. *Nat. Mater.* **2008**, *7*, 105−114.

(6) Heremans, J. P.; Jovovic, V.; Toberer, E. S.; Saramat, A.; Kurosaki, K.; Charoenphakdee, A.; Yamanaka, S.; Snyder, G. J. Enhancement of Thermoelectric Efficiency in PbTe by Distortion of the Electronic Density of States. *Science* **2008**, *321*, 554−557.

(7) Biswas, K.; He, J.; Blum, I. D.; Wu, C.-I.; Hogan, T. P.; Seidman, D. N.; Dravid, V. P.; Kanatzidis, M. G. High-performance bulk thermoelectrics with all-scale hierarchical architectures. *Nature* **2012**, *489*, 414−418.

(8) Gao, G.; Gao, W.; Cannuccia, E.; Taha-Tijerina, J.; Balicas, L.; Mathkar, A.; Narayanan, T. N.; Liu, Z.; Gupta, B. K.; Peng, J.; Yin, Y.; Rubio, A.; Ajayan, P. M. Artificially Stacked Atomic Layers: Toward New van der Waals Solids. *Nano Lett.* **2012**, *12*, 3518−3525.

(9) Rydberg, H.; Dion, M.; Jacobson, N.; Schröder, E.; Hyldgaard, P.; Simak, S. I.; Langreth, D. C.; Lundqvist, B. I. Van der Waals Density Functional for Layered Structures. *Phys. Rev. Lett.* **2003**, *91*, 126402.

(10) Björkman, T.; Gulans, A.; Krasheninnikov, A. V.; Nieminen, R. M. van der Waals Bonding in Layered Compounds from Advanced Density-Functional First-Principles Calculations. *Phys. Rev. Lett.* **2012**, *108*, 235502.

(11) Cocemasov, A. I.; Nika, D. L.; Balandin, A. A. Phonons in twisted bilayer graphene. *Phys. Rev. B: Condens. Matter Mater. Phys.* **2013**, *88*, 035428.

(12) Chuang, S.; Kapadia, R.; Fang, H.; Chia Chang, T.; Yen, W.-C.; Chueh, Y.-L.; Javey, A. Near-ideal electrical properties of InAs/WSe$_2$ van der Waals heterojunction diodes. *Appl. Phys. Lett.* **2013**, *102*, 242101.

(13) Geim, A. K.; Grigorieva, I. V. Van der Waals heterostructures. *Nature* **2013**, *499*, 419−425.

(14) Cahill, D. G.; Watson, S. K.; Pohl, R. O. Lower limit to the thermal conductivity of disordered crystals. *Phys. Rev. B: Condens. Matter Mater. Phys.* **1992**, *46*, 6131−6140.

(15) Chiritescu, C.; Cahill, D. G.; Heideman, C.; Lin, Q.; Mortensen, C.; Nguyen, N. T.; Johnson, D.; Rostek, R.; Böttner, H. Low thermal conductivity in nanoscale layered materials synthesized by the method of modulated elemental reactants. *J. Appl. Phys.* **2008**, *104*, 033533.

(16) Berman, R. *Thermal Conduction in Solids*; Clarendon Press: Oxford, U.K., 1976.

(17) Ziman, J. M. *Electrons and phonons*; Clarendon Press: Oxford, U.K., 1960.

(18) Li, W.; Carrete, J.; Katcho, N. A.; Mingo, N. ShengBTE: A solver of the Boltzmann transport equation for phonons. *Comput. Phys. Commun.* **2014**, *185*, 1747−1758.

(19) Li, W.; Carrete, J.; Mingo, N. Thermal conductivity and phonon linewidths of monolayer MoS2 from first principles. *Appl. Phys. Lett.* **2013**, *103*, 253103.

(20) Kumar, S.; Schwingenschlögl, U. Thermoelectric Response of Bulk and Monolayer MoSe$_2$ and WSe$_2$. *Chem. Mater.* **2015**, *27*, 1278−1284.

(21) Slack, G. A. In *Solid State Physics*; Ehrenreich, F. S. H., Turnbull, D., Eds.; Academic Press: San Diego, 1979; Vol. *34*, pp 1−71.

(22) The specific value of *b* is relatively unimportant as the analysis presented here is only very slightly affected as long as *b* is chosen from the range between approximately 0.7 and 1.1.

(23) Togo, A.; Oba, F.; Tanaka, I. First-principles calculations of the ferroelastic transition between rutile-type and CaCl$_2$-type SiO$_2$ at high pressures. *Phys. Rev. B: Condens. Matter Mater. Phys.* **2008**, *78*, 134106.

(24) (a) Blöchl, P. E. Projector augmented-wave method. *Phys. Rev. B: Condens. Matter Mater. Phys.* **1994**, *50*, 17953−17979; (b) Kresse, G.; Joubert, D. From ultrasoft pseudopotentials to the projector augmented-wave method. *Phys. Rev. B: Condens. Matter Mater. Phys.* **1999**, *59*, 1758−1775.

(25) (a) Kresse, G.; Hafner, J. Ab initio molecular dynamics for liquid metals. *Phys. Rev. B: Condens. Matter Mater. Phys.* **1993**, *47*, 558−561; (b) Kresse, G.; Furthmüller, J. Efficient iterative schemes for ab initio total-energy calculations using a plane-wave basis set. *Phys. Rev. B: Condens. Matter Mater. Phys.* **1996**, *54*, 11169.

(26) Dion, M.; Rydberg, H.; Schröder, E.; Langreth, D. C.; Lundqvist, B. I. Van der Waals Density Functional for General Geometries. *Phys. Rev. Lett.* **2004**, *92*, 246401.

(27) Thonhauser, T.; Cooper, V. R.; Li, S.; Puzder, A.; Hyldgaard, P.; Langreth, D. C. Van der Waals density functional: Self-consistent potential and the nature of the van der Waals bond. *Phys. Rev. B: Condens. Matter Mater. Phys.* **2007**, *76*, 125112.

(28) Berland, K.; Cooper, V. R.; Lee, K.; Schröder, E.; Thonhauser, T.; Hyldgaard, P.; Lundqvist, B. I. van der Waals forces in density functional theory: The vdW-DF method. *Rep. Prog. Phys.* **2015**, *78*, 066501.

(29) Berland, K.; Hyldgaard, P. Exchange functional that tests the robustness of the plasmon description of the van der Waals density functional. *Phys. Rev. B: Condens. Matter Mater. Phys.* **2014**, *89*, 035412.

(30) Klimeš, J.; Bowler, D. R.; Michaelides, A. Van der Waals density functionals applied to solids. *Phys. Rev. B: Condens. Matter Mater. Phys.* **2011**, *83*, 195131.

(31) Björkman, T. Testing several recent van der Waals density functionals for layered structures. *J. Chem. Phys.* **2014**, *141*, 074708.

(32) Schutte, W.; de Boer, J.; Jellinek, F. Crystal structures of tungsten disulfide and diselenide. *J. Solid State Chem.* **1987**, *70*, 207−209.

(33) Zhao, Y.; Luo, X.; Li, H.; Zhang, J.; Araujo, P. T.; Gan, C. K.; Wu, J.; Zhang, H.; Quek, S. Y.; Dresselhaus, M. S.; Xiong, Q. Interlayer Breathing and Shear Modes in Few-Trilayer MoS$_2$ and WSe$_2$. *Nano Lett.* **2013**, *13*, 1007−1015.

(34) Murray, É. D.; Lee, K.; Langreth, D. C. Investigation of Exchange Energy Density Functional Accuracy for Interacting Molecules. *J. Chem. Theory Comput.* **2009**, *5*, 2754−2762.

(35) Bahn, S. R.; Jacobsen, K. W. An object-oriented scripting interface to a legacy electronic structure code. *Comput. Sci. Eng.* **2002**, *4*, 56.

(36) Stukowski, A. Visualization and analysis of atomistic simulation data with OVITO − the Open Visualization Tool. *Modell. Simul. Mater. Sci. Eng.* **2010**, *18*, 015012.

(37) Note that the W sublattice is hexagonal close packed only by name as the axial ratio is more than twice as large as the ideal ratio of $\sqrt{8/3}$.

(38) Kim, S.; Zuo, J. M.; Nguyen, N. T.; Johnson, D. C.; Cahill, D. G. Structure of layered WSe$_2$ thin films with ultralow thermal conductivity. *J. Mater. Res.* **2008**, *23*, 1064−1067.

(39) Tasci, E.; de la Flor, G.; Orobengoa, D.; Capillas, C.; Perez-Mato, J.; Aroyo, M. An introduction to the tools hosted in the Bilbao Crystallographic Server. *EPJ Web Conf.* **2012**, *22*, 00009.

(40) Ding, Y.; Wang, Y.; Ni, J.; Shi, L.; Shi, S.; Tang, W. First principles study of structural, vibrational and electronic properties of graphene-like MX$_2$ (M = Mo, Nb, W, Ta; X = S, Se, Te) monolayers. *Phys. B* **2011**, *406*, 2254−2260.

(41) Mead, D. G.; Irwin, J. C. Long wavelength optic phonons in WSe$_2$. *Can. J. Phys.* **1977**, *55*, 379−382.

(42) Note that in ref 1 the c_{33} value was actually derived from the longitudinal sound velocity, which was measured to be 1.65 km/s perpendicular to the film.

(43) See, for example, Figure 3 in ref 38.

(44) Lee, S.-M.; Cahill, D. G.; Venkatasubramanian, R. Thermal conductivity of Si-Ge superlattices. *Appl. Phys. Lett.* **1997**, *70*, 2957.

(45) We have also considered Gaussian as well as truncated Gaussian distributions; in the latter case, the cutoff is given by the stability limit discussed in section 4. These distributions lead to results similar to those of the exponential distribution and do not change the conclusions presented here. The exponential distribution has the advantage of involving only a single parameter, which can be fixed using experimental input, whereas the Gaussian distribution requires two parameters to be specified.

(46) The condition $a\mu < 1$ must be fulfilled for the integral in eq 3 to be convergent. Using an *a* value of 25.5 calculated from a first-principles approach, one finds this condition implies $\mu < 0.04$, which is satisfied by the experimental value $\mu = \langle \varepsilon \rangle \approx 2.3\%$.

(47) Chen, G.; Tien, C. L.; Wu, X.; Smith, J. S. Thermal Diffusivity Measurement of GaAs/AlGaAs Thin-Film Structures. *J. Heat Transfer* **1994**, *116*, 325.

(48) Nika, D. L.; Pokatilov, E. P.; Askerov, A. S.; Balandin, A. A. Phonon thermal conduction in graphene: Role of Umklapp and edge roughness scattering. *Phys. Rev. B: Condens. Matter Mater. Phys.* **2009**, *79*, 155413.

(49) Note that interface scattering has been discussed quite extensively in connection with the reduction in thermal conductivity, in particular the in-plane component, in semiconductor superlattices (see, e.g., refs 55 and 56).

(50) The boundary scattering model is commonly employed to describe the effect of finite sample size on phonon-mediated thermal conduction, in which case d represents the sample dimension. It effectively implements a geometric constraint on the mean free path of the individual phonon modes, i.e., $\lambda = v_g \tau \lesssim d$. It is in this more general context that the model is employed in the work presented here. For the sake of simplicity, we consider the limit $p = 0$, which corresponds to completely incoherent scattering. Any larger value of p (keeping all other parameters the same) would imply an increase in the thermal conductivity and thus an increasingly strong deviation from the experimental data. This in turn indicates that the layer scattering is in fact incoherent.

(51) Hyldgaard, P.; Mahan, G. D. Phonon superlattice transport. *Phys. Rev. B: Condens. Matter Mater. Phys.* **1997**, *56*, 10754–10757.

(52) Balandin, A.; Wang, K. L. Significant decrease of the lattice thermal conductivity due to phonon confinement in a free-standing semiconductor quantum well. *Phys. Rev. B: Condens. Matter Mater. Phys.* **1998**, *58*, 1544–1549.

(53) Swartz, E. T.; Pohl, R. O. Thermal boundary resistance. *Rev. Mod. Phys.* **1989**, *61*, 605–668.

(54) Sakai, A.; Kanno, T.; Takahashi, K.; Tamaki, H.; Kusada, H.; Yamada, Y.; Abe, H. Breaking the trade-off between thermal and electrical conductivities in the thermoelectric material of an artificially tilted multilayer. *Sci. Rep.* **2014**, *4* DOI: 10.1038/srep06089.

(55) Chen, G. Size and Interface Effects on Thermal Conductivity of Superlattices and Periodic Thin-Film Structures. *J. Heat Transfer* **1997**, *119*, 220–229.

(56) Hyldgaard, P.; Mahan, G. D. Phonon Knudsen flow in GaAs/AlAs superlattices. *Proceedings of the Twenty-Third International Thermal Conductivity Conference*, Lancaster, PA, 1996; p 172.

Paper II

Thermal expansion and transport in van der Waals solids
Daniel O. Lindroth and Paul Erhart

Thermal transport in van der Waals solids from first-principles calculations

Daniel O. Lindroth[*] and Paul Erhart[†]

Chalmers University of Technology, Department of Physics, Gothenburg, Sweden
(Received 23 May 2016; published 14 September 2016)

The lattice thermal expansion and conductivity in bulk Mo and W-based transition metal dichalcogenides are investigated by means of density functional and Boltzmann transport theory calculations. To this end, a recent van der Waals density functional (vdW-DF-CX) is employed, which is shown to yield excellent agreement with reference data for the structural parameters. The calculated in-plane thermal conductivity compares well with experimental room-temperature values, when phonon-phonon and isotopic scattering are included. To explain the behavior over the entire available temperature range one must, however, include additional (temperature independent) scattering mechanisms that limit the mean free path. Generally, the primary heat carrying modes have mean free paths of $1\,\mu$m or more, which makes these materials very susceptible to structural defects. The conductivity of Mo- and W-based transition metal dichalcogenides is primarily determined by the chalcogenide species and increases in the order Te-Se-S. While for the tellurides and selenides the transition metal element has a negligible effect, the conductivity of WS_2 is notably higher than for MoS_2, which may be traced to the much larger phonon band gap of the former. Overall, the present study provides a consistent set of thermal conductivities that reveal chemical trends and constitute the basis for future investigations of van der Waals solids.

I. INTRODUCTION

In the advent of increasingly elaborate synthesis techniques [1,2], highly engineered van der Waals (vdW) solids are emerging as promising candidates for a manifold of applications including electronic components [3], optoelectronics [4–6], thermoelectrics [7], and spintronics [8]. Since thermal transport plays a key role in many of these situations, it is important to develop a detailed understanding of the thermal conductivity in vdW solids.

Unfortunately, the values for the thermal conductivities reported in the literature exhibit a wide spread. For example, in the case of nominally single-crystalline MoS_2, experimental values for the in-plane (basal plane) thermal lattice conductivity vary over one order of magnitude ranging from around 20 W/K m [9] up to 110 W/K m [10] at room temperature (Fig. 1). This can be partly attributed to the challenges associated with experimental measurements of the thermal conductivity in nanostructures with pronounced anisotropy, see, e.g., Refs. [10,11]. Possibly even more crucial are defects and sample size effects, as the growth of large high-quality transition metal dichalcogenide (TMD) single crystals is very time consuming [10]. The extreme sensitivity to structure has been possibly most impressively demonstrated in the case of WSe_2 [12,13], for which the out-of-plane (through plane) thermal conductivity $\kappa_\perp$ has been shown to vary by almost two orders of magnitude at room temperature. This variation can in fact be rationalized in terms of the microstructure, in particular planar defects such as stacking faults and subtle variations in layer spacing [14].

Similar to the experimental data, calculated values for the thermal conductivity cover a wide range as well. *Ab initio* calculations based on Boltzmann transport theory in combination with density functional theory have only become available relatively recently [15–19]. Still, as illustrated by the case of MoS_2 (Fig. 1), calculations have usually been restricted to monolayers [20–26]. This is at least in part due to the fact that computational studies of bulk systems [27,28] require taking into account the vdW forces that mediate interlayer binding. These interactions are, however, not captured by common semilocal exchange-correlation (XC) functionals [29], including widely popular functionals such as PBE [30] and PBEsol [31]. In some cases, this shortcoming has been addressed by using semiempirical methods [32]. As will be shown below, in general, the structural parameters of TMDs as well as other quantities that affect the thermal conductivity are, however, very sensitive to the treatment of exchange and correlation. Furthermore, since vdW forces are rather weak and computational noise can blur anharmonic effects, both the choice of the XC functional and the convergence of the computational parameters require special care.

This perspective motivates the present study, in which we have carefully evaluated both the in-plane and out-of-plane thermal conductivities of Mo and W-based TMDs. To this end, we employ a combination of density functional and Boltzmann transport theory calculations based on the vdW density functional method [37] in combination with a recently formulated consistent-exchange part [29,38], which has already been found to work very well, e.g., WSe_2 [14]. In the following, we first demonstrate that this approach yields an excellent description of the structural parameters of Mo and W-based TMDs at finite temperatures. We then carefully assess the relevant computational parameters before conducting a comprehensive investigation of the thermal conductivities. Since the largest contribution to the thermal conductivities stems from modes with mean free paths (phonon-phonon scattering limited) of more than 1μm, both in-plane and out-of-plane conductivities are in practice often limited by structural incoherence. The thermal conductivities κ are found to increase from the tellurides to the sulphides but, in opposition to the trend expected based on the group velocities, κ tends to be higher for WS_2 than for the respective Mo

_____

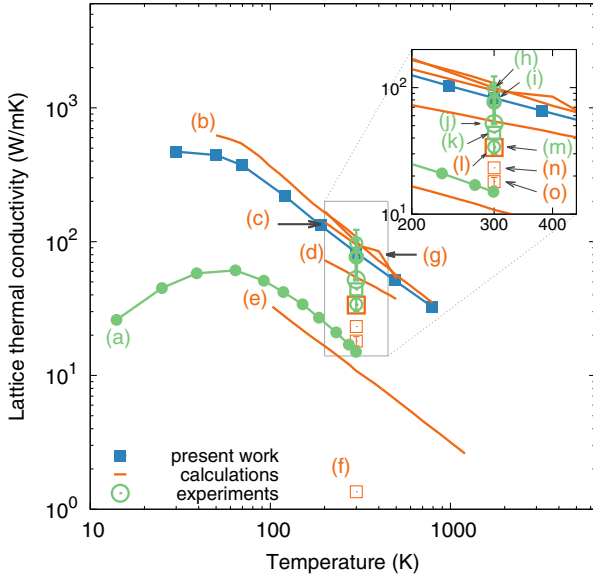[*]daniel.lindroth@chalmers.se
[†]erhart@chalmers.se

FIG. 1. Experimental and theoretical results for the in-plane (basal plane) thermal conductivity of MoS$_2$. Calculations and experiments are from (a) Ref. [9], (b) Ref. [20], (c) Ref. [21], (d) Ref. [22], (e) Ref. [28], (f) Ref. [23], (g) Ref. [24], (h) Ref. [10], (i) Ref. [33], (j) Ref. [34], (k) Ref. [35], (l) Ref. [25], (m) Ref. [36], (n) Ref. [26], and (o) Ref. [27]. Data from Refs. [20–26,33,36] were obtained for monolayers; the data from Ref. [34] are for few-layer systems.

compound. This behavior is shown to be due to higher lifetimes in the former case, which can be rationalized in terms of the scattering condition and the different phononic band gaps.

II. METHODOLOGY

A. Thermal conductivity

In general, the thermal conductivity comprises both an electronic κ_e and a phononic (lattice) part κ_l. According to the Wiedemann-Franz law the electronic contribution κ_e is closely related to the electrical conductivity. Since the TMDs of interest in the present work have comparably large (electronic) band gaps κ_e is usually much smaller than κ_l. For example, in the case of the in-plane conductivity in MoS$_2$, κ_e reaches only about 5% of the value of κ_l at room temperature [9] and the ratio is even smaller below 300 K. In the present work, we therefore focus entirely on the lattice contribution κ_l and from here on drop the subscript l.

To calculate the lattice thermal conductivity, we utilize Boltzmann transport theory within the relaxation time approximation. In this approximation, each mode $\lambda = (\boldsymbol{q}, p)$, where $\boldsymbol{q}$ is the phonon wave-vector and p is the band index, is associated with a relaxation time τ_λ. The total relaxation time is the result of several scattering processes, and in the present work, we consider phonon-phonon scattering as well as isotopic and boundary scattering. If one assumes that each scattering rate individually contributes in parallel, the total relaxation time for a phonon mode is given by Matthiessen's rule,

$$\tau_\lambda^{-1} = \tau_{\text{ph-ph},\lambda}^{-1} + \tau_{\text{iso},\lambda}^{-1} + \tau_{\text{boundary},\lambda}^{-1}. \qquad (1)$$

Isotopic scattering is the result of variations in the atomic masses due to the natural isotope distribution. The corresponding relaxation time contribution $\tau_{\text{iso},\lambda}$ has been calculated according to second-order perturbation theory [39] using isotope distributions and masses from Ref. [40].

Boundary scattering is accounted for by assuming that the mean free path (MFP) of any phonon mode is capped by a structural length scale L, which in the most simple case corresponds to the sample size [41],

$$\tau_{\text{boundary},\lambda}^{-1} = v_\lambda / L. \qquad (2)$$

This expression represents the limit, in which the scattering event is fully diffusive, equivalent to a vanishing specularity parameter [42,43]. Below we will treat this model as a means to establish the characteristic length scale L that is representative of the (temperature independent) structural homogeneity of the material. We note that the model was used in a similar fashion in Ref. [44] to describe the effect of nanostructuring in Zn chalcogenides.

Phonon-phonon scattering is computationally the most intricate contribution. The corresponding lifetime $\tau_{\text{ph-ph},\lambda}$ can be obtained using perturbation theory on top of a harmonic description of lattice vibrations. The phonon-phonon limited lifetime is then obtained as the inverse of the self energy $\tau_{\text{ph-ph},\lambda} = 1/2\Gamma_\lambda(\omega_\lambda)$, where the self-energy is given by [19]

$$\Gamma_\lambda(\omega) = \frac{18\pi}{\hbar^2} \sum_{\lambda'\lambda''} |\Phi_{-\lambda\lambda'\lambda''}|^2 \{(n_{\lambda'} + n_{\lambda''} + 1)\, \delta(\omega - \omega_{\lambda'} - \omega_{\lambda''})$$
$$+ (n_{\lambda'} - n_{\lambda''})[\delta(\omega + \omega_{\lambda'} - \omega_{\lambda''}) - \delta(\omega - \omega_{\lambda'} + \omega_{\lambda''})]\}. \qquad (3)$$

Here, $\Phi_{-\lambda\lambda'\lambda''}$ is obtained from the third-order interatomic force constant (IFC) matrix and n_λ is the Bose-Einstein distribution. The mode frequencies ω_λ can be obtained in the usual fashion from the second order IFCs [41].

Phonon scattering processes must obey (i) momentum conservation, $\boldsymbol{q}_\lambda + \boldsymbol{q}_{\lambda'} + \boldsymbol{q}_{\lambda''} + \boldsymbol{G} = 0$, where $\boldsymbol{G}$ is a reciprocal lattice vector, and (ii) energy conservation, $\delta(\omega_\lambda \pm \omega_{\lambda'} \pm \omega_{\lambda''})$, where the signs are determined by the type of scattering event. Condition (i) is included in the constructing of the third-order IFCs, while condition (ii) is apparent in Eq. (3). The structure of the self-energy and accordingly the lifetimes is thus determined to a large extent by the geometry of the Brillouin zone and the phonon dispersion [41]. This observation allows one to identify general trends in the lifetime spectrum already on the basis of the phonon dispersion and thus the second-order IFCs. In this context, the joint density of states (JDOS) is a very useful quantity. The JDOS is defined as

$$D_2(\boldsymbol{q}, \omega) = \frac{1}{N} \sum_{\lambda', \lambda''} \Delta(-\boldsymbol{q} + \boldsymbol{q}' + \boldsymbol{q}'')$$
$$\times \left\{ \left[\underbrace{\delta(\omega + \omega_{\lambda'} - \omega_{\lambda''}) - \delta(\omega - \omega_{\lambda'} + \omega_{\lambda''})}_{\text{Class 1 processes}} \right] \right.$$
$$\left. + \underbrace{\delta(\omega - \omega_{\lambda'} - \omega_{\lambda''})}_{\text{Class 2 processes}} \right\}, \qquad (4)$$

where N is the number of unit cells in the crystal and $\Delta(-\boldsymbol{q} + \boldsymbol{q}' + \boldsymbol{q}'')$ embodies the momentum conservation condition expressed above. $D_2(\boldsymbol{q}, \omega)$ thus effectively counts the number of collision and decay processes that contribute to the phonon-phonon scattering time of a given mode. By comparison with the full expression one recognizes as the main difference the occurrence of third-order derivatives of the total energy in Eq. (3),[1] which represent the efficiency of the scattering processes that are energy and momentum allowed. By contrast, Eq. (4) requires only knowledge of the second-order force constants.

Finally, the *full lattice thermal conductivity tensor* is obtained by summing over all modes [45]

$$\boldsymbol{\kappa}(T) = \frac{1}{N_q \Omega} \sum_\lambda \underbrace{\tau_\lambda(T) \boldsymbol{v}_\lambda}_{\boldsymbol{\Lambda}_\lambda(T)} \otimes \boldsymbol{v}_\lambda c_\lambda(T). \tag{5}$$

Here, Ω is the unit cell volume, N_q denotes the number of q points, $\boldsymbol{v}_\lambda = \nabla \omega_\lambda$ is the group velocity, $\boldsymbol{\Lambda}_\lambda$ is the phonon MFP, and $c_\lambda(T)$ is the mode specific heat capacity. For analyzing, e.g., the sensitivity of the thermal conductivity to structural inhomogeneities it is convenient to consider the cumulative thermal conductivity, which is given by

$$\bar{\boldsymbol{\kappa}}(\Lambda) = \frac{1}{N_q \Omega} \sum_\lambda^{\Lambda_\lambda < \Lambda} \boldsymbol{\Lambda}_\lambda(T) \otimes \boldsymbol{v}_\lambda c_\lambda(T). \tag{6}$$

If the MFP is uniformly limited to a constant value $\bar{\Lambda}$, one obtains the so-called small-grain conductivity [18], which is given by

$$\kappa_{\mathrm{sg}} = \frac{1}{N_q \Omega} \sum_\lambda v_\lambda c_\lambda(T). \tag{7}$$

The small-grain conductivity represents the limit, in which scattering is dominated by a structural length scale as for example in the case of nanostructuring.

B. Computational details

Density functional theory calculations were carried out using the projector augmented wave method [46,47] as implemented in the Vienna *ab initio* simulation package (VASP) [48,49]. To assess the sensitivity of our results to the treatment of exchange-correlation effects, we used both the local density approximation (LDA) and the van der Waals density functional (vdW-DF) method [50–53]. In the vdW-DF method, the correlation energy E_c^{nl} assumes a *nonlocal* form, which is expressed as a double integral over the spatial degrees of freedom [38]:

$$E_c^{nl}[\rho] = \frac{1}{2} \int \int \rho(\boldsymbol{r}) \phi(\boldsymbol{r}, \boldsymbol{r}') \rho(\boldsymbol{r}') d^3 \boldsymbol{r} \, d^3 \boldsymbol{r}', \tag{8}$$

where ρ is the electron density and the kernel $\phi(\boldsymbol{r}, \boldsymbol{r}')$ represents the nonlocal coupling of the electron density. The correlation energy is then complemented with a *semilocal* exchange functional giving the exchange-correlation energy

for the vdW-DF method:

$$E_{xc}^{vdW-DF}[\rho] = E_x^{sl}[\rho(\boldsymbol{r})] + E_c^{nl}[\rho(\boldsymbol{r})]. \tag{9}$$

We considered both the empirically adjusted PBE exchange part from Ref. [54] (vdW-DF-optPBE) and the recently developed nonempirical consistent exchange version (vdW-DF-CX) [29,38] as implemented in VASP [54,55].

The plane-wave energy cutoff energy was set to 290 eV in the calculations of WSe_2, $MoSe_2$, WTe_2, and $MoTe_2$ and to 336 eV in the calculations of WS_2 och MoS_2. In calculations based on the primitive cell, the Brillouin zone was sampled using a Γ-centered $12 \times 12 \times 3$ $\boldsymbol{k}$-point mesh.

Thermal conductivities and other phonon related quantities where obtained with the PHONOPY [56,57] and PHONO3PY [19] packages. The convergence of the lattice thermal conductivity with respect to $\boldsymbol{q}$-point sampling mesh, displacement amplitude, supercell size as well as the cutoff for the maximal range of force interactions was analyzed as described in Sec. III B below. The final calculations for both second- and third-order force constants were conducted using supercells comprising $3 \times 3 \times 1$ primitive unit cells while a Γ-centered $4 \times 4 \times 3$ grid was utilized for $\boldsymbol{k}$-point sampling. The displacement amplitude employed in the calculation of finite differences was set to 0.09 Å. This value was obtained by balancing the need to reduce the numerical noise in the computation of soft interlayer force components while remaining in the harmonic (linear response) regime. For computational efficiency, forces were only computed for pairs and triplets within a cutoff range of 3.8 Å; this includes interactions up to the third-nearest-neighbor shell for in-plane terms and between neighboring layers in the out-of-plane direction for all considered materials. For the lattice thermal conductivity calculations, a tetrahedron method was used for Brillouin zone integrations while employing a $21 \times 21 \times 13$ $\boldsymbol{q}$-point mesh.

The structural properties at finite temperature were obtained at the level of the quasiharmonic approximation as implemented in PHONOPY [56,57]. To this end, the second-order IFCs were computed at seven different volumes between 95% and 105% of the respective equilibrium volume.

III. RESULTS AND DISCUSSION

A. Description of van der Waals solids

1. Tungsten diselenide

Molybdenum and tungsten based TMDs are among the most widely investigated vdW solids. They adopt layered structures with stoichiometry MX_2 (M = Mo and W; X = S, Se, and Te) that are composed of two-dimensional sheets with strong intralayer bonding coupled to each other via comparably weak vdW interactions. With the exception of WTe_2 the equilibrium structures belong to space group $P6_3/mmc$ (International Tables of Crystallography No. 194, see Fig. 2). In equilibrium WTe_2 adopts an orthorhombic crystal structure that belongs to space group $Pmn2_1$ (ITC No. 31) [66]. It is included here in space group $P6_3/mmc$ to exhibit chemical trends and since it be incorporated in multilayer vdW solids with hexagonal symmetry.

For WSe_2, the structural parameters at 300 K were computed using the local density approximation (LDA) as

---

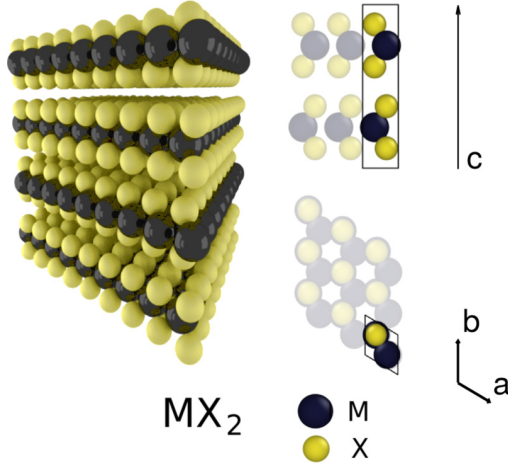[1]Also compare Eqs. (3.2.11-12) in Ref. [41] and Eq. (1) in Ref. [19].

FIG. 2. Crystal structure of molybdenum and tungsten based transition metal dichalcogenides (space group $P6_3/mmc$, ITC No. 194). The transition metal and chalcogenide species correspond to M and X, respectively. Structures were created using the atomic simulation environment [58] and visualized with OVITO [59] as well as Blender [60].

well as the vdW-DF-optPBE and vdW-DF-CX functionals [Table I and Fig. 3(a)]. We also considered the PBE functional but the lack of vdW binding gives rise to extremely weak interlayer binding and a very poor description of the structure, in particular the out-of-plane lattice parameter.

The closest agreement with the structural reference data is obtained for the vdW-DF-CX functional, which yields values for the in-plane and out-of-plane lattice parameters that are within respectively 0.1% and 0.3% of the experimental data. We are not aware of higher-level (experiment or calculation) reference data for the interlayer binding energy [Fig. 3(a)] but note that the vdW-DF-CX functional has been shown to yield excellent binding energies for other vdW bonded systems [53].

The vdW-DF-optPBE functional was obtained in semi-empirical fashion by combining the non-local vdW-DF
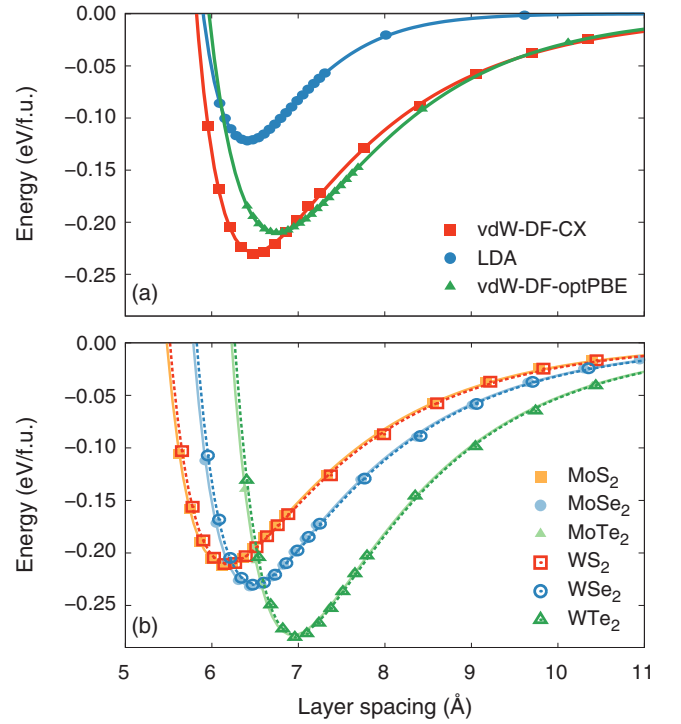

FIG. 3. Binding energy as a function of interlayer spacing (a) for WSe_2 as obtained using different XC functionals and (b) for Mo and W-based sulfides, selenides, and tellurides calculated using the vdW-DF-CX functional. The in-plane lattice constant was held fixed at the equilibrium value.

correlation with the rescaled exchange part of the PBE functional [30,54]. Here, it is found to overestimate both in-plane (1.7%) and out-of-plane (4.2%) lattice constants of WSe_2 notably; it also yields a slightly smaller value for the interlayer cohesion than the vdW-DF-CX functional.

The LDA results for both lattice constants are within 1% of the experimental values. This result is partially surprising in so far as the LDA actually does not account for dispersive vdW interactions, and the good agreement is rather the result of the characteristic LDA overbinding, which has been pointed out previously [50,68]. The LDA thus yields the correct result for the wrong reasons [69], which becomes more evident when considering the binding energy curve [Fig. 3(a)]. The asymptotic behavior of the LDA data clearly differs from the two vdW functionals and yields only about half of the interlayer binding energy. The energy landscape around the equilibrium spacing is, however, similar to the one obtained with the vdW-DF-CX functional.

2. Extension to other TMDs

Based on the results for WSe_2, we only considered the vdW-DF-CX functional for the analysis of the other Mo and W-based TMDs. This functional generally achieves very good agreement with experimental measurements (Table II) as the deviations from the reference data generally do not exceed 0.4% and are on average below 0.2%.

The results show the structural parameters are barely affected by the transition metal, while the chalcogenide species

TABLE I. Comparison of structural parameters for WSe_2 from experiment [61,62] and calculation. a and c are the in-plane and out-of-plane lattice constants (Å), respectively; z_{Se} is the internal parameter, which specifies the position of the Se atoms.

	Calculations			Experiment	
	LDA	vdW-optPBE	vdW-CX		
zero K excluding zero-point vibrations					
a	3.250	3.341	3.277		
c	12.819	13.550	12.942		
z_{Se}	0.620	0.626	0.620		
zero K with zero-point vibrations					
a	3.250	3.339	3.279		
c	12.824	13.500	12.991		
z_{Se}	0.620	0.625	0.620		
300 K					
a	3.250	3.339	3.279	3.282	3.286
c	12.832	13.508	12.998	12.960	12.960
z_{Se}	0.620	0.625	0.621	0.621	0.621

TABLE II. Comparison of structural parameters for di-sulfides, selenides, and tellurides of Mo and W in spacegroup $P6_3/mmc$ (ITC No. 194) as obtained from calculations using the vdW-DF-CX functional and experiment. Results from calculations that exclude of zero-point vibrations are shown in brackets. The in-plane and out-of-plane lattice constants a and c are given in units of angstroms.

Material	Calculation				Experiment	
	0 K		300 K		300 K	
MoS$_2$, Refs. [62,63]						
a	3.152	(3.149)	3.152		3.160	3.160
c	12.291	(12.225)	12.295		12.294	12.290
z_S	0.622	(0.621)	0.622		0.621	0.620
MoSe$_2$, Refs. [62,63]						
a	3.280	(3.278)	3.280		3.289	3.288
c	12.920	(12.875)	12.928		12.927	12.930
z_{Se}	0.620	(0.621)	0.621		0.621	0.620
MoTe$_2$, Refs. [64,65]						
a	3.504	(3.501)	3.504		3.519	3.518
c	13.904	(13.865)	13.913		13.964	13.974
z_{Te}	0.619	(0.619)	0.619		0.625	0.621
WS$_2$, Refs. [61,62]						
a	3.152	(3.150)	3.152		3.153	3.154
c	12.358	(12.288)	12.365		12.323	12.360
z_S	0.623	(0.622)	0.623		0.623	0.614
WSe$_2$, Refs. [61,62]						
a	3.279	(3.277)	3.279		3.282	3.286
c	12.991	(12.942)	12.998		12.960	12.980
z_{Se}	0.620	(0.620)	0.621		0.621	0.620
WTe$_2$						
a	3.506	(3.503)	3.506			
c	13.954	(13.916)	13.961			
z_{Te}	0.620	(0.619)	0.620			

has a very strong effect as the lattice parameters increase in the order S–Se–Te. As will be discussed in more detail below, this has a direct impact on the vibrational properties as the size of the Brillouin zone is inversely proportional to the lattice parameters (see Fig. 4).

B. Convergence of the thermal conductivity

Since the vdW forces acting between layers are much weaker than the covalent and ionic interactions in denser materials, they are more prone to numerical errors. This is partially compensated by using tight convergence parameters, e.g., for the plane wave cutoff energy and the termination of the electronic self-consistency loop. When calculating second and especially third-order derivatives using finite differences errors in the forces are, however, enhanced. We therefore carefully tested the effect of the displacement amplitude Δr used for computing the IFCs on the calculated lattice thermal conductivity.

The thermal conductivity is in fact very sensitive to the displacement amplitude Δr [Fig. 5(a)]. While in the case of silicon [inset in Fig. 5(a)] κ is only weakly dependent on Δr, for WSe$_2$ the thermal conductivity is dramatically underestimated for smaller values of Δr. Since one usually strives to use small values for Δr in order to remain in the linear

response regime, common (default) values for Δr typically fall in the range between 0.01 and 0.03 Å [18,19]. In the case of WSe$_2$ these values cause a pronounced error in κ, as Δr values $\gtrsim 0.05$ Å are required to obtain convergence. We therefore adopted a value of 0.09 Å for the bulk of our calculations.

The calculation of the thermal conductivity is also affected by supercell size and the cutoff imposed on the interaction range. Based on the results of our convergence study [Fig. 5(b)], production runs were conducted using supercells comprising $3 \times 3 \times 1$ unit cells and interactions were included up to the third-neighbor shell in-plane and the first neighbor shell out-of-plane (equivalent to a cutoff of 3.63 Å in the case of WSe$_2$).

Finally, the thermal conductivity is affected by the density of the q-point grid used for Brillouin zone integrations. In this regard, we find that a $19 \times 19 \times 12$ q-point mesh corresponding to approximately 4300 q points in the full Brillouin zone achieves a convergence level that is comparable to the other parameters considered here [Fig. 5(c)].

C. Thermal conductivity in WS$_2$ and WSe$_2$

Having established the quality of the underlying XC functional with regard to structural parameters (Sec. III A) as well as the numerical convergence of our calculations (Sec. III B), we can now compare the calculated thermal conductivities with experiment. To this end, we first consider WS$_2$ and WSe$_2$, for which experimental data over a wide temperature range is available for both the in-plane and out-of-plane conductivities of nominally single-crystalline material [12,70].

If only phonon-phonon scattering is included as a lifetime limiting mechanism in Eq. (1), the calculated thermal conductivity invariably exhibits a $1/T$ dependence as expected in this limit [71] (Fig. 6). Isotopic scattering lowers κ as well as the temperature exponent in particular for temperatures below 100 K. At room temperature the in-plane (out-of-plane) conductivity is reduced from 157 to 126 W/K m (5.4 to 4.7 W/K m) in the case of WS$_2$ and from 45 to 42 W/K m (3.1 to 3.0 W/K m) for WSe$_2$.

In the case of WS$_2$, the calculated in-plane conductivity at room temperature of 126 W/mk (including phonon-phonon as well as isotopic scattering) agrees very well with the measured value of 124 W/K m [70]. At lower temperatures, there is, however, a noticeable disparity suggesting that at least one other scattering mechanism is important for κ. In fact, if boundary scattering is taken into account via Eq. (2), it is possible to reproduce the experimental in-plane conductivity over the entire temperature range using $L = 4$ μm. Rather than thinking of this value as corresponding to the sample size, it should be understood as a characteristic structural length scale. It should also be recalled that Eq. (2) represents the extreme limit in which the scattering process is entirely diffusive whereas in reality some level of directional scattering can be expected [42,43].

The notion that not only the out-of-plane [12,14] but also the in-plane thermal conductivity is sensitive to structural inhomogeneities is further supported by observing that the major contributions to the thermal conductivity stem from modes with MFPs of at least 1 μm [Figs. 7(a) and 7(b)], which is substantially longer than, e.g., in the case of PbTe
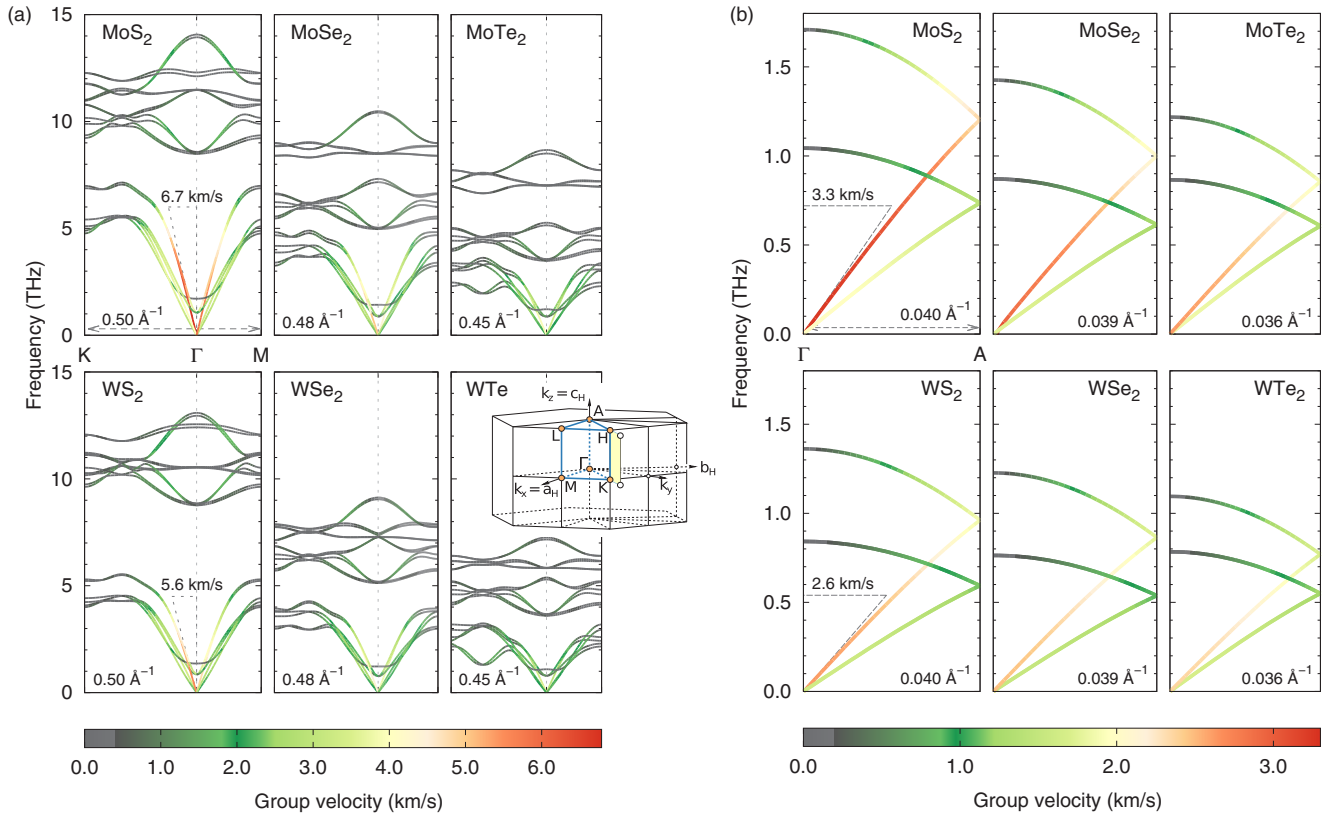
FIG. 4. (a) In-plane and (b) out-of-plane phonon dispersion for Mo and W-based TMDs color coded by group velocity. The inset in (a) shows the Brillouin zone for spacegroup $P6_3/mmc$ (ITC No. 194) [67]. The number in the left bottom corner of plot represents the dimension of the Brillouin zone along the direction shown by the dashed arrows. The longitudinal sound velocities along (a) Γ-K and (b) Γ-A are indicated by dashed triangles in the cases of MoS$_2$ and WS$_2$.

[Fig. 7(c)], a system, in which nanostructuring has been used with great success to lower the thermal conductivity [17,72]. The representative MFP for WS$_2$ and WSe$_2$ as well as other TMDs is rather comparable to Si [Fig. 7(c)], the synthesis of which—at least currently in contrast to

TMDs—can be extremely well controlled yielding very low defect densities.

The calculated out-of-plane conductivities exhibit a considerable deviation from experiment already at room temperature (WS$_2$: $\kappa_\perp^{\text{expt}} = 1.7$ W/K m versus $\kappa_\perp^{\text{calc}} = 5.4$ W/K m;
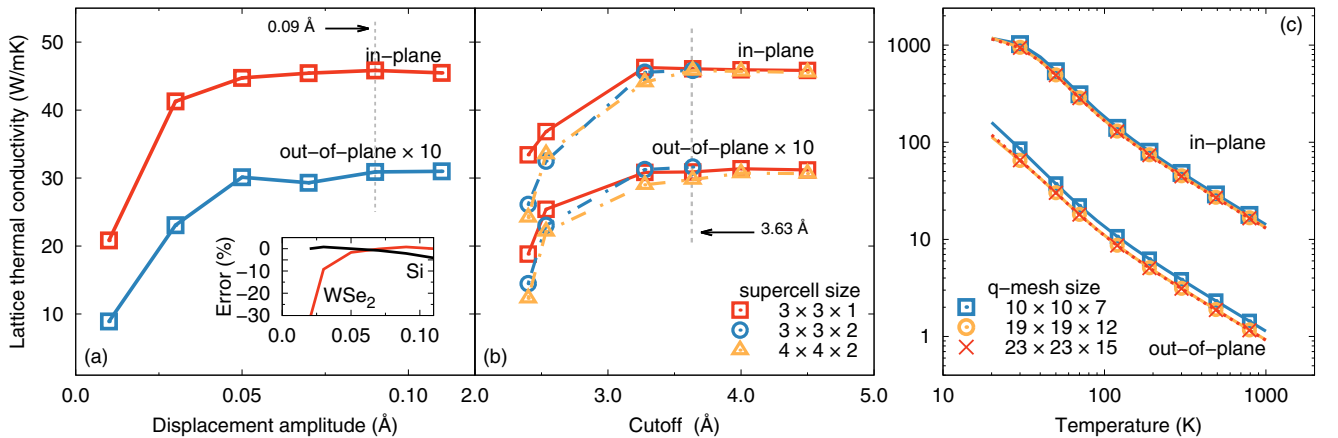

FIG. 5. Convergence of thermal conductivity with respect to different numerical parameters. (a) Calculated lattice thermal conductivity in WSe$_2$ at 300 K as a function of the displacement amplitude used for calculating the IFCs. The out-of-plane conductivity has been scaled by 10 for clarity. The inset compares the relative error in the in-plane conductivity for WSe$_2$ with the case of silicon, which is a purely covalently bonded material and much less sensitive to the choice of the displacement amplitude. (b) Convergence of κ at 300 K with respect to supercell size and interaction cutoff distance. (c) Convergence with respect to the $\boldsymbol{q}$-point mesh used for Brillouin zone integrations.
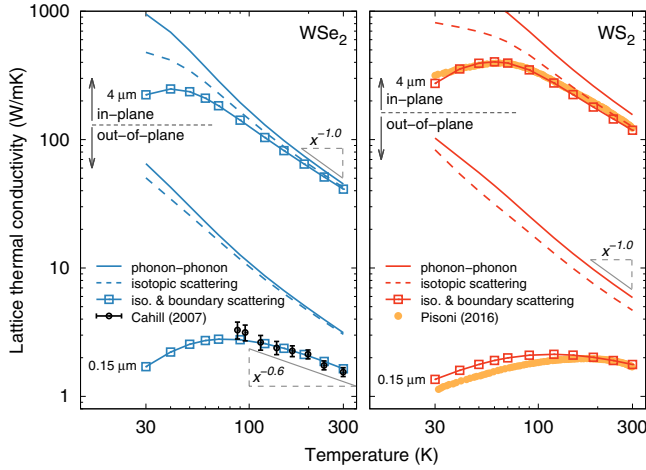
FIG. 6. Calculated lattice thermal conductivity of WSe_2 and WS_2 in comparison with experiment. Solid and dashed lines and lines with squares show the calculated thermal conductivity obtained when including phonon-phonon scattering, isotopic scattering and boundary scattering. The structural length scale L is set to $4\,\mu m$ for the in-plane and $0.15\,\mu m$ for the out-of-plane conductivity. Experimental data for WS_2 and WSe_2 were taken from Pisoni (2016) [70] and Chiritescu (2007) [12], respectively.

WSe_2: $\kappa_\perp^{expt} = 1.5$ W/K m versus $\kappa_\perp^{calc} = 3.1$ W/K m). Applying the same approach as in the case of the in-plane conductivity, we obtain a structural length scale of $L = 0.15\,\mu m$ for both materials [Figs. 7(a) and 7(b)], which yields an excellent match between calculation and experiment over the entire temperature range. Of course both experiment and calculation are subject to certain errors that are difficult to control either in the form of uncertainties concerning the interpretation of the experimental raw data [11] or intrinsic limitations of the theoretical description. In either case, the lower value compared to the in-plane case is consistent with the weaker binding along the c axis, which implies that it is relatively easy for the material to introduce (planar) defects that reduce the effective coherence length [13,14].

D. Extension to other chalcogenides

The analysis in the previous section has demonstrated both the level of accuracy of our calculations and the strong impact of impurities and other defects on many experimental measurements. These effects hinder a systematic investigation and understanding of the trends in thermal conductivity. In the following, we therefore analyze κ for Mo and W-based TMDs considering only phonon-phonon and isotopic scattering channels.

The calculations show a systematic variation of the lattice thermal conductivity that is primarily determined by the chalcogenide species and except for the sulfides is only weakly affected by the transition metal element (Fig. 8). The calculated in-plane conductivities at room temperature vary from 19 W/K m ($MoTe_2$, WTe_2) to 126 W/K m (WS_2), while the out-of-plane data range from 2.8 W/K m (WTe_2) to 5.1 W/K m (MoS_2). (Recall that these values represent the limit, in which only phonon-phonon and isotopic scattering
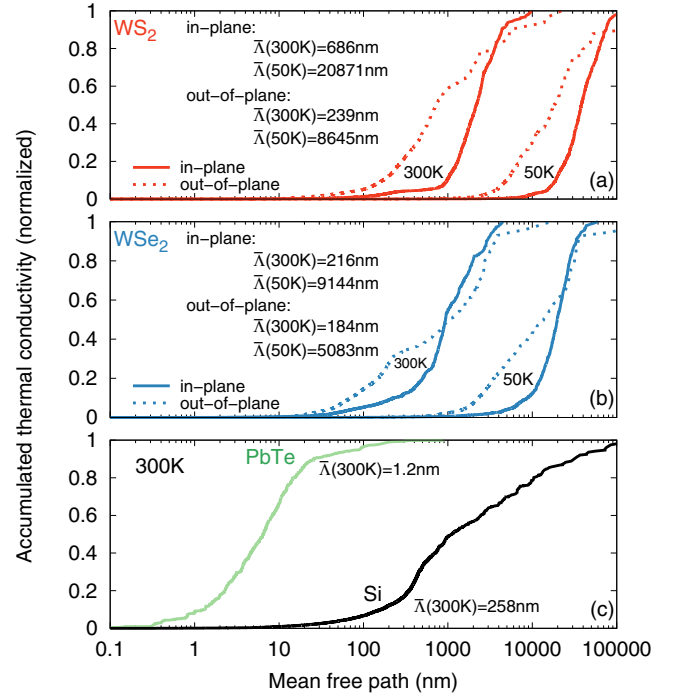

FIG. 7. Cumulative in-plane and out-of-plane lattice thermal conductivity $\bar{\kappa}$ according to Eq. (6) as a function of the mode specific MFP Λ_λ in (a) WS_2 and (b) WSe_2 at 50 and 300 K, and in (c) PbTe and Si at 300 K, calculated in the present work. The length scale $\bar{\Lambda}$ corresponds to the length scale related to the small grain conductivity [see Eq. (7)].

channels are available.) The thermal conductivity is thus highly anisotropic as the ratio between the in-plane and out-of-plane values ranges from 7 ($MoTe_2$) to 27 (WS_2) again following the sequence Te-Se-S.

The large anisotropy between in-plane and out-of-plane conductivity is largely due to the much smaller group velocities in the c direction [Fig. 4(b)]. They are the result of the interlayer (vdW) interactions being much weaker than the intralayer (mixed covalent/ionic) bonding. This anisotropy has also been shown to give rise to a phonon focusing effect and a much lower minimum thermal conductivity than in the case of isotropic materials [73].

The chemical trend for κ is analogous to the situation for the structural parameters, which was described in Sec. III A. The lattice parameters are the largest for the tellurides, which accordingly exhibit the smallest Brillouin zone (Fig. 4) and generally yield smaller group velocities resulting in lower thermal conductivities, see Eq. (5). One might thus be led to use the group velocities and thus the small-grain conductivity κ_{sg} as a (computationally much cheaper) predictor for the thermal conductivity. A closer inspection, however, reveals no correlation between κ_{sg} and the full thermal conductivity κ (Fig. 9), emphasizing the need to include phonon-phonon scattering at least at an approximate level, see, e.g., Ref. [74].

Compared to the other TMDs in the case of the sulfides the transition metal species has a much more pronounced effect on the in-plane lattice thermal conductivity (Fig. 8) with values of [83] and 126 W/K m for MoS_2 and WS_2,
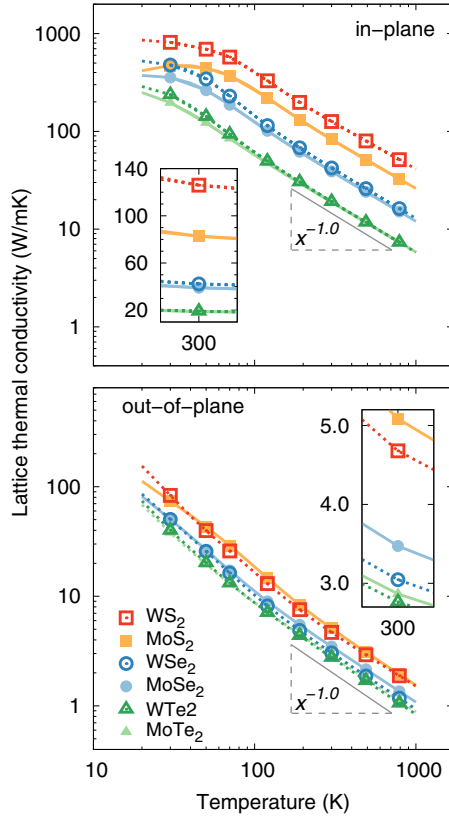
FIG. 8. Calculated in-plane and out-of-plane lattice thermal conductivities including phonon-phonon [$\tau_{\lambda,\mathrm{ph\text{-}ph}}$ in Eq. (1)] and isotopic scattering [$\tau_{\lambda,\mathrm{iso}}$ in Eq. (1)] for the TMDs considered in this study. The insets show close-ups of the values at 300 K on a linear scale and highlight the ordering of the materials.

FIG. 9. Comparison of the small-grain conductivity κ_{sg} according to Eq. (7) with the respective full lattice thermal conductivity κ according to Eq. (5) at 300 K.

respectively. This observation is supported by experimental data as measurements for bulk MoS_2 fall in the range between 85 and 110 W/K m [10] (also see Fig. 1), while a value of 124 W/K m was recently measured for WS_2 [70]. Since both the lattice parameters and the second-order IFCs of MoS_2 and WS_2 are similar, the differences in phonon dispersion and thus group velocities arise primarily from the mass difference between Mo and W (Fig. 4). The lighter mass of Mo leads to larger group velocities, which would suggest κ to be larger for MoS_2, yet the opposite is the case. The difference thus must be traceable to the lifetimes.

The largest contributions to the thermal conductivity in both materials come from modes with frequencies below 4.5 THz [Fig. 10(a)]. In the case of WS_2 the relative contributions in the interval between 2 and 5 THz are, however, notably larger than in MoS_2. In fact, the lifetimes, in particular between 3.5 and 4.5 THz are much larger in WS_2 [Fig. 10(c)] than in MoS_2 [Fig. 10(b)]. These longer lifetimes can be largely attributed to a much smaller number of allowed collision processes in this frequency range in the case of WS_2 [Fig. 10(d)], which can be traced to differences in the phonon band structures of WS_2 and MoS_2 (Fig. 4) as follows.

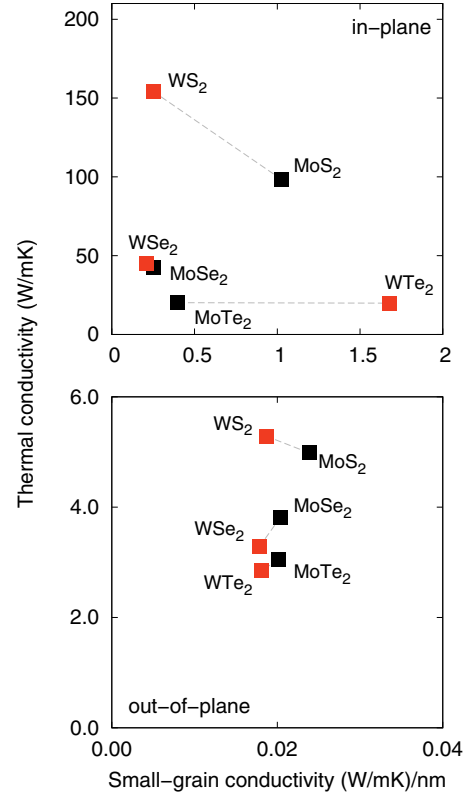The phonon band structure of WS_2 exhibits a band gap of 3.1 THz that separates the lower branches, which are dominated by W, from the higher branches, which have primarily S character (Fig. 4). The equivalent gap in MoS_2 amounts to only 1.5 THz. Any scattering process must obey energy and momentum conservation as evident from Eq. (4). The larger gap in the case WS_2 implies that fewer combinations of modes are allowed in the range between 3.5 and 4.5 THz, which leads to less scattering. To demonstrate this aspect quantitatively, we artifically modified the phonon band gap in WS_2 by rigidly shifting the upper branches by an amount Δ (scissors shift), while keeping all other contributions to Eq. (3) constant. Reducing the band gap from its original value of 3.1 THz causes a systematic reduction of the lifetimes in the energy range of interest and a monotonic decrease in the thermal conductivity (Fig. 11). Finally, if one reaches a value of 1.5 THz corresponding to MoS_2 one in fact observes a thermal conductivity, which is slightly smaller than in the case of MoS_2. This clearly demonstrates the causal relationship between the larger band gap and thermal conductivity in WS_2 compared to MoS_2. Note that if boundary scattering is included the relative importance of phonon-phonon scattering is reduced, which diminishes the difference between WS_2 and MoS_2 (Fig. 12).

Differences in lifetimes between Mo and W-based TMDs, albeit smaller than for the sulfides, are also present for the selenides and tellurides. In these materials the lifetime effect is, however, outweighed by the group velocity contribution (compare the insets in Fig. 8). The present analysis nonetheless demonstrates the importance of lifetime effects for understanding the thermal conductivity in these materials.
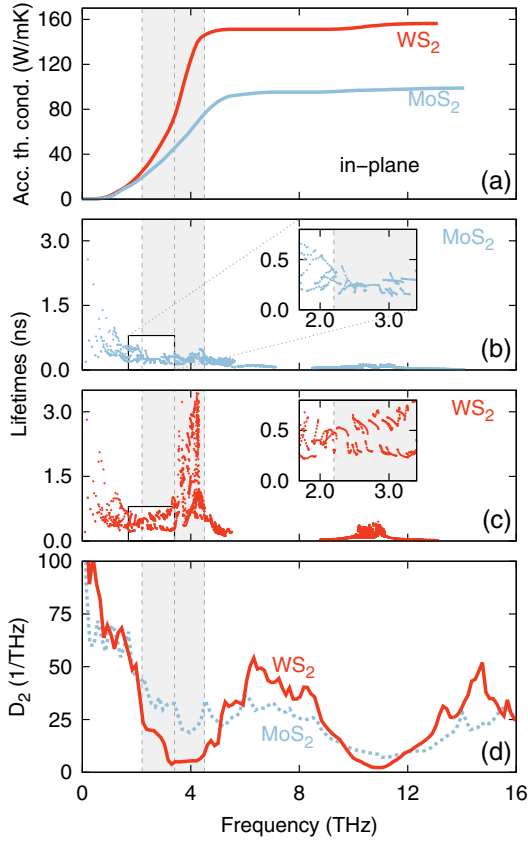
FIG. 10. (a) Cumulative in-plane thermal conductivity as a function of the frequency of the contributing modes in MoS$_2$ and WS$_2$ at 300 K. (b) and (c) Lifetimes in (b) in MoS$_2$ and (c) WS$_2$ at 300 K. (d) JDOS [see Eq. (4)] at the point $\boldsymbol{q} = (0.4, 0.4, 0)$ in reduced vector coordinates for WS$_2$ (solid line) and MoS$_2$ (dotted line). This point gives a representative JDOS for the whole hexagonal plane.

IV. CONCLUSIONS

In the present work, we investigated finite temperature properties as well as the lattice thermal conductivity in Mo and W-based TMDs employing a combination of density functional and Boltzmann transport theory. The calculations were carried out using the vdW-DF-CX functional, which was shown to yield excellent agreement with experimental lattice constants at room temperature with an average relative error below 0.2% (Table II).

The calculated in-plane conductivities at room temperature are in good agreement with experimental data for high-purity material, when only phonon-phonon and isotopic scattering are included (Figs. 1 and 6). Explaining the experimental data over the entire temperature, however, requires inclusion of at least one additional scattering mechanism (here boundary scattering) that limits the phonon MFP (Fig. 6). The latter effect is even more pronounced in the case of the out-of-plane conductivity, for which we obtain a structural length scale of $L = 0.15~\mu$m to be compared with $L = 4~\mu$m in the in-plane situation.

The sensitivity of the thermal conductivity to structural inhomogeneities can be explained in terms of the long MFP of the modes that contribute the most strongly to κ (Fig. 7). The
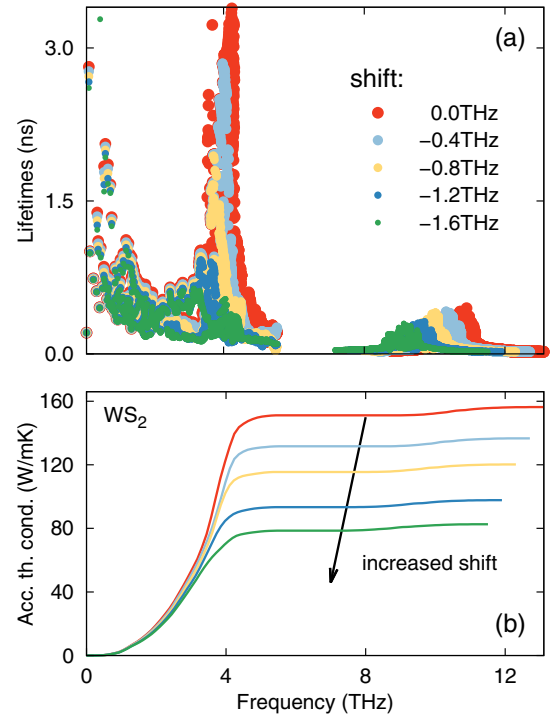

FIG. 11. The effect of the phonon band gap in WS$_2$ on (a) lifetimes and (b) thermal conductivity at 300 K.

MFP of these modes (including phonon-phonon and isotopic scattering) is at least 1 μm, which is comparable to silicon but much larger than, e.g., PbTe. This behavior is promising for thermoelectric applications, where lowering the lattice part of the thermal conductivity is a widely employed approach for increasing the thermodynamic efficiency. On the other hand, it can pose problems for electronic and optoelectronic applications, which require a large κ for rapid heat dissipation.

A comprehensive analysis shows that the thermal conductivity is primarily affected by the chalcogenide species and increases in the order Te–Se–S (Fig. 8). As expected from the elemental masses, MoTe$_2$ and MoSe$_2$ exhibit a higher conductivity than the respective W-based TMDs. For
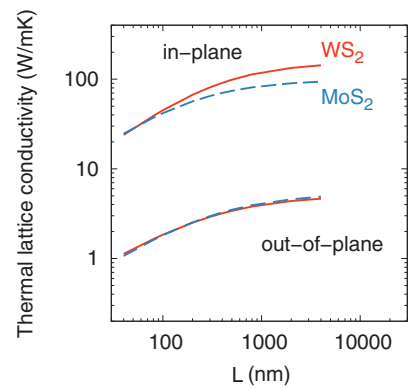

FIG. 12. Variation of in-plane and out-of-plane thermal conductivity of MoS$_2$ and WS$_2$ with boundary scattering dimension L [see Eq. (2)].

the sulfides the situation is inverted, which may be traced to the larger phononic band gap in the case of WS_2 (see Figs. 4 and 10). This observation suggests that in principle phonon-engineering can be achieved not only via the group velocity term in Eq. (5) and microstructuring but also via the phonon-phonon scattering.

The present work was in part motivated by considerable variations in experimental and computational data, based on which it was very difficult if not impossible to establish upper boundaries and chemical trends. Here, the present study contributes a systematic analysis that enables one to separate the contributions from scattering channels, which can be considered intrinsic (phonon-phonon, isotopic), and extrinsic ones (e.g., defects, boundaries, and interfaces), which are sensitive to synthesis conditions.

The structural length scale that was employed in the present work can originate from a variety of effects including, e.g., defects, interfaces, or sample boundaries (note that single crystalline TMD samples are usually very small). It is beyond the scope of the present work to provide detailed insight into the specific scattering mechanisms, as such an investigation is much more extensic in nature [14]. It is, however, noteworthy that for the TMDs, for which experimental data allowed a more careful comparison (WSe_2, WS_2), the structural length scale thus obtained amounted to 4 and 0.15 μm, respectively, for both materials.

In this sense, the present study provides a comprehensive set of lattice thermal conductivities for bulk TMDs that establishes bounds set by phonon-phonon scattering and structural length scales. It thereby forms the basis for future studies on these systems, which could focus, e.g., on vdW solids comprising different layers.

[1] A. K. Geim and I. V. Grigorieva, Nature (London) **499**, 419 (2013).

[2] Y. Gong, J. Lin, X. Wang, G. Shi, S. Lei, Z. Lin, X. Zou, G. Ye, R. Vajtai, B. I. Yakobson, H. Terrones, M. Terrones, B. K. Tay, J. Lou, S. T. Pantelides, Z. Liu, W. Zhou, and P. M. Ajayan, Nat. Mater. **13**, 1135 (2014).

[3] B. Radisavljevic, A. Radenovic, J. Brivio, V. Giacometti, and A. Kis, Nat. Nanotechnol. **6**, 147 (2011).

[4] Q. H. Wang, K. Kalantar-Zadeh, A. Kis, J. N. Coleman, and M. S. Strano, Nat. Nanotechnol. **7**, 699 (2012).

[5] X. Hong, J. Kim, S.-F. Shi, Y. Zhang, C. Jin, Y. Sun, S. Tongay, J. Wu, Y. Zhang, and F. Wang, Nat. Nanotechnol. **9**, 682 (2014).

[6] M. Massicotte, P. Schmidt, F. Vialla, K. G. Schädler, A. Reserbat-Plantey, K. Watanabe, T. Taniguchi, K. J. Tielrooij, and F. H. L. Koppens, Nat. Nanotechnol. **11**, 42 (2016).

[7] H. Guo, T. Yang, P. Tao, Y. Wang, and Z. Zhang, J. Appl. Phys. **113**, 013709 (2013).

[8] W. Han, APL Mater. **4**, 032401 (2016).

[9] A. Pisoni, J. Jacimovic, O. S. Barišić, A. Walter, B. Náfrádi, P. Bugnon, A. Magrez, H. Berger, Z. Revay, and L. Forró, J. Phys. Chem. C **119**, 3918 (2015).

[10] J. Liu, G.-M. Choi, and D. G. Cahill, J. Appl. Phys. **116**, 233107 (2014).

[11] R. B. Wilson and D. G. Cahill, Nat. Commun. **5**, 5075 (2014).

[12] C. Chiritescu, D. G. Cahill, N. Nguyen, D. Johnson, A. Bodapati, P. Keblinski, and P. Zschack, Science **315**, 351 (2007).

[13] N. T. Nguyen, P. A. Berseth, Q. Lin, C. Chiritescu, D. G. Cahill, A. Mavrokefalos, L. Shi, P. Zschack, M. D. Anderson, I. M. Anderson, and D. C. Johnson, Chem. Mater. **22**, 2750 (2010).

[14] P. Erhart, P. Hyldgaard, and D. O. Lindroth, Chem. Mater. **27**, 5511 (2015).

[15] L. Lindsay, D. A. Broido, and N. Mingo, Phys. Rev. B **82**, 115427 (2010).

[16] K. Esfarjani, G. Chen, and H. T. Stokes, Phys. Rev. B **84**, 085204 (2011).

[17] Z. Tian, J. Garg, K. Esfarjani, T. Shiga, J. Shiomi, and G. Chen, Phys. Rev. B **85**, 184303 (2012).

[18] W. Li, J. Carrete, N. A. Katcho, and N. Mingo, Comput. Phys. Commun. **185**, 1747 (2014).

[19] A. Togo, L. Chaput, and I. Tanaka, Phys. Rev. B **91**, 094306 (2015).

[20] W. Li, J. Carrete, and N. Mingo, Appl. Phys. Lett. **103**, 253103 (2013).

[21] B. Peng, H. Zhang, H. Shao, Y. Xu, X. Zhang, and H. Zhu, Annalen der Physik **528**, 504 (2016).

[22] X. Gu and R. Yang, Appl. Phys. Lett. **105**, 131903 (2014).

[23] X. Liu, G. Zhang, Q.-X. Pei, and Y.-W. Zhang, Appl. Phys. Lett. **103**, 133113 (2013).

[24] A. Kandemir, H. Yapicioglu, A. Kinaci, T. Çağin, and C. Sevik, Nanotechnology **27**, 055703 (2016).

[25] B. Peng, H. Zhang, H. Shao, Y. Xu, X. Zhang, and H. Zhu, RSC Adv. **6**, 5767 (2016).

[26] Y. Cai, J. Lan, G. Zhang, and Y.-W. Zhang, Phys. Rev. B **89**, 035438 (2014).

[27] V. Varshney, S. S. Patnaik, C. Muratore, A. K. Roy, A. A. Voevodin, and B. L. Farmer, Comput. Mater. Sci. **48**, 101 (2010).

[28] Y. Ding, M. Chen, and B. Xiao, RSC Adv. **6**, 7817 (2016).

[29] K. Berland and P. Hyldgaard, Phys. Rev. B **89**, 035412 (2014).

[30] J. P. Perdew, K. Burke, and M. Ernzerhof, Phys. Rev. Lett. **77**, 3865 (1996); **78**, 1396(E) (1997).

[31] J. P. Perdew, A. Ruzsinszky, G. I. Csonka, O. A. Vydrov, G. E. Scuseria, L. A. Constantin, X. Zhou, and K. Burke, Phys. Rev. Lett. **100**, 136406 (2008).

[32] A. N. Gandi and U. Schwingenschlögl, Chem. Mater. **26**, 6628 (2014).

[33] X. Zhang, D. Sun, Y. Li, G.-H. Lee, X. Cui, D. Chenet, Y. You, T. F. Heinz, and J. C. Hone, ACS Appl. Mater. Interfaces **7**, 25923 (2015).

[34] S. Sahoo, A. P. S. Gaur, M. Ahmadi, M. J.-F. Guinel, and R. S. Katiyar, J. Phys. Chem. C **117**, 9042 (2013).

[35] C. Muratore, V. Varshney, J. J. Gengler, J. J. Hu, J. E. Bultman, T. M. Smith, P. J. Shamberger, B. Qiu, X. Ruan, A. K. Roy, and A. A. Voevodin, Appl. Phys. Lett. **102**, 081604 (2013).

[36] R. Yan, J. R. Simpson, S. Bertolazzi, J. Brivio, M. Watson, X. Wu, A. Kis, T. Luo, A. R. H. Walker, and H. G. Xing, ACS Nano **8**, 986 (2014).

[37] D. C. Langreth, B. I. Lundqvist, S. D. Chakarova-Käck, V. R. Cooper, M. Dion, P. Hyldgaard, A. Kelkkanen, J. Kleis, L. Kong, S. Li, P. G. Moses, E. Murray, A. Puzder, H. Rydberg, E. Schröder, and T. Thonhauser, J. Phys. Condens. Matter **21**, 084203 (2009).

[38] K. Berland, C. Arter, V. R. Cooper, K. Lee, B. I. Lundqvist, E. Schröder, T. Thonhauser, and P. Hyldgaard, J. Chem. Phys. **140**, 18A539 (2014).

[39] S.-i. Tamura, Phys. Rev. B **27**, 858 (1983).

[40] J. R. de Laeter, J. K. Böhlke, P. D. Bièvre, H. Hidaka, H. S. Peiser, K. J. R. Rosman, and P. D. P. Taylor, Pure Appl. Chem. **75** (2003).

[41] J. M. Ziman, *Electrons and Phonons* (Clarendon Press, Oxford, 1960).

[42] G. Chen, C. L. Tien, X. Wu, and J. S. Smith, J. Heat Transfer **116**, 325 (1994).

[43] D. L. Nika, E. P. Pokatilov, A. S. Askerov, and A. A. Balandin, Phys. Rev. B **79**, 155413 (2009).

[44] A. Katre, A. Togo, I. Tanaka, and G. K. H. Madsen, J. Appl. Phys. **117**, 045102 (2015).

[45] G. P. Srivastava, *The physics of Phonons* (Hilger, Bristol, 1990).

[46] P. E. Blöchl, Phys. Rev. B **50**, 17953 (1994).

[47] G. Kresse and D. Joubert, Phys. Rev. B **59**, 1758 (1999).

[48] G. Kresse and J. Hafner, Phys. Rev. B **47**, 558 (1993).

[49] G. Kresse and J. Furthmüller, Comput. Mater. Sci. **6**, 15 (1996).

[50] H. Rydberg, M. Dion, N. Jacobson, E. Schröder, P. Hyldgaard, S. I. Simak, D. C. Langreth, and B. I. Lundqvist, Phys. Rev. Lett. **91**, 126402 (2003).

[51] M. Dion, H. Rydberg, E. Schröder, D. C. Langreth, and B. I. Lundqvist, Phys. Rev. Lett. **92**, 246401 (2004).

[52] T. Thonhauser, V. R. Cooper, S. Li, A. Puzder, P. Hyldgaard, and D. C. Langreth, Phys. Rev. B **76**, 125112 (2007).

[53] K. Berland, V. R. Cooper, K. Lee, E. Schröder, T. Thonhauser, P. Hyldgaard, and B. I. Lundqvist, Rep. Prog. Phys. **78**, 066501 (2015).

[54] J. Klimeš, D. R. Bowler, and A. Michaelides, Phys. Rev. B **83**, 195131 (2011).

[55] T. Björkman, J. Chem. Phys. **141**, 074708 (2014).

[56] A. Togo, F. Oba, and I. Tanaka, Phys. Rev. B **78**, 134106 (2008).

[57] A. Togo and I. Tanaka, Scr. Mater. **108**, 1 (2015).

[58] S. R. Bahn and K. W. Jacobsen, Comput. Sci. Eng. **4**, 56 (2002).

[59] A. Stukowski, Model. Simul. Mater. Sci. Eng. **18**, 015012 (2010).

[60] Blender Online Community, *Blender - a 3D Modeling and Rendering Package* (Blender Foundation, Amsterdam, 2015).

[61] W. Schutte, J. De Boer, and F. Jellinek, J. Solid State Chem. **70**, 207 (1987).

[62] V. L. Kalikhman, Izv. Akad. Nauk SSSR, Neorg. Mater **19**, 1060 (1983) [Inorg. Mater. **19**, 957 (1983)].

[63] K. D. Bronsema, J. L. De Boer, and F. Jellinek, Z. Anorg. Allg. Chem. **540**, 15 (1986).

[64] D. Puotinen and R. E. Newnham, Acta Crystallogr. **14**, 691 (1961).

[65] O. Knop and R. D. MacDonald, Can. J. Chem. **39**, 897 (1961).

[66] B. E. Brown, Acta Crystallogr. **20**, 268 (1966).

[67] E. Tasci, G. de la Flor, D. Orobengoa, C. Capillas, J. Perez-Mato, and M. Aroyo, EPJ Web of Conferences **22**, 00009 (2012).

[68] É. D. Murray, K. Lee, and D. C. Langreth, J. Chem. Theory Comput. **5**, 2754 (2009).

[69] A. Guḷãns, Ph.D. thesis, Aalto University School of Science, Espoo, Finland, 2012.

[70] A. Pisoni, J. Jacimovic, R. Gaál, B. Náfrádi, H. Berger, Z. Revay, and L. Forró, Scr. Mater. **114**, 48 (2016).

[71] G. Grimvall, in *Thermophysical Properties of Materials* (Elsevier Science B.V., Amsterdam, 1999), pp. 255–285.

[72] K. Biswas, J. He, I. D. Blum, C.-I. Wu, T. P. Hogan, D. N. Seidman, V. P. Dravid, and M. G. Kanatzidis, Nature (London) **489**, 414 (2012).

[73] Z. Chen and C. Dames, Appl. Phys. Lett. **107**, 193104 (2015).

[74] L. Bjerg, B. B. Iversen, and G. K. H. Madsen, Phys. Rev. B **89**, 024304 (2014).

Paper III

Chemical order and transport properties in an inorganic clathrate:
Optimal structures by computational design
Mattias Ångqvist, Daniel O. Lindroth and Paul Erhart

Optimization of the Thermoelectric Power Factor: Coupling between Chemical Order and Transport Properties

Mattias Ångqvist, Daniel O. Lindroth, and Paul Erhart*

Chalmers University of Technology, Department of Physics, S-412 96 Gothenburg, Sweden

S *Supporting Information*

ABSTRACT: Many thermoelectric materials are multicomponent systems that exhibit chemical ordering, which can affect both thermodynamic and transport properties. Here, we address the coupling between order and thermoelectric performance in the case of a prototypical inorganic clathrate ($Ba_8Ga_{16}Ge_{30}$) using a combination of density functional and Boltzmann transport theory as well as alloy cluster expansions and Monte Carlo simulations. The calculations describe the experimentally observed site occupancy factors and reproduce experimental data for the transport coefficients. By inverting the cluster expansion, we demonstrate that the power factor can be increased by more than 60% for certain chemical ordering patterns that involve reducing the number of the trivalent species on the 6c Wyckoff site. This enhancement is traced to specific features of the electronic band structure. The approach taken in the present work can be readily adapted to other materials and enables a very general form of band structure engineering. In this fashion, it can guide the computational design of compounds with optimal transport properties.
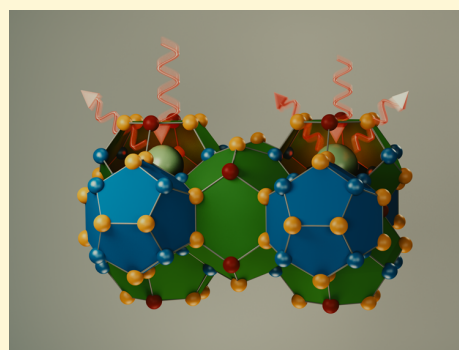
1. INTRODUCTION

Thermoelectric materials allow one to extract electrical currents from thermal gradients and vice versa.[1,2] They have found applications in various areas including, for example, power generation in remote locations, waste heat recuperation, and active cooling. The thermodynamic efficiency of the conversion process is quantified by the thermoelectric figure of merit zT. The latter depends on the Seebeck coefficient S, which measures the coupling strength between a thermal gradient and the generated potential difference, the electrical conductivity σ as well as the thermal conductivity κ according to

$$zT = TS^2\sigma/\kappa \qquad (1)$$

The $S^2\sigma$ term in the enumerator is known as the thermoelectric power factor.[3] While in efforts to increase zT it has received relatively less attention than the thermal conductivity κ,[4−7] several strategies for its enhancement have been proposed. The key challenge is that S and σ are anticorrelated insofar as the Seebeck coefficient usually decreases with carrier concentration, whereas the electrical conductivity increases.[3] To mitigate this situation, Hicks and Dresselhaus suggested to reduce dimensionality by means of quantum well structures,[8,9] while Mahan and Sofo showed conceptually that optimal conditions are obtained for a very narrow distribution of states with high group velocities.[10] These ideas were in fact later realized, for example., in the form of nanostructuring,[11−13] which also is useful for reducing the thermal conductivity, resonant levels,[3] and band structure engineering.[14−16] It is also worthwhile noting the extremely high power factors that were achieved at low temperatures in $FeSb_2$.[17,18] They have been attributed to

strong electronic correlation resulting from the interplay between localization and partially occupied states.

While most of the aforementioned approaches have been devised in the context of "simple" lattice structures, many thermoelectric materials including skutterudites, inorganic clathrates as well as other Zintl compounds, and half-Heusler alloys[2] are multicomponent systems that exhibit some form of chemical order. Here, using the prototypical inorganic clathrate[19,20] $Ba_8Ga_{16}Ge_{30}$ (Figure 1) as an example, we demonstrate that the power factor can be enhanced by more than 60% by optimizing the chemical order. To this end, we first resolve the coupling between the chemical order and
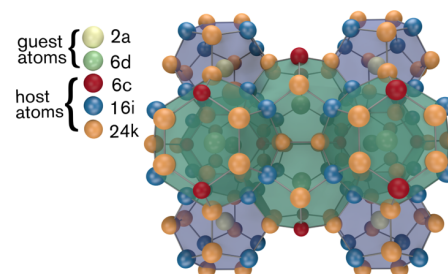

Figure 1. Crystal structure of type I clathrates. The guest species (Ba) occupies Wyckoff sites of type 2a and 6d, while the host species (Ga, Ge) occupy Wyckoff sites of type 6c, 16i, and 24k.

6877

transport properties, in particular the power factor, and we then employ an inverse design approach to identify the structure that maximizes the power factor. This approach yields a clear guideline for maximizing the power factor by structural optimization that we anticipate to be in principle transferable to other inorganic clathrates.

In this work, we employ a combination of density functional theory (DFT) and Boltzmann transport theory (BTT) calculations with alloy cluster expansions (CE) and Monte Carlo (MC) simulations (Figure 2). This approach is directly
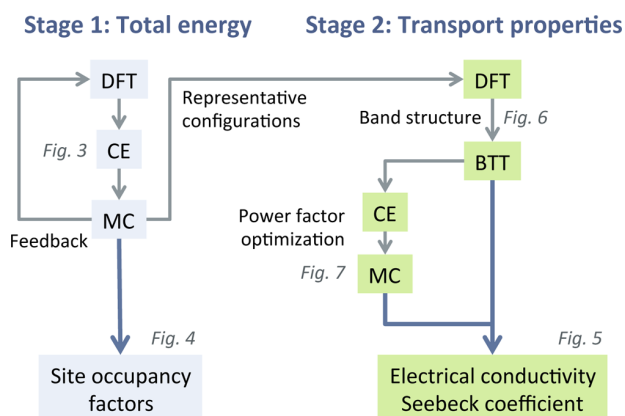

Figure 2. Schematic illustration of the relation between the methods employed in the present work. DFT: density functional theory; MC: Monte Carlo simulations; CE: alloy cluster expansion; BTT: Boltzmann transport theory.

applicable to other materials that exhibit a variable chemical order. It thereby opens up the avenue for a more controlled and systematic design of structures with optimal transport properties that is not limited to thermoelectric materials.

The remainder of the paper is organized as follows. In the following section, we construct a model for the chemical order based on electronic structure calculations and describe the variation of the site occupancy factors with temperature. Using configurations that are representative for the chemical order at different temperatures, we then analyze the transport properties and construct a model that maps ordering patterns to the power factor at 900 K. This model is subsequently employed to determine the chemical ordering that maximizes the power factor.

2. CALCULATION METHODS

2.1. Chemical Ordering. Density functional theory (DFT) calculations were carried out using the projector augmented wave method[21,22] as implemented in the Vienna ab initio simulation package.[23,24] Exchange–correlation effects were treated within the generalized gradient approximation as parametrized by Perdew, Burke, and Ernzerhof (PBE).[25] A set of 200 structures based on the 54-atom primitive unit cell was created by randomly assigning Ga and Ge atoms to different Wyckoff sites that comprise the host structure. A further set of 100 structures was created in the same fashion but subject to the condition that Ga–Ga first-nearest neighbors were disallowed. For each structure, both the ionic positions and the cell metric were fully relaxed until all atomic forces were less than 10 meV/Å and absolute stresses below 0.1 kbar. In these calculations, the Brillouin zone was sampled using a Γ-centered $3 \times 3 \times 3$ k-point mesh, the plane wave basis set was

expanded up to a cutoff energy of 243 eV, and the electronic self-consistency loop was terminated if the change in the total energy dropped below 10^{-5} eV between consecutive iterations.

Subsequently, the DFT energy landscape as well as quantities such as the band gap and the power factor were represented by cluster expansions (CE) of the form[26,27]

$$A = A_0 + \sum_{\alpha} m_\alpha J_\alpha \bar{\Pi}_\alpha(\mathbf{\Sigma}) \tag{2}$$

where A denotes the respective quantity of interest and the summation runs over all symmetry distinct clusters (singlets, pairs, triplets....). Each cluster has a multiplicity m_α and is associated with an effective cluster interaction (ECI) J_α. The cluster correlations $\bar{\Pi}_\alpha$ are computed as symmetrized averages of products over the pseudospin vector $\mathbf{\Sigma}$. The latter represents the lattice sites associated with the host matrix where $\Sigma = \pm 1$ for Ge and Ga, respectively.

The ECIs were obtained using the compressive sampling technique[28] adapted for CE construction.[29] The split Bregman algorithm[30,31] was employed to solve the optimization problem using parameters of $\mu = 0.001$ (which controls the sparseness of the solution) and $\lambda = 100$ (see refs 29, 31 for details concerning the role of these parameters). A range of different values for μ and λ were tested. Within reasonable bounds (see e.g., ref 29), these parameters were found to have inconsequential effects on the results presented here.

Each CE was carefully tested with respect to its predictive power using both cross-validation and ground-state searches. Due to the large number of different crystallographic sites, there is a large number of distinct clusters, 3 singlets, 13 pairs, and 26 triplets relative to a 5 Å cutoff radius, respectively. These numbers are noticeably larger than for simpler structures such as face-centered cubic (see Figure S7), whence the compressive sampling approach is particularly useful.[29]

The CEs were sampled using Monte Carlo (MC) simulations in the canonical ensemble. Supercells typically comprising $2 \times 2 \times 2$ unit cells were initialized at a temperature of 1200 K and then cooled to 0 K at a rate of 50 K per MC cycle (1 MC cycle is equivalent to N trial moves, where N is the number of sites in the simulation). At each new temperature, the system was first equilibrated for 50 000 MC cycles and then sampled for 100 000 MC cycles. The effect of supercell size on the SOFs is illustrated in Figure S8.

2.2. Electrical Transport Properties. For several configurations, the wave function of the fully relaxed structure was converged using a Γ-centered $4 \times 4 \times 4$ k-point mesh, followed by a non self-consistent computation of the eigenenergy spectra on a Γ-centered $20 \times 20 \times 20$ mesh. Using the interpolated eigenenergy spectra and electronic group velocities, the electrical conductivity and the Seebeck coefficient were computed using both an in-house and the BOLTZTRAP code[32] by evaluating the following expressions that are obtained within the relaxation time approximation to the Boltzmann transport equation[32−34]

$$\boldsymbol{\sigma} = \frac{2e^2}{\Omega} \sum_{ik} g_k \boldsymbol{v}_{ik} \otimes \boldsymbol{v}_{ik} \tau_{ik} \left(\frac{\partial f}{\partial \epsilon} \right)_{\epsilon = \epsilon_{ik}} \tag{3}$$

$$\mathbf{S} = \frac{\boldsymbol{\sigma}^{-1}}{eT} \sum_{ik} g_k \boldsymbol{v}_{ik} \otimes \boldsymbol{v}_{ik} \tau_{ik} [\epsilon_{ik} - \mu_e] \left(\frac{\partial f}{\partial \epsilon} \right)_{\epsilon = \epsilon_{ik}} \tag{4}$$

Here, Ω is the unit cell volume, g_k is the k-point weight, i refers to the band index, τ_{ik} is the mode and momentum dependent

lifetime, $v_{ik} = \hbar^{-1}\partial\varepsilon_{ik}/\partial k$ is the group velocity, f is the occupation function, and μ_e is the electron chemical potential. In the present work, the scattering time was assumed to be momentum- and state-independent as commonly done in calculations of this type.[32,34,35]

We note that semilocal exchange–correlation functionals such as the PBE functional used in the present work are known to systematically underestimate the band gap. This error can have a strong impact on the transport properties in weakly doped materials. In the present work we are, however, concerned with very high charge carrier concentrations as thermoelectrics are typically heavily (degenerately) doped semiconductors. As shown in Figure S3, under these conditions, the magnitude of the band gap (while assuming rigid bands) has a very small effect on the transport properties, whence the band gap underestimation is of minor concern for the present work.

As a further validation, we also carried out calculations for selected structures using the modified Becke–Johnson (mBJ) functional,[36,37] which yields much improved band gaps and band structures compared to PBE-DFT. The results (Figure S4) demonstrate that, apart from an increase in the band gap, the conduction and valence band structure near the band edges are, however, very similar between PBE and mBJ-DFT, especially in the region that determines the transport properties under degenerate doping conditions. For all calculations reported below, we therefore employ the PBE-DFT band structure.

3. CHEMICAL ORDERING

Inorganic clathrates of type I, such as $Ba_8Ga_{16}Ge_{30}$, belong to space group[38] $Pm\bar{3}n$ (international tables of crystallography number 223) and feature two smaller and six larger cages per unit cell.[19,20,39] $Ba_8Ga_{16}Ge_{30}$ has been investigated extensively both experimentally[40–45] and theoretically,[35,41,46–48] especially because of its promising thermoelectric properties. Here, the host structure is composed of Ga and Ge atoms, which occupy $6c$, $16i$, and $24k$ Wyckoff sites (Figure 1)[49] as revealed by experimental measurements of the site occupancy factors (SOFs).[39] Analysis of diffraction data yields for example Ga occupancies between 60 and 76% for the $6c$ site, which deviates considerably from the value of Ga/(Ga+Ge) = 16/(16 + 30) = 35% corresponding to the nominal stoichiometry of the compound.[43] The experimental observations have been condensed into a set of rules for the SOFs,[39] partially based on calculations,[46] which have shown that bonds between trivalent species, in the present case Ga atoms, are energetically unfavorable.

Here, in order to model the chemical order, we constructed an alloy CE based on a set of total energies for two hundred structures that were obtained from DFT calculations. The structures were generated by randomly assigning Ga and Ge atoms to lattice sites, while maintaining a ratio of 16:30. The number of structures can be compared to the total number of *possible* configurations, which, excluding symmetry, is close to 10^{12} for the 54-atom primitive unit cell. The CE nonetheless yields a very low cross-validation score of 0.9 meV/atom and excellent overall agreement with the reference data as illustrated by a juxtaposition of total energies from DFT and CE (Figure 3a). The final CE includes 3 singlet, 13 pair, and 24 triplet terms and is rather short ranged (Figure 3b).

It must be noted that the stoichiometry of experimentally synthesized clathrates often deviates from the ideal ratio of
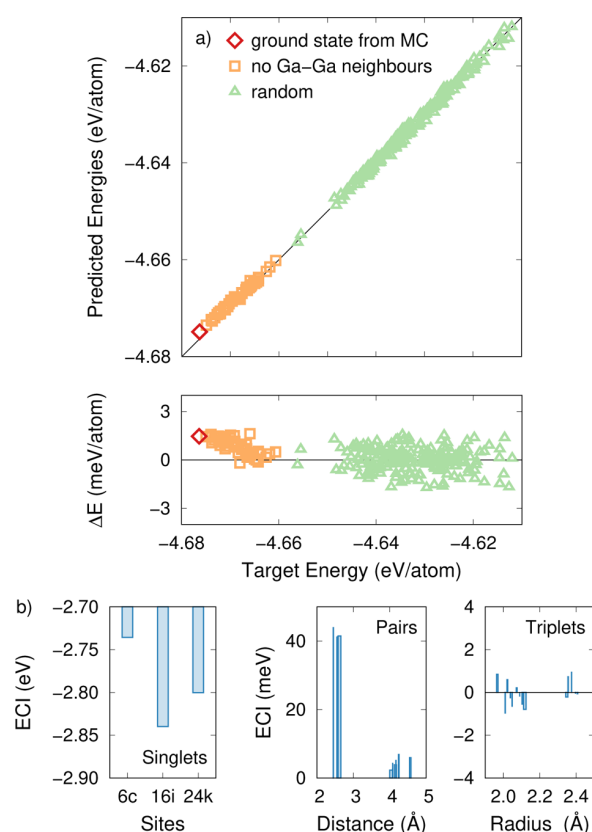

Figure 3. (a) Total energies obtained from cluster expansion (predicted) and electronic structure calculations (target). The data points shown by triangles were employed for constructing a cluster expansion for the total energy. Squares indicate data from structures without first-nearest-neighbor Ga–Ga bonds, whereas diamonds represent the structure obtained via a simulated annealing procedure from MC simulations. (b) Effective cluster interactions (ECI) of the total energy cluster expansion as a function of cluster size.

8:16:30 for Ba:Ga:Ge.[39,50] These effects can in fact be represented using the total energy CE used in the present work.[51] In the case of $Ba_8Ga_{16}Ge_{30}$, the variation of the SOFs with composition is, however, relatively weak and, as apparent from the comparison below, its description is not essential for achieving good agreement with experimental transport coefficients. The effect of composition on ordering will therefore be the topic of a separate publication.[51]

The temperature dependence of the Ga SOFs was extracted by sampling the total energy CE with Monte Carlo (MC) simulations (Figure 4a). From the data, it is apparent that already close to the melting temperature the SOFs deviate strongly from the stoichiometric ratio, which would imply a value of 16/(16 + 30) = 35%, indicating that the configurational entropy does not entirely override the energy associated with ordering even at these temperatures. As the temperature is reduced, the SOFs deviate more strongly from 35%, as the chemical distribution is increasingly dictated by energy. The variation in the SOFs is primarily the result of the energy penalty on trivalent (Ga) first-nearest-neighbor pairs that has been pointed out earlier[46] and is also apparent in the ECIs (Figure 3b). It is therefore logical that the number of Ga–Ga bonds monotonically decreases with decreasing temperature, as shown in Figure 4b.
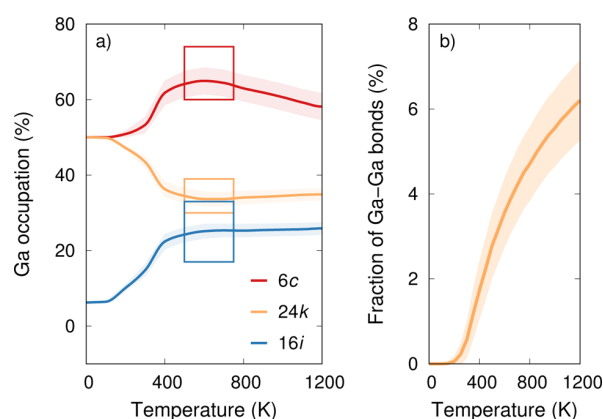
Figure 4. (a) Gallium site occupancy factors as a function of temperature from MC simulations using a 2 × 2 × 2 supercell. The shaded regions indicate one standard deviation. The boxes represent the range of the experimental SOF data and roughly indicate the temperature range, over which the chemical order appears to be frozen during sample preparation. (b) Fraction of first-nearest Ga−Ga bonds as a function of temperature. For comparison, the average fraction of Ga−Ga bonds for a completely random structure is $c_{Ga}^2 = 12.1\%$.

The experimentally observed SOF ranges are indicated by rectangles in Figure 4a. In experimental settings, chemical ordering will at some temperature become kinetically hindered as it requires atomic rearrangement, which is a temperature activated process. The precise conditions, at which freezing of the chemical order occurs, are unknown whence a temperature window between 550 and 720 K has been indicated in Figure 4a. Within the indicated temperature range, the agreement between experiment and model is actually excellent, supporting the present approach. The experimentally observed structure can thus be considered as a state of intermediate chemical order, which has been established during cooling as the result of slowing kinetics.

At low temperatures, the system eventually reaches a fully ordered state with rhombohedral symmetry (space group R3, ITC no. 146, see Table S1 for a compilation of the crystallographic parameters). As a further validation of the CE, the total energy of this ordered-state structure was calculated with DFT, which gave a value that deviates by less than 2 meV/atom from the CE value, demonstrating not only the accuracy but the predictive quality of the latter. This fact is even more remarkable given that the structures used for CE construction, which were obtained by random sampling, generally contain a much larger number of Ga−Ga bonds than the configurations observed during the MC simulations, even at temperatures close to the melting point.

The ordered configuration, from here on referred to as the ground-state structure, is characterized by the absence of Ga−Ga bonds in the first neighbor shell and a minimal number of Ga−Ga bonds in the second and third shell. In addition, it also minimizes the Ga SOF for Wyckoff site 16i.

4. ELECTRICAL TRANSPORT PROPERTIES

4.1. Comparison to Experiment. The electrical transport properties of $Ba_8Ga_{16}Ge_{30}$ have been previously investigated using first-principles calculations employing either structures that were constructed using intuition and energy minimization[34,35,46] or the virtual crystal approximation.[47] Here, we therefore systematically discriminate the effect of thermally

induced disorder on these properties. Specifically, we target n-type material, which is commonly associated with Ge-excess. In this section, we benchmark our structural model and establish two crucial parameters, namely, the charge carrier density and the effective electronic lifetime, by comparing our calculations with experimental transport data for n-type $Ba_8Ga_{16}Ge_{30}$.[42,44,52−55]

Five representative configurations per temperature were extracted from MC simulations at 600, 900, and 1200 K, respectively. The average and standard deviation of the total energy of these configurations correspond to the energy distribution at the respective temperatures sampled by MC simulations. In addition, we considered ten random structures and the ground-state structure. The electrical conductivity σ and the Seebeck coefficient S were computed within the framework of the Boltzmann transport equation,[32] as described in the above.

We first consider the Seebeck coefficient S (see eq 4), which varies with the charge carrier concentration n_e (Figure S1). For $n_e = 3 \times 10^{20}$ cm^{-3}, the calculations for the MC generated structures agree well with the experimental data (Figure 5a).[42,44,52,53] This charge carrier density in turn is in good agreement with previous estimates based on experimental data.[35,47] While the variation among the MC generated structures—regardless of the temperature they represent—is rather small, the results for the random structures—and to a lesser extent the ground-state structure—differ more notably both in magnitude and the temperature at which S is extremal.

We note that with regard to the Seebeck coefficient, the temperature dependence in the experiments appears slightly more linear than in the calculations, which leads to some deviation at low temperatures. This behavior could be related to the assumption of a mode- and momentum-independent relaxation time (compare section on Calculation Methods) and also affects the power factor (see below).

After having established the carrier density, which is kept constant at $n_e = 3 \times 10^{20}$ cm^{-3} from this point onward, it is possible to assess the electrical conductivity σ (see eq 3). The electronic lifetimes were assumed to be mode- and momentum-independent $\tau_{eff} \approx \tau_i(k)$ (see e.g., refs 32, 34, 35, 46, 47.).[56] Since an explicit calculation of $\tau_i(k)$ for $Ba_8Ga_{16}Ge_{30}$ is computationally currently impractical, we use an effective lifetime model with a simple temperature dependence $\tau_{eff} = \tau_{300}(300 \text{ K}/T)^{1/2}$ to represent acoustic phonon (piezoelectric) scattering,[57] which using $\tau_{300} = 15$ fs yields very good agreement with experimental data (Figure 5b). The thus obtained effective lifetime at 300 K is in fact very similar to values from previous studies (see e.g., refs 35, 47), which, however, neglected the variation of τ with temperature. It is apparent that the electrical conductivity σ again shows only a modest variation among the MC structures.

Given the Seebeck coefficient S and the electrical conductivity σ, we can now evaluate the power factor $S^2\sigma$, which most clearly highlights the effect of order on the electrical transport properties (Figure 5c). The MC-generated structures yield power factors of 15 to 18 μW/K^{2}cm at 900 K, which agrees well with experimental data.[42,44,52,53] The maximum power factor occurs at approximately 800−900 K, which matches the range observed in most experiments. By comparison, the ground-state (14 μW/K^{2}cm at 900 K) and random structures (9.6 ± 3.7 μW/K^{2}cm at 900 K) yield somewhat lower maxima. This suggests that the chemical ordering that is naturally established during synthesis
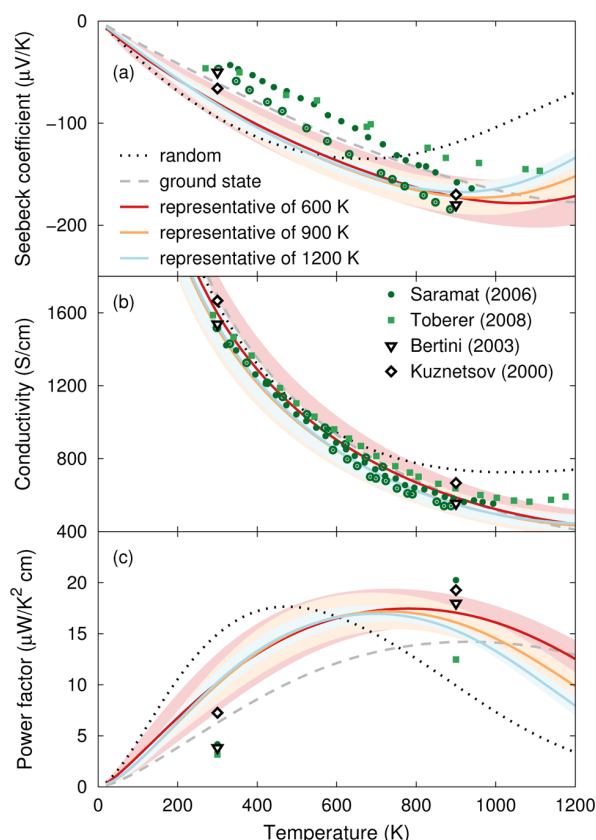
Figure 5. Electrical transport properties of n-type material at a carrier density of 3×10^{20} cm^{-3}. (a) Seebeck coefficient, (b) electrical conductivity, and (c) power factor as a function of temperature from calculations in comparison with experimental data from refs 42, 44, 52, 53. The degree of chemical order has a clear effect on the electrical transport properties as is evident by comparing the results from samples with a random distribution (dotted lines), the ground-state structure (dashed lines), and configurations representative of the chemical order at 600 K (solid red), 900 K (solid orange), and 1200 K (solid blue). In the case of the MC-generated structures, the corresponding shaded areas represent one standard deviation.

corresponds to relatively optimal conditions with regard to the power factor, an observation that will be explored in detail below. Furthermore, we find that maximizing the power factor by variation of the charge carrier density n_e (Figure S2) yields only a slight improvement of about 5%. This suggests that the experimental samples are already close to optimality with regard to n_e.

4.2. Order and Electronic Structure. The data presented above demonstrates that the power factor changes non-monotonically as a function of chemical order: The MC generated structures (intermediate level of order) exhibit on average higher power factors than both the ground state (highest degree of order) and the random structures (lowest degree of order). To resolve this behavior, it is instructive to explore the effect of chemical order on the electronic structure as both Seebeck coefficient S and electrical conductivity σ are primarily determined by the electronic eigenenergies and group velocities, see eqs 3 and 4.

The electronic band structures of configurations representing different degrees of chemical order (Figure 6) reveal that decreasing chemical order causes a systematic lowering of the band gap and a reduction in the dispersion of the lowermost conduction band level, which implies decreasing group velocities. With regard to the electrical conductivity σ, these two effects oppose each other as the $(\partial f/\partial \epsilon)_\epsilon = \epsilon_{ik}$ term in eq 3 increases with decreasing band gap, whereas smaller group velocities $v_i(k)$ cause a reduction of the other term in the integrand. (In the widely adopted effective mass approximation, this is equivalent to asserting an increase in the charge carrier concentration and a reduction of the mobility due to a higher effective mass (smaller curvature), see e.g., ref 2.) In the current case, the two terms appear to largely cancel each other as the net effect of order on σ is comparably small (Figure 5b).

To further resolve the coupling between order and the electrical transport properties, a closer inspection of the underlying band structures is instructive. To this end, we analyzed the mode-resolved contributions to the power factor, which are most sensitive to the group velocity. It is found that for the ground-state configuration, the largest contribution to S stems from states in the vicinity of the M point, which is the location of the CBM [fully ordered, Figure 6a, $S^2\sigma = 14.2$ μW/
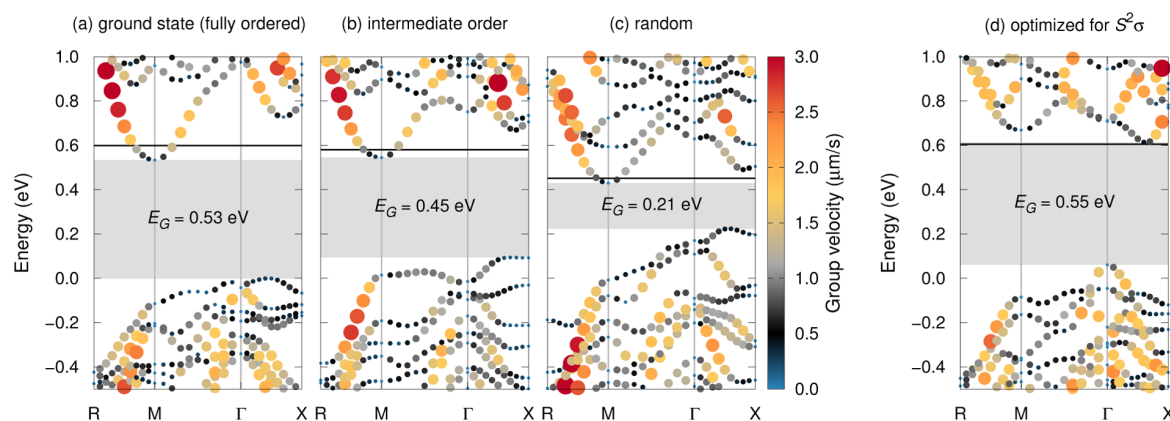
Figure 6. Effect of chemical order on the electronic structure. Band structures representing (a) the fully ordered ground state, (b) a configuration with intermediate order extracted from a MC simulation, (c) a random distribution, and (d) the structure optimized for maximum power factor at 900 K. The color scale and the size of the circles indicate the group velocity. The position of the Fermi level is shown by horizontal dashed lines. The energy scales of the different configurations were aligned using the Ba-1s states as described in ref 58, and the VBM of the ground state was arbitrarily set to zero.

K^2 cm at 900 K and $n_e = 3 \times 10^{20}$/cm^3]. While in the case of intermediate chemical order the relative contribution of these states is reduced, higher lying states for example along the Γ-X direction are shifted downward and thus closer to the Fermi level, providing a significantly larger contribution than in the case of the ground-state structure (Figure 6b, $S^2\sigma$ = 18.7 μW/ K^2 cm). The gain in the density of states in the vicinity of $\mu_e + k_BT$ outweighs the reduced dispersion (smaller group velocities) around the *M*-point and gives rise to a slight increase of the power factor relative to the ground-state configuration. If the degree of chemical order is further reduced, the effect of an increase in the density of states near the Fermi energy levels off (Figure 6c, $S^2\sigma$ = 12.2 μW/K^2 cm), whereas level localization (and thus reduction of the group velocities) proceeds, causing the power factor to drop again.

The origin of the reduction of band gap and level of dispersion with decreasing chemical order can be understood by recalling some general principles from defect physics. The ground-state structure represents a fully ordered structure, whereas disordering can be thought of as the insertion of antisite defects.[59] As these are intrinsic defects with small lattice distortions, the associated defect states are hybridized with band states (see e.g., refs 3, 60, 61); yet, the associated levels are to some extent localized. In Ba$_8$Ga$_{16}$Ge$_{30}$ (and similar systems), the formation energies for such antisites are obviously very small, whence defect concentrations are easily in the percent range and the collective effect on the band structure becomes significant.

4.3. Power Factor Optimized Structures. To substantiate the above argumentation, additional CEs were constructed for the band gap E_G as well as the power factor at 900 K ($n_e = 3 \times 10^{20}$/ cm^3), for which we obtained cross-validation scores of 0.05 eV and 1.5 μW/cmK^2, respectively. The CEs were subsequently sampled using MC simulations based on the CE for the total energy constructed earlier. Using the total energy as order parameter,[62] these simulations confirm for a large data sample that the band gap decreases monotonically with chemical disordering (Figure 7b), whereas the power factor exhibits a maximum at a finite amount of disorder, which quite closely coincides with the *average* level of order between 600 and 1200 K.

Based on the CE for the power factor, we are now in a position to search for chemical ordering patterns that maximize the power factor. To this end, simulated annealing runs were carried out on the landscape corresponding to $-S^2\sigma$ with an appropriate effective temperature scale. In this fashion, several structures were obtained with predicted power factors of approximately $S^2\sigma$ = 24 μW/K^2 cm, which were confirmed by a subsequent DFT-BTT calculation yielding about 27 μW/K^2 cm(Table S1).

The optimized structures are only about 8 meV/atom higher than the ground-state structure, and thus, they are energetically comparable to the structures obtained during the MC simulations described above. The most striking difference to both the ground state and MC-generated representative structures described above is the redistribution of Ga occupation from the 6*c* to the 16*i* site (ground-state structure: SOF(6*c*) = 50%; power factor optimized structure: SOF(6*c*) = 0%; see Table S1), whereas the average occupation of 24*k* sites is unaffected. In terms of the electronic structure, this redistribution gives rise to a significantly higher density of states in the vicinity of the conduction band edge along with a notably larger contribution from Ga atoms on 24*k* sites than in
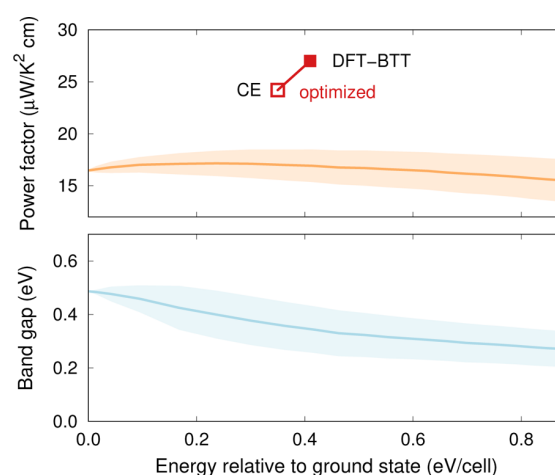

Figure 7. (a) Power factor and (b) band gap as a function of order (measured by the total energy) from MC-CE simulations. The maximum attainable power factor according to CE and DFT-BTT is indicated by red symbols. The shaded regions represent one standard deviation.

either the ground state or the MC-generated structures (Figure S6). Here, the vanishing Ga occupancy of 6*c* Wyckoff sites is a key feature as we generally find that larger power factors are correlated with a low 6*c* SOF.

It is now very instructive to analyze the features of the electronic structure that underlie the outstanding power factor of this configuration. A closer inspection of the band structure (Figure 6d) reveals that unlike the other structures (Figure 6a–c), all of which feature a CBM at the *M*-point, for the optimized structure the CBM is located along the Γ-X direction. This is the result of the lower energy of the corresponding states compared to the other structures. At the same time, the high degree of order ensures that the configuration has a large band gap (E_G = 0.55 eV) comparable in magnitude to the ground-state structure (E_G = 0.54 eV).

The integrand in the expression for the Seebeck coefficient eq 4 is maximal if the group velocity at approximately $\mu_e + 1.5k_BT$ is large, which requires dispersed (delocalized) states. At the same time, it is desirable to have many states in this energy window, which would be achieved by localization (nondispersed states). Since similar considerations apply to σ, optimizing $S^2\sigma$ thus tries to strike a balance between two diametrically opposed features. A three-dimensional visualization of the CBM (Figure S5) shows that the optimized configuration achieves a large power factor by featuring multiple CBM pockets with large group velocities in the relevant energy range.

Similar features in the band structure involving "complex carrier pocket shapes"[63] were found to enhance thermoelectric performance also in other materials (see e.g., refs 14, 16, 63−65) The electronic structures that were observed in these cases can be thought of as realizations of the conditions formulated by Mahan and Sofo[10] according to which one seeks a narrow distribution of states near the Fermi level with high group velocities. While enhanced thermoelectric performance due the existence of multiple band extrema has been shown to be intrinsic to some materials,[64,65] it has been demonstrated that the relevant features can also be engineered by, for example, nanoinclusions,[14] careful selection of the components,[16] or volumetric band alignment via alloying.[63] The

present results show that this level of band structure engineering can even be accomplished by controlling the chemical order in a material. Furthermore, the present approach demonstrates that the identification of materials and compositions can be achieved using models that do not explicitly describe the electronic structure as long as they are properly trained with respect to higher-level calculations.

5. CONCLUSIONS

In the present work, we used density functional theory calculations in conjunction with Monte Carlo simulations, alloy cluster expansions, and Boltzmann transport theory to investigate the coupling between chemical order and the electrical transport properties in the prototypical inorganic clathrate $Ba_8Ga_{16}Ge_{30}$.

The temperature dependence of the SOFs obtained from MC−CE simulations shows a strong asymmetry between different Wyckoff sites. The predicted SOFs in the temperature range between 550 and 720 K are in good agreement with experimental data. This observation provides a very sensible estimate for the temperature range, in which the chemical order is kinetically frozen in as the material cools down after synthesis. A simulated annealing procedure furthermore lead to a ground-state structure that is primarily characterized by the absence of first-nearest neighbor Ga−Ga bonds.

Subsequently, the electrical conductivity σ and Seebeck coefficient S were computed for n-type conditions using a DFT−BTT approach for the ground-state structure, a set of configurations representing the chemical order at different temperatures, as well as several random structures. The magnitude and temperature dependence of the Seebeck coefficient calculated for the representative structures at an electron concentration of $n_e = 3 \times 10^{20}/cm^3$ was shown to match experimental data. Using a minimal model for the electronic lifetime based on scattering by acoustic phonons, we then achieved close agreement between experiment and calculations for both the electrical conductivity σ and power factor $S^2\sigma$. Thus-equipped, the relation between chemical order and the power factor was scrutinized. It was shown that the power factor exhibits a nonmonotonic dependence on order (and temperature) with its average value exhibiting a maximum roughly in the range found in previous experiments.

Using a direct combination of DFT−BTT and MC−CE, we then identified structural motifs that maximize the power factor. Specifically, it was demonstrated that this can be achieved by minimizing the Ga SOF for $6c$ Wyckoff sites, which gives yields calculated power factors up to 27 $\mu W/K^2cm$, corresponding to an improvement of about 60% compared to the "normal" order. The enhancement can be traced to an increase in the density of states near the conduction band edge with only a small reduction in the group velocities.

It is beyond the scope of this work to provide a recipe for synthesizing the exact structure in question, but the relatively small energy cost associated with the depopulation of the $6c$ site suggests that it is thermodynamically within reach. It is possible, for example, that alloyed clathrates[66−69] provide means to control order more consciously, albeit at the cost of a much more complex parameter range. Other materials that exhibit partial ordering/disordering such as the cobaltates and skutterudites, Zintl compounds, as well as complex alloys[2,16,70−75] can be anticipated to exhibit similar features and thus also warrant further study.

Here, modeling and simulation could provide useful guidance for navigating the complex and multidimensional composition space. In this context, the approach utilized in the present work, which combines electronic structure calculations of transport properties with machine learning protocols, could prove to be highly useful for band structure engineering. In this fashion, it can guide the computational design of compounds with optimal transport properties.

■ ASSOCIATED CONTENT

ⓢ Supporting Information

The Supporting Information is available free of charge on the ACS Publications website at DOI: 10.1021/acs.chemmater.6b02117.

Additional crystallographic information for the ground-state structure (CIF)

Additional crystallographic information for the power-factor-optimized structure (CIF)

Table with additional information for the two structures; supplementary figures documenting the temperature, doping level, and carrier density dependence of Seebeck coefficient and power factor, the sensitiviy of the band structure to the exchange−correlation functional, the structure and composition of the band egdes, the number of ECIs as a function of cluster size, as well as the convergence of the SOFs with supercell size (PDF)

■ AUTHOR INFORMATION

Corresponding Author

*E-mail: erhart@chalmers.se.

Notes

The authors declare no competing financial interest.

■ REFERENCES

(1) *Thermoelectrics Handbook: Macro to Nano*; Rowe, D., Ed.; CRC Press: Boca Raton, FL, 2005.

(2) Snyder, G. J.; Toberer, E. S. Complex thermoelectric materials. *Nat. Mater.* **2008**, 7, 105−114.

(3) Heremans, J. P.; Wiendlocha, B.; Chamoire, A. M. Resonant levels in bulk thermoelectric semiconductors. *Energy Environ. Sci.* **2012**, 5, 5510−5530.

(4) Feldman, J. L.; Singh, D. J.; Kendziora, C.; Mandrus, D.; Sales, B. C. Lattice dynamics of filled skutterudites: La(Fe,Co)_4Sb_12. *Phys. Rev. B: Condens. Matter Mater. Phys.* **2003**, 68, 094301.

(5) Garg, J.; Bonini, N.; Kozinsky, B.; Marzari, N. Role of Disorder and Anharmonicity in the Thermal Conductivity of Silicon-Germanium Alloys: A First-Principles Study. *Phys. Rev. Lett.* **2011**, 106, 045901.

(6) Biswas, K.; He, J.; Zhang, Q.; Wang, G.; Uher, C.; Dravid, V. P.; Kanatzidis, M. G. Strained endotaxial nanostructures with high thermoelectric figure of merit. *Nat. Chem.* **2011**, 3, 160−166.

(7) Biswas, K.; He, J.; Blum, I. D.; Wu, C.-I.; Hogan, T. P.; Seidman, D. N.; Dravid, V. P.; Kanatzidis, M. G. High-performance bulk thermoelectrics with all-scale hierarchical architectures. *Nature* **2012**, 489, 414−418.

(8) Hicks, L. D.; Dresselhaus, M. S. Effect of quantum-well structures on the thermoelectric figure of merit. *Phys. Rev. B: Condens. Matter Mater. Phys.* **1993**, *47*, 12727−12731.

(9) Heremans, J. P.; Dresselhaus, M. S.; Bell, L. E.; Morelli, D. T. When thermoelectrics reached the nanoscale. *Nat. Nanotechnol.* **2013**, *8*, 471−473.

(10) Mahan, G. D.; Sofo, J. O. The best thermoelectric. *Proc. Natl. Acad. Sci. U. S. A.* **1996**, *93*, 7436−7439.

(11) Heremans, J. P.; Thrush, C. M.; Morelli, D. T. Thermopower enhancement in PbTe with Pb precipitates. *J. Appl. Phys.* **2005**, *98*, 063703−063703−6.

(12) Heremans, J. P.; Jovovic, V.; Toberer, E. S.; Saramat, A.; Kurosaki, K.; Charoenphakdee, A.; Yamanaka, S.; Snyder, G. J. Enhancement of Thermoelectric Efficiency in PbTe by Distortion of the Electronic Density of States. *Science* **2008**, *321*, 554−557.

(13) Faleev, S. V.; Léonard, F. Theory of enhancement of thermoelectric properties of materials with nanoinclusions. *Phys. Rev. B: Condens. Matter Mater. Phys.* **2008**, *77*, 214304.

(14) Zhao, L.-D.; Dravid, V. P.; Kanatzidis, M. G. The panoscopic approach to high performance thermoelectrics. *Energy Environ. Sci.* **2014**, *7*, 251−268.

(15) Zhao, L.-D.; Tan, G.; Hao, S.; He, J.; Pei, Y.; Chi, H.; Wang, H.; Gong, S.; Xu, H.; David, V. P.; Uher, C.; Snyder, G. J.; Wolverton, C.; Kanatzidis, M. G. Ultrahigh power factor and thermoelectric performance in hole-doped single-crystal SnSe. *Science* **2016**, *351*, 141−144.

(16) Bilc, D. I.; Hautier, G.; Waroquiers, D.; Rignanese, G.-M.; Ghosez, P. Low-Dimensional Transport and Large Thermoelectric Power Factors in Bulk Semiconductors by Band Engineering of Highly Directional Electronic States. *Phys. Rev. Lett.* **2015**, *114*, 136601.

(17) Bentien, A.; Madsen, G. K. H.; Johnsen, S.; Iversen, B. B. Experimental and theoretical investigations of strongly correlated $FeSb_{2-x}Sn_x$. *Phys. Rev. B: Condens. Matter Mater. Phys.* **2006**, *74*, 205105.

(18) Bentien, A.; Johnsen, S.; Madsen, G. K. H.; Iversen, B. B.; Steglich, F. Colossal Seebeck coefficient in strongly correlated semiconductor $FeSb_2$. *Europhysics Letters (EPL)* **2007**, *80*, 17008.

(19) Rogl, P. *Thermoelectrics Handbook*; CRC Press: Boca Raton, FL, 2005; Chapter 32, pp 1−24.

(20) Shevelkov, A. V.; Kovnir, K. In *Zintl Phases*; Fässler, T. F., Ed.; Structure and Bonding 139; Springer: Berlin Heidelberg, 2011; pp 97−142.

(21) Blöchl, P. E. Projector augmented-wave method. *Phys. Rev. B: Condens. Matter Mater. Phys.* **1994**, *50*, 17953−17979.

(22) Kresse, G.; Joubert, D. From ultrasoft pseudopotentials to the projector augmented-wave method. *Phys. Rev. B: Condens. Matter Mater. Phys.* **1999**, *59*, 1758−1775.

(23) Kresse, G.; Hafner, J. Ab initio molecular dynamics for liquid metals. *Phys. Rev. B: Condens. Matter Mater. Phys.* **1993**, *47*, 558−561.

(24) Kresse, G.; Furthmüller, J. Efficiency of ab-initio total energy calculations for metals and semiconductors using a plane-wave basis set. *Comput. Mater. Sci.* **1996**, *6*, 15−50.

(25) Perdew, J. P.; Burke, K.; Ernzerhof, M. Generalized Gradient Approximation Made Simple. *Phys. Rev. Lett.* **1996**, *77*, 3865−3868; Erratum: Generalized Gradient Approximation Made Simple. *Phys. Rev. Lett.* **1997**, *78*, 1396.

(26) Sanchez, J. M.; Ducastelle, F.; Gratias, D. Generalized cluster description of multicomponent systems. *Phys. A* **1984**, *128*, 334.

(27) Sanchez, J. M. Cluster expansion and the configurational theory of alloys. *Phys. Rev. B: Condens. Matter Mater. Phys.* **2010**, *81*, 224202.

(28) Candes, E.; Wakin, M. An Introduction To Compressive Sampling. *Signal Processing Magazine, IEEE* **2008**, *25*, 21−30.

(29) Nelson, L. J.; Hart, G. L. W.; Zhou, F.; Ozolins, V. Compressive sensing as a new paradigm for model building. *Phys. Rev. B: Condens. Matter Mater. Phys.* **2013**, *87*, 035125.

(30) Yin, W.; Osher, S.; Goldfarb, D.; Darbon, J. Bregman Iterative Algorithms for l_1-Minimization with Applications to Compressed Sensing. *SIAM Journal on Imaging Sciences* **2008**, *1*, 143−168.

(31) Goldstein, T.; Osher, S. The Split Bregman Method for L1-Regularized Problems. *SIAM Journal on Imaging Sciences* **2009**, *2*, 323−343.

(32) Madsen, G. K.; Singh, D. J. BoltzTraP. A code for calculating band-structure dependent quantities. *Comput. Phys. Commun.* **2006**, *175*, 67−71.

(33) Ziman, J. M. *Electrons and Phonons*; Clarendon Press: Oxford, 1960.

(34) Blake, N. P.; Møllnitz, L.; Kresse, G.; Metiu, H. Why clathrates are good thermoelectrics: A theoretical study of $Sr_8Ga_{16}Ge_{30}$. *J. Chem. Phys.* **1999**, *111*, 3133.

(35) Blake, N. P.; Latturner, S.; Bryan, J. D.; Stucky, G. D.; Metiu, H. Band structures and thermoelectric properties of the clathrates $Ba_8Ga_{16}Ge_{30}$, $Sr_8Ga_{16}Ge_{30}$, $Ba_8Ga_{16}Si_{30}$, and $Ba_8In_{16}Sn_{30}$. *J. Chem. Phys.* **2001**, *115*, 8060.

(36) Becke, A. D.; Johnson, E. R. A simple effective potential for exchange. *J. Chem. Phys.* **2006**, *124*, 221101.

(37) Tran, F.; Blaha, P. Accurate Band Gaps of Semiconductors and Insulators with a Semilocal Exchange-Correlation Potential. *Phys. Rev. Lett.* **2009**, *102*, 226401.

(38) Symmetry analyses were carried out using the spglib library written by Togo, A. See the following: http://atztogo.github.io/spglib.

(39) Christensen, M.; Johnsen, S.; Iversen, B. B. Thermoelectric clathrates of type I. *Dalton Trans.* **2010**, *39*, 978−992.

(40) Sales, B. C.; Chakoumakos, B. C.; Jin, R.; Thompson, J. R.; Mandrus, D. Structural, magnetic, thermal, and transport properties of $X_8Ga_{16}Ge_{30}$ (X = Eu, Sr, Ba) single crystals. *Phys. Rev. B: Condens. Matter Mater. Phys.* **2001**, *63*, 245113.

(41) Bryan, J. D.; Blake, N. P.; Metiu, H.; Stucky, G. D.; Iversen, B. B.; Poulsen, R. D.; Bentien, A. Nonstoichiometry and chemical purity effects in thermoelectric $Ba_8Ga_{16}Ge_{30}$ clathrate. *J. Appl. Phys.* **2002**, *92*, 7281−7290.

(42) Saramat, A.; Svensson, G.; Palmqvist, A. E. C.; Stiewe, C.; Mueller, E.; Platzek, D.; Williams, S. G. K.; Rowe, D. M.; Bryan, J. D.; Stucky, G. D. Large thermoelectric figure of merit at high temperature in Czochralski-grown clathrate $Ba_8Ga_{16}Ge_{30}$. *J. Appl. Phys.* **2006**, *99*, 023708.

(43) Christensen, M.; Lock, N.; Overgaard, J.; Iversen, B. B. Crystal Structures of Thermoelectric n- and p-type $Ba_8Ga_{16}Ge_{30}$ Studied by Single Crystal, Multitemperature, Neutron Diffraction, Conventional X-ray Diffraction and Resonant Synchrotron X-ray Diffraction. *J. Am. Chem. Soc.* **2006**, *128*, 15657−15665.

(44) Toberer, E. S.; Christensen, M.; Iversen, B. B.; Snyder, G. J. High temperature thermoelectric efficiency in $Ba_8Ga_{16}Ge_{30}$. *Phys. Rev. B: Condens. Matter Mater. Phys.* **2008**, *77*, 075203.

(45) Cederkrantz, D.; Saramat, A.; Snyder, G. J.; Palmqvist, A. E. C. Thermal stability and thermoelectric properties of p-type $Ba_8Ga_{16}Ge_{30}$ clathrates. *J. Appl. Phys.* **2009**, *106*, 074509.

(46) Blake, N. P.; Bryan, D.; Latturner, S.; Møllnitz, L.; Stucky, G. D.; Metiu, H. Structure and stability of the clathrates $Ba_8Ga_{16}Ge_{30}$, $Sr_8Ga_{16}Ge_{30}$, $Ba_8Ga_{16}Si_{30}$, and $Ba_8In_{16}Sn_{30}$. *J. Chem. Phys.* **2001**, *114*, 10063−10074.

(47) Madsen, G. K. H.; Schwarz, K.; Blaha, P.; Singh, D. J. Electronic structure and transport in type-I and type-VIII clathrates containing strontium, barium, and europium. *Phys. Rev. B: Condens. Matter Mater. Phys.* **2003**, *68*, 125212.

(48) Madsen, G. K. H.; Santi, G. Anharmonic lattice dynamics in type-I clathrates from first-principles calculations. *Phys. Rev. B: Condens. Matter Mater. Phys.* **2005**, *72*, 220301.

(49) Eisenmann, B.; Schäfer, H.; Zagler, R. Die Verbindungen $A_8^{II}B_{16}^{III}B_{30}^{IV}$ (A^{II} = Sr, Ba; B^{III} = Al, Ga; B^{IV} = Si, Ge, Sn) und ihre Käfigstrukturen. *J. Less-Common Met.* **1986**, *118*, 43−55.

(50) Christensen, M.; Iversen, B. B. Host Structure Engineering in Thermoelectric Clathrates. *Chem. Mater.* **2007**, *19*, 4896.

(51) Ångqvist, M.; Erhart, P., in preparation.

(52) Bertini, L.; et al. Thermoelectric performance of large single crystal clathrate $Ba_8Ga_{16}Ge_{30}$. *International Conference on Thermoelectrics Proceedings* **2003**, 127.

(53) Kuznetsov, V. L.; Kuznetsova, L. A.; Kaliazin, A. E.; Rowe, D. M. Preparation and thermoelectric properties of $A_8^{II}B_{16}^{III}B_{30}^{IV}$ clathrate compounds. *J. Appl. Phys.* **2000**, *87*, 7871−7875.

(54) Okamoto, N. L.; Kishida, K.; Tanaka, K.; Inui, H. Crystal structure and thermoelectric properties of type-I clathrate compounds in the Ba-Ga-Ge system. *J. Appl. Phys.* **2006**, *100*, 073504.

(55) Okamoto, N. L.; Kishida, K.; Tanaka, K.; Inui, H. Effect of In additions on the thermoelectric properties of the type-I clathrate compound $Ba_8Ga_{16}Ge_{30}$. *J. Appl. Phys.* **2007**, *101*, 113525.

(56) Note that in general, one also requires the electronic lifetimes for computing the Seebeck coefficient. This dependence, however, vanishes if the lifetime is assumed to be momentum- and mode-independent.

(57) Yu, P. Y.; Cardona, M. *Fundamentals of Semiconductors*, 4th ed.; Springer: Berlin, 2001; Chapter 5.2.

(58) Pfeifer, V.; Erhart, P.; Li, S.; Rachut, K.; Morasch, J.; Brötz, J.; Reckers, P.; Mayer, T.; Rühle, S.; Zaban, A.; Mora Seró, I.; Bisquert, J.; Jaegermann, W.; Klein, A. Energy Band Alignment between Anatase and Rutile TiO_2. *J. Phys. Chem. Lett.* **2013**, *4*, 4182−4187.

(59) Note that while other defects, most notably vacancies, are present in real materials, their numbers are relatively smaller than the number of such antisite defects. For simplicity, they were therefore not considered in the present work.

(60) Lany, S.; Zunger, A. Assessment of correction methods for the band-gap problem and for finite-size effects in supercell defect calculations: Case studies for ZnO and GaAs. *Phys. Rev. B: Condens. Matter Mater. Phys.* **2008**, *78*, 235104.

(61) Erhart, P.; Åberg, D.; Lordi, V. Extrinsic point defects in aluminum antimonide. *Phys. Rev. B: Condens. Matter Mater. Phys.* **2010**, *81*, 195216.

(62) Order parameters are commonly used to describe phase transitions, which is, however, not the objective here. Rather, we use the total energy merely as a convenient (single scalar) parameter to discriminate different structures by order.

(63) Bhattacharya, S.; Madsen, G. K. H. High-throughput exploration of alloying as design strategy for thermoelectrics. *Phys. Rev. B: Condens. Matter Mater. Phys.* **2015**, *92*, 085205.

(64) Usui, H.; Shibata, S.; Kuroki, K. Origin of coexisting large Seebeck coefficient and metallic conductivity in the electron doped $SrTiO_3$ and $KTaO_3$. *Phys. Rev. B: Condens. Matter Mater. Phys.* **2010**, *81*, 205121.

(65) Hao, S.; Shi, F.; Dravid, V. P.; Kanatzidis, M. G.; Wolverton, C. Computational Prediction of High Thermoelectric Performance in Hole Doped Layered GeSe. *Chem. Mater.* **2016**, *28*, 3218−3226.

(66) Christensen, M.; Johnsen, S.; Söndergaard, M.; Overgaard, J.; Birkedal, H.; Iversen, B. B. Fast Preparation and Characterization of Quarternary Thermoelectric Clathrates. *Chem. Mater.* **2009**, *21*, 122−127.

(67) Martin, J.; Erickson, S.; Nolas, G. S.; Alboni, P.; Tritt, T. M.; Yang, J. Structural and transport properties of $Ba_8Ga_{16}Si_xGe_{30−x}$ clathrates. *J. Appl. Phys.* **2006**, *99*, 044903.

(68) Martin, J.; Nolas, G. S.; Wang, H.; Yang, J. Thermoelectric properties of silicon-germanium type I clathrates. *J. Appl. Phys.* **2007**, *102*, 103719.

(69) Deng, S.; Tang, X.; Li, P.; Zhang, Q. High temperature thermoelectric transport properties of p-type $Ba_8Ga_{16}Al_xGe_{30−x}$ type-I clathrates with high performance. *J. Appl. Phys.* **2008**, *103*, 073503.

(70) Voneshen, D. J.; et al. Suppression of thermal conductivity by rattling modes in thermoelectric sodium cobaltate. *Nat. Mater.* **2013**, *12*, 1028.

(71) Barabash, S. V.; Ozolins, V.; Wolverton, C. First-Principles Theory of Competing Order Types, Phase Separation, and Phonon Spectra in Thermoelectric $AgPb_mSbTe_{m+2}$ Alloys. *Phys. Rev. Lett.* **2008**, *101*, 155704.

(72) Barabash, S. V.; Ozolins, V.; Wolverton, C. First-principles theory of the coherency strain, defect energetics, and solvus boundaries in the $PbTe-AgSbTe_2$ system. *Phys. Rev. B: Condens. Matter Mater. Phys.* **2008**, *78*, 214109.

(73) Schröder, T.; Rosenthal, T.; Giesbrecht, N.; Nentwig, M.; Maier, S.; Wang, H.; Snyder, G. J.; Oeckler, O. Nanostructures in Te/Sb/Ge/Ag (TAGS) Thermoelectric Materials Induced by Phase Transitions Associated with Vacancy Ordering. *Inorg. Chem.* **2014**, *53*, 7722−7729.

(74) Shafeie, S.; Guo, S.; Hu, Q.; Fahlquist, H.; Erhart, P.; Palmqvist, A. High-entropy alloys as high-temperature thermoelectric materials. *J. Appl. Phys.* **2015**, *118*, 184905.

(75) Kazem, N.; Zaikina, J. V.; Ohno, S.; Snyder, G. J.; Kauzlarich, S. M. Coinage-Metal-Stuffed $Eu_9Cd_4Sb_9$: Metallic Compounds with Anomalous Low Thermal Conductivities. *Chem. Mater.* **2015**, *27*, 7508−7519.

Paper IV

Electronic and lattice thermal conductivity in intermetallic clathrates:
A first principles perspective
Daniel O. Lindroth, Erik Fransson, Fredrik Eriksson, Joakim Brorsson, Anders Palmqvist and Paul Erhart
(In preparation)

Thermal conductivity in intermetallic clathrates: A first principles perspective

Daniel O. Lindroth,[1] Joakim Brorsson,[2] Erik Fransson,[1] Fredrik Eriksson,[1] Anders Palmqvist,[2] and Paul Erhart[1]

[1]*Chalmers University of Technology, Department of Physics, Gothenburg, Sweden*
[2]*Chalmers University of Technology, Department of Chemistry and Chemical Technology, Gothenburg, Sweden*

Clathrates exhibit a very low thermal conductivity, which has been attribute to phonon-glass like transport properties. Yet a quantitative computational description of this important property has proven difficult, in part due to the large unit cell, the role of disorder, and the fact that both electronic carriers and phonons contribute to transport. Here, we conduct a systematic investigation of thermal transport in the prototypical inorganic clathrate material $Ba_8Ga_{16}Ge_{30}$. We find chemical composition and order to be of minor importance. By contrast, it is crucial to account for the effect of phonon-phonon interactions on the lowest frequency modes in order to obtain an accurate description of the lattice part of the thermal conductivity, which is achieved here by means of temperature dependent effective interatomic force constants. At room temperature and above most phonon modes are heavily damped or overdamped consistent with a glass-like transport mechanism. Furthermore, it is shown that the Wiedemann-Franz law is only approximately fulfilled and that it is crucial to employ the correct pre-factor when doing so.

I. INTRODUCTION

Thermoelectric materials enable the extraction of electrical power from a thermal gradient, as well as the reverse process, cooling through electrical power.[1,2] As a result these materials are interesting for applications such as power generation in remote locations, waste heat recuperation, and active cooling. Specifically, in the high-temperature region, which is of interest for example with regard to waste heat recuperation from combustion processes, inorganic clathrates are among the most efficient thermoelectric materials[3,4] with studies reporting figure-of-merit (zT) values above one.[5,6]

Clathrates are chemical substances with a defined lattice structure that can trap atomic or molecular species.[7,8] For thermoelectric applications one usually considers inorganic clathrates, examples of which include compounds such as $Ba_8Ga_{16}Ge_{30}$ or $Sr_8Ga_{16}Sn_{30}$.[9,10] Here, the earth alkaline atoms act as guest species that occupy the cages provided by the host structure, where the latter is most commonly composed of elements from groups 13 and 14. In the present paper, we focus on $Ba_8Ga_{16}Ge_{30}$, which belongs to space group $P m \bar{3} n$ (international tables of crystallography number 223) and features two smaller and six larger cages per unit cell [Fig. 1].[9–11] $Ba_8Ga_{16}Ge_{30}$ has been investigated extensively both experimentally[5,6,12–15] and theoretically,[13,16–22] especially because of its promising thermoelectric properties.

Generally these materials exhibit a very low thermal conductivity comparable to that of glasses,[3,23] which is crucial for their good thermoelectric performance, and accordingly clathrates are commonly regarded as realizations of the "phonon glass-electron crystal" concept.[24] This behavior can be attributed to the "rattler"-like atomic motion of the guest species, which results from their relatively small size compared to the host cage.[19,25]

While experimental measurements agree with respect to the general magnitude of the thermal conductivity in clathrates they exhibit some noticeable differences (illustrated for the case of $Ba_8Ga_{16}Ge_{30}$ in Fig. 5 below). These variations can originate from several factors including for example sample preparation, thermal emission, and the general difficulties associated with measuring small thermal conductivities. Furthermore, as one is often interested in separating out the contribution to the thermal conductivity from lattice vibrations, one must make assumptions with respect to the electronic contribution, which adds another source of uncertainty.

In this situation, predictive modeling on the basis of first-principles calculations cannot only provide very valuable insight but guide the development of new materials. As a result of the large unit cell and the additional complexity of chemical ordering in these materials[11,20,21,26] there are, however, hardly any such studies.[22]

Here, we present a comprehensive study of the thermal conductivity in $Ba_8Ga_{16}Ge_{30}$ as a prototypical clathrate, which combines Boltzmann transport theory with first-
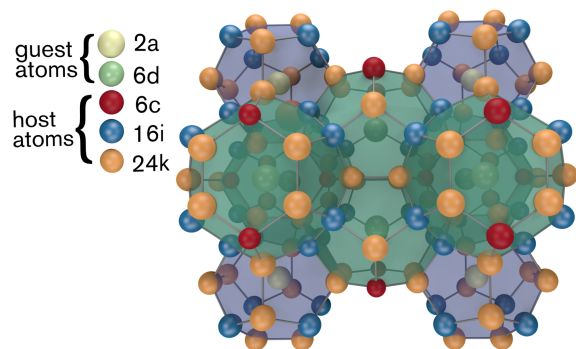

FIG. 1. Crystal structure of type I clathrates. The guest species (Ba) occupies Wyckoff sites of type $2a$ and $6d$, while the host species (Ga, Ge) occupy Wyckoff sites of type $6c$, $16i$, and $24k$.

principles calculations within the framework of density functional theory. We address separately the electronic and vibrational contributions, account for finite-temperature effects on vibrational frequencies and lifetimes, consider the impact of the exchange-correlation functional, and conduct a careful comparison with experimental data. It is demonstrated that while the Wiedemann-Franz law provides a reasonable approximation to the electronic thermal conductivity, it is crucial to use the appropriate pre-factor, an aspect that is often overlooked in the analysis of experimental data.

Furthermore it is shown that the rattler-mode frequencies calculated in the static (zero temperature) limit systematically underestimate the experimental data, which leads to a striking underestimation of the lattice thermal conductivity. To overcome this limitation one must take into account phonon renormalization, which is accomplished effectively by using temperature dependent force constants. The resulting model reproduces the experimentally measured temperature dependence of the rattler-mode frequencies and leads to an increase of the thermal conductivity by more than a factor of two, which brings the predicted data in good agreement with experimental data. Finally, we provide a careful examination of the contributions to the thermal conductivity, which shines light on the "phonon glass" picture and reveals that more modes contribute to the thermal conductivity than previously assumed.

The remainder of this paper is organized as follows: The next section provides an overview of the methodological aspects of this work including computational details as well as a review of the most important relations from Boltzmann transport theory. The first part of the Results and Discussion section then focuses on the suitability of different exchange-correlation functionals to describe the clathrate structures. This is followed by an examination of the phonon dispersion, especially the rattler modes, emphasizing their temperature dependence as well as the effect of order and composition. This sets up a comprehensive analysis of the vibrational and electronic contributions to the thermal conductivity. Finally, we summarize the key results and conclusions in Sect. IV.

II. METHODOLOGY

A. Thermal conductivity

The thermal conductivity κ in a solid chiefly comprises contributions from electronic carriers κ_e and lattice vibrations (phonons) κ_l,

$$\kappa = \kappa_e + \kappa_l. \tag{1}$$

In the following we outline the approach taken to compute the two terms in the above equation.

1. Lattice thermal conductivity

The lattice (phononic) contribution $\boldsymbol{\kappa}_l$ to the thermal conductivity can be computed by solving the phonon Boltzmann transport equation (BTE).[27] In the present treatment, we limit our analysis to the framework of the relaxation time approximation (RTA) of the phonon BTE, in which the lattice thermal conductivity is

$$\boldsymbol{\kappa}_l = \frac{1}{\Omega} \sum_{i\boldsymbol{q}} g_{\boldsymbol{q}} \boldsymbol{v}_{i\boldsymbol{q}} \otimes \boldsymbol{v}_{i\boldsymbol{q}} \tau_{i\boldsymbol{q}} c_{i\boldsymbol{q}}. \tag{2}$$

Here, Ω is the unit cell volume, $g_{\boldsymbol{q}}$ is the $\boldsymbol{q}$-point weight, and $\boldsymbol{v}_{i\boldsymbol{q}} = \nabla_{\boldsymbol{q}} \omega_{i\boldsymbol{q}}$ is the group velocity of mode i at point $\boldsymbol{q}$ of the Brillouin zone with $\omega_{i\boldsymbol{q}}$ being the mode frequency. Both phonon frequencies and group velocities can be derived from the second-order force constant matrix, which is given by the second derivative of the energy E with respect to the atomic displacements $u_\alpha(il)$[27]

$$\Phi_{\alpha\beta}(il, i'l') = \frac{\partial^2 E}{\partial u_\alpha(il) \partial u_\beta(i'l')}, \tag{3}$$

where α and β are Cartesian directions, i is the site index relative to the unit cell basis, and l an index enumerating the unit cells. From the force constant matrix one can readily compute the dynamical matrix at any momentum vector $\boldsymbol{q}$,

$$D_{\alpha\beta}(jj', \boldsymbol{q}) = \frac{1}{\sqrt{m_j m_{j'}}} \sum_{l'} \Phi_{\alpha\beta}(j0, j'l') e^{i\boldsymbol{q}\cdot(r_{j'l'} - r_{j0})}, \tag{4}$$

where m_j is the atomic mass of the species occupying site j. Diagonalization of $D_{\alpha\beta}(jj', \boldsymbol{q})$ then yields normal modes and phonon frequencies $\omega_{i\boldsymbol{q}}$, from which the mode-specific heat capacity $c_{i\boldsymbol{q}}$ at temperature T can be obtained via

$$c_{i\boldsymbol{q}} = k_B \frac{x^2 \exp x}{(1 - \exp x)^2} \quad \text{with} \quad x = \frac{\hbar \omega_{i\boldsymbol{q}}}{k_B T}. \tag{5}$$

The relaxation time $\tau_{i\boldsymbol{q}}$, or phonon lifetime, which appears in Eq. (2), comprises contributions from different scattering processes including, e.g., phonon-phonon interaction, isotope mass variation, boundary scattering, alloying, and disorder. Here, we consider phonon-phonon interaction and isotope mass variation. According to the most simple approximation, known as Matthiessen's rule, the different scattering processes are assumed to be independent, i.e. their scattering rates (or inverse lifetimes) are additive

$$\tau_{i\boldsymbol{q}}^{-1} = \tau_{ph-ph,i\boldsymbol{q}}^{-1} + \tau_{iso,i\boldsymbol{q}}^{-1}. \tag{6}$$

In the present work scattering due to isotope mass variation ($\tau_{iso,i\boldsymbol{q}}$) has been treated according to second order perturbation theory[28] whereas the contribution due to phonon-phonon scattering ($\tau_{ph-ph,i\boldsymbol{q}}^{-1}$) was treated at the

level of first-order perturbation theory,[27] which requires knowledge of not only the second but also third-order interatomic force constants (IFCs).[29,30] As detailed in Sect. II B, we computed IFCs both in the static (0 K) limit using the finite displacement method and from molecular dynamics (MD) simulations.

2. Electronic thermal conductivity

In the relaxation time approximation (RTA) to the linearized Boltzmann transport equation (BTE) the electronic contribution to the thermal conductivity $\boldsymbol{\kappa}_e$ is given by

$$\boldsymbol{\kappa}_e = \boldsymbol{\kappa}^0 - \boldsymbol{S}^2 \boldsymbol{\sigma} T \tag{7}$$

with[27,31,32]

$$\boldsymbol{\sigma} = \frac{2e^2}{\Omega} \sum_{i\boldsymbol{k}} g_{\boldsymbol{k}} \boldsymbol{v}_{i\boldsymbol{k}} \otimes \boldsymbol{v}_{i\boldsymbol{k}} \tau_{i\boldsymbol{k}} \left(\frac{\partial f}{\partial \varepsilon}\right)_{\varepsilon=\varepsilon_{i\boldsymbol{k}}} \tag{8}$$

$$\boldsymbol{S} = \frac{\boldsymbol{\sigma}^{-1}}{eT} \sum_{i\boldsymbol{k}} g_{\boldsymbol{k}} \boldsymbol{v}_{i\boldsymbol{k}} \otimes \boldsymbol{v}_{i\boldsymbol{k}} \tau_{i\boldsymbol{k}} \left[\varepsilon_{i\boldsymbol{k}} - \mu_e\right] \left(\frac{\partial f}{\partial \varepsilon}\right)_{\varepsilon=\varepsilon_{i\boldsymbol{k}}} \tag{9}$$

$$\boldsymbol{\kappa}^0 = \frac{e}{T\Omega} \sum_{i\boldsymbol{k}} g_{\boldsymbol{k}} \boldsymbol{v}_{i\boldsymbol{k}} \otimes \boldsymbol{v}_{i\boldsymbol{k}} \tau_{i\boldsymbol{k}} \left[\varepsilon_{i\boldsymbol{k}} - \mu_e\right]^2 \left(\frac{\partial f}{\partial \varepsilon}\right)_{\varepsilon=\varepsilon_{i\boldsymbol{k}}}. \tag{10}$$

Here, Ω is the unit cell volume, $g_{\boldsymbol{k}}$ is the $\boldsymbol{k}$-point weight, i refers to the band index, $\tau_{i\boldsymbol{k}}$ is the mode and momentum dependent lifetime, $\boldsymbol{v}_{i\boldsymbol{k}} = \hbar^{-1}\partial\varepsilon_{i\boldsymbol{k}}/\partial\boldsymbol{k}$ is the group velocity, f is the occupation function, and μ_e is the electron chemical potential.

We have previously studied the electronic conductivity $\boldsymbol{\sigma}$ and the Seebeck coefficient $\boldsymbol{S}$ for $Ba_8Ga_{16}Ge_{30}$ and conducted a systematic comparison with experiment.[20] Using a charge carrier concentration of $n_e = 3 \times 10^{20}$ cm^3 and a mode and momentum-independent effective lifetime model with $\tau_{\text{eff}} = \tau_{300}(300\,\text{K}/T)^{1/2}$ we were able to achieve very good agreement with experimental data, and accordingly this approach is also adopted in the present work.

B. Computational details

1. General

DFT calculations were performed using the projector augmented wave method[33] as implemented in the Vienna *ab initio* simulation package.[34] To assess the sensitivity of our results to the treatment of exchange-correlation effects, we used both the PBE functional[35] and the van der Waals density functional method[36] with consistent exchange (vdW-DF)[37] as implemented in VASP.[38]

The plane-wave energy cutoff energy were set to 243 eV ($Ba_8Ga_{16}Ge_{30}$) and 319 eV ($Ba_8Al_{16}Si_{30}$), respectively, and Gaussian smearing with a width of 0.1 eV was used

throughout. Structural relaxations were performed using a Γ-centered $3 \times 3 \times 3$ $\boldsymbol{k}$-point mesh until the residual forces were below 10 meV/Å and absolute stresses were below 0.1 kbar.

2. Vibrational spectra and lattice thermal conductivity

The static second and third-order IFCS as well as the thermal conductivity were computed using the SHENG-BTE[29,39,40] and PHONOPY[41] codes. Calculations were carried out using $2 \times 2 \times 2$ supercells (432 atoms) and included displacements up to the fifth neighbor shell. The Brillouin zone was sampled using a $9 \times 9 \times 9$ $\boldsymbol{q}$-point mesh and a smearing parameter of $\sigma = 0.01$. There was no indication of any significant difference between the results within the framework of RTA-BTE, and the fully converged solution to the BTE, hence the full set of computations were limited to the RTA. The second-order IFCs obtained in this process were also used to model the thermal expansion within the quasi-harmonic approximation.

As will be shown below, using the IFCs obtained in the static (0 K) limit to predict the thermal conductivity leads to a substantial underestimation. We therefore also determined effective temperature dependent IFCs similar to the approach described in Ref. 42. To this end, we carried out first-principles molecular dynamics (MD) simulations in the canonical ensemble at temperatures of 100, 200, 300, and 600 K. We employed primitive 54-atom cells, which were sampled using a Γ-centered $3 \times 3 \times 3$ $\boldsymbol{k}$-point mesh. The equations of motion were integrated for a total of about 5,500 time step using a time step of 5 fs. After discarding the first 1,000 steps for equilibration, snap shots at a spacing of 180 MD steps (0.9 ps) were used to train via least-squares fitting temperature dependent models (TDEM) using our in-house HIPHIVE code. Finally, the resulting IFCs were used with SHENG-BTE to obtain the thermal conductivity.

3. Vibrational spectra of non-stoichiometric compounds

Additional calculations of the vibrational spectra were carried out for $Ba_8Ga_xGe_{46-x}$ and $Ba_8Al_xSi_{46-x}$ for $14 \leq x \leq 18$. To this end, we employed 54-atom cells and structures obtained previously by Monte Carlo simulations that are representative of the actual chemical order in the material. In total data was obtained for 20 structures per composition, equivalent to 200 configurations in total.

4. Electronic contribution to the thermal conductivity

To calculate the electronic contribution to the thermal conductivity we considered both the chemically ordered ground state structure and the chemically disordered structures obtained by Monte Carlo simulations.[20]

The latter configurations are representative of the actual chemical (dis)order in the material at 600, 900, and 1200 K as described in detail in Ref. 20. Results were averaged over five structures per temperature. The wave function of the fully relaxed structures were converged using a Γ-centered $4 \times 4 \times 4$ $\boldsymbol{k}$-point mesh, which was followed by a non-self-consistent computation of the eigenenergy spectra on a Γ-centered $20 \times 20 \times 20$ mesh. The terms in Eq. (7) were subsequently computed using the BOLTZTRAP code.[32]

III. RESULTS AND DISCUSSION

A. Structure and thermal expansion

An accurate description of the vibrational properties is important for modeling the thermal conductivity. While the PBE functional has been used extensively in the past in electronic structure calculations of inorganic clathrates (see e.g., Refs. 19 and 22), it is known to underestimate the bond stiffness (see e.g., Ref. 43). In the present work, we therefore also considered the vdW-DF-cx method (see Sect. II B), which has been found to yield an excellent description of finite temperature properties for other materials.[43,44]

As a first step in assessing the performance of these functionals we determined the temperature dependence of the lattice structure of the four stoichiometric compounds $Ba_8Ga_{16}Ge_{30}$, $Ba_8Ga_{16}Si_{30}$, $Ba_8Al_{16}Ge_{30}$, and $Ba_8Al_{16}Si_{30}$ based on the ordered ground state (0 K) structure determined in Ref. 21. In this context it must be noted that it is not always possible to find experimental data for the lattice parameters for the stoichiometric compounds. This applies in particular for the Si-based clathrates,[11,45–47] which is presumably because of the solubility limit being about $x = 15$,[45,46] for both Ga in $Ba_8Ga_xSi_{46-x}$ and Al in $Ba_8Al_xSi_{46-x}$. The lattice parameters for the composition corresponding to $x = 16$

have been estimated by performing a linear least-squares fit for each data set. It shall also be noted that the experimentally determined lattice parameters and compositions can vary markedly depending on the measurement technique.[11,26,45]

Both functionals overestimate the lattice parameter compared to experiment, with PBE always giving the higher estimate (Table I and Fig. 2). Overall the agreement achieved by the vdW-DF-cx calculations is very good with an average deviation of 0.6% (1.5% for PBE).

It should be noted that chemical disordering, which is generally present in these compounds,[11] has an effect on the lattice parameter. Based on our earlier analysis,[21] one can assume that as the material is cooled down after synthesis the chemical order is frozen in at a temperature of about 600 K. At this temperature the lattice parameter in $Ba_8Ga_{16}Ge_{30}$ has been predicted to be increased by 0.028 Å relative to the ground state structure, decreased by about 0.028 Å in the case of $Ba_8Ga_{16}Si_{30}$ and relatively unchanged in the case of $Ba_8Al_{16}Ge_{30}$ and $Ba_8Al_{16}Si_{30}$. These contributions, however, barely affect the agreement with experiment and leave the average errors unchanged.

B. Phonon dispersion in the static (0 K)imit

Due to the large mass of the Ba atoms as well as their weak coupling to the host structure, the associated rattler modes show up as low-frequency optical modes in the phonon spectrum (Fig. 3). They appear at higher frequencies in the vdW-DF-cx calculations [Fig. 3(a)] than in the case of the PBE functional [Fig. 3(b)] as expected based on the known "softness" of the latter. For both

TABLE I. Finite temperature lattice parameters from calculation and experiment. The values in brackets denote the lattice parameters obtained without taking into account zero-point vibrations. In the calculations the temperature dependence was described at the level of the quasi-harmonic approximation.

Material	Calculation			Experiment	
	0 K		300 K	300 K	
$Ba_8Ga_{16}Ge_{30}$				Ref. 48	Ref. 14
PBE	10.98	(10.96)	11.02	10.76^1	10.80^1
vdW-DF-cx	10.86	(10.85)	10.90		
$Ba_8Ga_{16}Si_{30}$				Ref. 11	Ref. 45
PBE	10.68	(10.66)	10.71	10.54^2	10.57^2
vdW-DF-cx	10.60	(10.58)	10.62		
$Ba_8Al_{16}Si_{30}$				Ref. 47	Ref. 46
PBE	10.74	(10.72)	10.76	10.64^2	10.65^2
vdW-DF-cx	10.67	(10.65)	10.69		
$Ba_8Al_{16}Ge_{30}$				Ref. 26	Ref. 49
PBE	11.01	(10.99)	11.04	10.85^1	10.88^2
vdW-DF-cx	10.91	(10.90)	10.94		

[1] Interpolated
[2] Extrapolated
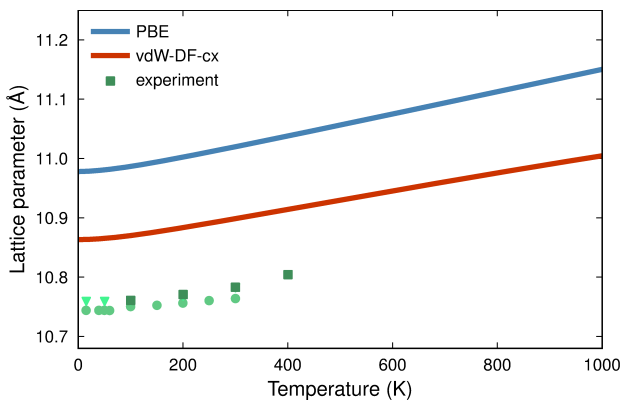

FIG. 2. Temperature dependence of the lattice parameter for $Ba_8Ga_{16}Ge_{30}$ obtained within the quasi-harmonic approximation. Experimental data are from Ref. 11.
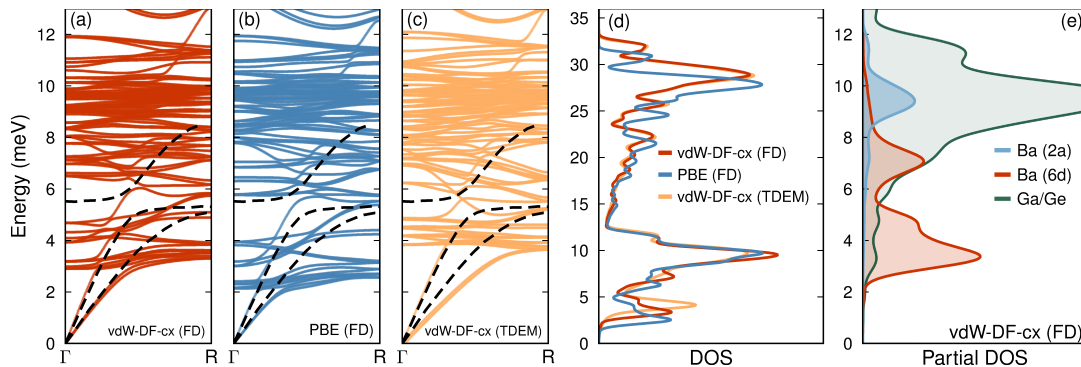
FIG. 3. (a-c) Phonon dispersion of $Ba_8Ga_{16}Ge_{30}$ showing the low frequency region along the Γ-R direction derived (a,b) from IFCs obtained in the static (0 K) limit by the finite-displacement (FD) method and (c) from a temperature dependent effective model (TDEM) corresponding to a temperature of 300 K. Black dashed lines indicate the phonon dispersion branches determined experimentally by inelastic neutron scattering.[25] (d) Total phonon densities of states. (e) Partial densities of states showing the contributions from Ba on 2a Wyckoff sites (blue line), Ba on 6d sites (red line) and contributions from the Ga/Ge cage structure (green).

functionals one observes the phonon modes in the zero temperature limit to be lower than the experimentally measured frequencies [black dashed lines in Fig. 3(a-c)].[25]

C. Phonon dispersion at finite temperatures

As will be shown below the thermal conductivity calculated on the basis of the static IFCs systematically and substantially underestimates experimental data (also see Ref. 22). As will become apparent in the analysis of the thermal conductivity (Sect. III E) lower frequencies of the rattler modes reduce the Brillouin zone volume corresponding to propagating modes, which translates into a lower thermal conductivity. It is therefore a very relevant question to which extent phonon-phonon interactions affect the rattler mode frequencies. In fact the low frequencies of the rattler modes imply that they are fully activated already at low temperatures and thus phonon-phonon interaction driven frequency shifts can already occur below room temperature. This notion is supported by experimental data from both inelastic neutron and Raman scattering[25] that reveals a notable temperature dependence of the rattler modes.

Using a series of temperature dependent effective models (TDEMs, see Sect. II B), we therefore calculated the vibrational spectrum as a function of temperature. The full phonon dispersion at 300 K [Fig. 3(c)] does indeed reveal an upward shift of the lowermost optical branches. A comprehensive comparison with experimental data [Fig. 4(c)] demonstrates that the TDEMs can also rather accurately reproduced both the absolute values and the temperature dependence of the rattler modes.[57] As will be discussed below these effects are actually crucial for being able to predict correctly the thermal conductivity.

D. Chemical composition and ordering

According to experimental,[26,46,47,53,58-63] theoretical[21,64] as well as combined[49,65] studies, the structural and physical properties of, ternary, inorganic clathrates vary markedly with chemical composition. Specifically, it has been shown that the displacement of the guest atom from the 6d site[21,26] and the associated vibrational frequencies[53,58] depend on the number of Al or Ga atoms per unit cell, in ternary compounds of the type $Ba_8\{Al,Ga\}_x\{Si,Ge\}_{46-x}$. There is, moreover, experimental evidence[51,52] that the degree of off-centering, the frequencies of the lowest Raman active modes and the lattice thermal conductivity are correlated for compounds in the structurally similar, quaternary system $Sr_8Ga_{16}Si_xGe_{30-x}$.

Given these results, it is reasonable to assume that the lattice thermal conductivity also varies to some degree with chemical composition. We therefore computed the variation of the 18 lowest-frequency phonon modes, associated with the Ba atom at the 6d site[66], with the number of group-13 atoms not only in $Ba_8Ga_xGe_{46-x}$ but also $Ba_8Al_xSi_{46-x}$, where the latter was included as it represents the limit of a host matrix made up of light elements. Specifically, we extracted and averaged the Γ-point frequencies for 20 representative configurations (Sect. II B 3) for each composition in the range $14 \leq x \leq 18$. The modes naturally fall into three groups, with six modes in each [Fig. 4 (a,b)]. The splitting of the modes can be viewed as a consequence of the facts that (i) the guest atom are not located at the immediate center of the cage, (ii) the latter is shaped like a tetrakaidekahedron, and (iii) the Al and Ga atoms are not necessarily symmetrically distributed between the framework sites.[21]

For $Ba_8Al_xSi_{46-x}$ the phonon modes slightly soften with increasing x; a similar trend albeit even weaker can also be observed for the lower two groups in the case of
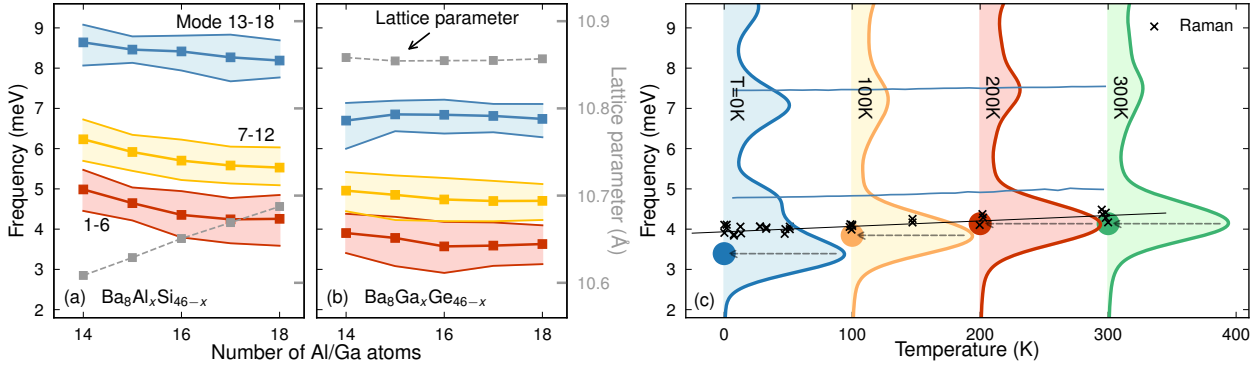
FIG. 4. (a,b) Composition dependence of the lowest lying rattler modes in (a) $Ba_8Ga_xGe_{46-x}$ and (b) $Ba_8Al_xSi_{46-x}$ along with the variation of the lattice constant (in gray). Specifically, the red, yellow and blue lines correspond to the average frequencies for modes 1–7, 8–13 and 13–18, respectively. The standard deviations obtained by averaging over 20 representative configurations at each composition are indicated by shaded filled curves. Experimental data obtained at 2–7 K from Raman scattering[50–53] as well as THz spectroscopy[54–56] is shown by symbols in (b). (c) Temperature dependence of the partial density of states associated with Ba atoms on 6d Wyckoff sites (shaded filled curves, compare Fig. 3(e)) in comparison with experimental data from inelastic neutron scattering on powder (PINS) and single crystalline (SINS) samples,[25] Raman Scattering[25,50–53] and THz spectroscopy.[54–56]

$Ba_8Ga_{16}Ge_{30}$. This behavior correlates with the increase in the lattice constant, which is larger for $Ba_8Al_xSi_{46-x}$ than for $Ba_8Ga_xGe_{46-x}$ [gray lines in Fig. 4 (a,b)]. A larger lattice parameter implies that the size of the cages occupied by Ba atoms increases, which leads to weaker restoring forces and, hence, lower vibrational frequencies. Overall one must conclude, however, that the phonon frequencies, associated with the vibrations of the Ba atom at the 6d Wyckoff, are relatively insensitive to the chemical composition, since the difference between $x = 14$ and $x = 18$ is of the same magnitude as the spread of the frequencies. This applies in particular to $Ba_8Ga_xGe_{46-x}$ and thus the *lattice* thermal conductivity can be expected to be almost independent of x for $14 \leq x \leq 18$.

E. Thermal conductivity: lattice contribution

1. Comparison of scattering channels

Based on the analysis of the vibrational properties described in the previous sections we computed the lattice contribution to the thermal conductivity. These calculations were carried out for the chemically ordered ground state structure of $Ba_8Ga_{16}Ge_{30}$[20,21] using both the PBE functional and the vdW-DF-cx method.

When limiting the analysis to phonon-phonon scattering, one obtains a strong variation with temperature that follows a T^{-2} and behavior at low temperatures and a T^{-1} trend at temperatures $\gtrsim 100$ K [Fig. 5 (a)]. Isotope scattering affects only the very low temperature region leading to a peak in the conductivity below 10 K.

The chemical disordering at finite temperatures that was already alluded to above is inevitably associated with mass mixing, which affects both the frequencies via Eq. (4) and the lifetimes in a way analogous to isotope scattering. The effect on the frequencies is modest as evident from the analysis in Sect. III D and also the impact on the lifetimes is only discernible at very low temperatures [dashed gray line in Fig. 5(a)].

2. Overview of experimental data

The total thermal conductivity κ has been measured using a variety of techniques for both single and polycrystalline samples, see e.g., Refs. 5, 6, 59, and 68. To extract the lattice contribution to the thermal conductivity, it is customary to remove the electronic part by the use of Wiedemann-Franz law. Yet, as discussed in Sect. III F, the Wiedemann-Franz law is in fact only approximately valid under the relevant conditions. For the sake of consistency, here we nonetheless use the data reported in the original papers and focus on single crystalline samples.

The compilation of the experimental results [Fig. 5 (b)] illustrates a noticeable spread in the data, especially at low temperatures. The strong temperature dependence along with the pronounced low-temperature peak in the data by Christensen *et al.*[68] indicates a phonon-limited thermal conductivity down to very low temperatures. By contrast, the much weaker temperature dependence and low-temperature plateau in the results from Avila *et al.*[59] is rather suggestive of a temperature independent (likely structural) limit on the mean free path $\lambda = v\tau$. Such a plateau corresponds more closely to the so-called small grain thermal conductivity [compare the dotted line in Fig. 5 (a)].

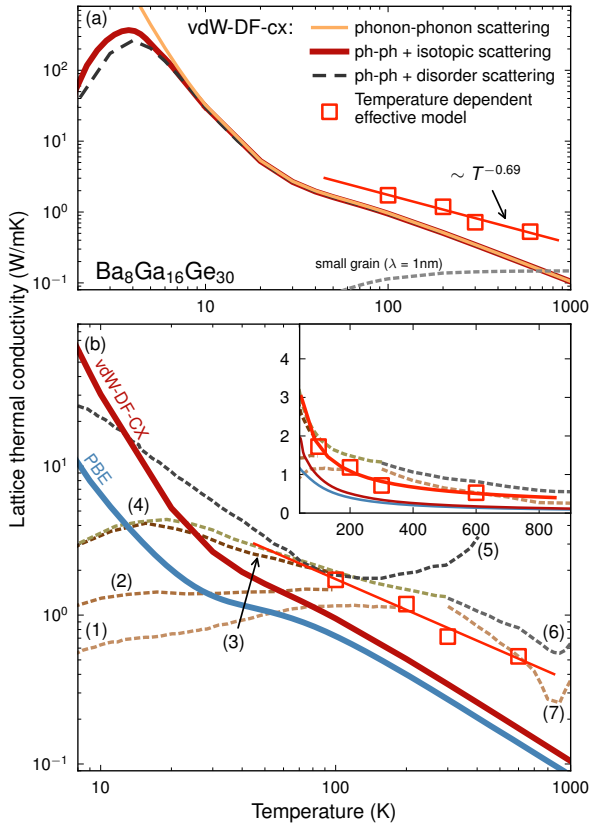One plausible explanation for the variation in the experimental data could phonon scattering by defects.

FIG. 5. Lattice thermal conductivity κ_l of $Ba_8Ga_{16}Ge_{30}$ as a function of temperature. (a) Comparison of κ_l due to different included scattering channels, calculated using IFCs achieved with the vdW-DF-cx functional, as well as a comparison to the computations using temperature dependent effective IFCs. (b) Comparison between computations, using IFCs from the vdW-DF-cx functional (red solid line), the PBE functional (solid blue line), temperature dependent effective models (squares) and experimental data sets (dashed lines marked by numbers). The inset shows the same data on a linear scale. The experimental data are from Refs. 67 (1), 60 (2, 3), 12 (4), 68 (5), 69 (6, 7). The authors of Ref. 68 (5) point out that due to the large surface to volume ratio, their measurements become unreliable above approximately 100 K due to thermal emission. The data sets from Ref. 60 (2 and 3) correspond to p respectively n-doped samples.

In the relevant temperature range below approximately $600\,\mathrm{K}^{21}$ it is reasonable to assume the defect concentration to be frozen in, which would be consistent with a weak temperature dependence. Moreover while sizable vacancy concentrations have been reported for some samples they are also likely to be sensitive to the synthesis conditions, which would provide a rationale for the large variation between studies.[14] A comprehensive treatment of the contribution of defect scattering would in principle be possible using the approach described in Ref. 70. The computations needed, however, exceed the scope of the present work and in the following we rather focus on

the importance of addressing the role of temperature on phonon-phonon interactions.

3. Comparison between calculations and experiment

The lattice thermal conductivities derived from IFCs obtained in the static limit by either PBE or vdW-DF-cx substantially underestimate the experimental data [Fig. 5, also see Ref. 22]. This is a rather unusual observation as one more commonly finds calculations to overestimate the experimental data (see e.g., Ref. 44) as computational analysis commonly account only for some of the scattering mechanisms that are active in reality.

The behavior observed here can, however, be understood by considering the expression for the lattice thermal conductivity Eq. (2) and the phonon dispersions (Fig. 3). Since in the case of the static IFC calculations the rattler modes are located at lower frequencies than in the experimental data the avoided crossings with the acoustic modes[25] occur at smaller q vectors and as a result the relative fraction of propagating modes that contributes to the thermal conductivity is reduced. This mechanism can also explain the lower thermal conductivity obtained from PBE relative to vdW-DF-cx calculations.

As shown above one must account for the effect of phonon-phonon coupling on the frequency spectrum in order to obtain closer agreement with experiment (Fig. 3). Accordingly using temperature dependent IFCs (TDEM) in Eq. (2) leads to a substantial increase in the thermal conductivity by a factor of two at 100 K up to a factor of three at 600 K As a result the TDEM calculations are in very good agreement with the experimental data in this temperature range. One also observes that the temperature dependence of κ_l shifts from $\kappa_l \propto T^{-1}$ to $\kappa_l \propto T^{-0.69}$, which rather closely follows the experimental trend.

4. Microscopic contributions

Inorganic clathrates have repeatedly been shown to exhibit very low thermal conductivities[3,5,6,59,68] and have been discussed as realizations of the so-called phonon glass-electron crystal (PGEC) concept.[1] Accordingly, the mechanisms that give rise to the very low thermal conductivity in clathrates have been scrutinized experimentally as well as by theory and simulation, see, e.g., Refs. 19, 23, 25, and 71. The primary object of attention has been the phonon dispersion,[19,25] which provides information about vibrational frequencies and group velocities and is more readily accessible both in experiments and calculations. The phonon lifetimes in these materials have only been very recently addressed using an approximate lifetime model for $Ba_8Ga_{16}Si_{30}$[71] as well as perturbation theory in the case $Ba_8Ga_{16}Ge_{30}$.[22]
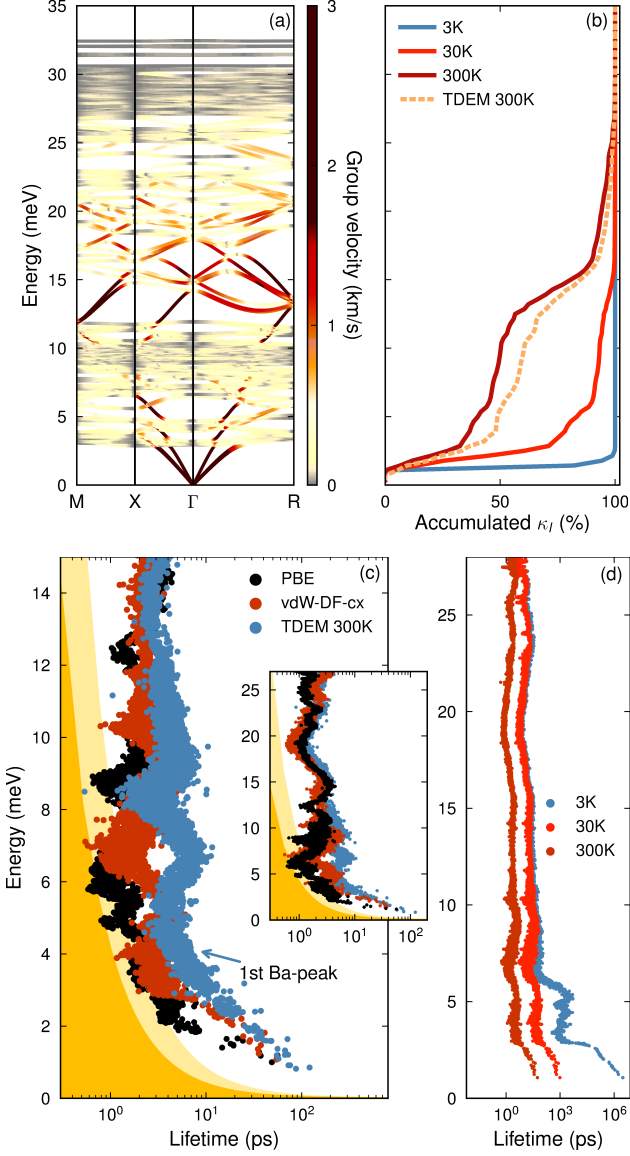
FIG. 6. (a) Phonon dispersion in $Ba_8Ga_{16}Ge_{30}$ from static vdW-DF-cx IFCs. (b) Normalized accumulated lattice thermal conductivity with respect to energy as computed with static vdW-DF-cx IFCs at 3, 30 and 300 K (solid lines), compared to calculations based on the TDEM IFCs at 300 K. (c) Phonon-phonon limited lifetimes at 300 K computed with PBE (black markers), vdW-DF-cx (red markers) and TDEM (blue markers) IFCs. The filled yellow curves indicate the overdamped region for a classical harmonic oscillator. (d) Comparison of lifetimes computed from static vdW-DF-cx IFCs at 3, 30 and 300 K.

The present calculations allow us to scrutinize the individual contributions to the lattice thermal conductivity according to Eq. (2), including group velocities and lifetimes, and thereby to gain further insight into the glass-like thermal conduction in inorganic clathrates. From the phonon dispersion [Fig. 6(a)] two energy regions $\omega <$

3 meV and 12 meV $< \hbar\omega <$ 16 meV can be identified with large group velocities. At low temperatures, the contribution to κ_L stems mainly from the region $\omega < 2$ meV [Fig. 6 (b)]. Yet already at about 300 K almost half of the heat transport is accomplished by modes with frequencies above 3 meV. This behavior is the result of two concurrent processes: (i) from about 300 K on all modes are occupied and the mode specific heat capacity Eq. (5) saturates; (ii) the lifetimes of the acoustic modes in the lower energy window drop substantially whereas the lifetimes of the higher lying modes are relatively less affected [Fig. 6(d)]. Compared to previous studies, which focused primarily on the low energy region, the present results thus demonstrate that important contributions stem from higher energy modes and must be included to obtain a sound description of the thermal conductivity.

When considering the static IFCs it appears that a large number of modes is actual either strongly damped or even overdamped [Fig. 6(c)]. The oscillation period of these modes is thus comparable to their lifetime. While at this point a phononic description of these modes inevitably reaches its limit, it can be interpreted as the onset of a hopping (glass-like) transport mode. In the case of the TDEM IFCs the lifetimes are notably longer, which reflects the effective (albeit not formal) renormalization of the modes.

Overall, in agreement with previous work the present calculations demonstrate that weak coupling between host and low-lying guest (Ba) modes gives rise to avoided band crossings in the phonon dispersion,[19,25] which in turn cause a dramatic reduction in the group velocities of almost all modes with frequencies above the lowest guest mode.[19,25] The few dispersed modes above this threshold are strongly damped and accordingly do not contribute notably to κ_l. The very small thermal conductivity is thus the result of the extremely small Brillouin zone volume available to propagating phonon modes. It should also be noted that since the effective mean free path drops to about 1 nm already at 300 K, further reduction of κ_l by e.g., microstructural engineering[72] does not appear to be very promising. It should also be recalled out that in the temperature range relevant for thermoelectric applications, the electronic contribution κ_e is already comparable to if not larger than κ_l (see Sect. III F).

F. Thermal conductivity: electronic contribution

When conducting experiments only the total thermal conductivity κ is directly accessible. To resolve each contribution one therefore commonly resorts to the Wiedemann-Franz law. The Wiedemann-Franz law couples the electrical conductivity σ to the electronic thermal conductivity

$$\kappa_e = L\sigma T, \tag{11}$$

by which the lattice thermal conductivity κ_l is estimated. Here, $L = L_0(k_B^2/e^2)$ is the Lorenz number.
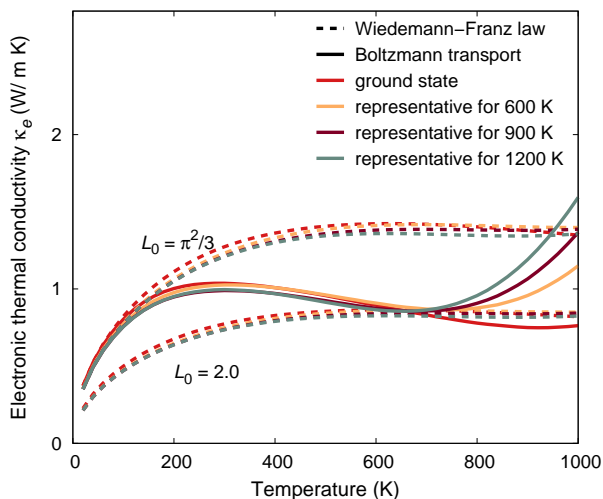
FIG. 7. Electronic contribution κ_e to the thermal conductivity calculated for the ground state structure as well as for structures extracted from Monte Carlo simulations[20] representative of the chemical order at different temperatures. Data obtained using the Wiedemann-Franz law $\kappa_e = L\sigma T$ are shown by dashed lines, whereas the thermal conductivity obtained within the framework of Boltzmann transport theory[32,73] is shown by solid lines. Note that below 900 K the two sets of data deviate by as much as 25%, whereas above approximately 900 K the BTT data indicates a sharp rise which is not predicted by the Wiedemann-Franz law.

When resolving experimental data it is common to use $L_0 = \pi^2/3 \approx 3.3$, which is obtained for a degenerate electron gas, or not to specify the value of L_0 used. As noted e.g., in Ref. 74 for a degenerate semiconductor (such as a typical thermoelectric clathrate) a value of $L_0 = 2$ should be used. Even then the Wiedemann-Franz law ought to be considered a low level approximation to the actual behavior as L_0 is not a universal constant.

As the final point in our the analysis of the thermal conductivity in the prototypical inorganic clathrate $Ba_8Ga_{16}Ge_{30}$ we therefore now consider the electronic contribution κ_e (Fig. 7). At low temperatures $\lesssim$ 200 K the thus obtained κ_e agrees rather well with the Wiedemann-Franz law assuming a degenerate electron gas ($L_0 \approx 3.3$), whereas at higher temperatures $\gtrsim$ 400K the semiconductor value $L_0 = 2$ yields better agreement.

Above approximately 900 K the κ_e from Boltzmann transport theory reveals a sharp rise for some structural models. In this context one should note that the integrand in the expression for the electronic thermal conductivity[32,73] Eq. (10) includes a term $(\varepsilon_{i\boldsymbol{k}} - \mu_e)^2$. As a result, κ_e is most sensitive to contributions from states about $k_B T$ above and below the Fermi level μ_e, rather than to states in the immediate vicinity of μ_e, which dominate in the case of σ. The deviation at higher temperatures could, therefore, be an indication for shortcomings of the effective lifetime model, which does not distinguish these states. In any case, the present analysis suggests that the Wiedemann-Franz law should be applied with caution when trying to discriminate the electronic and lattice thermal conductivities, and that a value of L_0 corresponding to a degenerate semiconductor is more appropriate for describing the situation in inorganic clathrates.

IV. CONCLUSIONS

The very low thermal conductivities observed in inorganic clathrates are challenging to address both experimentally and computationally. In the present study, focusing on $Ba_8Ga_{16}Ge_{30}$, we have undertaken a systematic computational analysis of the various mechanisms and features that contribute to this property.

Firstly, we have addressed the role of the exchange-correlation functional in describing both structure and vibrational spectra, from which we concluded that the vdW-DF-cx method provides a well balanced description of inorganic clathrates. Next by using temperature dependent interatomic force constants we demonstrated that phonon-phonon coupling (and thus temperature) must be taken into account in order to accurately capture the frequencies of the rattler modes, which also allowed us to predict correctly the experimentally observed temperature dependence of these modes. On the other hand, the composition dependence of the rattler mode frequencies was shown to be small.

Based on this level of understanding we then predicted both the lattice and the electronic thermal conductivity. For the former we obtained very good agreement with experiment using temperature dependent IFCs whereas we observed a pronounced underestimation when using IFCs representing the static limit. The κ_l values obtained using different IFCs could be rationalized by considering the relative Brillouin zone volume of propagating (heat carrying) modes. Specifically, the underestimation of the rattler modes is associated with the onset of avoided crossings at a lower $\boldsymbol{q}$ vector. The analysis furthermore reveals that IFCs obtained in the static limit yield heavily damped as well as overdamped quasiparticles, which is suggestive of glass-like transport. Taking into account phonon-phonon coupling via temperature dependent IFCs (and thus introducing effectively renormalization) leads to larger lifetimes and more well defined quasi-particles.

Finally, a comparison of predictions for the electronic contribution to the thermal conductivity demonstrates the Wiedemann-Franz law must be applied with more care when separating experimental thermal conductivity data as the L_0 pre-factor can vary between 2 (degenerate semi-conductor) and 3.3 (free electron gas) across the temperature range of interest.

The present results provide a very detailed perspective on the thermal conductivity in inorganic clathrates. They also shed light on the application of Boltzmann transport theory for predicting systems with strongly

damped quasi-particles. Here, we emphasize in particular the importance of taking into account the effect of phonon-phonon coupling on the vibrational spectrum. In the present work we restricted ourselves to an effective description using temperature dependent IFCs. A future extension of this work could consider a rigorous application of self-consistent phonon theory, which requires taking into account IFCs beyond the third-order.

[1] D. Rowe, ed., *Thermoelectrics Handbook: Macro to Nano* (CRC Press, 2005).

[2] G. J. Snyder and E. S. Toberer, Nature Materials **7**, 105 (2008).

[3] J. L. Cohn, G. S. Nolas, V. Fessatidis, T. H. Metcalf, and G. A. Slack, Physical Review Letters **82**, 779 (1999).

[4] B. B. Iversen, A. E. Palmqvist, D. E. Cox, G. S. Nolas, G. D. Stucky, N. P. Blake, and H. Metiu, Journal of Solid State Chemistry **149**, 455 (2000).

[5] A. Saramat, G. Svensson, A. E. C. Palmqvist, C. Stiewe, E. Mueller, D. Platzek, S. G. K. Williams, D. M. Rowe, J. D. Bryan, and G. D. Stucky, Journal of Applied Physics **99**, 023708 (2006).

[6] E. S. Toberer, M. Christensen, B. B. Iversen, and G. J. Snyder, Physical Review B **77**, 075203 (2008).

[7] A. D. McNaught and A. Wilkinson, *IUPAC. Compendium of Chemical Terminology*, 2nd ed. (Blackwell Scientific Publications, Oxford, 1997) XML on-line corrected version: http://goldbook.iupac.org (2006-) created by M. Nic, J. Jirat, B. Kosata; updates compiled by A. Jenkins.

[8] G. P. Moss, P. A. S. Smith, and D. Tavernier, Pure and Applied Chemistry **67**, 1307 (2009).

[9] P. Rogl, in *Thermoelectrics Handbook* (CRC Press, 2005) Chap. 32, pp. 1–24.

[10] A. V. Shevelkov and K. Kovnir, in *Zintl Phases*, Structure and Bonding No. 139, edited by T. F. Fässler (Springer Berlin Heidelberg, 2011) pp. 97–142.

[11] M. Christensen, S. Johnsen, and B. B. Iversen, Dalton Trans. **39**, 978 (2010).

[12] B. C. Sales, B. C. Chakoumakos, R. Jin, J. R. Thompson, and D. Mandrus, Physical Review B **63**, 245113 (2001).

[13] J. D. Bryan, N. P. Blake, H. Metiu, G. D. Stucky, B. B. Iversen, R. D. Poulsen, and A. Bentien, Journal of Applied Physics **92**, 7281 (2002).

[14] M. Christensen, N. Lock, J. Overgaard, and B. B. Iversen, Journal of the American Chemical Society **128**, 15657 (2006).

[15] D. Cederkrantz, A. Saramat, G. J. Snyder, and A. E. C. Palmqvist, Journal of Applied Physics **106**, 074509 (2009).

[16] N. P. Blake, S. Latturner, J. D. Bryan, G. D. Stucky, and H. Metiu, Journal of Chemical Physics **115**, 8060 (2001).

[17] N. P. Blake, D. Bryan, S. Latturner, L. Møllnitz, G. D. Stucky, and H. Metiu, Journal of Chemical Physics **114**, 10063 (2001).

[18] G. K. H. Madsen, K. Schwarz, P. Blaha, and D. J. Singh, Physical Review B **68**, 125212 (2003).

[19] G. K. H. Madsen and G. Santi, Physical Review B **72**, 220301 (2005).

[20] M. Ångqvist, D. O. Lindroth, and P. Erhart, Chemistry of Materials **28**, 6877 (2016).

[21] M. ngqvist and P. Erhart, Chemistry of Materials **29**, 7554 (2017).

[22] T. Tadano, Y. Gohda, and S. Tsuneyuki, Physical Review Letters **114**, 095501 (2015).

[23] J. Dong, O. F. Sankey, and C. W. Myles, Physical Review Letters **86**, 2361 (2001).

[24] D. Rowe, ed., *CRC Handbook of Thermoelectrics* (CRC Press, 1995).

[25] M. Christensen, A. B. Abrahamsen, N. B. Christensen, F. Juranyi, N. H. Andersen, K. Lefmann, J. Andreasson, C. R. H. Bahl, and B. B. Iversen, Nature Materials **7**, 811 (2008).

[26] M. Christensen and B. B. Iversen, Chem. Mater. **19**, 4896 (2007).

[27] J. M. Ziman, *Electrons and phonons* (Clarendon Press, Oxford, 1960).

[28] S.-i. Tamura, Physical Review B **27**, 858 (1983).

[29] W. Li, J. Carrete, N. A. Katcho, and N. Mingo, Computer Physics Communications **185**, 1747 (2014).

[30] W. Li, J. Carrete, and N. Mingo, Applied Physics Letters **103**, 253103 (2013).

[31] N. P. Blake, L. Møllnitz, G. Kresse, and H. Metiu, Journal of Chemical Physics **111**, 3133 (1999).

[32] G. K. Madsen and D. J. Singh, Computer Physics Communications **175**, 67 (2006).

[33] P. E. Blöchl, Physical Review B **50**, 17953 (1994); G. Kresse and D. Joubert, Physical Review B **59**, 1758 (1999).

[34] G. Kresse and J. Furthmüller, Computational Materials Science **6**, 15 (1996).

[35] J. P. Perdew, K. Burke, and M. Ernzerhof, Physical Review Letters **77**, 3865 (1996), erratum, *ibid.* **78**, 1396(E) (1997).

[36] K. Berland, V. R. Cooper, K. Lee, E. Schröder, T. Thonhauser, P. Hyldgaard, and B. I. Lundqvist, Reports on Progress in Physics **78**, 066501 (2015).

[37] K. Berland and P. Hyldgaard, Physical Review B **89**, 035412 (2014).

[38] J. Klimeš, D. R. Bowler, and A. Michaelides, Physical Review B **83**, 195131 (2011); T. Björkman, Journal of Chemical Physics **141**, 074708 (2014).

[39] W. Li, N. Mingo, L. Lindsay, D. A. Broido, D. A. Stewart, and N. A. Katcho, Physical Review B **85**, 195436 (2012).

[40] W. Li, L. Lindsay, D. A. Broido, D. A. Stewart, and N. Mingo, Physical Review B **86**, 174307 (2012).

[41] A. Togo, F. Oba, and I. Tanaka, Physical Review B **78**, 134106 (2008).

[42] O. Hellman and I. A. Abrikosov, Physical Review B **88**, 144301 (2013).

[43] L. Gharaee, P. Erhart, and P. Hyldgaard, Physical Review B **95**, 085147 (2017).

[44] D. O. Lindroth and P. Erhart, Physical Review B **94**, 115205 (2016).

[45] H. Anno, H. Yamada, T. Nakabayashi, M. Hokazono, and R. Shirataki, Journal of Solid State Chemistry **193**, 94 (2012), solid State Chemistry and Materials Science of Thermoelectric Materials.

[46] N. Tsujii, J. H. Roudebush, A. Zevalkink, C. A. Cox-Uvarov, G. J. Snyder, and S. M. Kauzlarich, Journal of Solid State Chemistry **184**, 1293 (2011).

[47] Y. Nagatomo, N. Mugita, Y. Nakakohara, M. Saisho, M. Tajiri, R. Teranishi, and S. Munetoh, Journal of Physics: Conference Series **379**, 012008 (2012).

[48] N. L. Okamoto, K. Kishida, K. Tanaka, and H. Inui, Journal of Applied Physics **100**, 073504 (2006).

[49] S. Y. Rodriguez, L. Saribaev, and J. H. Ross, Physical Review B **82**, 064111 (2010).

[50] Y. Takasu, T. Hasegawa, N. Ogita, M. Udagawa, M. A. Avila, K. Suekuni, I. Ishii, T. Suzuki, and T. Takabatake, Physical Review B **74**, 174303 (2006).

[51] Y. Takasu, T. Hasegawa, N. Ogita, M. Udagawa, M. A. Avila, K. Suekuni, and T. Takabatake, Journal of the Physical Society of Japan **77**, 254 (2008).

[52] Y. Takasu, T. Hasegawa, N. Ogita, M. Udagawa, M. A. Avila, K. Suekuni, and T. Takabatake, Physical Review Letters **100**, 165503 (2008).

[53] Y. Takasu, T. Hasegawa, N. Ogita, M. Udagawa, M. A. Avila, K. Suekuni, and T. Takabatake, Physical Review B **82**, 134302 (2010).

[54] T. Mori, S. Goshima, K. Iwamoto, S. Kushibiki, H. Matsumoto, N. Toyota, K. Suekuni, M. A. Avila, T. Takabatake, T. Hasegawa, N. Ogita, and M. Udagawa, Physical Review B **79**, 212301 (2009).

[55] K. Iwamoto, T. Mori, S. Kushibiki, H. Honda, H. Matsumoto, K. Suekuni, M. Avila, T. Takabatake, and N. Toyota, in *Materials Integration*, Key Engineering Materials, Vol. 508 (Trans Tech Publications, 2012) pp. 341–346.

[56] K. Iwamoto, S. Kushibiki, H. Honda, S. Kajitani, T. Mori, H. Matsumoto, N. Toyota, K. Suekuni, M. A. Avila, and T. Takabatake, Journal of the Physical Society of Japan **82**, 024601 (2013).

[57] We note that since only certain vibrational motions can be detected with Raman and THz spectroscopy techniques, it is possible to indirectly draw some conclusions regarding the symmetries of the modes. Specifically, those that are Raman active have either T_{2g} or E_g symmetries and represent vibrations parallel to the [100] and [110] directions.[53] With THz spectroscopy, however, the only visible, guest atom modes are those that are infrared active, and have T_{1u} symmetries.[54] Presumably, the lower and higher of these two modes correspond to motions perpendicular and parallel to the [001] direction (the out-of-plane direction in Fig. 1), respectively.

[58] D. Nataraj and J. Nagao, Journal of Solid State Chemistry **177**, 1905 (2004).

[59] M. A. Avila, K. Suekuni, K. Umeo, H. Fukuoka, S. Yamanaka, and T. Takabatake, Physical Review B **74**, 125109 (2006).

[60] M. Avila, K. Suekuni, K. Umeo, and T. Takabatake, Physica B **383**, 124 (2006).

[61] J. Martin, H. Wang, and G. S. Nolas, Applied Physics Letters **92**, 222110 (2008).

[62] A. F. May, E. S. Toberer, A. Saramat, and G. J. Snyder, Physical Review B **80**, 125205 (2009).

[63] J. Tang, R. Kumashiro, J. Ju, Z. Li, M. A. Avila, K. Suekuni, T. Takabatake, F. Guo, K. Kobayashi, and K. Tanigaki, Chemical Physics Letters **472**, 60 (2009).

[64] M. Troppenz, S. Rigamonti, and C. Draxl, Chemistry of Materials **29**, 2414 (2017).

[65] T. Uemura, K. Akai, K. Koga, T. Tanaka, H. Kurisu, S. Yamamoto, K. Kishimoto, T. Koyanagi, and M. Matsuura, Journal of Applied Physics **104**, 013702 (2008).

[66] The "center" for each of the $3 \times 54 = 162$ phonon modes, in the form of the eigenvalues of the Hessian matrix, was taken as the atom that gave the largest contribution to the phonon density of states at that particular frequency.

[67] A. Bentien, M. Christensen, J. D. Bryan, A. Sanchez, S. Paschen, F. Steglich, G. D. Stucky, and B. B. Iversen, Physical Review B **69**, 045107 (2004).

[68] M. Christensen, S. Johnsen, M. Söndergaard, J. Overgaard, H. Birkedal, and B. B. Iversen, Chem. Mater. **21**, 122 (2009).

[69] X. Hou, Y. Zhou, L. Wang, W. Zhang, W. Zhang, and L. Chen, Journal of Alloys and Compounds **482**, 544 (2009).

[70] A. Katre, J. Carrete, B. Dongre, G. K. Madsen, and N. Mingo, Physical Review Letters **119**, 075902 (2017).

[71] G. K. H. Madsen, A. Katre, and C. Bera, Phys. Status Solidi A **213**, 802 (2016).

[72] K. Biswas, J. He, I. D. Blum, C.-I. Wu, T. P. Hogan, D. N. Seidman, V. P. Dravid, and M. G. Kanatzidis, Nature **489**, 414 (2012).

[73] T. J. Scheidemantel, C. Ambrosch-Draxl, T. Thonhauser, J. V. Badding, and J. O. Sofo, Physical Review B **68**, 125210 (2003).

[74] G. D. Mahan and M. Bartkowiak, Applied Physics Letters **74**, 953 (1999).